The Effect of Steel Fibres on Moment Redistribution in High Strength Reinforced Concrete Beams

Frank Küsel

2018

UNIVERSITEIT VAN PRETORIA
UNIVERSITY OF PRETORIA
YUNIBESITHI YA PRETORIA

The Effect of Steel Fibres on Moment Redistribution in High Strength Reinforced Concrete Beams

Frank Küsel

A dissertation submitted in partial fulfilment of the requirements for the degree of

MASTER OF ENGINEERING (STRUCTURAL ENGINEERING)

In the

FACULTY OF ENGINEERING

UNIVERSITY OF PRETORIA

December 2018

PROJECT REPORT SUMMARY

THE EFFECT OF STEEL FIBRES ON MOMENT REDISTRIBUTION IN HIGH STRENGTH REINFORCED CONCRETE BEAMS

Frank Küsel

Supervisor: Professor E.P. Kearsley

Department: Civil Engineering

University: University of Pretoria

Degree: Master of Engineering (Structural Engineering)

The use of short, randomly distributed fibres in reinforcing concrete has led to improved durability and ductility, the latter of which is a key characteristic in the redistribution of moments. Steel fibres can be specified in the design of structural flexural members, as the only reinforcing, or in combination with traditional reinforcing bars. Practical material tests have been developed, although the added complexity inherent in the behaviour of FRC may result in shortcomings in sufficiently describing the mechanical properties of the structure.

Although steel fibres improve the general behaviour of a structure in terms of reducing crack widths and minimising deflections, the variability in the post cracking strength may lead to a less beneficial impact on moment redistribution. The overall change in the structural performance was therefore investigated, with the focus of this study being on the effects of different percentages and combinations of steel fibres and steel reinforcing bars on moment redistribution in statically indeterminate high strength concrete beams.

The experimental framework consisted of characterising the material properties of the FRC with fibre volume contents of 0 kg/m^3, 80 kg/m^3 (1.0%), 120 kg/m^3 (1.5%), and 160 kg/m^3 (2.0%) in 80 MPa concrete. An inverse analysis technique was used to determine the stress-strain properties of the FRC from the results of FPBTs.

A total of fifteen 5.0 m beams were cast, each with a different combination of steel fibres and steel bar reinforcing ranging from 0 to 3 bars. The change in structural behaviour was characterised into three major groups; loads and deflections, moment related results, and energy. An in-depth analysis of the

effects of the steel fibres was conducted to determine where the differences in behaviour could be explained by the material properties. The addition of fibres did not lead to significant increases in the load capacity, however deflections at relatively low loads were reduced. The optimum fibre content varied, depending on which aspect of the structural performance was considered. For ultimate relative deflections, the optimum fibre content increased with an increase in the number of reinforcing bars.

An optimum steel fibre content resulting in the maximum moment redistribution was found at a fibre content of 1.5%. Significant elastic moment redistribution occurred after cracking before any plastic behaviour occurred. Fibres were found to be less effective when combined with reinforcing bars, however their effectiveness increased with an increase in the number of reinforcing bars.

The outcome of this research was to provide greater understanding into the effect of varying amounts of steel fibres on structural behaviour and to clarify the complex inter-related mechanisms at work in the deformation of a beam.

DECLARATION

I, the undersigned hereby declare that:

- I understand what plagiarism is and I am aware of the University's policy in this regard;
- The work contained in this thesis is my own original work;
- I did not refer to work of current or previous students, lecture notes, handbooks or any other study material without proper referencing;
- Where other people's work has been used this has been properly acknowledged and referenced;
- I have not allowed anyone to copy any part of my thesis;
- I have not previously in its entirety or in part submitted this thesis at any university for a degree.

DISCLAIMER

The work presented in this report is that of the student alone. Students were encouraged to take ownership of their projects and to develop and execute their experiments with limited guidance and assistance. The content of the research does not necessarily represent the views of the supervisor or any staff member of the University of Pretoria, Department of Civil Engineering. The supervisor did not edit the final report and is not responsible for any technical inaccuracies, statements or errors. The conclusions and recommendations given in the report are also not necessarily that of the supervisor, sponsors or companies involved in the research.

Signature of student: 

Name of student: Frank Küsel

Student number: 13034619

Date: 05/12/2018

ACKNOWLEDGEMENTS

I would like to express my sincere gratitude to my supervisor, *Professor E.P. Kearsley* for advice and support during my study. Thank you for allowing me to interrupt your day with countless quick questions which often turned into hours of discussions. Your input in terms of technical advice and especially time is greatly appreciated and is a major factor in reaching the completion of this research. Thank you for the opportunities provided throughout these past two years.

I also wish to express my gratitude towards the *Concrete Institute* for providing the funding over the course of my studies.

I would also like to thank the following laboratory staff at the University of Pretoria:

- *Mr Derek Mostert* for his advice and assistance with the concrete mix designs, the testing of many concrete samples, and general help around the concrete laboratory,
- *Mr Johan Scholtz* for his advice and manufacturing of the equipment for the experiments and logistical aid in the concrete laboratory,
- *Mr Jaco Botha* for his preparation of the testing area and advice on the experimental tests,
- *Mr Rikus Kok* for his emergency technical help with the testing equipment,
- *The concrete laboratory staff: Jonas Selwadi, Samuel Nkadimeng, Richard Nchabaleng, Daniel Motloung, and Beua,* without whom this research would have remained purely theoretical. Thank you for all the effort and practical experience provided in the preparation and manufacturing of all concrete samples.

I would also like to acknowledge *Tiaan Bosman* for his time offered in the laboratory and ideas provided in the many cappuccino fuelled conversations.

The scale of the concrete casting also required the added manpower of *Martin Küsel, Martin Fechter, Stuart Hofmeyr and Nicholas Schoeman*, whose help at short notices I am very grateful for.

Finally, I have to mention the love and support provided by my parents, sister, grandmother, cousins and extended family. To my dad, *Ron*, thank you for your ideas and interest in my research, even though the similarities with farming are minimal, as well as your guidance and advice in life outside research. To my mom, *Anke*, thank you for the unlimited supply of encouragement, reassurance and phone calls. To my sister, *Petra*, thank you for making life at the flat enjoyable when the research wasn't, and Masterchef meals during the long hours. Thank you for allowing me to pursue a further two years of study. This work would not have been possible without your help.

TABLE OF CONTENTS

LIST OF TABLES

LIST OF FIGURES

LIST OF SYMBOLS

A	area of the cross-section	[mm^2]
α	slope of a portion pf the tensile stress-strain relationship	[MPa/ ε]
b	width of the beam cross-section	[mm]
b_c	width of the loading strip for the split cylinder test	[mm]
φ_{max}	curvature at maximum moment	[1/m]
φ_1	curvature corresponding to M_1	[1/m]
φ	curvature	[1/m]
δ	vertical deflection	[mm]
δ_m	deflection due to the moments	[mm]
δ_V	deflection due to shear forces	[mm]
Δ	sum of moment and shear deflections	[mm]
β	slope of a portion of the tensile stress-strain relationship	[MPa/ ε]
D	diameter if the concrete cylinders	[mm]
ε_{c0}	strain at the maximum linear elastic compressive stress	[MPa]
E	modulus of elasticity	[GPa]
G	shear modulus	[GPa]
h	depth of the section	[mm]
I	moment of inertia	[mm^4]
P	load	[kN]
P_i	load per mm length of the concrete cylinders	[kN/mm]
σ_{cu}	maximum compressive stress	[MPa]
σ_{t0}	cracking stress	[MPa]
σ_{t1}	residual stress (1)	[MPa]
M_{el}	elastic bending moment	[kNm]
M_L	moments due to the actual load	[kNm]
M_u	moments due to a unit load	[kNm]
M_{max}	maximum moment in the moment curvature relationship	[kNm]
M_{exp}	experimentally obtained bending moment	[kNm]
M_1	moment after peak moment in the moment curvature relationship	[kNm]
V_u	shear forces due to the actual load	[kNm]
V_L	shear forces due to a unit load	[kNm]
V_{max}	maximum shear force	[kN]
W_{int}	total internal work done	[J]
x	neutral axis depth	[mm]
y	distance from neutral axis	[mm]

ε	longitudinal strain
ε_{top}	compressive strain near the top of the beam cross-section
ε_{bot}	tensile strain near the bottom of the beam cross-section
$\varepsilon_{\mathrm{cu}}$	ultimate compressive strain
$\varepsilon_{\mathrm{t0}}$	cracking strain
$\varepsilon_{\mathrm{t1}}$	residual tensile strain (1)
$\varepsilon_{\mathrm{tu}}$	ultimate tensile strain
f_s	form factor for shear
K_{MR}	moment redistribution percentage
k_u	neutral axis depth over effective depth factor
γ	shear strain

CHAPTER 1

INTRODUCTION

1.1. BACKGROUND

The ability of steel fibres to improve the performance of a structure by improving the strength, reducing crack widths and minimising deflections can be attributed to the enhanced post-cracking properties. The brittle nature of concrete can be reduced with the addition of steel fibres, which improve the ductility, particularly in high strength concrete, a necessary characteristic for moment redistribution. This enhanced concrete material is commonly known as Fibre-Reinforced Concrete (FRC) and is widely used to improve the durability of a structure by limiting crack growth. In certain cases, the amounts of traditional reinforcing bars can be reduced by adding steel fibres, a practical solution which reduces steel congestion and labour required. The increased cost of fibres can thus be balanced by reduced overall production costs and reduced maintenance.

Moment redistribution is a complex mechanism which has been simplified to a great extent in guidelines for design. Steel reinforcing bars usually exhibit a strain hardening behaviour with a moment curvature behaviour in which an almost flat moment plateau is reached after the steel yields. This shape is often simplified into a bilinear curve which simplifies the calculations for moment redistribution. Steel fibres however exhibit characteristics which can deviate significantly from the ideal bilinear shape, and thus result in complex behaviours which are difficult to predict.

The widespread acceptance of steel fibres in the use of ordinary structures is based on the confidence of the designing Engineer. Confidence which requires firstly a complete understanding of structural performance changes caused by the addition of steel fibres, as well as the availability of reliable practical design methods. The behaviour of beams reinforced with only steel fibres has provided insight into how the material properties of fibres translate into actual behavioural changes in structures.

Of particular interest is the effect on indeterminate beams reinforced with both steel fibres and reinforcing bars. Since fibres are added to structures to improve the durability by limiting crack widths and deflections, the impact on moment redistribution capabilities might not be as beneficial. The shape of the post-cracking curve is a major indicator of the possibility of moment redistribution, where a strain hardening shape is desired. However, although fibres may show deflection softening behaviour, which is detrimental towards moment redistribution, the improved ductility of the concrete in compression may act as a countermeasure. The overall structural behaviour of indeterminate beams must therefore be investigated to weigh the various parameters of interest against one another so that the total effect of steel fibre reinforced high strength concrete is better understood.

1.2. OBJECTIVE OF THE STUDY

The aim of this research is to investigate the effects of different percentages and combinations of steel fibres and reinforcing bars on moment redistribution in high strength concrete. The main objectives of this study are as follows:

- To determine an optimum fibre and reinforcing bar combination ratio in terms of moment redistribution and overall structural behaviour using experimental results,
- To investigate the effects of different fibre and reinforcing bar ratios on the structural performance,
- To investigate whether an optimum fibre and reinforcing bar content can be determined theoretically from standard material properties.

Greater insight into the overall behaviour of an indeterminate structures is to be provided from this research by comparing the difference in behaviour of high strength concrete reinforced with only reinforcing bars, only steel fibres, or a combination of the two.

1.3. SCOPE OF THE STUDY

This research considers hooked ended steel fibre contents of 1.0%, 1.5%, and 2.0% in high strength concrete of 80 MPa with different amounts of Y12 (450 MPa yield strength) reinforcing bars.

The study is limited to:

- One concrete strength of 80 MPa
- One concrete mix composition
- One specific fibre type
- One reinforcing bar yield strength, bar diameter and length
- Only one specimen was cast for each different beam type

The material properties investigated for the indeterminate beams included:

- Compressive cube tests to obtain the compressive behaviour of the concrete,
- Cylinder tests to obtain the concrete modulus of elasticity,
- Flexural tests to obtain an indirect tensile response of not only the concrete alone, but also for concrete containing different percentages of steel fibres,
- Split cylinder tests to obtain a tensile strength parameter for the different concrete mixtures,
- Direct tension tests to determine the tensile behaviour of the steel reinforcing bars

The properties of the fibres themselves and their bond to the concrete were not investigated as the flexural tests were used to provide a composite material property for the fibre reinforced concrete. The bond strength between the reinforcing bars and the concrete was not considered and the reinforcing bars

were assumed to be sufficiently anchored. Material samples were cast with the same depth as that of the large-scale continuous beams to minimise size effect, which was excluded from the scope of the study.

Changes in the structural behaviour were evaluated in terms of the following measured parameters:

- Load and deflections measurements
- Curvature and strain measurements
- Surface deformation measurements

These measurements were used to evaluate structural characteristics such as moment-curvature, moment redistribution, crack spacing and plastic hinge lengths. The changes in moment redistribution were ascribed solely to the change in the volume of steel fibres and reinforcing bars, while all other parameters were kept constant.

1.4. METHODOLOGY

An outline of the methodology followed, to investigate the changes in structural behaviour of an indeterminate reinforced concrete structure, is as follows:

- A literature study was conducted which included an introduction to steel fibres and their influence on the behaviour of Steel Fibre Reinforced Concrete (SFRC). Test methods to characterise SFRC were discussed. The concept of moment redistribution was described theoretically before research on moment redistribution and the overall behaviour of SFRC and concrete reinforced with steel bars was reviewed.
- The experimental procedure was executed in two parts. The first part entails the tests required to obtain the material properties. An additional chapter deals with an inverse analysis procedure required to calculate the tensile properties form flexural tests. In the second part of the experimental procedure the setup used for the actual indeterminate tests is described followed by the discussion of the test results.
- The discussion of the results are categorised into load and deflection results, moment related results, and energy related results.

1.5. ORGANISATION OF THE REPORT

The dissertation consists of eight chapters, followed by a list of references. A brief overview of each chapter is as follows:

Chapter 1: INTRODUCTION

An overview of the entire study. The background and objective of the research is introduced, followed by the scope, limitations, methodology, and organisation of the report.

Chapter 2: LITERATURE REVIEW

A literature study is conducted on the effects of SFRC in terms of material properties and overall structural behaviour. Tests methods to characterise the material properties used within this study are discussed. Moment redistribution is introduced as theory after which research is presented on various factors influencing the overall structural behaviour.

Chapter 3: ELEMENT TESTING AND RESULTS

In this chapter, standard tests are performed, followed by their respective material property results. The tensile behaviour of SFRC is, however, not presented as a material property, but instead as a tensile splitting strength, load-deflection response and a moment-curvature relationship.

Chapter 4: STRESS-STRAIN RELATIONSHIP

This chapter describes an inverse analysis procedure used to convert the load-deflection and moment-curvature responses into tensile stress-strain material properties. Assumptions in these calculations are stated, and the output is a simplified stress-strain property of each concrete mix.

Chapter 5: EXPERIMENTAL SETUP

The indeterminate continuous beam setup is illustrated in this chapter. The different aspects of the structural behaviour to be measured is discussed, which includes the calculations required to convert the readings to meaningful results. The accuracy of measuring equipment is also verified by a comparison between the results obtained from the Linear Variable Differential Transformer (LVDTs) and Particle Image Velocimetry (PIV).

Chapter 6: LOAD DEFLECTION RESULTS

An in-depth discussion of the continuous beams is presented. This chapter is divided into two major sections, load related and deflection related results.

Chapter 7: MOMENT REDISTRIBUTION RESULTS

The moment related results are presented in this chapter. Moment redistribution results are discussed as well as the evolution of moments along the length of the beam and in

terms of the external load applied. Theoretical moment curvatures and neutral axes are discussed in light of the results.

Chapter 8: ENERGY

The concept of the overall energy absorbed by the beams is described based on the load deflection results. Crack spacing, and hinge lengths are described shortly to explain behaviour.

Chapter 9: CONCLUSIONS AND RECOMMENDATIONS

This chapter summarises the main conclusions reached throughout this study and includes recommendations for further research.

CHAPTER 2

LITERATURE REVIEW

2.1. HISTORICAL BACKGROUND

The use of fibres in concrete is a concept which dates back many years, and one can consider the patent granted in 1874 (Berard, 1874) as the official starting point of fibre reinforced concrete. It was only later in the 1960's where research into FRC gained momentum again (Naaman, 2007). This renewed interest was led by Romualdi and Mandel (1964). In their studies they revealed that the brittleness of concrete, one of its major limitations as a material, could be reduced with the addition of short steel fibres. The benefits of fibre reinforced concrete attracted an increasing number of researchers during the 19070's, expanding the field to include different fibre types including different materials such as glass, carbon and synthetics (Aveston and Kelly, 1973, Hannant, 1978, Naaman and Shah, 1979, Shah and Rangan, 1971, Swamy et al., 1974).

The results of the research led to a significant enhancement in the ductility of FRC. However, although the toughness of the material was increased with the addition of fibres, the improvement in ductility was limited. Although the fibres bridged the crack, failure usually occurred in a single crack since the fibres were unable to cause the development of additional cracks. Therefore, there was not much improvement in the ductility of FRC until the end of the 1970's where multiple cracking was reported. One of the earliest publications reporting multiple cracking in bending and tension were published by Naaman and Shah (1979).

The complexity of FRC does not allow for brevity, therefore, only major milestones in its history are summarised in this dissertation to reveal how the concept of FRC came about and the reason it has gained so much interest. In short, the addition of fibres improves the ductility and toughness of concrete overcoming a major weakness of concrete; brittleness. Fast forward to the present time and the study of FRC has evolved into a vast ocean of knowledge through continuous research from a multitude of different perspectives. In essence FRC is a composite material that can be characterised by enhanced post-cracking tensile residual strength due to the fibres bridging the crack surfaces (di Prisco et al., 2009).

In any composite material, the fibres are added to improve the material behaviour. Since cement-based materials create a brittle matrix, the fibres are added to improve the toughness. To optimise the performance of the composite material one must consider the following main controlling factors (Löfgren, 2015):

1. The volume of fibres.
2. The physical properties of the fibres and the matrix.
3. The strength and bond between the fibres and the matrix.

The scope of this research covers only steel fibres which will be described in the following sections.

2.2. STEEL FIBRES

A definition for steel fibres can be found in the European Standard which describes them as '*straight or deformed pieces of cold-drawn steel wire, straight or deformed cut sheet fibres, melt extracted fibres, shaved cold drawn wire fibres and fibres milled from steel blocks which are suitable to be homogeneously mixed into concrete or mortar*' (EN 14889-1, 2007). Several different types of steel fibres exist, some of which are shown in Figure 2-1 (Naaman, 2003). Adhesion and friction are the basic components of bond between concrete and smooth fibres with an additional mechanical component of bond created when the fibre is deformed (Sujivorakul et al., 2000). The hooked ended steel fibres are most commonly used in industry due to the improved fibre-matrix bond and increased fibre efficiency (Brandt, 2008).

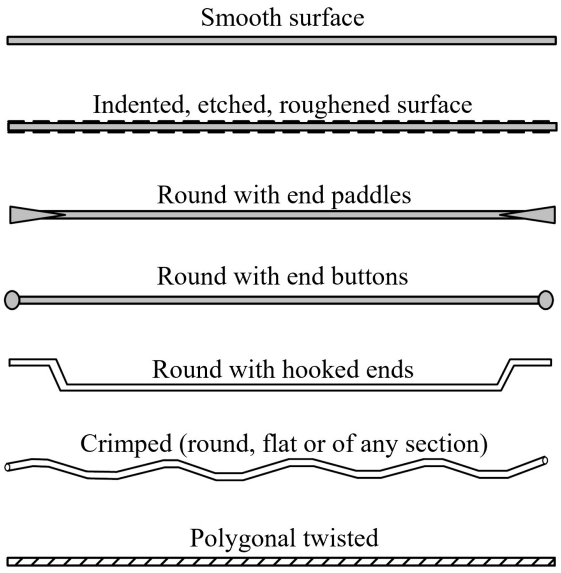

Figure 2-1: Different types of steel fibres (taken from Naaman, 2003)

The stresses in a straight fibre are shown in Figure 2-2. A certain length of fibre is required for effective strengthening of the composite material. This critical length, l_c, depends on the tensile strength of the fibre, the fibre diameter, and the fibre-matrix bond strength. As the fibre length increase beyond the critical length the fibre reinforcement becomes more effective as more tensile stresses can be resisted (Illston & Domone, 2002). Fibres with hooked ends or deformations provide additional mechanical strength in addition to the stresses shown in Figure 2-2.

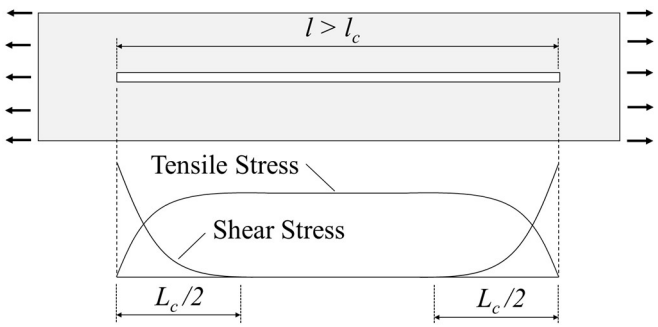

Figure 2-2: A schematic representation of a fibre embedded in a matrix subject to axial stress

For the fibres to be effective in cementitious materials they should have the following properties (Naaman, 2003):

1. Tensile strength significantly higher than that of concrete (two or three orders of magnitude).
2. A bond strength with the concrete matrix preferably of the same order as, or higher than, the tensile strength of the matrix.
3. An elastic modulus in tension significantly higher than that of the matrix.
4. Sufficient ductility so that the fibre does not fracture.

In addition, the Poisson's ratio and coefficient of thermal expansion should preferably be of the same order for the fibres and the matrix to prevent debonding. Even if the fibres are effective, their performance is further controlled by other factors and the primary variables used to control the fibre performance are; (1) the aspect ratio; (2) the fibre geometry; and (3) surface treatment (Löfgren, 2005). The aspect ratio will determine the number of fibres that cross a cracking plane. For instance, for short fibres with a high aspect ratio, a much higher number of steel fibres will cross a plane when compared to more conventional steel fibres when considering the same volume fraction of fibres. An optimal aspect ratio will ensure that the fibre will fail at the same load causing pull-out of the fibres. The geometry of the fibres includes the length and diameter of the fibre, where longer fibres are able to bridge across larger cracks. However, the shape of the fibre, will influence how the fibre interacts with the concrete. Fibres with hooked ends, or crimped wires, or any other geometry other than a straight wire do not need to rely solely on the bond between the wire and the concrete due to the mechanical anchorage. Straight wires in particular may require surface treatments such as a roughened or indented surface to provide improved bond between the fibre and the concrete.

A vast range of different combinations of fibre geometries, lengths and aspect ratios to name a few variables can be chosen to improve the performance of the SFRC to the point where it exhibits a deflection hardening response in bending (Paegle, 2015). This improved post-cracking strength is the key to the success of the composite and will be discussed in greater depth in the following sections.

2.3. MECHANICAL PROPERTIES

Generally, the property by which concrete is classified is the compressive strength. However, for fibre reinforced concrete, the increase in toughness and residual strength is not portrayed by the compressive strength. The influence of steel fibres on the compressive, tensile and shear properties will be discussed briefly.

2.3.1. COMPRESSION

A linear stress-strain response is observed up to about 30% of the compressive strength of concrete. This is followed by a gradual loss in linearity up to the peak stress beyond which strain softening take place. The difference between ordinary concrete and fibre reinforced concrete is illustrated in Figure 2-3 (Löfgren, 2005). Neville (1997) proposed that the curvilinear shape is a result of the interfaces between the aggregate and the hardened cement paste in which microcracks develop. As the concrete strength increases, the concrete becomes more brittle.

With fibres present in the matrix, the ductility is improved as the fibres provide tensile resistance against the cracks formed. At the macrocrack level the ability for fibres to resist the crack growth results in increased energy absorption capacity. The addition of fibres generally does not necessarily increase the compressive strength by much (Maidl, 1995, König & Kützing, 1999), but can in rare cases increase the strength by up to 25% as reported by Balaguru and Shah (1992). An increase in toughness is one major contributing factor of steel fibres, which results in increased strains during and after the peak stress, an increase which is slightly more evident in lower grade concrete than higher grade concrete (Nataraja et al., 1999). The main advantage in terms of compressive behaviour is that concrete does not crush but holds its integrity at much higher deformations (Olivito and Zuccarello, 2010).

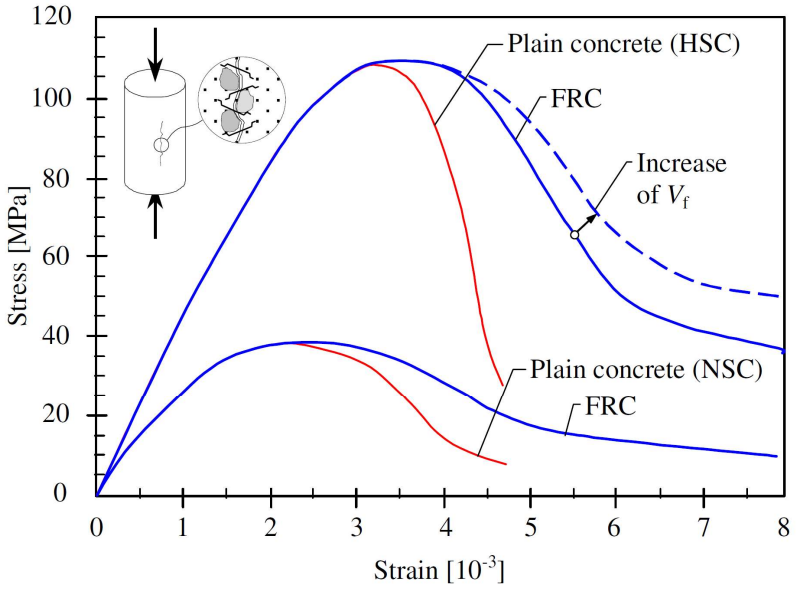

Figure 2-3: Behaviour of concrete and FRC in compression (taken from Löfgren, 2005)

2.3.2. TENSION

Concrete is characterised by its brittle failure in tension, which is what steel fibres aim to avoid by introducing more ductility. The tension behaviour of SFRC can be classified as either strain-softening, or strain-hardening and is illustrated in Figure 2-4 (Löfgren, 2005). Softening behaviour is usually accompanied by a concentration of deformation in a single crack (Paegle, 2015). If the maximum load capacity occurs after the first crack strength, the composite is strain hardening, the magnitude of which is governed by the fibre bridging strength.

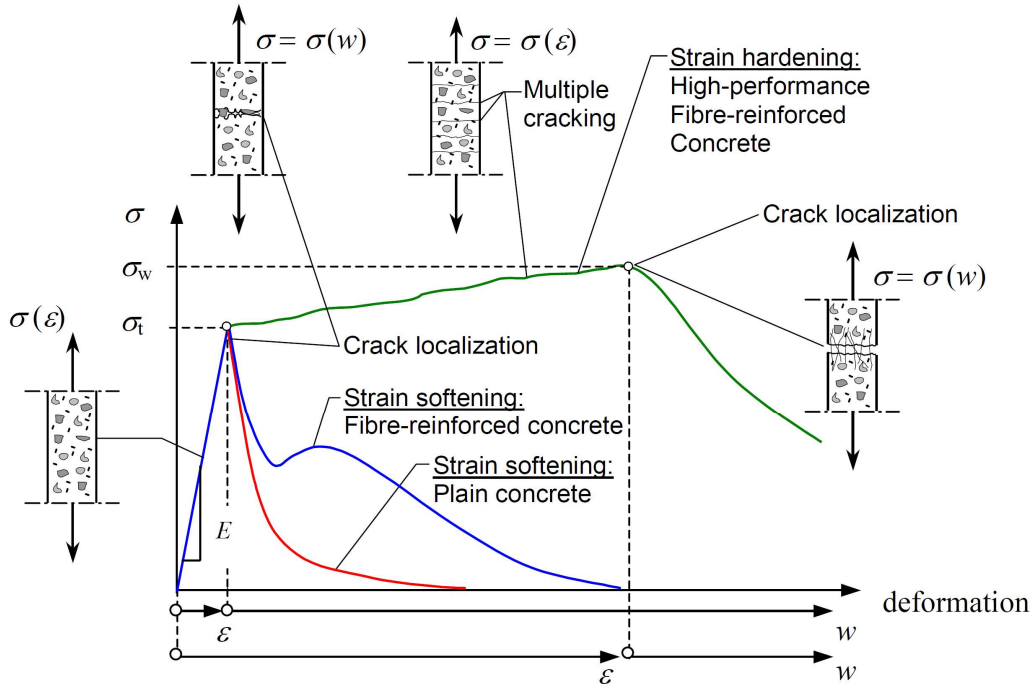

Figure 2-4: Classification of tensile behaviour of cement-based materials (taken from Löfgren, 2005)

The tensile behaviour can be divided in to three stages; a linear elastic stage, a micro-cracking stage, and a macro-cracking stage (Kooiman, 2000). A change in steel fibre content has little effect on the linear elastic stage since the contribution to the Young's modulus of the composite is hardly affected by the addition of fibres. The bond between the fibre and matrix are very important when considering the micro-cracking stage. After a macro-crack has formed and the peak load has been reached, a steep reduction in load is often found in uni-axial tensile tests. Various factors influence the post crack localisation behaviour, some of which include the frictional stresses at the fibre matrix interface, fibre type and volume, fibre orientation and the distribution of fibres.

It is evident that the most distinctive feature of FRC is the ability for the fibres to transfer stresses across a fractured surface. While aggregate interlock provides only a very limited stress transfer in conventional concrete, fibres allow significant stress transfer across cracks until the fibre either pulls out or ruptures. The crack opening process depends on the ability of the fibre to transfer these stresses

resulting in various load-deformation responses. Characterising this tensile behaviour can be done through uni-axial tension tests, or flexural tests as shown in Figure 2-5. However, the problem is that a strain softening material can exhibit a load-deflection behaviour which differs from the shape of the stress-strain response, which depends on the toughness and geometry of the specimen. For instance, a beam initially showing a load-deflection shape similar to that of strain hardening behaviour may tend towards a softening shape as the depth of the beam is increased. Since the material of the beam has not been changed, the strain softening or hardening behaviour remains unchanged, hence the softening or hardening behaviour may differ for strain responses when compared to deflection responses. (Löfgren, 2005).

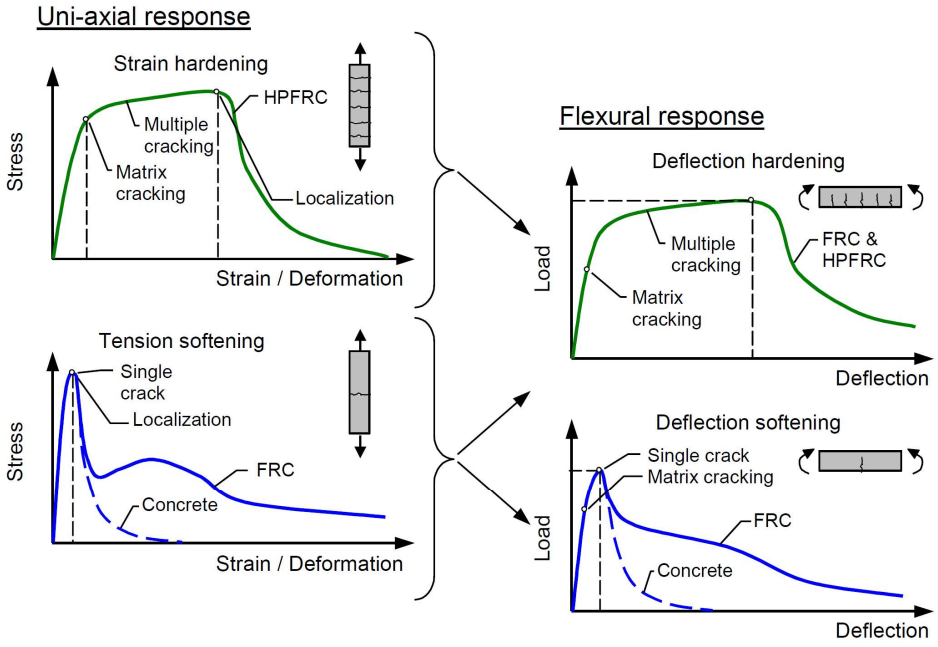

Figure 2-5: Characterisation of the tensile and flexural behaviour taken from Löfgren (2005)

An increment in fibre content results in an increase in ductility, flexural strength, and if the bond between the fibres and matrix is sufficient, a possible increase in the first cracking strength (Olivito, 20010, Kang et al., 2009). The increase in tensile resistance, resulting from an increase in fibres, relies on a similar increase in the effective number of fibres crossing the cracked surfaces (Barros et al., 2004).

2.4. TEST METHODS TO CHARACTERISE THE TENSILE BEHAVIOUR OF SFRC

There is a need in structural engineering to verify material properties to ensure that parameters used in design comply with in-situ properties. Standardised test methods that are not only quick and simple, but can also characterise material properties with a sufficient degree of precision and accuracy, are essential before any new material can be accepted in designs. Herein lies the obstacle preventing the widespread use of steel fibre reinforced concrete. The problem is that laboratory tests which attempt to characterise

the material behaviour often fail since steel fibre reinforced concrete is subject to size effects. Therefore, the defined material properties are in fact not material properties as they are affected by geometry, rendering them meaningless in the design of a structure. Fortunately, many standardised test methods exist now which attempt to instil confidence in the design of fibre reinforced concrete.

The different compressive and indirect tensile tests used for FRC will be discussed in the following section. Limitations and advantages of each method will be assessed based on strain hardening and strain softening behaviour.

The most important aspect of SFRC is the behaviour in tension since the advantage of adding steel fibres is that they generate a post-cracking residual strength in combination with a large tensile strain (fib, 2013). Since the behaviour of SFRC concrete is affected by many factors such as geometry, volume fraction, bond between the fibre and concrete, and fibre orientation, it is important to define suitable material parameters which best describe the post-peak tensile behaviour to be used in structural design.

Three main types of test setups used to evaluate the post-cracking response are:

- Uni-axial or direct tension test, with a prescribed crack or possible multiple cracking.
- Flexural tests performed on notched or un-notched prisms under three or four-point loading.
- Flexural panel or plate tests, on square panels with continuous supports or round panels with three point supports.

Other tests include the wedge-splitting test (WST) and other splitting tests which measures the splitting tensile strength (NT-Build511, 2005, JSCE, 2008, RILEM 162-TDF, 2001, EN 14651, 2007, fib, 2013, JCI-S-002, 2003, ASTM C1609, 2012, DAfStb, 2010, DBV, 2007, JCI-S-003, 2007). Considering that this report aims to evaluate the flexural behaviour of continuous beams, only the three and four-point bending tests will be discussed as well as splitting tests owing to the simplicity of the setup. The flexural tests would provide an indication of the shape of the load-deflection responses of the fibre reinforced concrete, which would not be possible with direct tensile tests. Furthermore, additional behaviour such as moment curvature responses can be measured from flexural tests which provide an insight into moment redistribution capabilities.

2.4.1. SPLITTING TESTS

One of the best-known splitting tests is known as the Brazilian splitting test which is performed on a cylinder as illustrated in Figure 2-6 (Neville, 1978). Although the test can be carried out in load control, if the post-cracking behaviour of the SFRC is required the test must be carried out in deformation control. The loads are applied at opposite ends of the cylinder's circumference, often with metal strips placed along the cylinder to avoid spalling. LVDTs are used to measure the horizontal displacement.

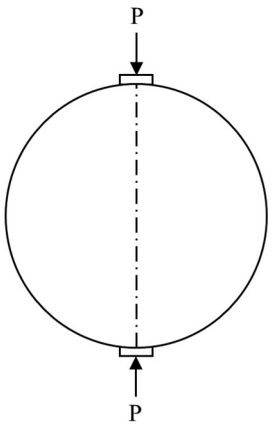

Figure 2-6: Brazilian splitting test (Neville, 1978)

The split cylinder test is a standard test method to obtain tensile strengths. Standards such as ASTM C496 (2008) indicate that the tensile splitting strength should be calculated from the peak load assuming continuum mechanics for a circle with two-point loads. However, the high post-cracking stress capacity of steel fibre reinforced concrete means that the peak load is no longer associated with the linear elastic stress condition along the loading plane. The equations provided by Timoshenko and Goodier (1970) for the stress calculation of two load points at opposite ends of a circle are also not entirely accurate as the specimen actually experiences the load across a loading strip with a certain width instead of through load points (Tang, 1994). The crack growth typically occurs in two stages, with a primary crack growth followed by secondary cracking (Rocco et al, 1999) and is illustrated in Figure 2-7.

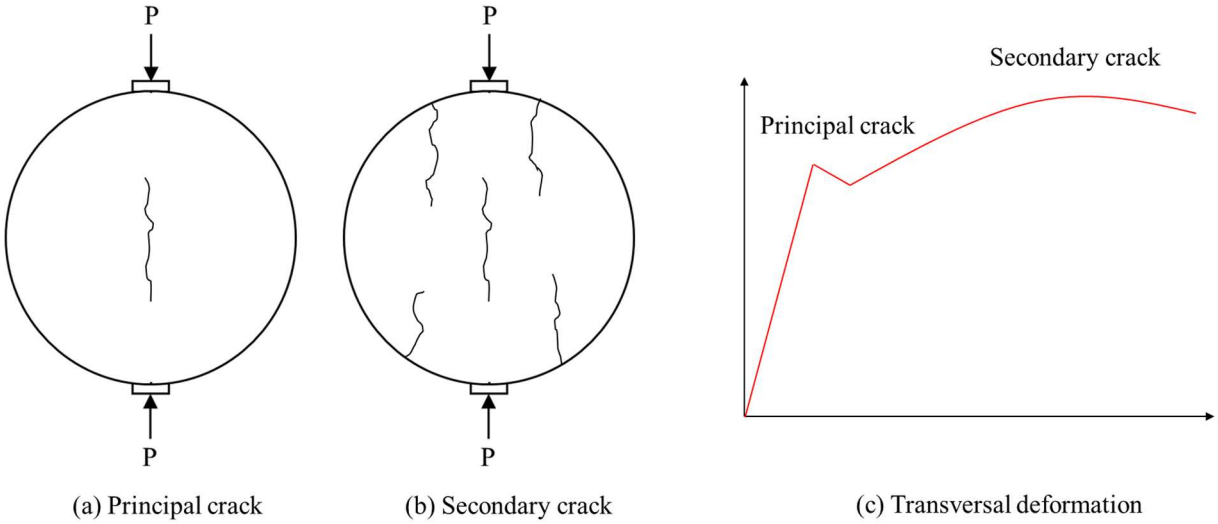

Figure 2-7: (a) Principle crack, (b) secondary crack formation, and (c) load vs displacement response

The transverse deformation of the cylinders is recorded on either side with LVDTs measuring the deformation between two rods drilled into the sample as shown in Figure 2-8. This is an improved method of measuring horizontal displacements shown by Denneman (2011) which differs from measuring the horizontal deformations using spring-loaded LVDTs pushing against the outer edges of the cylinder. Securing the LVDTs into the cylinder ensured improved precision as opposed to spring-loaded LVDTs which were mounted to the base plate of the testing machine which are separate from the concrete cylinder, and hence provided less consistent results when compared to the results of the LVTDs mounted on the cylinder (Denneman, 2011). Tensile strengths are calculated from the equation proposed by Tang (1994) which includes the correction for the load strip width:

$$f_t = \frac{2P_i}{\pi D}\left[1 - \left(\frac{b}{D}\right)^2\right]^{\frac{2}{3}} \qquad \textit{Equation 2.1}$$

Where P_i is the peak load at first cracking, D is the diameter of the cylinder, and b is the width of the loading strip.

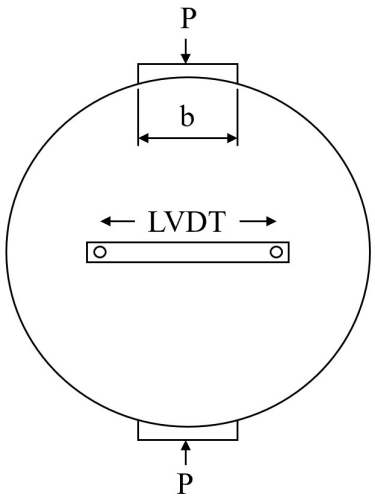

Figure 2-8: Split cylinder deformation measurements

2.4.2. FLEXURAL TESTS

The two most common flexural tests are the three-point and four-point bending test. The differences between the two test types is shown in Figure 2-9. In general, only the test specimen for 3PBT is notched. A general overview of each testing method will first be given. Thereafter, a suitable testing method will be chosen once both test methods have been assessed in terms of providing the most accurate predictions for the full-scale moment redistribution tests.

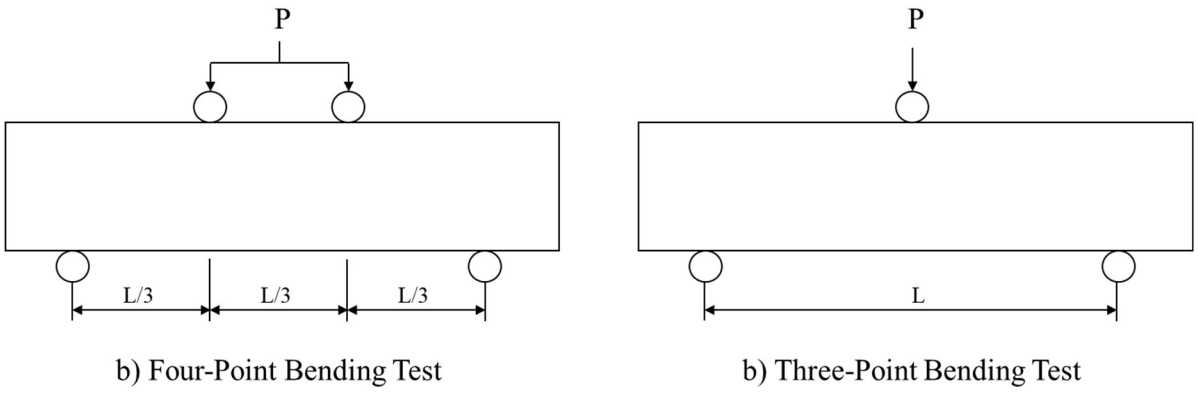

Figure 2-9: Three- and Four-Point Bending Tests

2.4.3. THREE POINT BENDING TEST

Several standards have adopted the three-point bending tests (TPBT), shown in Figure 2-9, including the European standard EN 14651 (2007), RILEM technical Committee guidelines (162-TDF, 2002), the Japanese Concrete Institute (JCI-S-002, 2003) and is the suggested standard in the fib Model Code (fib, 2013). Each standard suggests different test methods which are suitable only for specific specimen types and geometries. For instance, EN 14651 requires a specimen length between 550 mm and 700 mm whereas the JCI-S-002 (2003) allows the length to vary in relation to the specimen depth. However, each of the different test methods provides a relationship between the load and the crack mouth opening distance (CMOD) from which the tensile behaviour can be evaluated in terms of residual flexural tensile strength values. An example of a load CMOD response from a 3PBT test is shown in Figure 2-10.

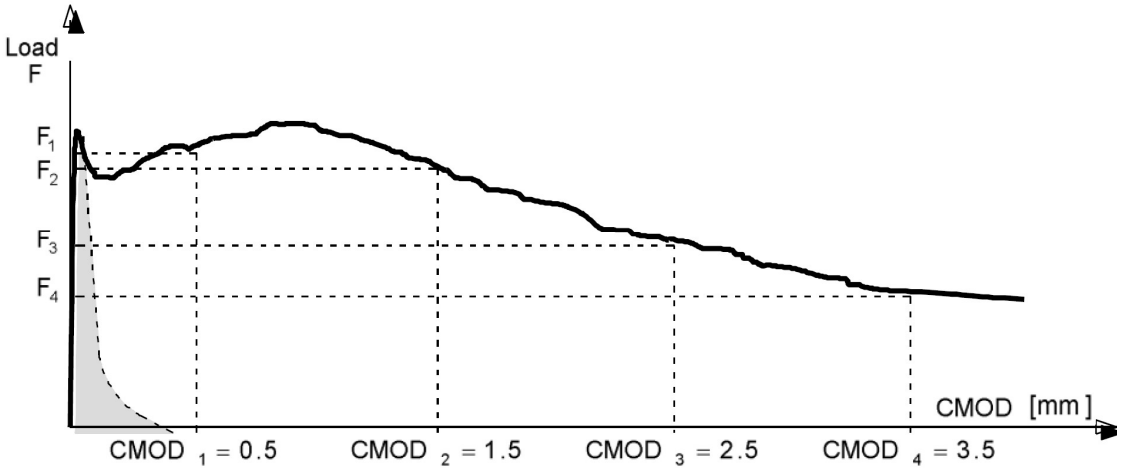

Figure 2-10: Load-crack mouth opening from a TPBT (fib, 2013)

The fib Model Code (fib, 2013) classifies the post-cracking strength of FRC by considering the residual strengths for service (f_{R1k}) and ultimate (f_{R3k}) conditions which correspond to $CMOD_1$ and $CMOD_3$, as well as F_1 and F_3. The designer would then classify the material according to the class, material of the fibre and the residual strength ratio (f_{R3k}/f_{R1k}). For structural design purposes, an inverse analysis is used to derive the stress-crack width relations.

One advantage of the notched 3PBTs is that a direct relationship can be found between the bending moment and the crack-width. However, the position of the notch in the midspan does not necessarily reflect the weakest cross-section. Another benefit is that the analysis of a single cross-section in bending is made possible by the 3PBT (Kooiman, 2000).

2.4.4. FOUR POINT BENDING TEST

Various standards have chosen to adopt the FPBT, including ASTM C1609 (2012), DAfStb (2010), DBV – Guide to Good Practice (2007) and the standard from the Japanese Concrete Institute (JCI-S-003, 2007). Again, each standard proposes different limitations on geometry and fibre lengths. An overview is given by Paegle et al. (2015), providing the specimen type and shape, fibre and aggregate limitations, test setup and results of each testing method. A typical load-deflection result of a FPBT is shown in Figure 2-11.

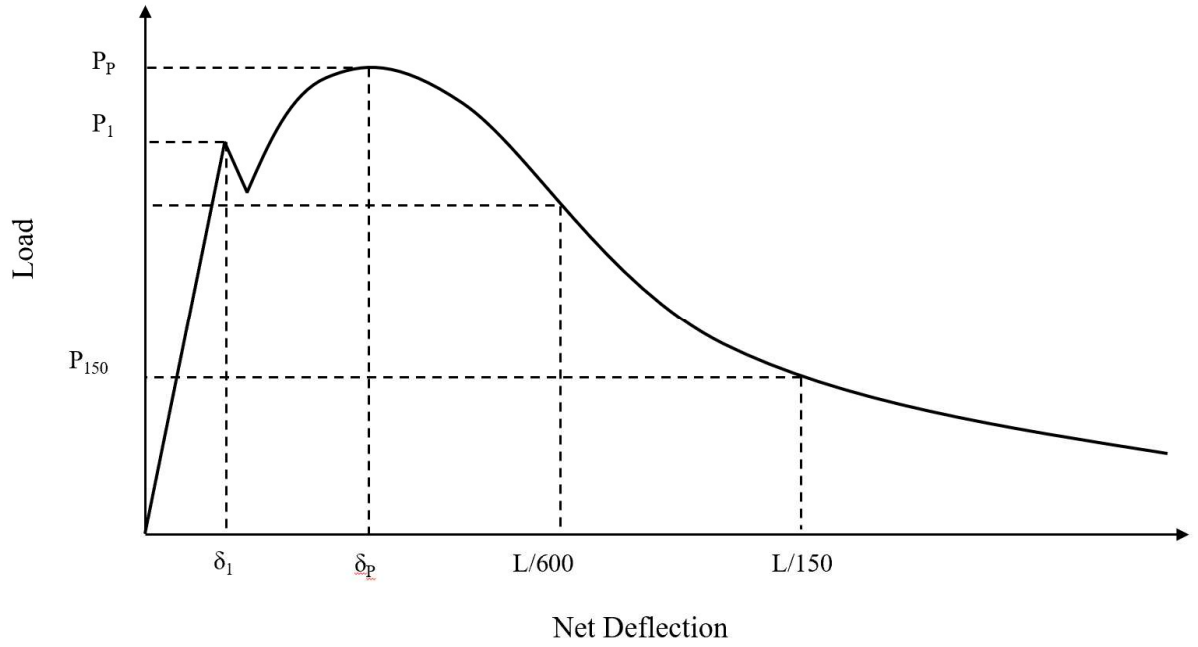

Figure 2-11: Load deflection response from a FPBT (ASTM C1609, 2012)

The effect of hooked ended steel fibres in combination with reinforcing bars was investigated by Holschemacher et al. (2010). An example of the difference in behaviour between beams with only fibres

and beams with fibres and steel reinforcing bars (500 MPa yield strength) is illustrated in Figure 2-12 (a) and (b). The beams with only fibres (a) show a softening load deflection behaviour which turns to deflection hardening when reinforcing bars are added (b). The ability for the steel fibres to increase the load capacity reduces as they are combined with more reinforcing bars. Figure 2-12 (a) and (b) illustrates this concept by plotting the parts of the load deflection curves contributed by the steel fibres. For the beam specimens shown, the load bearing capacity of fibres in beams without reinforcing bars was always higher at lower deflections for any fibre content. This behaviour indicates that the bars initially absorbed a big portion of the first crack energy as a result of better bonding between the reinforcing bars and the concrete. The additional load bearing capacity introduced by the fibres becomes evident at higher deflections and becomes less effective as the number of reinforcing bars increases relative to the fibre content.

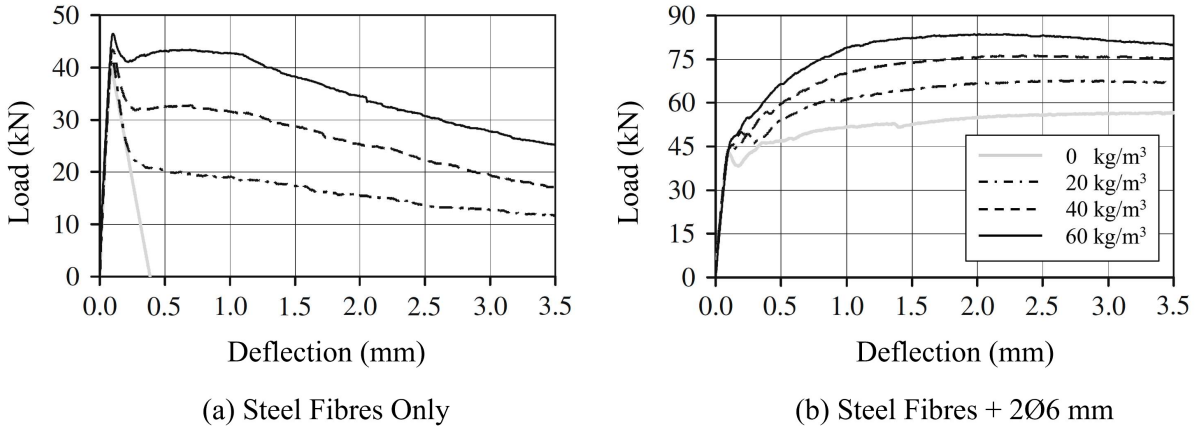

Figure 2-12: Load deflection response of beams containing steel fibres and steel reinforcing (Holschemacher et al., 2010)

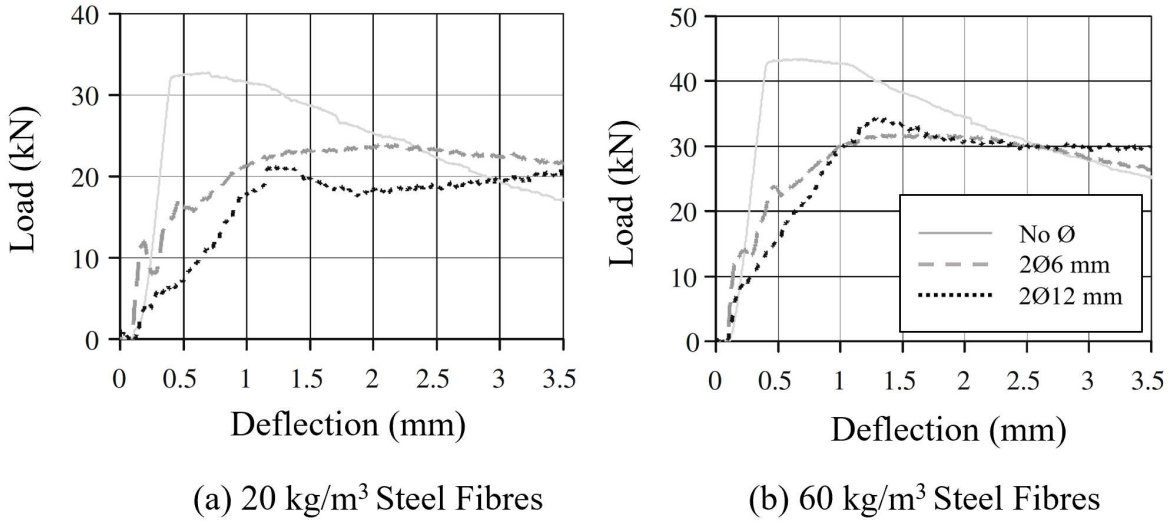

Figure 2-13: Load deflection contribution of the steel fibres in beams with reinforcing bars (Holschemacher et al., 2010)

Additionally, a direct moment-curvature relationship can be obtained when utilising the setup in the JCI-S-003 (2007). Here, the strains near the top and the bottom of the beam are recorded to deduce the curvature. A typical graph obtained from such a setup is shown in Figure 2-14.

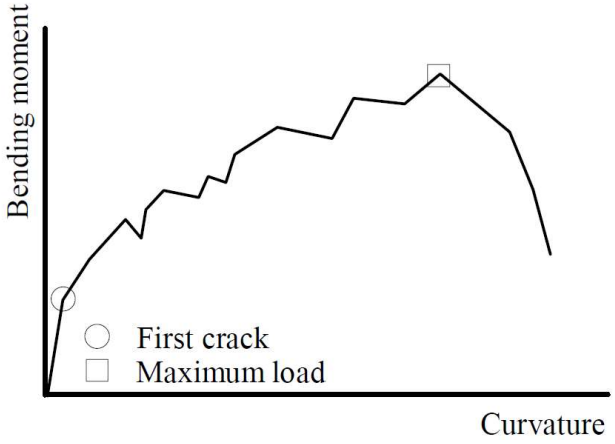

Figure 2-14: Moment curvature response from a FPBT (JCI-S-003, 2007)

FRC is characterised by an equivalent or residual flexural strength (f_{eq}) at a specific deflection. The residual flexural strengths are calculated from the loads corresponding to net deflections of L/600 or L/150, where L is the span length according to the ASTM-C1609 (2012) method. Other methods to characterise the flexural strength include a dimensionless toughness index, which is a measure of the energy absorption capacity, at prescribed deflections as used by ASTM-C1609 (2012).

The constant moment region between the two-point loads of a FPBT ensures a greater possibility of crack formation in the weakest section of the specimen. Whereas the TPBT was limited to strain softening materials, the constant moment region in FPBTs allows the formation of multiple cracks in deflection hardening materials. However, as noted by Kooiman (2000), it is difficult to measure crack opening displacements since the location of the discrete crack or cracks cannot be predicted.

2.5. MOMENT REDISTRIBUTION

The following section on moment redistribution deals with the theoretical concepts governing the behaviour which defines moment redistribution. Although the theoretical derivations and definitions of the parameters involved are clearly defined, the practical aspects of measuring certain variables can be a complicated process. The problems related to calculating the variables involved in moment redistribution from experiments will be discussed in a later section.

The danger of brittle failure in concrete members is averted with steel reinforcing by suitable design to ensure ductile behaviour. In the rare event that a structure is loaded to failure, sufficient ductility will allow large deflections to serve as a warning before collapse. Without ductility there would be no

tolerance between the design of a structure and the actual construction of it. The imperfect nature of construction lends its success to the ability of members to deform when a fit is not perfect. The ductility of a member is what allows possible redistributions of forces in statically indeterminate structures.

Moment redistribution depends on the ductility of the section and results in a distribution of bending moments that differ from the moments obtained from an elastic analysis. This behaviour is possible if plastic rotation can occur in sections reaching their ultimate load. A further load increase is then possible if the critical section forms a plastic hinge. The moment is therefore maintained at the first plastic hinge whilst further loading increases the moments in other sections until they reach their limit. The load can increase until sufficient plastic hinges have formed to create a collapse mechanism. Most codes allow some degree of moment redistribution which has the benefit of reducing the hogging moment at supports thereby reducing the congestion of reinforcement (Park & Paulay, 1975). Savings in reinforcing costs are also possible by shifting the moments away from less efficient to more efficient cross-sections. The flexural behaviour can best be described by the moment curvature characteristics.

2.5.1. MOMENT CURVATURE

An initially straight member of reinforced concrete will deform as shown in Figure 2-15 when subject to equal end moments and axial forces. The neutral axis depth will vary along the length of the member as cracks from. The radius of curvature *R* is measured to the neutral axis and will therefore also vary along the member (Gere & Goodno, 2011). Considering a small length *dx* of the member, the rotation between the ends can be described by:

$$\frac{dx}{R} = \frac{\varepsilon_x dx}{kd} = \frac{\varepsilon_s dx}{d(1-k)} \qquad \textit{Equation 2.2}$$

$$\frac{1}{R} = \frac{\varepsilon_c}{kd} = \frac{\varepsilon_s}{d(1-k)} \qquad \textit{Equation 2.3}$$

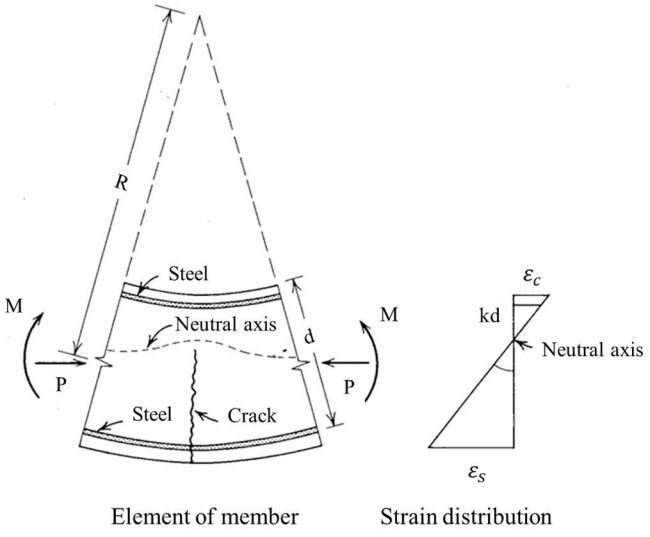

Figure 2-15: Deformation of a flexural member (Park & Paulay, 1975)

The curvature (φ) of the element is defined as $1/R$, resulting in the following equation which shows that the curvature is the gradient of the strain profile:

$$\varphi = \frac{\varepsilon_c}{kd} = \frac{\varepsilon_s}{d(1-k)} = \frac{\varepsilon_c + \varepsilon_s}{d} \qquad \textit{Equation 2.4}$$

The moment curvature relationship for a section may be obtained by measuring the strains over a short length such that the curvature can be calculated as the moment increases. The contrast between failure in tension and compression is illustrated in Figure 2-16. Initially both moment curvature curves are linear until the concrete cracks.

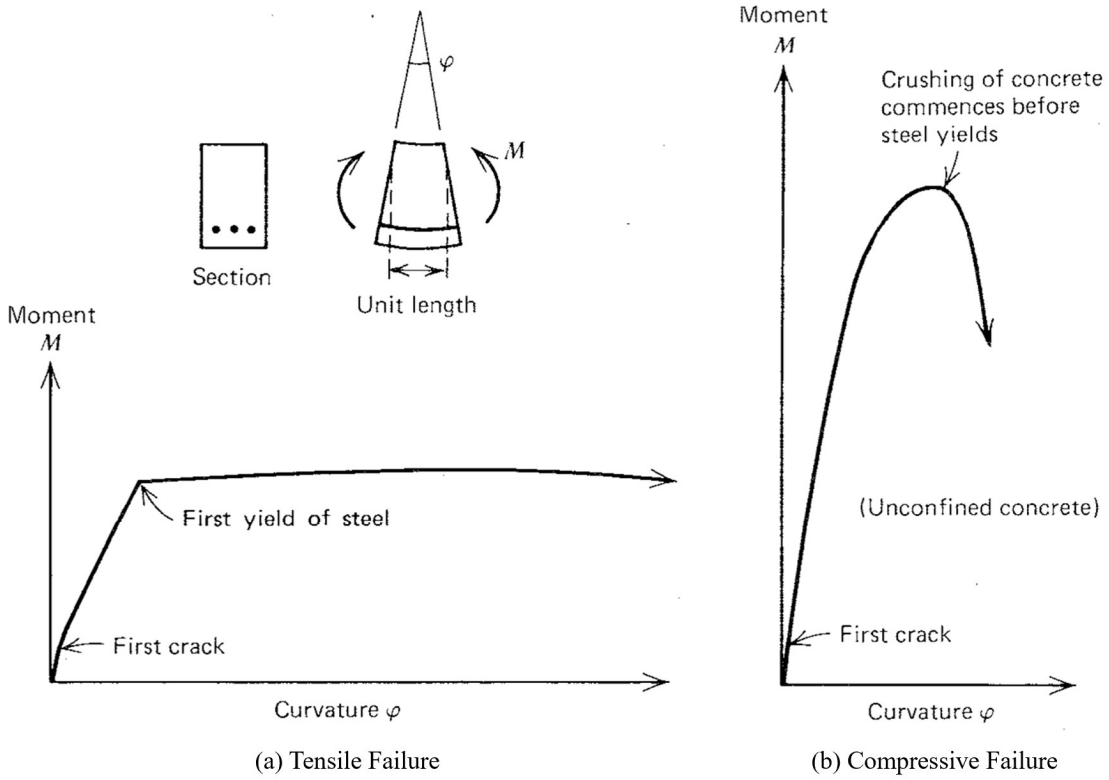

Figure 2-16: Moment-curvature relationships for tensile and compressive failures (Park & Paulay, 1975)

The relationship between the moment and the curvature in uncracked concrete is given by the elastic equation:

$$EI = MR = \frac{M}{\varphi} \qquad \textit{Equation 2.5}$$

Where *EI* is the flexural rigidity of the section. Once the concrete begins to crack the flexural rigidity is reduced. The amount of steel reinforcing determines the behaviour after cracking. Lightly reinforced concrete members failing in tensions show a practically linear moment curvature relationship after concrete cracking up until the steel has yielded. Thereafter a large increase in curvature occurs at a near constant moment, the shape of the curve depending on the post yielding behaviour of the reinforcing

material. In contrast over-reinforced sections fail in a brittle manner with the concrete crushing. The curve after concrete cracking becomes nonlinear once the concrete reaches its inelastic part. Since the steel does not yield, the moment will increase and drop suddenly when the concrete crushes. Sudden failure can occur at small curvatures, if the concrete is not confined by closed stirrups. The importance of ductile behaviour is thus highlighted as the reason why beams are designed with steel contents low enough for the steel to yield before the concrete crushes (Park & Paulay, 1975). Now that the moment curvature relationships have been discussed, the concept of plastic hinges and collapse mechanisms, upon which moment redistribution is based, can be described in greater depth.

2.5.2. PLASTIC HINGE ROTATION AND MOMENT REDISTRIBUTION

The nonlinearity evident in moment curvature relationships points to the fact that once the structure is loaded beyond the service load range the actual moments will differ from the moments derived from linear elastic structural analysis. Assuming that plastic hinges can occur, sections reaching their ultimate moment capacity will rotate significantly thereby allowing the load to increase further until other sections reach their ultimate moment capacity. Thus, moment redistribution can result in an increase in the load carrying capacity of the structure, since all critical sections can reach their ultimate moment of resistance.

The simple example of a two-span continuous beam with uniform cross-section, as shown in Figure 2-17 (a) is considered (Park & Paulay, 1975). The ultimate moment of resistance for the positive (hogging) and negative (sagging) bending moments is M'_u and M_u respectively. The moment-curvature relationship is idealised as a bilinear relationship for a ductile section and is shown in Figure 2-17 (b).

The two concentrated point loads shown in Figure 2-17 (a) lead to the bending moment diagram in Figure 2-17 (c) based on elastic theory. Since the beam has a constant flexural rigidity and the moment is highest across the middle support it is evident that this critical section would be the first to reach its ultimate moment of resistance. This moment is defined as M'_u. Further loading depends on the capacity for plastic rotation at the centre support. In this case, the ductile moment curvature relationship allows the formation of a plastic hinge which rotates as the load is increased whilst maintaining the moment M'_u (Reddy, 2007). Therefore, the moments caused by increasing the load are redistributed towards the next critical sections at the sagging moments until they reach their ultimate moment of resistance M'_u.

Once three hinges have formed the structure is no longer statically indeterminate and it is at this point that a collapse mechanism has formed. If the section was brittle, rotation would not be possible, and the moment of resistance would drop suddenly, causing the beam to fail at a much lower load. Figure 2-17 (f) traces the increase in moments at the hogging and sagging sections with the increase in load and clearly shows the increase in load carrying capacity made possible by moment redistribution.

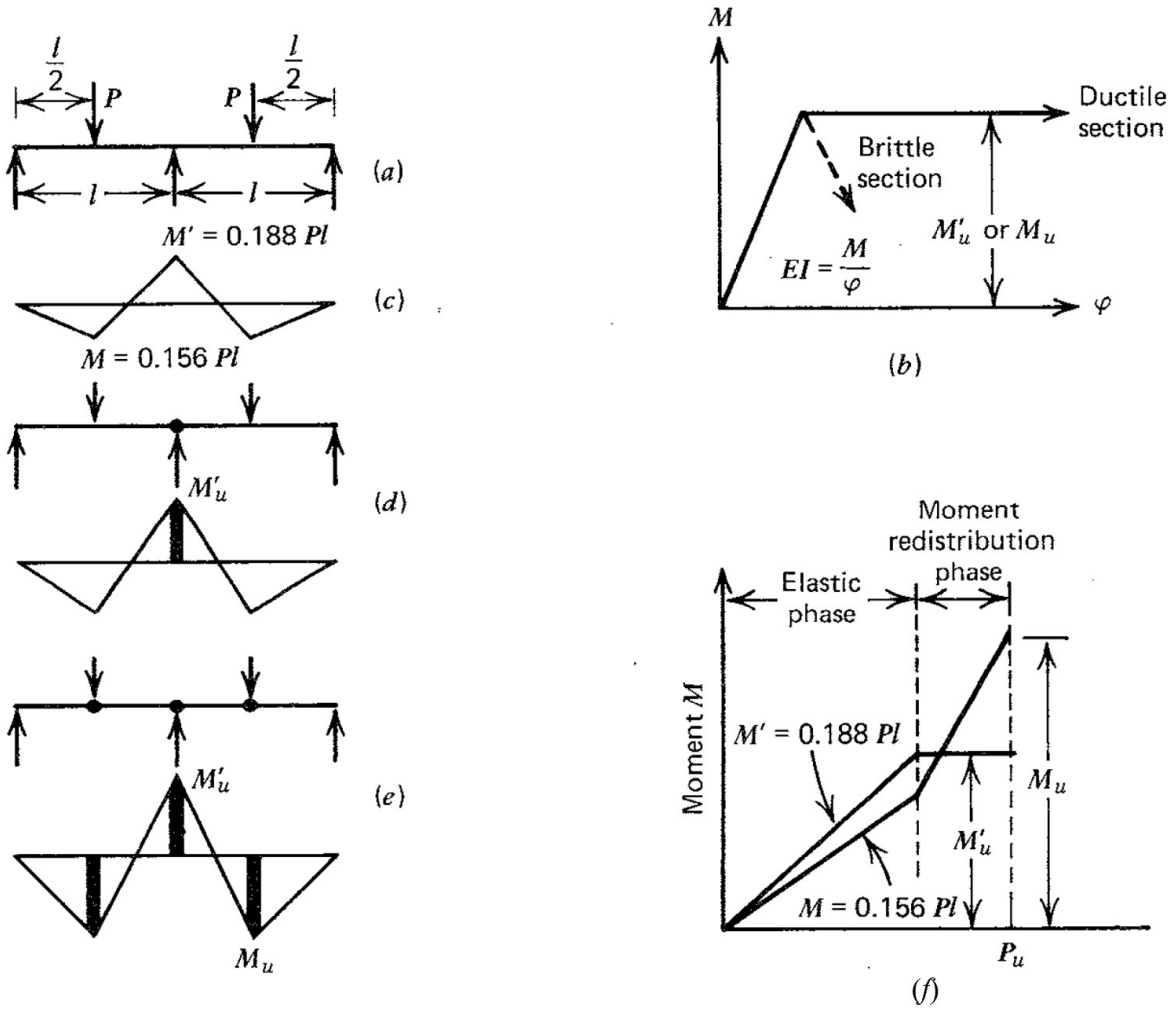

Figure 2-17: Moment redistribution and formation of a collapse mechanism (Park & Paulay, 1975)

So far, the mechanism of moment redistribution has been described. Ductility, illustrated by the moment curvature relationships, allows plastic hinges to form which are required for moment redistribution to occur. Therefore, the degree of moment redistribution depends on the rotation capacity of the member, which will be quantified in the following section.

2.5.3. ROTATION CAPACITY

It must be noted that equilibrium is required at all stages according to Equation 2.6, which satisfies equilibrium at the midspan for the beam in Figure 2-17:

$$M + \frac{M'}{2} = \frac{PL}{4} \qquad \textit{Equation 2.6}$$

Therefore:

$$P = \frac{4}{L}\left(M + \frac{M'}{2}\right) \qquad \textit{Equation 2.7}$$

If the moment at the centre remains constant at M'$_u$ whilst the load increases up to the load resulting in a moment M_u developing at the midspan, equilibrium results in:

$$P_u = \frac{4}{L}\left(M_u + \frac{M'_u}{2}\right) \qquad \textit{Equation 2.8}$$

From these equations it is apparent that the bending moment distributions can differ significantly from those calculated using elastic theory. When considering reinforced concrete, the ductility at the first hinge may be insufficient to allow full moment redistribution to take place. Therefore, the required plastic rotation for the two-span continuous beam will be calculated for the case where the first hinge forms at the support.

Figure 2-18 shows the stage at which enough plastic rotation has occurred at the support for M_u to be developed at the midspan, and hence P_u has just been reached. Plastic curvature is considered to occur over a plastic hinge length l_p each side of the hinge (Guo, 2014).

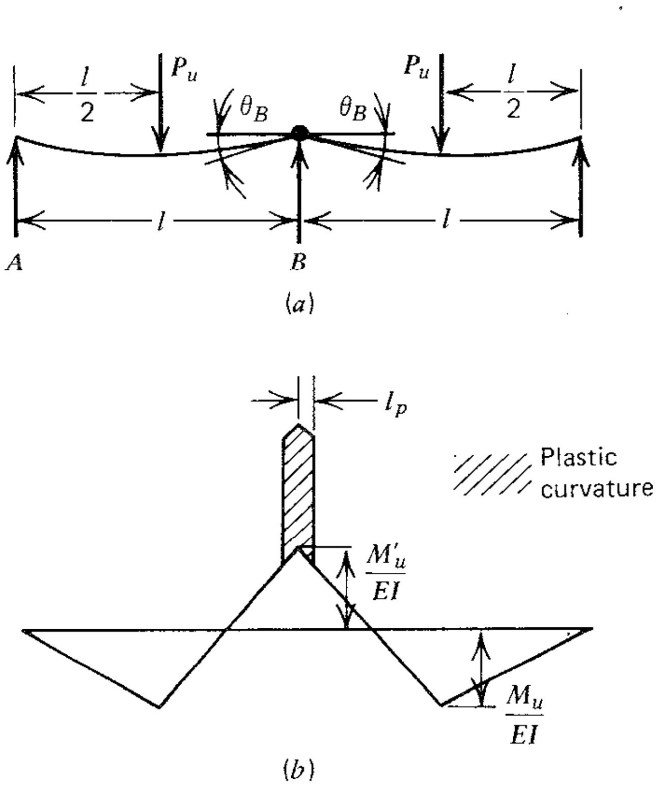

Figure 2-18: Formation of a plastic hinge (Park & Paulay, 1975)

The plastic hinge length l_p is simplified in Figure 2-18 (b) and will be discussed in greater depth in the next section. The curvature can be separated into the elastic and inelastic regions. The elastic contribution can be calculated from Equation 2.5. The plastic rotation Θ_p at the centre support is the discontinuity of slope between the ends of the adjacent members, and $\Theta_p = 2\Theta_B$ as shown in Figure 2-18 (a).

To calculate Θ_p the elastic contribution in carrying the load P_u must be determined. This is done by replacing the plastic hinge at B with a frictionless hinge as shown in Figure 2-19.

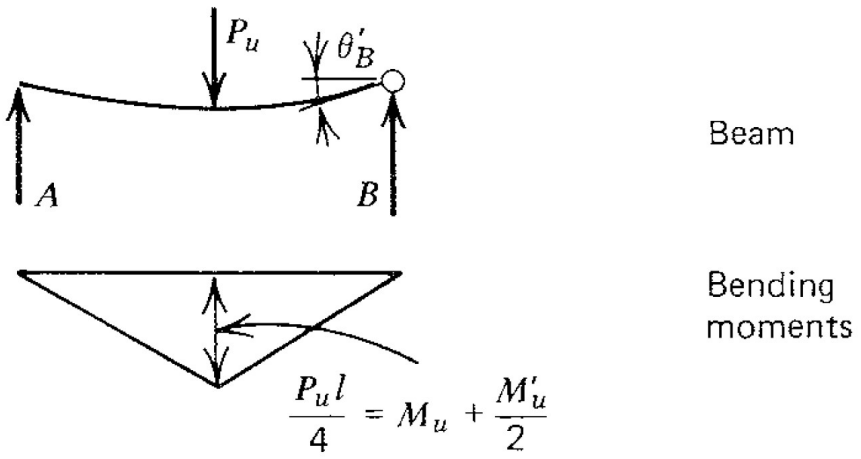

Figure 2-19: Bending moment diagram for a continuous beam with a frictionless hinge (Park & Paulay, 1975)

Using the moment area theorem, the rotation at B due to the load P_u on one span is:

$$\theta'_B = \frac{(M_u + 0.5M'_u)L}{4EI} \qquad \textit{Equation 2.9}$$

Considering now the effect of the ultimate support moment M'_u acting at the frictionless hinge as shown in Figure 2-20, the rotation at B due to only M'_u is;

$$\theta''_B = \frac{M'_u L}{3EI} \qquad \textit{Equation 2.10}$$

Therefore:

$$\theta_B = \theta'_B - \theta''_B = \frac{L}{4EI}\left(M_u - \frac{5}{6}M'_u\right) \qquad \textit{Equation 2.11}$$

Therefore:

$$\theta_P = 2\theta_B = \frac{L}{2EI}\left(M_u - \frac{5}{6}M'_u\right) \qquad \textit{Equation 2.12}$$

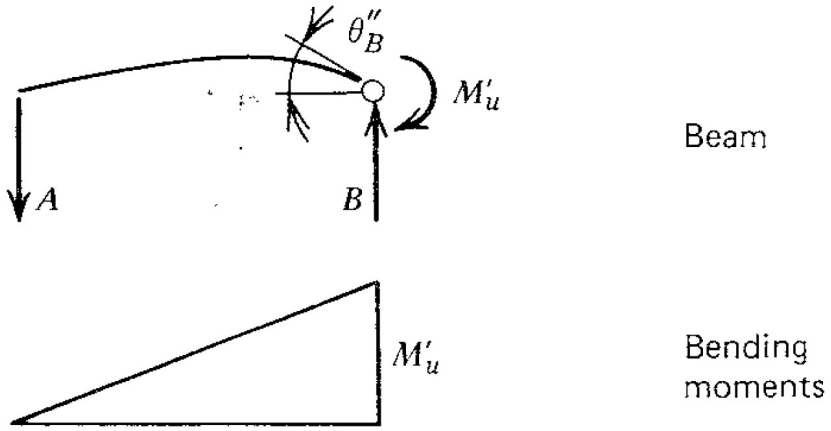

Figure 2-20: Calculation of plastic hinge rotation (Park & Paulay, 1975)

Equation 2.12 is valid in giving the required rotation at the plastic hinge if $M_u > 5/6M'_u$. This means that if the sagging moment M_u is equal to $5/6M'_u$ no moment redistribution is required, since this is the ratio of moments given by elastic theory. If M_u is smaller than $5/6M'_u$ the conditions would no longer be valid as the plastic hinges would first form under the load points in the midspans. In this example, moment redistribution can occur until the ultimate moment develops at each critical section if:

$$\frac{L}{2EI}\left(M_u - \frac{5}{6}M'_u\right) \leq \left(\frac{\varepsilon_c}{c} - \frac{\varepsilon_{ce}}{kd}\right)2L_p \qquad \textit{Equation 2.13}$$

Where ε_c = concrete strain at the extreme compression fibre at the ultimate curvature, ε_{ce} = concrete strain at the extreme compression fibre when yield curvature is reached, c neutral axis depth at the ultimate moment, kd = neutral axis depth when the yield curvature is reached, l_p = equivalent plastic hinge length each side of the critical section.

Rotation capacity can therefore be defined as the ratio of the ultimate curvature at the onset of strain weakening to the curvature consistent with the development of fully plastic moments. This inelastic rotation can only occur if the critical section possesses sufficient rotation capacity. The length across which plastic rotation can occur depends on the length of the section along which the applied moment equals the plastic moment of the section.

2.5.4. PLASTIC HINGE LENGTH

The simplified plastic hinge length is discussed here in further detail. Consider the same example from the previous section (see Figure 2-17), the plastic hinge length next to the critical section is shown along one span. Contributions of the elastic and inelastic regions to the curvature are shown in Figure 2-21. The elastic contribution can be calculated from Equation 2.5.

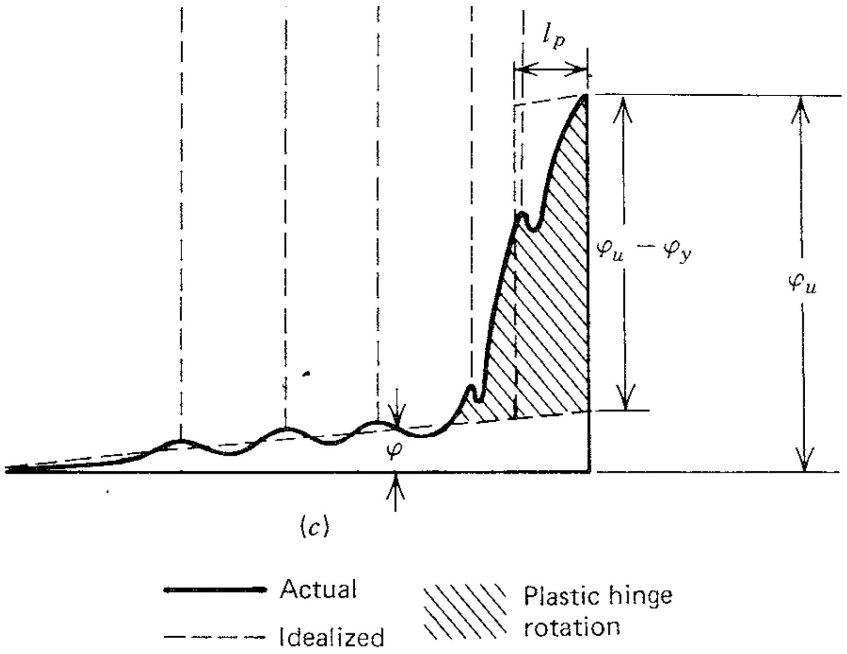

Figure 2-21: Curvature distribution and plastic hinge length (Park & Paulay, 1975)

When considering the contribution of the elastic rotation across the full length of the beam, the unshaded area in Figure 2-21, the following equation can be used:

$$\theta = \int_A^B \frac{M}{EI} dx \qquad \textit{Equation 2.14}$$

If the member is fully cracked, the flexural rigidity is given by:

$$E_c I_e = \frac{M_y}{\varphi_y} \qquad \textit{Equation 2.15}$$

Where:

$$I_e = \left(\frac{M_{cr}}{M_a}\right)^3 I_g + \left[1 - \left(\frac{M_{cr}}{M_a}\right)^3\right] I_{cr} \qquad \textit{Equation 2.16}$$

Where M_{cr} is the moment at first cracking, M_a is the maximum moment in the member at the stage for which deflection is being calculated, I_g is the moment of inertia of the gross concrete section about the centroidal axis ignoring the reinforcing, and I_{cr} is the moment of inertia of the cracked transformed section.

The shaded area in Figure 2-21 represents the inelastic rotation that can occur at the plastic hinge near the critical section and thus represents the additional rotation that can occur in addition to the elastic rotation at the ultimate limit state. The inelastic area can be replaced by an equivalent rectangle having the same area as the actual inelastic curvature distribution with a height φ_u - φ_y and width L_p. Hence, the plastic rotation occurring on one side of the hinge may be written as:

$$\theta_P = (\varphi_u - \varphi_y)L_P \qquad \textit{Equation 2.17}$$

As a result, the resulting curvature distribution can be simplified into the diagram shown in Figure 2-22.

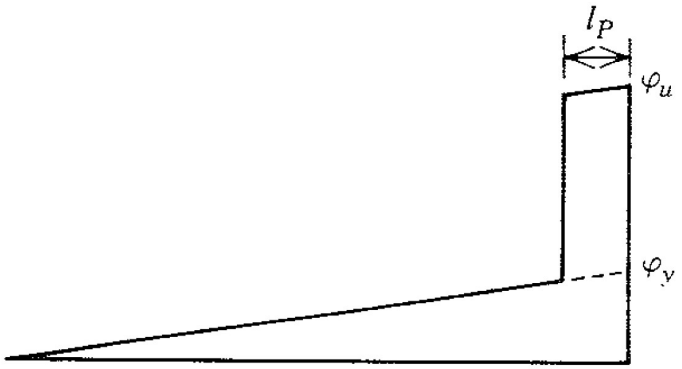

Figure 2-22: Simplified curvature distribution (Park & Paulay, 1975)

2.6. BEHAVIOUR OF CONTINUOUS REINFORCED CONCRETE BEAMS

Ductility is one of the most important aspects in the design of reinforced concrete structures and determines the ability of a structure to redistribute moments. Depending on the ductility of an indeterminate structure, the full capacity of non-critical sections may be reached with the formation of plastic hinges which is the mechanism that allows for the redistribution of moments. Current standards adopt a wide range of permissible moment redistribution values which is a testament to the complexity in quantifying moment redistribution. The root of the problem lies in the difficulty of quantifying a moment-rotation capacity for a concrete member due to the interaction of various parameters involved in the behaviour of critical sections (Wood, 1968). Many national standards have opted to base allowable moment redistributions on the neutral axis depth factor which is the depth to the neutral axis as a proportion of the effective depth (BS 8110, 1995, DIN1045, 1997, CAN-A23.2, 1994, CEB-FIP, 1990). Some codes limit reinforcing ratios which are based on extensive testing to ensure adequate ductility (ACI 318, 2014).

The inclusion of fibres, in combination with, or without steel reinforcing bars, complicates an already complex behaviour. Apart from moment redistribution, the addition of different fibre types to concrete generally improves the structural behaviour such as load capacity, reducing crack widths and minimising deflections. Whilst the positive impacts of fibres are known, a greater understanding is required into changes in behaviours caused by the addition of fibres in concrete of different strengths, and in combination with different steel reinforcing ratios.

2.6.1. FIBRE REINFORCED CONCRETE

The influence of different fibre types on moment redistribution in particular has been studied by various researchers (El-Mogy et al., 2010, Santos et al, 2013, Gravina & Smith, 2007, Mohr, 2012, Kara & Ashour, 2013, Lou et al., 2014a & 2015, Schumacher, 2006, Visintin, 2018). Parameters of interest as well as the methods in which the results are described vary between researchers. Although different reinforcing materials will result in different moment redistribution capabilities, the mechanics of moment redistribution remain the same.

Glass fibre is one alternative for concrete reinforcement in areas with harsh environments. The non-corrodibility of glass fibres, as well as their low self-weight, high strength and electromagnetic transparency are some of the main advantages which are, however, offset by their low elasticity modulus and linear behaviour until failure. Glass fibres therefore provide no contribution towards the ductility of the structure which results in limited moment redistribution capabilities. Santos (2013) showed that beams reinforced with glass fibre reinforced polymer (GFRP) bars led to higher stiffnesses and lower deflections at higher load capacities. Increasing the GFRP ratio in the spans at the expense of reducing the hogging section reinforcement resulted in an increase in stiffness of the spans relative the stiffness across the hoggins section and thereby allowed more moment redistribution from the central support towards the spans.

Moment redistribution for brittle materials such as GFRP beams is, however, different from moment redistribution calculated in the design of steel reinforced concrete beams. Owing to the linear elastic properties of the GFRP bars, moment redistribution, when compared against elastic moments, occurs after cracking up until a sudden brittle failure as indicated in Figure 2-23. All moment-load relationships are for beams reinforced with varying amounts of glass fibre reinforced polymer bars. For all cases, even if the moments deviate early on from the elastic moments, there is no region in which the peak moments are maintained with a further load increase. This behaviour differs from that of ductile members in which the majority of moment redistribution occurs during the formation of plastic hinges with sufficient rotation capacity. However, for both ductile and brittle members, the reduction in stiffness in the region where the section has cracked results in bending moments which are lower than predicted by conventional elastic analysis. The difference in actual moments and moments predicted by conventional elastic analysis is therefore evident throughout the behaviour of the structure, caused initially by the reduction in flexural stiffness where cracks have formed, and then by plastic rotation if the structure possesses sufficient ductility.

Moment redistribution in beams without much ductility occurs during the reduction of bending moments in the critical sections caused by flexural cracking. These cracks cause a change in the flexural stiffness for a length of the member where the applied moment exceeds the cracking moment of the section.

The redistribution of moments therefore occurs after cracking as the stiffness of the section changes, however the ability to reach any increased capacity in non-critical sections is minimal since the material behaves linearly elastic until failure, and hence the moment capacity at the critical section reduces almost completely after a certain rotation. As a result, since almost no plastic rotation occurs in brittle members, no redistribution of moments can occur at this stage.

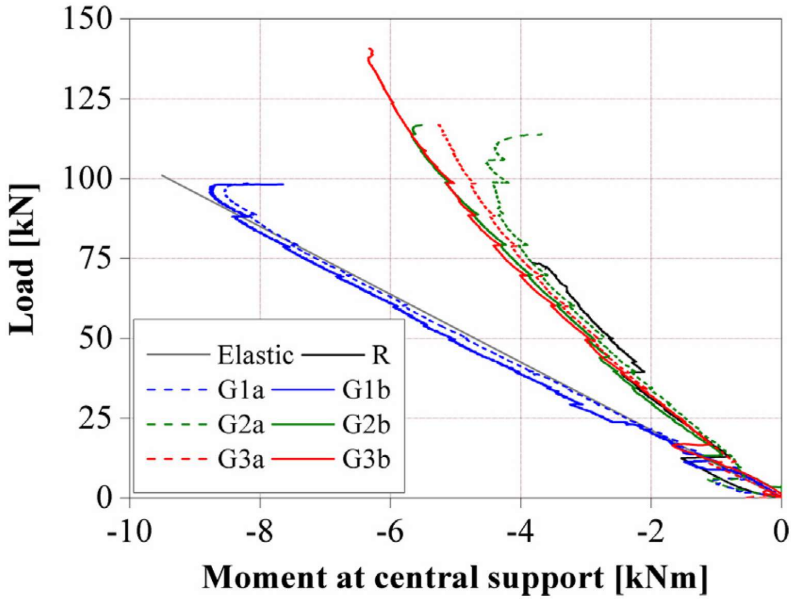

Figure 2-23: Moment-load relationship in GFRP beams (Santos et al., 2013)

Presenting any sort of moment redistribution capabilities for brittle materials might be misleading since the concept of moment redistribution is based around the idea of increasing the moment capacity in non-critical sections after the maximum moment capacity of the original critical section has already been reached. The outcome is that the structure can carry an additional load beyond the load at which the capacity of the critical section is reached. This is not possible in brittle members. The elastic moment redistribution is therefore merely a change in the rate at which the hogging and sagging moments increase relative to the increased in load on the structure. In other words, the slope of the hogging moment vs load graph shown in Figure 2-23 changes, however once the hogging moment capacity is reached, the structure is not able to carry an additional load. Therefore, codes such as ACI 440.1R-06 (2006) recommend that no moment redistribution in statically indeterminate structures be allowed for FRP beams with a brittle nature.

Other brittle fibres such as Carbon have also been used to study the effects on moment redistribution, with similar results (Gravina & Smith, 2008). The ratio of the hogging and sagging moments changes after cracking as the load increases, resulting in the redistribution of moments during elastic behaviour.

It is only in beams containing steel reinforcing which then allow a further redistribution in moments after the steel has yielded. The difference between moment redistribution during elastic behaviour and moment redistribution during plastic behaviour is mentioned by Kara & Ashour (2013) when comparing carbon fibre reinforced polymer (CFRP) bars with steel bars. The low elasticity of FRP beams led to high curvatures at rupture, however failure was sudden and did not allow moment redistribution to occur. Moment redistribution occurred as a result of cracking and de-bonding between FRP and concrete. The experiments done by Kara & Ashour (2013) indicated that when compared to the elastic moments, the actual hogging moments were most often less, and the sagging moments greater than expected, however the ultimate moment capacities in the sagging regions could not be achieved due to the brittle nature of the material.

The difference in moment redistribution behaviours is illustrated clearly by the experiments conducted by Lou et al., (2015) in which GFRP, CFRP and steel reinforcing was compared as illustrated in Figure 2-24. The lower axial stiffness of GFRP when compared to CFRP allows more redistribution. However, both the GFRP and CFRP indicate no further increase in moment redistribution at higher loads as the steel does, which renders those members ineffective in attaining additional load bearing capacity.

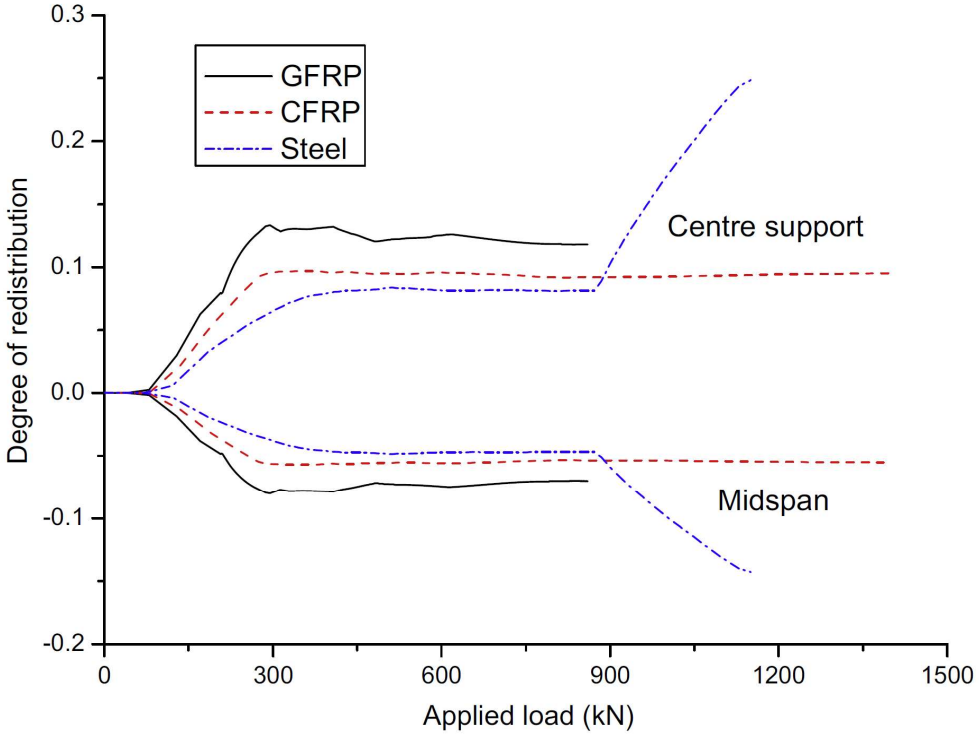

Figure 2-24: Development of moment redistribution for different reinforcement types (Lou et al., 2015)

It is therefore evident that although moment redistribution is possible in highly brittle structures, this redistribution of moments is not effective in terms of achieving additional load capacity and improving efficiency by nearing the moment capacity of non-critical sections. Materials that allow plastic

behaviour are much better suited, such as steel fibres. Much research has been done on the compressive and tensile characteristics of fibres, and the means in which their material properties translate to overall structural behaviours will now be discussed in terms of different structural characteristics.

2.6.2. LOAD DISPLACEMENT BEHAVIOUR

One incentive for using fibre-reinforced concrete is to reduce the amount of steel reinforcing. The different material properties of fibres when compared to steel reinforcing results in differing load-deflection behaviours. A determinate setup of strip slabs with a 750 x 250 mm cross-section and a span length of 3750 mm were tested by Lofgren (2005) and the load deflection results were compared for identical members with changes in the amounts of fibres used. Initial responses before cracking were similar and almost independent of the type of mix and reinforcement. Once cracks had formed, a non-linear load vs deflection characteristic was obtained, with the gradients of the curves and the peak loads affected by the fibre content. An increased fibre content led to higher peak loads, and stiffer behaviour after cracking. Shorter fibres had the ability to increase the peak load, but the behaviour was less ductile.

The fibre type and dosage also altered the shape of the load-deflection response. F our-point bending tests were performed by Ackerman (2011) to reveal that a lower fibre content can provide improved structural behaviour as shown in Figure 2-25. An improved load capacity was found at higher deflections with a lower fibre content for a different fibre type. This shape would be ideal for moment redistribution.

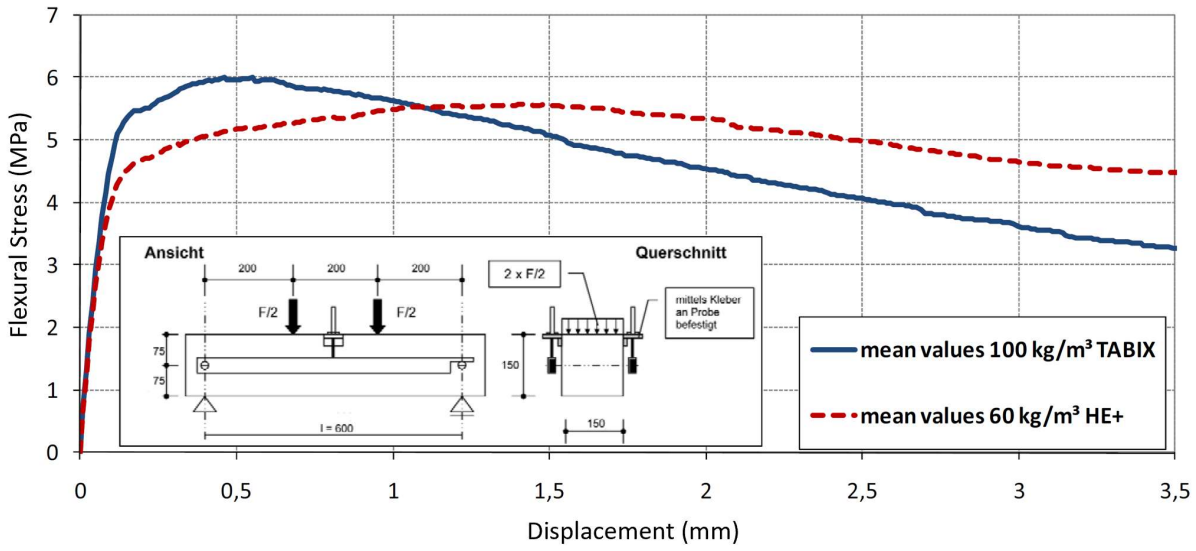

Figure 2-25: Stress-displacement curves for SFRC concrete mixes (Ackerman, 2011)

The typical load-deflection curve shape changes when testing a statically indeterminate structure. A typical load-deflection curve containing steel reinforcing is illustrated in Figure 2-26 and can be divided

into three stages. The first stage is mostly linear before cracking, followed by a change in the slope as the number of cracks increase. The final stage occurs when the steel yields at the critical section (Lin & Chien, 2000, Gravina & Smith, 2008, Aiello & Ombres, 2011, Ashour & Habeeb, 2008). Once the reinforcing steel has yielded, the large increase in deflection and rotation leads to either tensile failure when the bars rupture, or compressive failure where the concrete crushes at the hinge.

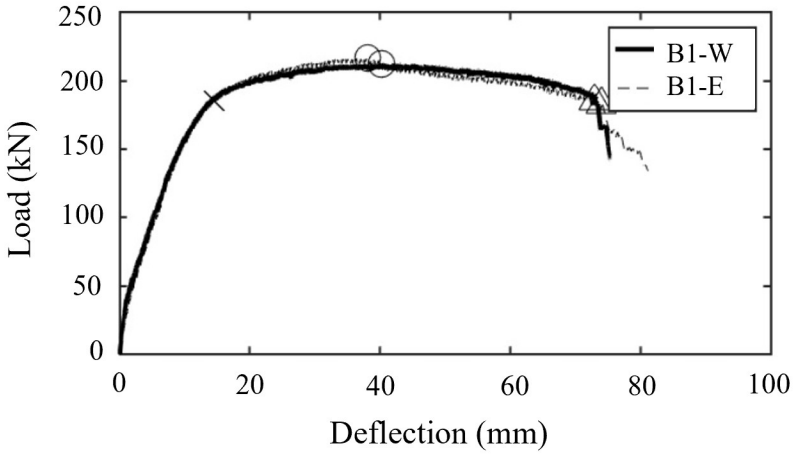

Figure 2-26: Typical load-deflection response for a continuous beam (Vistinin et al., 2018)

This load-deflection behaviour is not evident in members reinforced with brittle materials (Gravina & Smith, 2008). The shape of the load deflection response will differ for steel fibres and will be similar to the load deflection responses discussed in the previous section for the load deflection results obtained from FPBTs. The ability for steel fibre reinforced beams to behave similarly to members reinforced with steel bars depends on the post peak stress behaviour of the fibres. Most steel fibre reinforced concrete exhibits a residual strength after concrete cracking which may be higher than cracking load, however upon further deflection the load capacity decreases instead of remaining constant as with steel bars.

In general, an increase in fibres leads to higher load capacities, however the decreasing load-deflection slope after the maximum load has been reached is more sever for higher fibre contents (Yoo & Banthia, 2016) as indicated in Figure 2-27. This loss in load capacity as the deflections increase after the maximum strength has been reached, is worse in fibre reinforced members with high strength concrete than in normal strength concrete. The toughness at deflection points L/150 and L/75 improved with a higher fibre content regardless of the concrete strength owing to the improvement in fibre crack bridging capacity. An interesting find was that the toughness at a certain fibre content was reduced in higher strength concrete (Banthia & Trottier, 1994 & 1995, Balaguru & Shah, 1992). This behaviour was explained by the increase in matrix strength which led to the fracture of inclined fibres before complete

pull-out due to their improved anchorage. Therefore, a lower post-peak ductility was achieved for high strength concrete than for normal strength concrete.

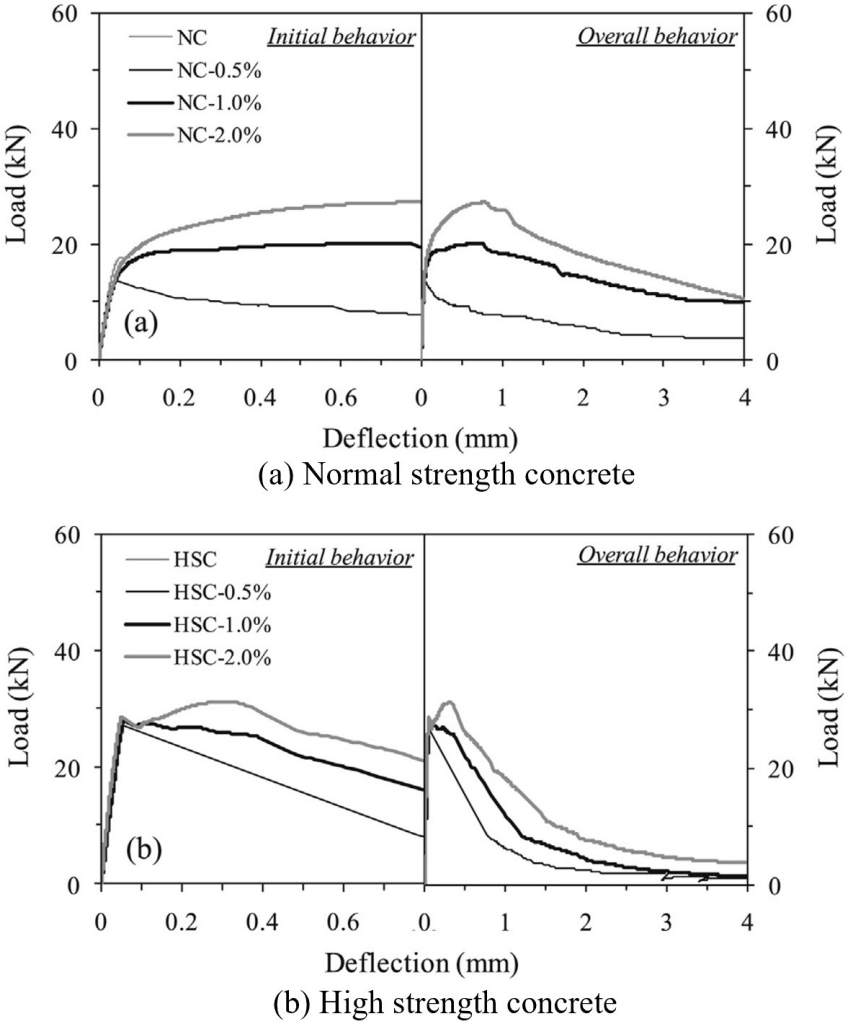

Figure 2-27: Load deflection responses in (a) normal and (b) high strength fibre reinforced concrete (Yoo & Banthia, 2016)

Beams with a combination of 30 mm hooked ended steel fibres and 16 mm diameter reinforcing bars (450 MPa) were tested by Lim et al. (1987). Under-reinforced beams containing two bars with fibre contents of 0.0%, 0.5% and 1.0% showed a slight increase in flexural strength with an increase in fibre content. An increase in the deflections after steel yielding was possible without losing strength for beams with 1.0% fibres. This increase reduced as the amount of fibres was reduced. Beams containing four 16 mm diameter bars failed suddenly through shear failure, however, for these beams the increase in load capacity was much greater with an increase in the amount of steel fibres than the increase shown in beams containing only two reinforcing bars. This behaviour was explained by the ability of the fibres to act as shear supports and hence the greater improvement in load capacity was seen with more steel fibres.

2.6.3. MOMENT DISTRIBUTION ALONG THE BEAM

Moment redistribution results in reduced moments at the critical sections (usually hogging) and increased moments at the non-critical sections (sagging). In Figure 2-28 the elastic moment distribution is compared against the actual moments at failure (Visintin et al., 2018). The hogging moment is lower than the elastic moment and the sagging moments are higher. An elastic analysis is conducted by assuming the flexural stiffness (EI) along the beam. As an example, the effect of changing the ratio of flexural stiffnesses between hogging and sagging moment regions is illustrated for the span between supports of a propped cantilever in Figure 2-29 (Scott & Whittle, 2005). Increasing the stiffness in the sagging region will reduce moments in the hogging region and increase the moments in the span and tends towards the behaviour of a simply supported beam in the extreme case where the stiffness in the span is infinitely higher than at the fixed support.

In design, where the amount of reinforcing is only determined at the end of the process, codes such as BS 8110 (1995) use a concrete section approach, which assumes a constant flexural stiffness along the length of the beam. However, in most cases, the reinforcing ratio will vary along the beam, and hence the flexural stiffness will vary. Thus, the actual moment redistribution developed will differ from the analysis even at serviceability limit state (SLS). This redistribution is elastic moment redistribution as it occurs whilst the cross-section properties are still in the linear elastic stages (Scott, 2008).

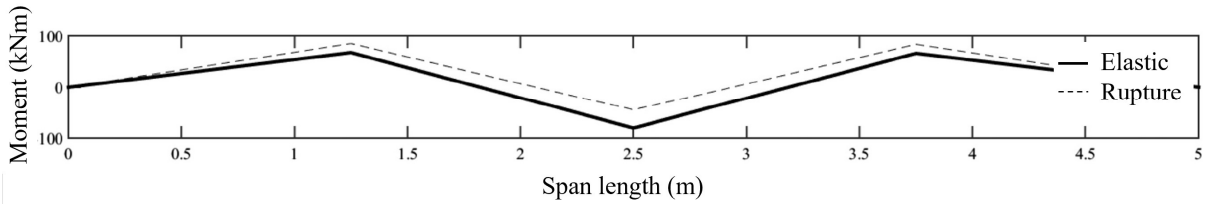

Figure 2-28: Moment distribution along the beam (Visintin et al., 2018)

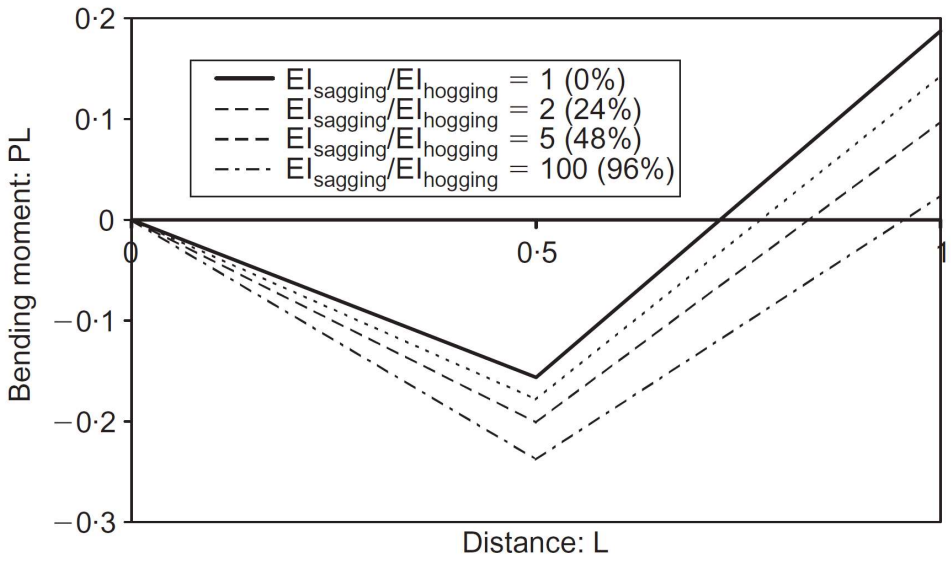

Figure 2-29: Influence of flexural stiffness on moment redistribution (Scott & Whittle, 2005)

2.6.4. MOMENT EVOLUTION WITH APPLIED LOAD

Plotting the evolution of hogging and sagging moments against the total applied load creates a visual indication as to when moment redistribution occurs. An example of a moment vs load graph has already been shown in Figure 2-23 (Santos, 2013). Comparing the evolution of the actual moments against the theoretical expected elastic moments highlights the deviations from elastic behaviour as cracks are introduced, and later yielding occurs causing plastic behaviour. Continuous beam tests have shown moment ratios between hogging and sagging regions that differ from the elastic moment ratios from the start of testing (Visintin, 2017). Once cracking starts, elastic moment redistribution occurs even though the section still behaves in a linear elastic fashion (Scott & Whittle, 2008).

As previously discussed, this behaviour occurs due to the changes in flexural stiffness caused by the cracks which result in moments deviating from linearly elastic behaviour (Ackerman & Schnell, 2011, Santos et al., 2013, do Carmo & Lopes, 2005). Visintin et al. (2018) showed that after the initial spike in redistribution caused by cracking, redistribution becomes more dependent on the reinforcing ratio between the hogging and sagging regions.

Experimental results from Lou et al. (2014a & 2014b) agree with the stages of moment redistribution and are illustrated in Figure 2-30 in terms of moment ratios against the applied load. A clear change in moment ratios is observed at the start of cracking, after which it remains constant and then changes again once the steel begins to yield. The constant region occurs due to the neutral axis stabilising, and the length of this stabilised region depends on the material properties of the concrete and reinforcing (Visintin et al., 2018).

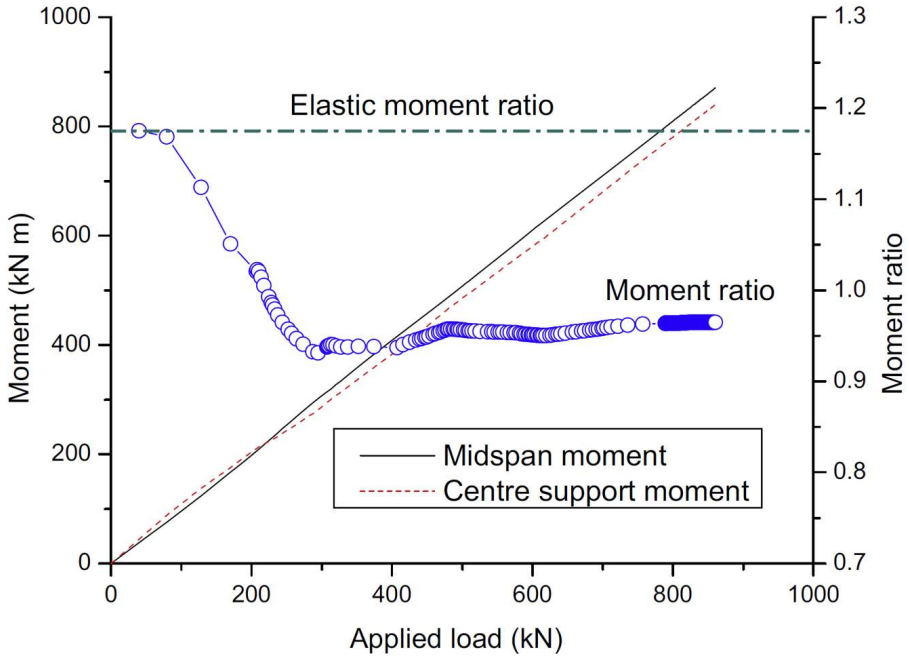

(a)

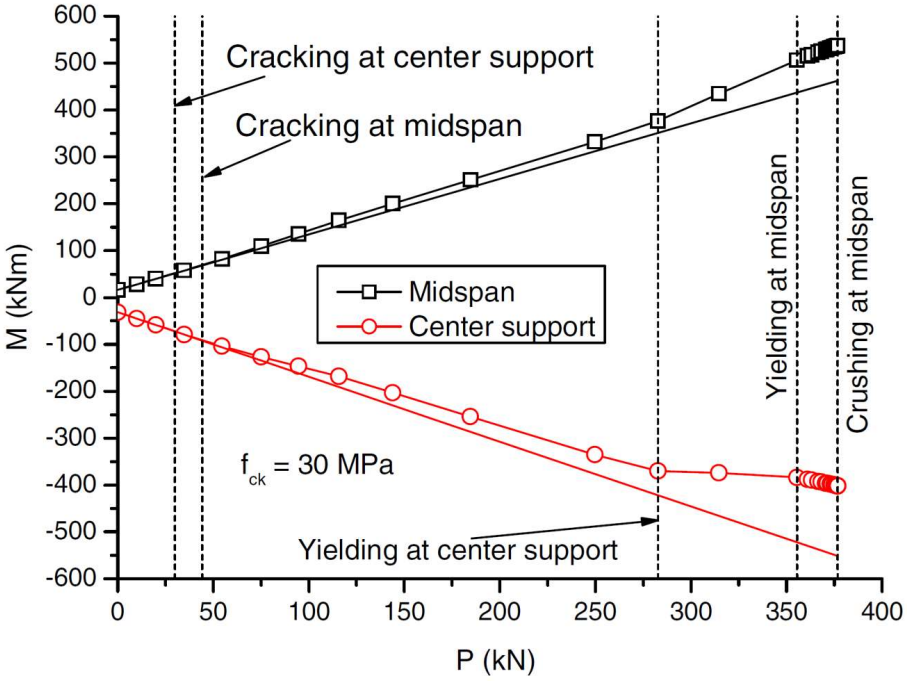

(b)

Figure 2-30: Development of moment ratios for continuous beams ((a)Lou et al., 2015, (b) Lou et al., 2014a).

2.6.5. MOMENT REDISTRIBUTION

Experimental studies performed in the 1950's showed inconsistent redistribution results. For some beams full moment redistribution was possible (Morice & Lewis, 1995, Guyon, 1960) whereas others failed far before fully plastic behaviour had been achieved (Lin & Chien, 2000, Macchi, 1957). These experiments led to three primary theories attempting to explain the difference in moment redistribution behaviour of different concrete structures.

Guyon (1960) used a compatibility approach in combination in which the deflected shape could be calculated if the moment-curvature behaviour of all sections were known. The difficulties in obtaining the moment-curvature relationship was reduced by neglecting elastic curvatures as being small in relation to plastic curvatures.

Macchi (1957) proposed a method to calculate moment redistribution at any load above the load required to cause cracking. Moments in the structure are calculated by a unit rotation at each hinge, a rotation which is calculated from a moment-curvature behaviour. This method assumes that deflections can be represented by elastic portions connected by hinges where the inelastic rotations occur. Again, the flexural rigidity is required when calculating the moments induced by the inelastic rotations.

A design check was developed by Baker (1956) to check the redistribution capabilities of continuous structures. A structure that is indeterminate to the *n*th degree is made determinate through the formation of $n + 1$ plastic hinges. The rotations of these plastic hinges have to be determined to ensure that the rotations are not too large for the physical conditions of each hinge. Initial limitations on the safe allowable rotation were based on a limiting strain acting across a hinge length equal to the effective depth. A more in-depth discussion on the definition of a plastic hinge length follows in the next section. The method proposed by Baker (1956) provided an approximate estimation at ultimate load conditions and required the flexural rigidity to be known.

The complex behaviour of moment redistribution results in assumptions required for each of the theories. Moment curvature behaviours are simplified, and plastic hinge lengths are estimated. In its simplest form, moment redistribution can be defined as the difference between the actual structural behaviour and the behaviour obtained from a linear elastic analysis. The elastic bending moment diagram thus forms a baseline from which moment redistribution is calculated, and thus any assumptions made will affect the amount of moment redistribution calculated (Scott & Whittle, 2008). The expression for percentage moment redistribution can be written as follows:

$$Moment\ Redistribution\ \% = \frac{M_{actual} - M_{elastic}}{M_{elastic}} \times 100 \qquad \textit{Equation 2.17}$$

Calculating the percentage moment redistribution is therefore simple enough, it is however difficult to know how accurate that answer is, due to the fact that the answer depends on the assumptions and simplifications made in the elastic analysis. The first step in predicting moment redistribution is to understand how a structure should deform to accommodate the non-elastic distribution of moments. The second step is to determine whether the deformation capacity of the structure is capable of this required deformation (Oehlers et al., 2004a). Two approaches can be followed, a hinge approach, and a flexural rigidity (EI) approach. The difference in the two methods is discussed by Oehlers et al. (2004b) and illustrated in Figure 2-31.

The hinge approach assumes that a discontinuity occurs at the supports as shown in Figure 2-31 (c) across a small length defined as the plastic hinge length. This plastic hinge length accommodates the discontinuity in the slope, and since it is often very small, it is often assumed that the curvature within the hinge is constant. The rotation capacity can then simply be defined as the product of curvature and the hinge length. However, the problem lies in determine the plastic hinge length, a problem which has led to numerous expressions for plastic hinge lengths (Mortezai & Ronagh, 2012).

The flexural rigidity approach assumes that the slope at the supports is zero, as shown in Figure 2-31 (f) which is an assumption made possible by allowing variations in the flexural rigidity (EI) along the length of the beam (Oehlers et al., 2004). For this method, different EI values are assigned to the

hogging and sagging regions, where the ratio between the EI values of the two controls the amount of moment redistribution, a concept which was previously briefly discussed from the research of Scott & Whittle (2008).

This difference in flexural stiffness, which is often neglected in design can lead to significant elastic moment redistributions and has been observed by various researchers (Visintin et al., 2018, do Carmo & Lopes, 2005, Mohr, 2012, Schumacher, 2006, Scott & Whittle, 2008). Do Carmo & Lopes (2005) reported elastic moment redistributions of up to 20%, similar to the 25% elastic moment redistribution reported by Scott & Whittle (2008). These results obviously depend on the range of reinforcement ratios they used, however, the key is that these elastic moment redistributions can be significant when not considered in design.

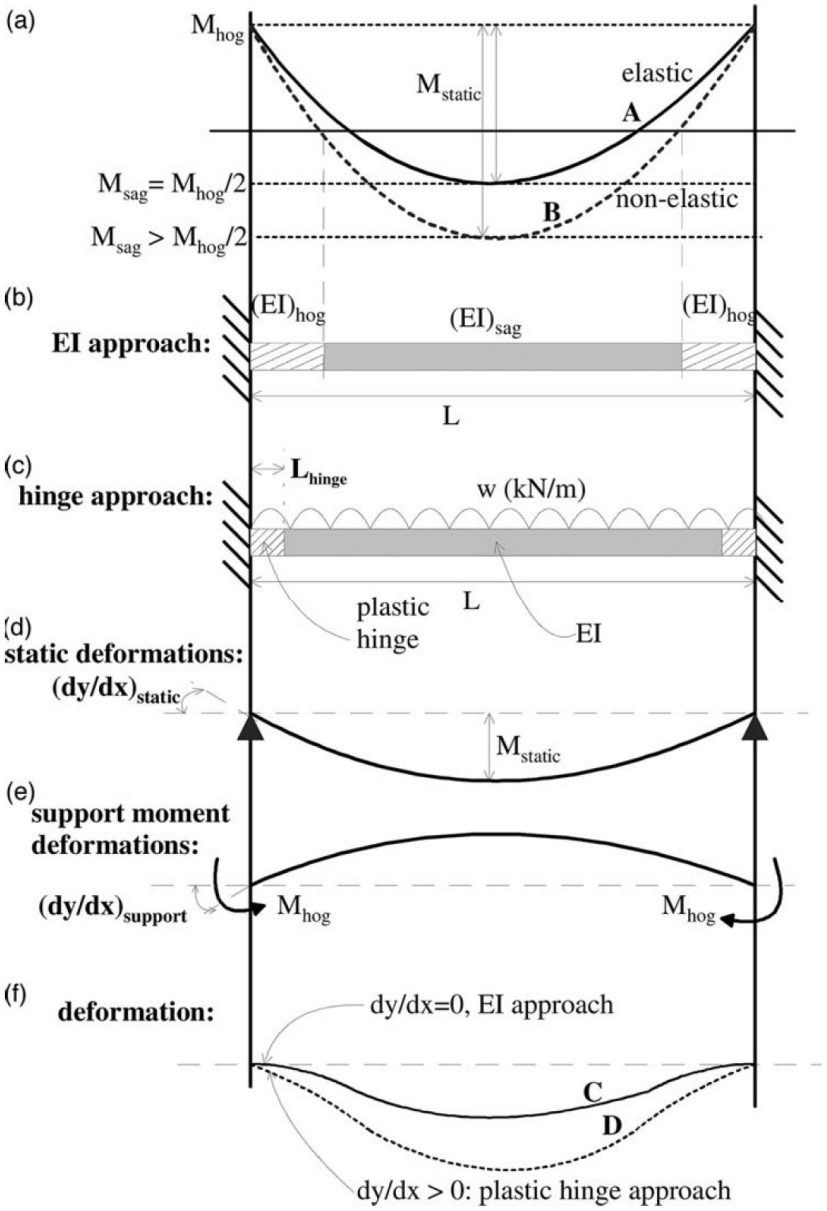

Figure 2-31: Capability of moment redistribution (Oehlers et al., 2004b)

A consequence of simplified design assumptions is that beams designed for no moment redistribution at the ULS can undergo plastic redistribution to offset the elastic redistribution due to varying reinforcing ratios and cracking along the beam (Scott & Whittle, 2008). Considering the actual distribution of the beam stiffness allows a more accurate analysis of moment redistribution as suggested by BS 8110's (1995) transformed section option. However, since the reinforcing layout is not usually known to start with, this approach is unsuitable for practical design purposes.

2.6.6. PLASTIC HINGE LENGTH

As discussed previously, the length of the plastic hinge is an essential parameter required to predict moment redistribution behaviour. Initial estimates set the plastic hinge length equal to the effective depth of the section (Baker, 1956). Upon further research the conclusion was made that this restriction on the length was conservative, therefore an expression for the hinge length included the effects of concrete strength, type of steel and distance from the critical section to the inflection point (I.C.E., 1964).

In reality, the factors influencing the plastic hinge length are numerous. A list of some parameters given by Mortezaie & Ronagh (2012) includes section geometry, material properties, reinforcement in compression, tension and transverse reinforcement, support conditions and bond-slip characteristics between the concrete and steel. The material properties itself includes the stress-strain relationships of all materials which will affect the moment-curvature behaviour. Also included is the definition of yielding and ultimate curvatures.

Simplified expressions are therefore required for practical purposes, some of which are summarised in Table 2-1. These expressions provide not the actual plastic hinge length, but an equivalent length over which a constant plastic curvature is assumed to act to allow for integration of the curvature along the length of the member to solve the deflection and plastic rotation capacity (Park & Pauley, 1975). An analytical study showed that the plastic hinge length varies with different tension reinforcing since the moment curvature behaviour is affected (Mortezai & Ronagh, 2012). Past expressions from Baker (1956) express the plastic hinge length as a constant in terms of the section geometry. The expression of Baker and Amarakone (1964) adds the effect of concrete cover as a linear relationship with the length of the plastic hinge. Similar expressions are given by Herbert and Sawyer (1964), Park et al. (1982) and Priestley and Park (1987) where the plastic hinge length is defined in terms of the section height, effective depth or distance from the critical section to the point of contraflexure.

More recent expressions by Paulay and Priestley (1992) and Berry et al. (2008) include the effect of the reinforcing strength and reinforcing bar diameter. Zhao et al. (2011) performed a parametric study to determine the effects of various parameters on the extent of the rebar yielding zone, concrete crushing zone, curvature localisation and the real plastic hinge length. Parameters of interest were the yield

strength of the reinforcing, the concrete compressive strength, the shear span of the beam (z), the effective depth, and the shear span over sectional depth ratio (z/h).

Table 2-1: Plastic hinge length expressions

RESEARCHER	EXPRESSION
Baker (1956)	$l_p = k_1 k_2 k_3 \left(\frac{z}{d}\right)^{0.25} d$
Baker and Amarakone (1964)	$l_p = 0.8 k_1 k_3 \left(\frac{z}{d}\right) c$
Corley (1966)	$l_p = 0.5d + 0.2\sqrt{d}\left(\frac{z}{d}\right)$
Herbert and Sawyer (1964)	$l_p = 0.25d + 0.075z$
Park et al (1982)	$l_p = 0.42h$
Priestley and Park (1987)	$l_p = 0.08z + 6d_b$
Paulay and Priestley (1992)	$l_p = 0.08z + 0.022 d_b f_y$
Berry et al (2008)	$l_p = 0.05z + \frac{0.008 f_y d_b}{\sqrt{f_y'}}$

Where: l_p = effective plastic hinge length, d = effective depth of beam, d_b = diameter of longitudinal reinforcing, h = overall depth of the beam, z = distance from critical section to point of contraflexure, c = depth of concrete cover, f_y = yield strength of the reinforcing

The length of the crushing zone was found to decrease as the concrete and reinforcing strength increased. An increase in the effective depth and the z/h ratio resulted in an increase in the length of the rebar yielding zone. The length of curvature localisation was found to be insensitive to the concrete compressive strength and reinforcing strength, but closely related to z/h and z (Zhao et al., 2011).

The expressions for the plastic hinge length discussed determine the plastic hinge length only at the ultimate load. However, this length may vary when the displacement of the member increases beyond the displacement that causes yielding of the reinforcement (Jiang, 2015). The results of Jiang (2015) show a rapid increase in plastic hinge length once the yield point has been reached, and then a more gradual increase or even decrease as the displacement is increased further. The decrease in the plastic hinge length is however dependent on a decreasing moment, which can occur as a result of moment redistribution.

2.6.7. ROTATION CAPACITY AND CRACK SPACING

To achieve the maximum plastic rotation capacity, the compressive strength of the concrete, and the tensile strength of the reinforcing should be utilised as much as possible, hence the failure of the concrete and reinforcing should occur at the same time. In ductile failure, seen in under-reinforced concrete, a smaller steel area results in earlier steel reinforcing failure, thereby limiting the plastic rotation capacity. Therefore, increasing the area of steel will increase the plastic rotation capacity if ductile failure still occurs. A further increasing in reinforcing will result in brittle failure where the

concrete crushes. Here the effect of increasing the reinforcing will result in lower tensile strains in the steel before the concrete crushes, and therefore a reduction in plastic rotation capacity.

Investigations into the rotation capacity of SFRC beams by Schumacher (2006) indicated a reduction in the rotation capacity with an increase in fibres. This behaviour was explained by the strain softening behaviour of the fibre which caused crack localisation instead of the multiple cracks seen in concrete reinforced with steel bars. As a result, deformations were concentrated around one crack since plastic steel strains could not be obtained in neighbouring cracks due to the additional tensile resistance of the steel fibres.

This localisation of plastic strains in one crack has also been observed by other researchers in SFRC (Löfgren, 2005; Jungwirth, 2006, Shionaga, 2006, Dancygier et al., 2017). However, at lower serviceability loads, the addition of fibres leads to smaller crack spacings and smaller crack widths (Bischoff, 2000, Bischoff, 2003, Conforti et al., 2018, Chao et al., 2009). This also showed how the addition of fibres leads to not only a reduction in crack width, but also an improvement in the bond strength between the reinforcing bars and concrete. It is the overall softening or hardening behaviour of a structure which determines whether deformations will occur in a single crack or across multiple cracks. If the softening behaviour of the fibres is dominant, the deformations will localise in one crack. In contrast, if the fibres exhibit strain hardening properties, or if the strain hardening properties of the reinforcing bars overshadows any strain softening behaviour of the fibres, deformations will be spread across multiple cracks.

The combination of steel bars and steel fibres can therefore lead to very different deformation behaviours, and hence affect the rotation capacity (Deluce & Vecchio, 2013). The shape of the stress-strain curve as well as the relative magnitudes of the stresses and strains will affect the structural behaviour if steel fibres are added to reinforcing bars. Some researchers have attempted to quantify the reinforcing bar content required to diminish crack localisation for different fibre contents, where a higher fibre content required more reinforcing bars to reduce crack localisation (Werzbrger et al., 2017, Dancygier & Berkover, 2016, Dancygier et al., 2017).

2.6.8. NEUTRAL AXIS DEPTH

A commonly used approach for controlling moment redistribution in reinforced concrete structures depends on the concrete crushing and an idealised moment curvature relationship which exhibits a horizontal plateau after the maximum moment has been reached. As described previously, this has led to codes limiting moment redistribution, K_{MR}, in terms of a neutral axis depth factor, k_u, (neutral axis depth over effective depth) as illustrated in Figure 2-32. These guidelines are based upon the fact that the ductility of the reinforcing steel is high enough so that failure does not occur by the bars rupturing, but by the crushing of the concrete. In this way, ductile behaviour occurs once the steel bars have

yielded, and their full strength is reached, after which further deformations can occur at possibly higher loads, as the full compressive capacity of the concrete is reached as well.

However, Oehlers et al. (2004b) has shown that members in which the ideal moment curvature relationship is not observed, the neutral axis depth factor approach is unsuitable. Although his research focussed on steel plated reinforced concrete members, the effect of steel fibres is also expected to introduce a change in the shape of the moment curvature behaviour when combined with reinforcing bars.

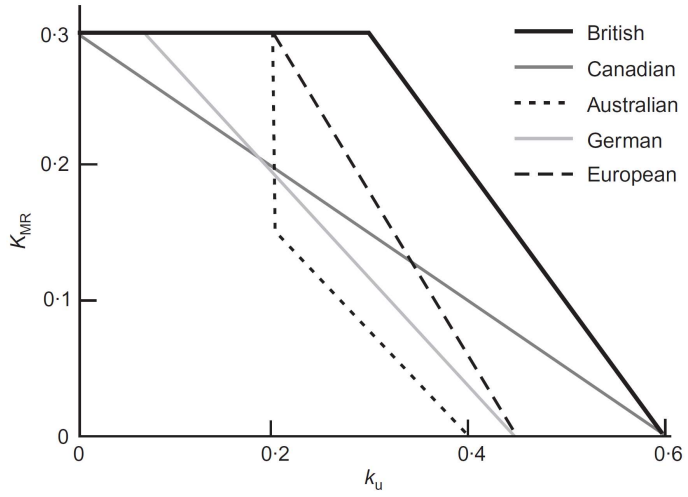

Figure 2-32: Allowable moment redistribution in codes (Oehlers et al., 2010)

The change in the neutral axis depth is what causes the change in the load deflection response, or the moment load responses. Figure 2-33 illustrates the development of the neutral axis depth with an applied load (Lou et al., 2015). The neutral axis remains constant until the concrete cracks, which results in a sudden decrease in the neutral axis depth after which the decrease in the neutral axis depth slows down with an increase in the applied load. For steel reinforced beams, there is another rapid decrease when the steel yields, which is not observed in members reinforced with brittle materials. It is this second rapid decrease in the neutral axis depth which allows the formation of a plastic hinge and therefore a redistribution of moments.

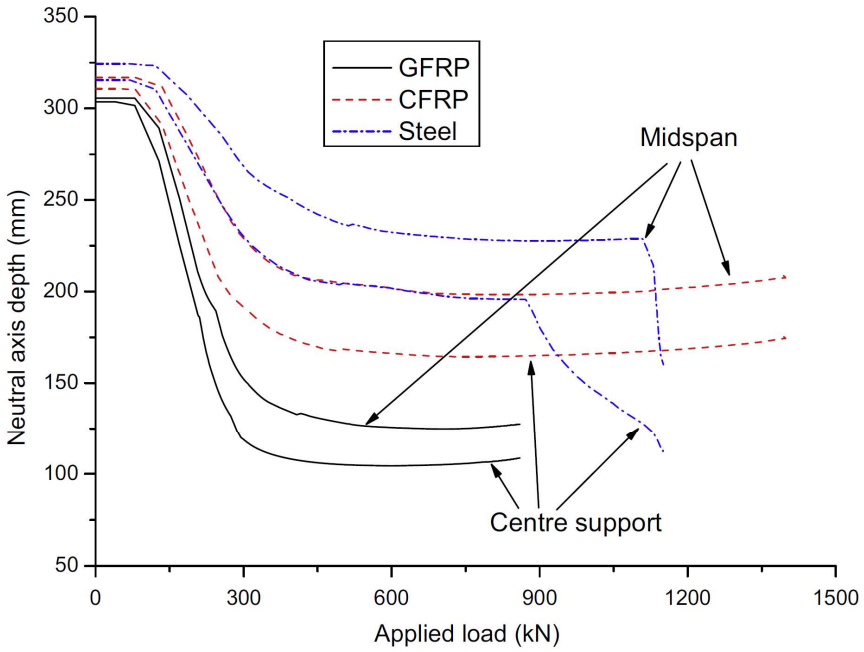

Figure 2-33: development of neutral axis depth with an applied load (Lou et al., 2015)

2.6.9. BEHAVIOURAL CHANGES CAUSED BY STEEL FIBRES

An important and potentially dangerous effect of SFRC is the possible localisation of deformations in one crack as observed by Schumacher (2006). In ordinary reinforced concrete, the strain hardening properties of reinforcing steel result in overall deflection hardening behaviour of the beam. However, in SFRC the softening behaviour can be dominant which effectively prevents sufficient stresses from building up to open neighbouring cracks. As a result, the deformation is localised in one crack resulting in reinforcement rupture instead of concrete compressive failure. Therefore, do Carmo et al. (2005) also recommended that steel with sufficiently high tensile strains should be used with SFRC.

When adding steel fibres to steel reinforced concrete it is important to consider a change in failure behaviour as reported by Visintin et al. (2018) where the addition of steel fibres shifted the failure mode from concrete crushing to reinforcement rupture. In this case, the improved compressive ductility of the concrete introduced by the steel fibres resulted in the steel rupturing before the concrete failed in compression.

The effect of only steel fibre reinforcing can be seen clearly in the work of Mohr (2012). In the study, moment redistribution is investigated in two-span continuous beams using three different fibre contents; 0.5 %, 0.75% and 1.0%. An increase in fibre content increased the bending capacity, ductility in terms of deflections and tensile resistance in comparison to a decreasing amount of moment redistribution. The post-peak moment-curvature behaviour was revealed to provide the greatest insight into the expected degree of moment redistribution. In Mohr's study, an increase in fibre content led to higher

moment capacity, however, the angle of declination after the peak was greater, therefore the bending capacity could not be maintained at the plastic hinge upon further curvature. A flatter post-peak moment curvature behaviour, nearing that of strain hardening reinforcing steel, would result in greater moment redistribution ability.

It is however important to note that Mohr used only 40 MPa concrete which limited the fibre efficiency since failure occurred due to fibre pull-out instead of fibre fracture. As a result, increasing the fibre content led to a greater reduction in the effectiveness of the fibres. This reduction in fibre efficiency is avoided in high strength concrete where the increased bond between fibres and concrete result in fibre fracture, thereby allowing the full strength of the fibres to be used. An optimum fibre content also exists in high strength concrete with the difference between normal strength concrete potentially being an increased optimal amount.

2.7. CONCLUDING SUMMARY

The behaviour of steel fibres has been discussed, along with the test methods used to determine the material properties, which includes a discussion on the assumptions made in obtaining the tensile properties. Thereafter, the concept of moment redistribution was introduced theoretically to highlight aspects of a structures behaviour which will influence the degree of moment redistribution. Finally, the behaviour of structures with ordinary steel bars, steel fibres and a combination of the two has been discussed through the findings of various researchers.

In conclusion, the difficulty in defining moment redistribution has been emphasized. A number of factors influence moment redistribution, such as the plastic hinge length and the moment curvature behaviour, which themselves are affected by complex material behaviours. The factors influencing the structural behaviour and the way a structures behaviour can be presented will be used to establish comparisons between the different structural properties in the experiments to follow.

The influence of steel fibres alone and reinforcing bars alone has been discussed, as well as the potential for crack localisation when concrete is reinforced with steel bars and fibres. The research to be conducted therefore follows a similar order than the literature presented, starting from establishing the material properties which then leads to the different structural behaviours observed.

CHAPTER 3

ELEMENT TESTING AND RESULTS

3.1. INTRODUCTION

The process of assessing the effects of steel fibres and steel reinforcing on the changes in the structural behaviour of an indeterminate beam begins with determining the material properties. This chapter sets the foundation of reasoning by making the behaviour and properties of all materials known. A methodology was created to reduce the number of assumptions required to reach each required outcome. To achieve this, all variables affecting the results had to be monitored and redundancies put into the testing setups to allow unexpected outcomes to be explained with greater confidence.

The methodology is structured in order of complexity, wherein each successive test is built upon the results of the previous. Such a process allows the final full-scale test to be discussed not only from directly measured results, but also to be explained form the fundamental laws governing such behaviour. A logical outline of the methodology is best described from the end, starting with the desired outcome of moment redistribution and general structural behaviour, and then stepping back to see which tests are required to explain this phenomenon until one reaches the point where one must choose the specific ingredients to which the outcome will relate to.

3.2. EXPERIMENTAL OVERVIEW

Moment redistribution is only possible in an indeterminate structure, however standard material property tests must be carried out to bring meaning to the full-scale test results. These material properties will depend on the chosen mix design of the concrete, the steel reinforcing and the steel fibres. An additional step required to obtain the tensile material properties of SFRC is an inverse analysis method when using indirect tensile test methods as discussed in Chapter 4. The reasoning behind each test method will be discussed in further detail following the methodology outline shown in Figure 3-1.

To investigate the effects of steel fibres and steel reinforcing on moment redistribution in the indeterminate test setup, samples were cast in the form of a grid as shown in Figure 3-2 where both the fibre and reinforcing content varied. The number of reinforcing bars is indicated by the number of dots in the table shown in Figure 3-2. The total steel content in a single beam ranges from a minimum of 0.8 % to a maximum of 4.2 %. The sample grid reveals the impact of increasing only the steel fibre content without reinforcing, or vice versa which provides the necessary insight required to explain the behavioural changes for the combined fibre and reinforcing steel samples.

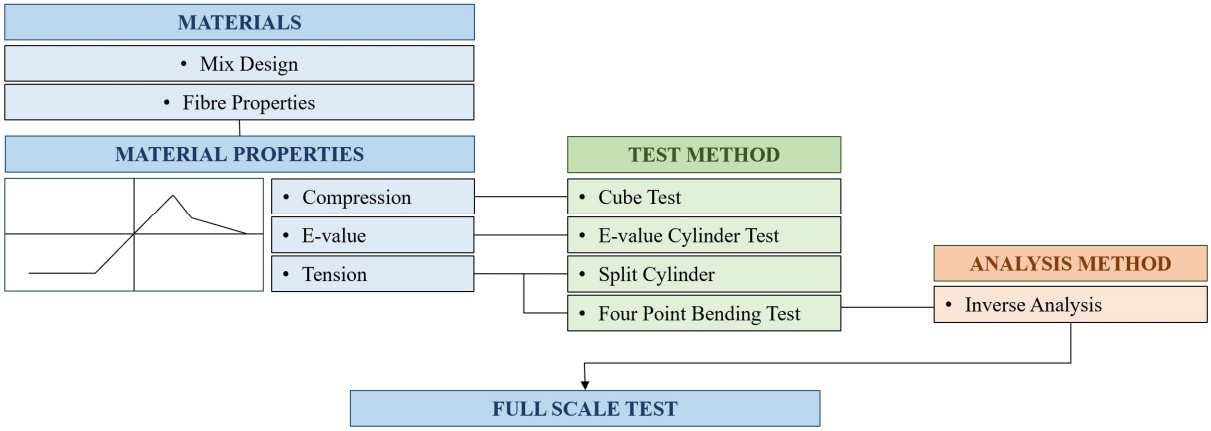

Figure 3-1: Overview of methodology

Variable		Reinforcement Ratio			
		0,0 %	0,7 %	1,4 %	2,2 %
Fibre Content	0,0 %		•	• •	• • •
	1,0 %		•	• •	• • •
	1,5 %		•	• •	• • •
	2,0 %		•	• •	• • •

Figure 3-2: Beam samples with steel fibre and bar reinforcing contents

The concrete was cast in four batches, with each batch containing a different fibre content. A batch with a certain fibre content would therefore be split into four moulds (apart from the batch with no steel fibres where no beam was cast containing no reinforcing) of increasing reinforcing steel content. This method was the most efficient as only four different batches of concrete were cast into moulds containing different reinforcing amounts.

3.3. MATERIALS

3.3.1. MIX DESIGN

A mix design suitable for high strength concrete of about 80 MPa was prepared. The concrete strength for all beam setups was to be constant with the only variable being the amount of steel fibres and steel reinforcing. The four mix designs are shown in Table 3-1. Slight variations in the amount of sand were required to maintain a workable mix with high fibre contents.

Table 3-1: Mix design for different fibre contents

Material	RD	0% Fibres (kg/m^3)	1.0% Fibres (kg/m^3)	1.5% Fibres (kg/m^3)	2.0% Fibres (kg/m^3)
Cement	3.14	700	700	700	700
Dolomite Stone	2.85	790	790	790	790
Dolomite Sand	2.85	808	776	761	744
Water	1	210	210	210	210
Superplasticiser	1.06	7.0	7.7	10.5	11.2
Steel Fibres	7.9	0	79	119	160
Total		**2515**	**2563**	**2591**	**2615**

3.3.2. FIBRE PROPERTIES

The fibres used were hooked ended steel fibres. A fibre length of 30 mm was chosen over 60 mm fibres due to the shallow depth of the beams. Whilst the choice of fibre can have a large effect on the results, the trends observed in terms of moment redistribution should be similar. Since the main objective was to observe the effect of replacing reinforcing steel with steel fibres, only one specific fibre type was used. If there are fibres that are more effective than the specific type chosen in the research, the trends observed in the results should be similar, apart from the amplitude of change brought about by varying the fibre content. To limit the variables only one specific fibre type was used, a large factor in the chosen 30 mm length being the workability of the concrete in the highly reinforced full-scale beams. The fibre type is shown in Figure 3-3 and the properties are summarised in Table 3-2.

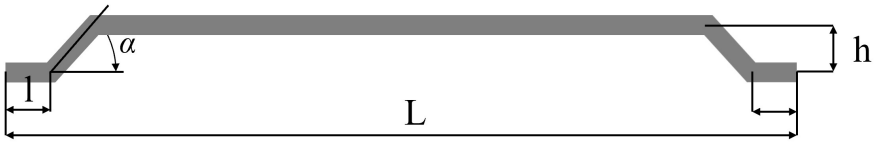

Figure 3-3: Fibre dimensions

Table 3-2: Fibre Properties

DIMENSIONS	30 mm x 0.5 mm
Wire diameter (d)	0.5 mm + 0.0.01 mm/ -0.02 mm
Fibre length (L)	30 mm ± 1.5 mm
Hook length (l)	1.5 – 4 mm
Hook depth (h)	2.0 ± 1 mm
Bending angle (α)	45º (min 30 º)
Aspect ratio (L/d)	55
Torsion angle of the fibre	< 30 º
Typical tensile strength	> 1100 N/mm^2

3.4. MATERIAL PROPERTY TESTS AND RESULTS

To fully describe the stress-strain behaviour of the material, three material property tests were conducted. Compression tests were carried out to characterise the entire compressive behaviour of the four concrete mix designs. The elastic modulus test was performed on cylinders, which were also used to obtain load vs crack opening relationships in split cylinder tests. Tensile behaviour was characterised by a four-point bending test. Testing was conducted on mature samples that were left to cure for at least 28 days.

The large size of the indeterminate beams meant that the beams had to be cured outside on the laboratory test floor, covered with plastic as well as a thermal blanket to keep the temperatures as consistent as possible throughout the day. The samples used to obtain the material properties for the indeterminate beams were therefore kept in the same environment, with the beams under the plastic and thermal blanket. Additional samples were cast from the same concrete batches which were cured in water for at least 28 days as a control. All samples, including the large beams were demoulded after 24 hours.

3.4.1. COMPRESSION TESTS AND RESULTS

Standard compression tests provide only a single value for the compressive strength of concrete. Since the compressive stress-strain behaviour of concrete is usually assumed to be a bilinear relationship, only an elastic modulus and a compressive strength is required. However, the inclusion of steel fibres tends towards a more ductile failure, resulting in a less defined point of maximum compressive stress in the stress-strain diagram. Further accuracy in describing the compressive behaviour is also required for the inputs of modelling software, especially in highly reinforced concrete structures in which the compressive strength of the concrete may be exceeded.

In total twenty-four 100mm x 100 mm cubes were crushed, and the stress-strain relationship recorded. The material samples were the same depth than the depth of the large-scale beams, thus minimising the changes in behaviour caused by edge effects. Six cubes for each of the mix designs were tested, three being cured in air right next to the respective full-scale beams, and three in water as a reference. Average (air cured) compressive stress-strain diagrams for the mix designs are shown in Figure 3-4. These results indicate that the inclusion of fibres results in a marginal increase in concrete compressive strength. The dotted sections of the lines in Figure 3-4 are linearly extrapolated results because testing stopped shortly after the peak load.

As no significant post peak stress-strain behaviours were recorded, post peak behaviours had to be extrapolated. Although it is known that the post peak behaviour is not linear, a simplification was necessary to provide an indication, possibly overestimating the compressive strength, as to the possible post peak behaviour. The linear extrapolations were a continuation of the slope of the measured results.

The shape of the compressive stress-strain behaviour of concrete of similar strength, with steel fibres contents covering the range of steel fibre percentages used were investigated by Bencardino et al. (2008). Based on these results the simplified extrapolation was deemed suitable since the post peak behaviour of steel fibre reinforced concrete was shown to exhibit significant post peak strength. In any case, the flexural tests were expected to produce only small concrete strains within the linear region due to the relatively low tensile strength provided by the steel fibres.

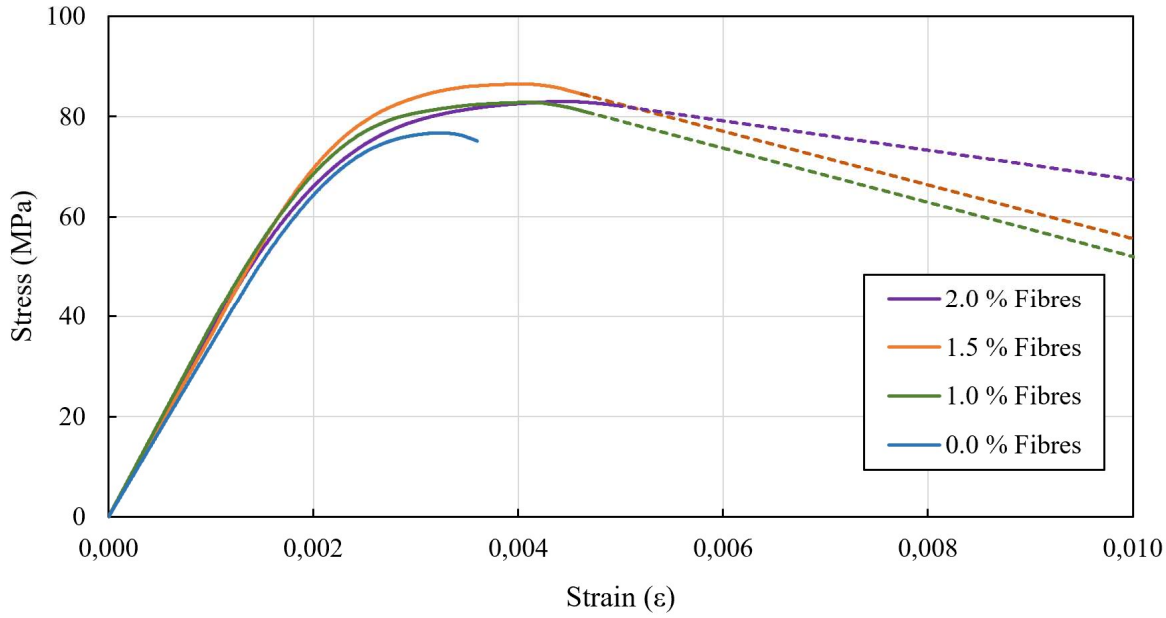

Figure 3-4: Average compressive stress-strain relationships

The ultimate compressive strengths are summarised in Table 3-3 which also shows the strains at peak stresses. Although a general trend of increasing compressive strengths would be expected, the fact that the four mix designs were cast on different days, as well as the increasing superplasticiser dosage with increasing fibre content, meant that some degree of inconsistency was introduced. However, due to the high concrete strength, it was expected that failure in concrete compression would not occur, and hence the slight variation in concrete compressive strengths would have an insignificant effect on the load carrying capacity of the full-scale beams.

For the air cured samples containing no fibres, the range of compressive results differed by 4.0 MPa, a range of 5.2% when compared against the average compressive stress. The air-cured samples containing steel fibres showed less variation, where the ranges compressive results represented 4.4%, 0.8%, and 2.1% of the respective average compressive stresses. The scatter of compressive stresses for the fibre reinforced concrete cubes was therefore less than in cubes without fibres. The same trend was observed in the water cured samples.

Table 3-3: Average compressive values

Concrete Batch	0.0 % Fibres	1.0 % Fibres	1.5 % Fibres	2.0 % Fibres
Cube 1 Stress (MPa)	74.5 (77.7)*	84.1 (93.9)*	85.8 (102.0)*	84.1 (101.4)*
Cube 2 Stress (MPa)	76.8 (85.9)*	81.5 (90.4)*	83.0 (103.1)*	77.4 (104.1)*
Cube 3 Stress (MPa)	78.5 (87.1)*	80.5 (90.5)*	86.5 (97.9)*	82.4
Average max stress (MPa)	**76.8** (83.6)*	**82.0** (91.6)*	**85.1** (101.0)*	**81.3** (102.8)*
Average strain at max stress (ε)	**0.00323** (0.00327)*	**0.00412** (0.00384)*	**0.00402** (0.00380)*	**0.00444** (0.00365)*

**Water cured samples*

The change in ductility of the material with the presence of steel fibres is revealed in the results of Table 3-3. The inclusion of fibres leads to a slight increase in compressive strength with slightly higher strains at the peak stresses. The decrease in peak stresses in the 2.0% fibre samples indicates that the fibre content may be beyond the optimum amount and hence the 2.0% samples have a slightly lower strength than the samples with 1,5% fibres.

3.4.2. ELASTIC MODULUS TESTS AND RESULTS

A total of sixteen 150 x 300 mm cylinders were cast from the four concrete batches, with four cylinders representing each batch, where two were cured in a water bath and two cured in air near the respective full-scale beam. The cylinders were loaded to 40% of the characteristic compressive strength before being unloaded. This process was repeated three times for each cylinder upon which an average elastic modulus was calculated of the results of the air-cured and water cured samples are shown in Table 3-4. These results indicate that the inclusion of fibres had an insignificant effect on the concrete stiffness.

Table 3-4: Elastic moduli

Concrete Batch	0.0 % Fibres	1.0 % Fibres	1.5 % Fibres	2.0 % Fibres
Cylinder 1 *E* (GPa)	36.30 (44.6)*	36.40 (41.8)*	37.40 (45.5)*	37.50 (447)*
Cylinder 2 *E* (GPa)	36.20 (44.0)*	37.80 (41.8)*	38.20 (45.0)*	36.80 (38.1)*
Average *E* (GPa)	**36.28** (44.3)*	**37.11** (41.8)*	**37.77** (45.2)*	**37.18** (41.4)*

**Water cured samples*

3.4.3. SPLIT CYLINDER TESTS AND RESULTS

The split cylinder test setup used by Denneman (2011) and discussed in the literature study is used. Tensile strengths are calculated from the equation proposed by Tang (1994) which includes the correction for the load strip width:

$$f_{ti} = \frac{2P_i}{\pi D}\left[1 - \left(\frac{b_c}{D}\right)^2\right]^{\frac{2}{3}} \qquad \textit{Equation 3.1}$$

Where P_i is the peak load at first cracking or the overall peak load (in terms of load per mm length of the sample), D is the diameter of the cylinder, and b_c is the width of the loading strip. Figure 3-5

indicates the load vs transverse deformation results of the cylinders containing fibres and cured in air. The transverse deformation was measured over a distance of 50 mm between rods drilled into the cylinder. Two load peaks can be seen in most results, with the first peak occurring with the first crack, and then a secondary peak forming as a result of the residual strength of the fibres. A summary of tensile strengths for the steel fibre reinforced cylinders is given in Table 3-5.

Table 3-5: Tensile split cylinder strengths

Concrete Batch	1.0 % Fibres	1.5 % Fibres	2.0 % Fibres
Cracking stress (MPa)	3.06 (3.66)*	4.81 (4.56)*	4.61 (5.52)*
Maximum tensile stress (MPa)	5.16 (5.35)*	7.06 (7.14)*	8.95 (9.33)*

**Water cured samples*

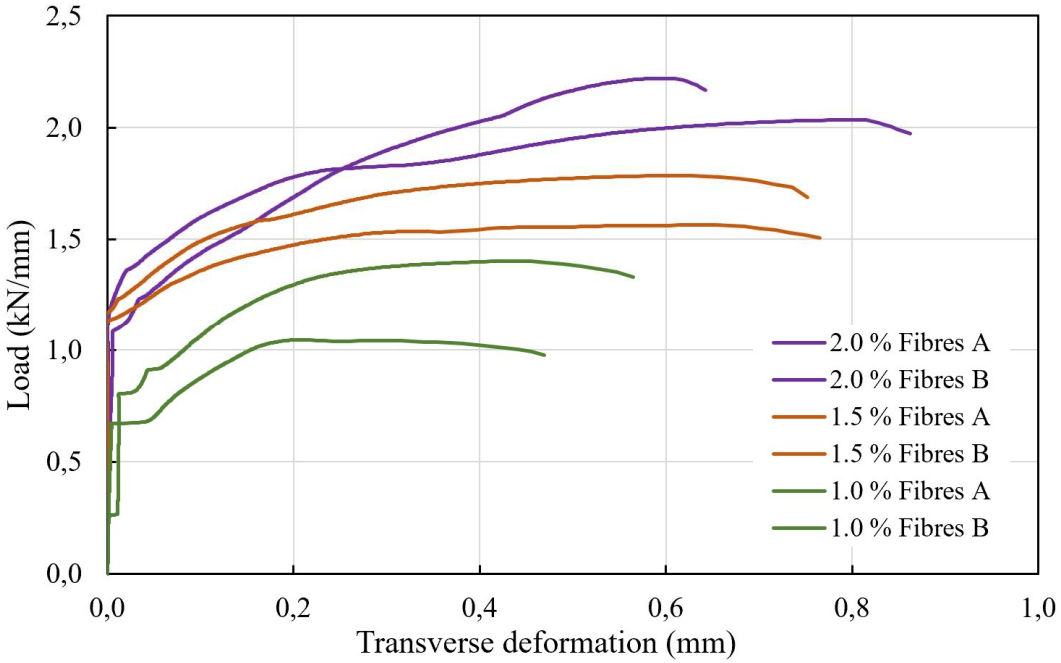

Figure 3-5: Transverse deformation for split cylinder tests

3.5. FOUR-POINT BENDING TEST SETUP

The tensile response of a material can be evaluated either through direct or indirect tensile tests. In theory the direct tensile tests seem simple, however, the influence of specimen size and boundary conditions lead to a complex process in obtaining reliable results. Indirect tensile tests, such as split cylinder tests and three-point or four-point bending tests (FPBT), provide an easier practical solution. The drawback of a simplified test setup is that it adds complexity in the processing of the results to obtain the uni-axial tensile response. For FPBTs an inverse analysis must be performed to convert the data from either a load vs deflection or load vs crack-mouth-opening to a stress-strain relationship. An added benefit of the FPBT flexural test is that a direct measurement of moment curvature can be

obtained. It was therefore decided to conduct FPBTs to evaluate both the tensile behaviour as well as the moment curvature behaviour of the beam specimens as well as split cylinder tests for comparison.

The geometry of the FPB beams was based on the height of the large-scale indeterminate beams to minimise size and edge effects between the FPB beams and the large-scale beams. Having the same beam depths of 100 mm for all specimens would ensure greater consistency in fibre orientation and therefore help to reduce the unwanted size effect variable. The geometry of the beam is indicated in Figure 3-6 and lies within the recommendations of the Japanese (JCI-S-003, 2007) and American (ASTM-C1609, 2012) codes. As with the cube samples, a total of 24 beams were cast, six per batch, where three were cured in curing baths and three were cured in air next to the respective full-scale beam. Particle Image Velocimetry (PIV) was used to measure curvature and will be discussed in the following sections.

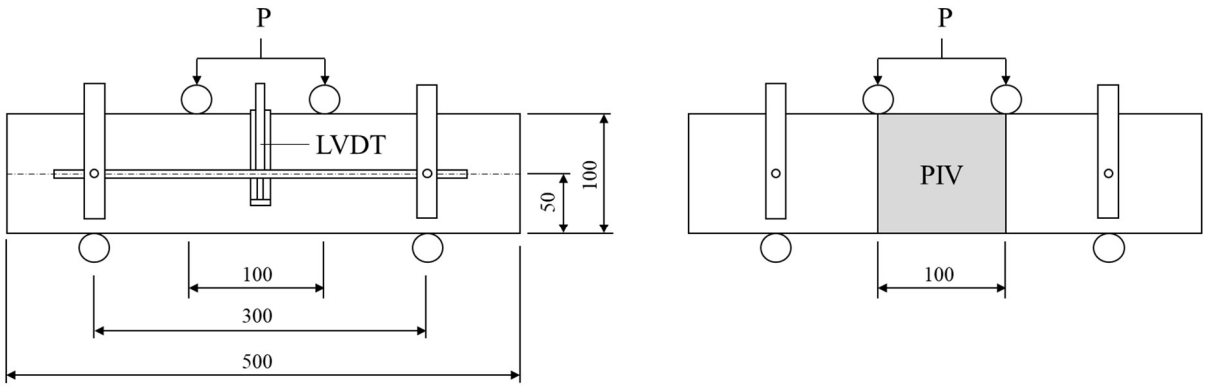

a) Deflection measurements b) PIV measurements for curvature

Figure 3-6: FPBT beam dimensions

Testing was conducted under deflection control at a rate of 0.3 mm per minute. Loading was increased until a deflection of at least 5 mm was obtained for each specimen. Even though the maximum required deflection according to the ASTM 1609 (2012) recommendations is L/150, where L is the span length, which equates to only 2 mm in this case, observing the response beyond a 2 mm deflection would provide greater insight into the behaviour of the different fibre contents. Deflection was measured using LVDTs at the centre of the beam span at mid-height, relative to the mid-height end points above the supports. A photo of a flexural test is shown in Figure 3-7.

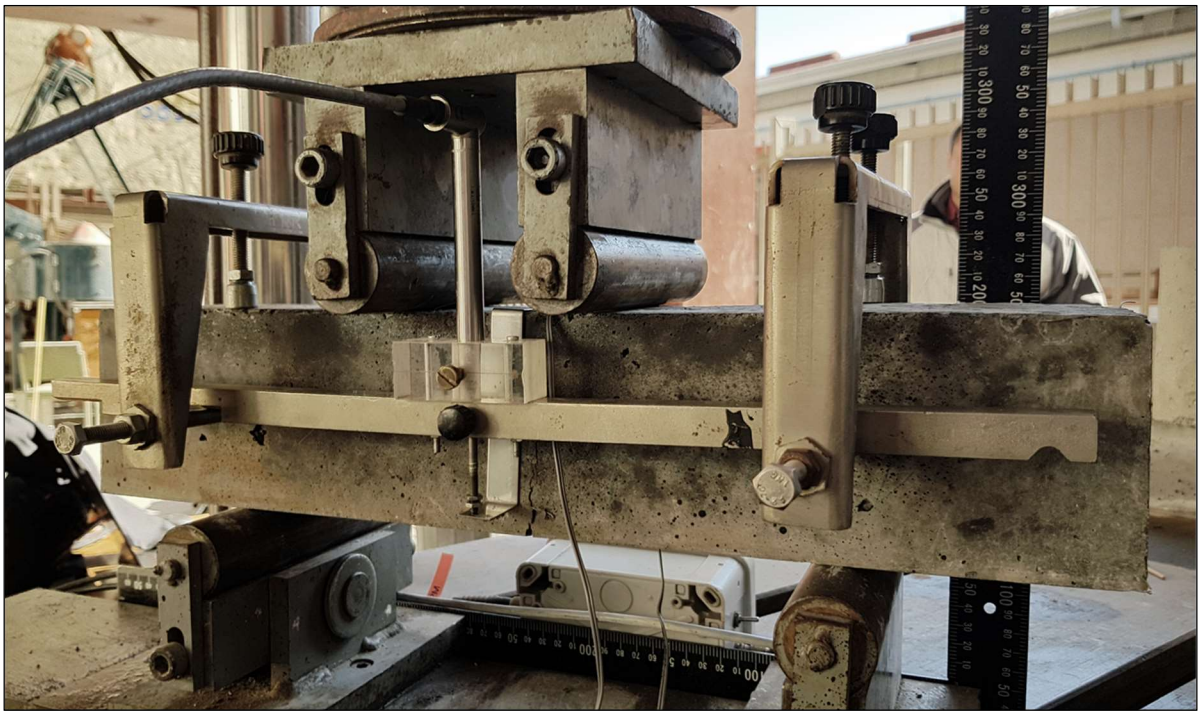

Figure 3-7: Four Point Bending Test

In addition to the load-deflection response, moment curvature was measured. Initially, LVDTs were used to record the strains near the top and bottom of the beam as shown in Figure 3-8. Although the readings were accurate, the high deflections resulted in excess rotations which were not suited to the fixed LVDT setup.

Figure 3-8: FPBT causing bending in the LVDTs

The alternative was to use PIV software to track the surface of the concrete as it deformed (White, 2002, Take, 2002). A Canon EOS 100D camera was used in full manual mode to take photos at 2 second intervals. The photos were then processed in GEO-PIV 8 to create a trackable mesh across the surface

of the specimen. Tracking accuracy was improved by creating a contrasting surface on the concrete using black or white spray paint. The simplicity of the setup is shown in Figure 3-9 and, if proven reliable, can be a cost-effective solution to record both load-deflection and moment-curvature behaviour. Furthermore, since the strain measurements can be calculated anywhere across the meshed surface, there is no risk of losing data as with cracks forming outside the set range of the LVDTs.

Figure 3-9: PIV setup for the FPBTs

To ensure greater precision before cracking strain gauges were placed on the top and bottom surface of the beam at the centre of the span. Once cracking occurred, the bottom tensile strain gauge would be rendered useless and at this point the recorded strains are taken as the PIV calculated strains. Since none of the specimens failed in compression the top strain gauge could be used for the compressive strain behaviour throughout the test. The outcome was that curvature was based on the top compressive strains provided by the strain gauge, and the bottom tensile strains provided by a combination of the strain gauge and PIV.

3.5.1. USING PIV TO CALCULATE CURVATURE

A benefit of image analysis is that the behaviour of the structure can be recorded as a whole to give an overview of the deformed shape, followed by a more in-depth analysis at specific regions along the member. The level of detail to which one can zoom into the deformed shape depends on the resolution of the image, and hence the precision of the results is a function of the image resolution. Other factors within the camera settings will also play a role, such as the F-stop, ISO, shutter speed and also the quality of the lens used.

For the software to track points across the surface of the member, the image is divided into a mesh with patches of uniform size. Data from the image is stored in terms of three brightness intensity values (RGB). The mesh therefore separates this data into smaller patches which each contain their own unique combination of brightness intensity values. When another photo is analysed and certain parts within the

image have moved, each patch can be repositioned by searching where its own original brightness values have moved to. This is the fundamental concept of the PIV technique (White, 2002, Take, 2002).

Since this method depends on having uniquely identifiable elements, the surface requires good texture. This texture is created by spraying black paint across the concrete to provide randomly varying brightness values across the image. However, for a large surface area divided into small patches, the chances of having similarly defined patches are increased resulting in patches overlapping or relocating to completely different areas within the image. To minimise this occurrence, a search area is defined around each patch. For each patch therefore, the search for its characteristic brightness values is limited to a small defined area where a best match is found. The search area must however be large enough to include the movement of pixels due to deformation.

The optimum patch size for accurate tracking depends on the quality of the image and the type of testing. For instance, a lower quality image will require larger patch sizes so that enough texture is contained within each patch to make it unique. A balance must be reached between the size of the patches and the required detail from the tracking points. More patches mean more tracking points and therefore a more detailed analysis, however, this comes at the cost of reduced accuracy since the small patches are defined by fewer pixels. Larger patch sizes reduce tracking errors but result in less detailed but more accurate results.

3.5.2. DEFINING THE MESH

The first step is to define a mesh area, as well as the size of the mesh. Figure 3-10 shows an example of a mesh taken from a FPBT. A finely divided mesh was chosen for this example so that the location of the crack could be more clearly defined. Since the aim of this analysis was only to calculate the curvature within the constant moment region, only the top and bottom row of elements were used in the analysis to reduce the computation time.

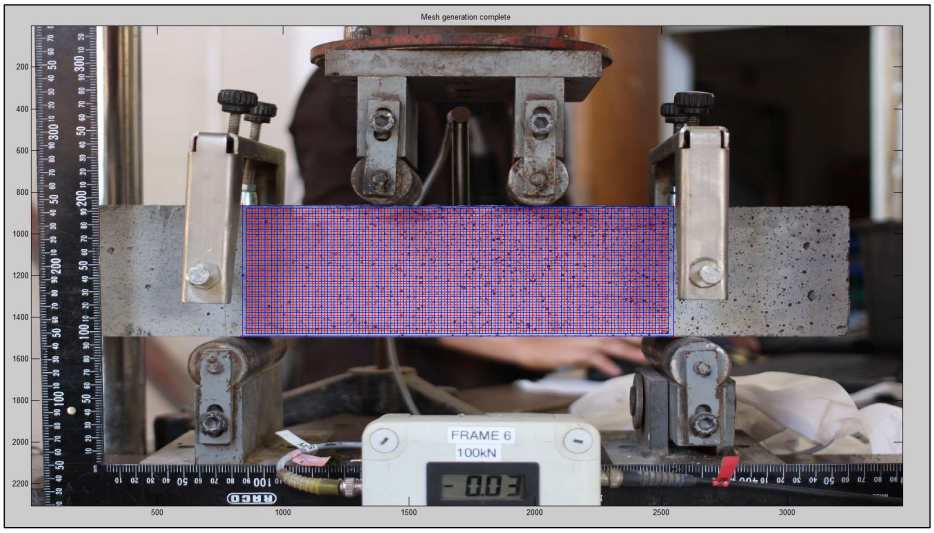

Figure 3-10: Mesh generation

3.5.3. INTERPRETING THE RESULTS

Figure 3-11 indicates the location of the patches before and after the test. The patches across which the crack formed resulted in tracking errors since a match of the original brightness values can no longer be found. By visual inspection, the tracking can be successfully performed as the only lost patches are the ones across deformed surfaces over which tracking is not possible. The x- and y-coordinates of each patch is stored in a matrix in terms of the pixel number which can be used to calculate the distances between elements. The ruler within the picture is used to convert pixel distances into millimetre distances. For curvature calculations, the strain between two patches under the load points in the top row and two patches in the bottom row are used. These strains are calculated by comparing the distance between these patches in any image taken throughout the test with the original distance between them in the first image. In essence, to obtain the moment curvature diagram comparable to that from the LVDTs only four patches were required for these FPBTs. However, for the full scale-test the curvature distribution along the length of the beam was to be obtained which requires a row of patches along the top and bottom of the beam as in Figure 3-11.

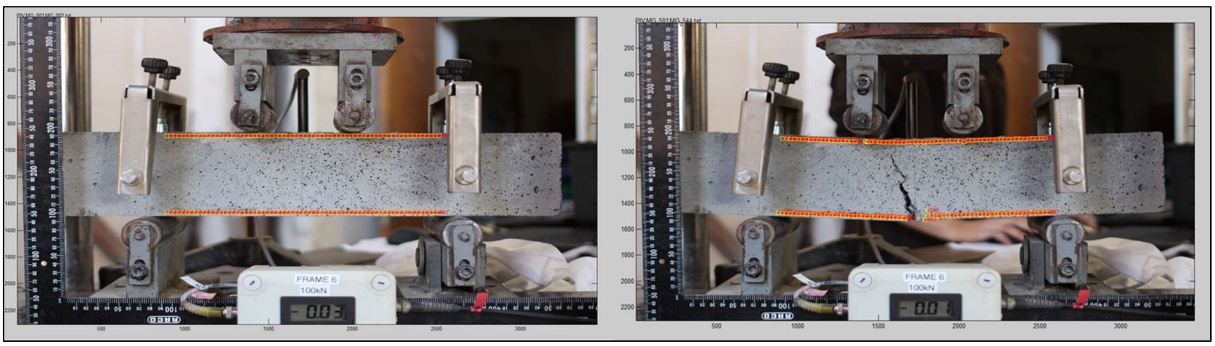

Figure 3-11: PIV analysis before and after testing

The problem with defining a curvature distribution along the length of the beam is that the magnitude of the curvature will depend on the distance across which the strains were measured. A schematic of this problem is shown in Figure 3-12. Assuming a certain mesh size has been defined, strains can be calculated between each consecutive patch, or between patches of a constant length apart. When a crack forms, the strain calculated over a short distance across the crack will be much higher than the strain calculated across a longer length. This difference will translate into a difference in curvature as indicated by the peak curvatures in Figure 3-12.

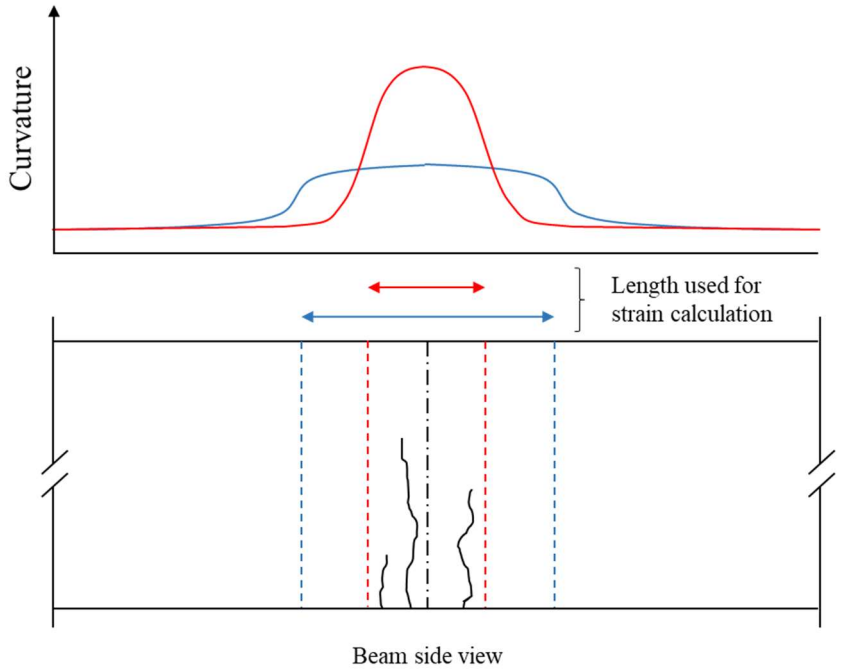

Figure 3-12: Curvature values across different widths

The rate of decrease in curvature around the peak is also different. Strains between closely spaced patches will rapidly decrease when moving away from the crack since the strains are no longer referenced to both sides of the crack. The strain calculated across longer distances reduces at a slower rate since the crack still falls between the reference points for patches further away from the crack. The resulting curvature distributions are clearly different which introduces the issue of choosing the length over which the curvature should be calculated.

3.5.4. EFFECTS OF DIFFERENT ELEMENT SIZES

The effect of the patch size was not discussed in the FPBTs since the curvature between the load points is assumed to be the same within the constant moment region. However, for the indeterminate tests, the moment envelope varies constantly which suggests that the curvature should be measured across an infinitely short distance. As this is clearly not possible, the length of 100 mm was chosen as standard across which all beams were compared. This length would therefore provide a certain moment curvature distribution across the length of the beam that would look different to curvature distributions calculated across different lengths.

Since the curvature distribution across the length of the beam is dependent on the element spacing, the distribution provides more of a graphic presentation of the curvature of the beam where the length across which the curvature is measured acts as resolution. The smaller the length, the greater the resolution, where in theory smaller distances can be used until the exact positions of each crack will be

revealed. However, practically this is not possible as the quality of the images in the PIV analysis requires a minimum length to reduce the noise in the results.

To add to the problem, tests were conducted on different days without the ability to control the lighting conditions. This meant that the input variables such as element size and spacing for the PIV analysis of each beam was slightly different. As a result, the curvature distributions could only be used as a visual aid in highlighting the locations of cracks.

One way to overcome the problem of element sizes, was to investigate the total area under the curvature distribution. Since energy must be absorbed by the structure to deform, it stands to reason that the area underneath the curvature graphs could represent this energy, leading to the assumption that the area under the curvature distribution is independent of the element size.

To investigate the assumption of a constant area under a curvature distribution, regardless of the length across which the curvature was based, the test results of the beam in Figure 3-11 (1.5% steel fibres) will be used. The curvature distribution across the constant moment zone is calculated based on strains calculated from elements at four different distances apart. Each of the four distributions are taken at different stages in the test and are indicated in Figure 3-13.

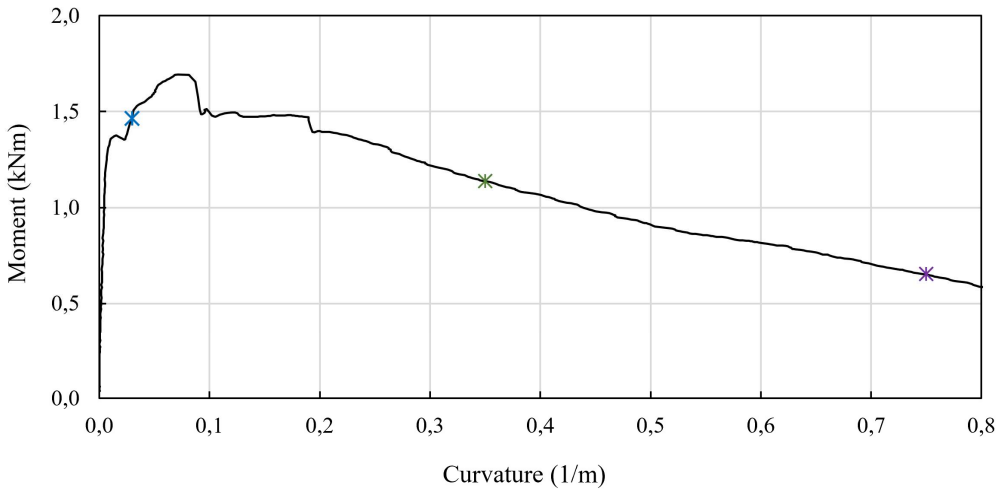

Figure 3-13: Moment curvature relationship indicating the curvatures considered

The distances across which the strains are measured start at the width of the constant moment region of 100 mm and decreases to 10 mm. The exact distances are shown in Figure 3-14 along with the respective curvature distributions throughout the different loading stages. For clarity only three loading stages are included in Figure 3-14. Each colour corresponds to the loading stage shown in Figure 3-13, and the intensity of the colour represents a different width across which the curvature was measured. As expected, the curvature is constant across the constant moment region when considering a width of 100 mm (L/3). Decreasing the width results in increasingly sharp peaks in the curvature distribution.

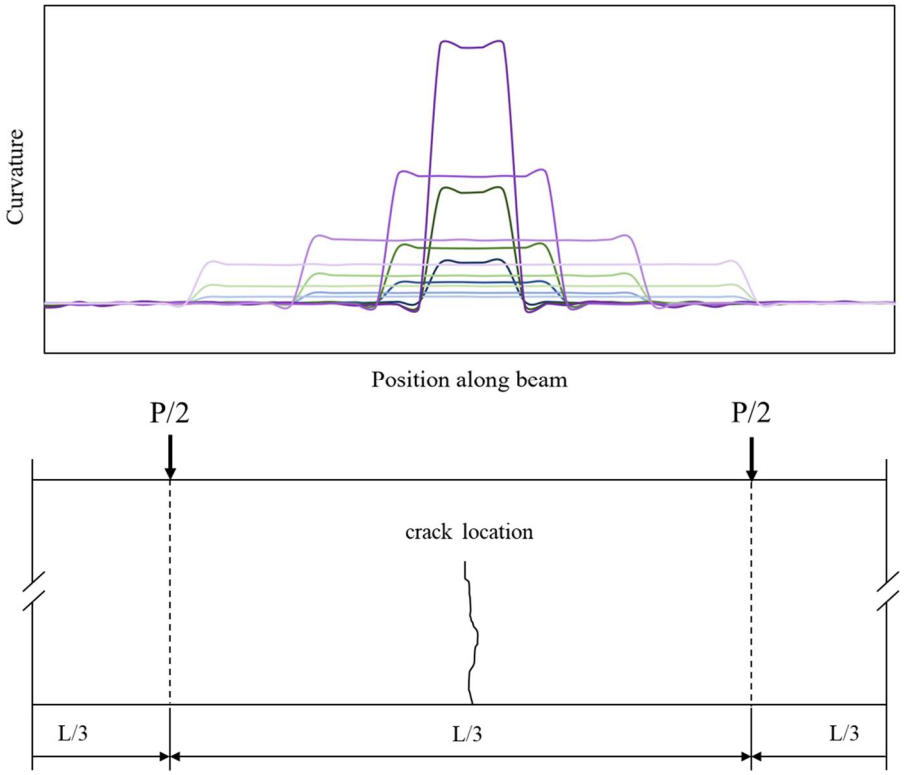

Figure 3-14: Curvature distributions across the beam for different element sizes

The next step is to calculate the area underneath the curves. Two aspects will be considered when comparing the areas. One aspect is how similar the areas are at a certain stage in the test between the four widths considered. The other is how the similarities in areas change at different stages of curvature. At one stage in the curvature an average of the areas was calculated from the four different widths. A percentage difference was then calculated for each of the four widths compared to the average area. This process was repeated for the other three curvature values in the moment-curvature diagram. It was found that the maximum percentage differences were 4.4 % for the lowest curvature, 1.4 % for the second curvature values, followed by 0.49 % and 0.28 % for the third and fourth curvature values respectively.

The areas underneath the curvature distribution therefore seem to converge as the curvature increases. Since the curvature distribution across the indeterminate beam will only be investigated at high curvatures, it can be safely assumed that the chosen width across which the curvature will be calculated will not cause any significant differences in the total area under the curvature distribution.

3.5.5. LOAD-DEFLECTION RESULTS

The load deflection responses for all beam specimens are shown in Figure 3-15 to give an indication of the variability in the results. Although the primary cracks were expected to form in the constant moment region, the random dispersion of fibres occasionally caused cracks to form outside the load points.

Specimens showing such behaviour were omitted from the calculated average load deflection and moment curvature relationships, however, the load deflection results for all specimens are still shown to make it possible to observe whether such failure types present any significant behavioural trends.

The predicted behavioural changes accrued by the inclusion of steel fibres is most evident in the results observed in the flexural tests. In the results of these tests one can see the increased load bearing capacity, changes in moment curvature and most importantly the post-peak behaviour where the fibres have the greatest influence. The test results from these flexural tests also provided the data set for the development of representative tensile stress-strain relationships based on a suitable inverse analysis procedure.

All load deflection graphs are plotted on the same scale so that any differences in load and shape of the curve can be easily observed. The range of results for the air cured beams is highlighted in grey in Figure 3-15. Water cured beam specimens are included in the results as dotted lines as reference for beams cured in a controlled environment. There is no obvious improvement in test result repeatability with the water cured specimens, which indicates that the underlying cause in variability is the random distribution and orientation of the steel fibres. As such, a certain degree of variability will always be expected when carrying out flexural tests on beams containing steel fibres.

A summary of key points on the load-deflection graphs is given in Table 3-6. There is a noticeable increase in peak load, with the 2 % fibres carrying more than twice the load at 44.0 kN when compared to the beams with no fibres at 18.6 kN. This increase in load capacity indicates the beneficial post cracking strength brought about by the steel fibres. In addition, the deflection at the peak loads decreases with an increasing fibre content even though the peak loads increase. The decrease in deflection is more evident between the 1 % and 1.5 % fibre samples, a decrease of 0.29 mm, than the 0.02 mm decrease in deflection between the 1.5 % and 2 % fibre samples. This behaviour is another indicator that there exists a certain optimum fibre content after which an increase in fibre content leads to less improvements in structural performance. However, the optimum may be defined differently based on which structural improvements are required, such as minimising deflections or increasing the load capacity.

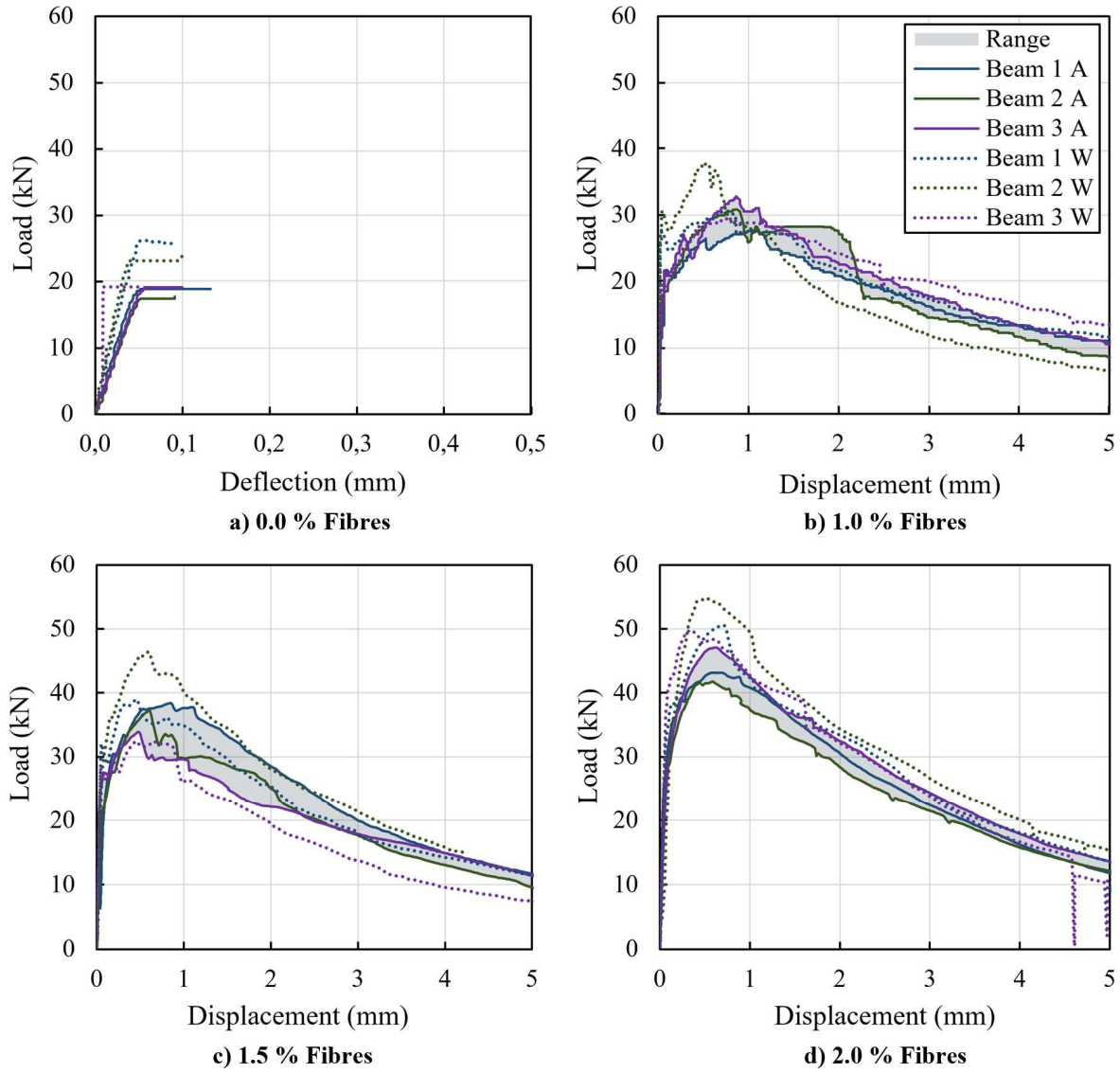

Figure 3-15: Load deflection responses

Table 3-6: Load-deflection results

Parameter	0.0 % Fibres	1.0 % Fibres	1.5 % Fibres	2.0 % Fibres
Average peak load (kN)	18.6	30.5	36.5	44.0
Average displacement at peak load (mm)	0.09	0.93	0.64	0.63

The average load-deflection results for the specimens are shown in Figure 3-16. These curves will be used as parameters for not only the inverse analysis used to determine the tensile strength of the concrete, but also to establish the moment-curvature relationships which will be discussed next.

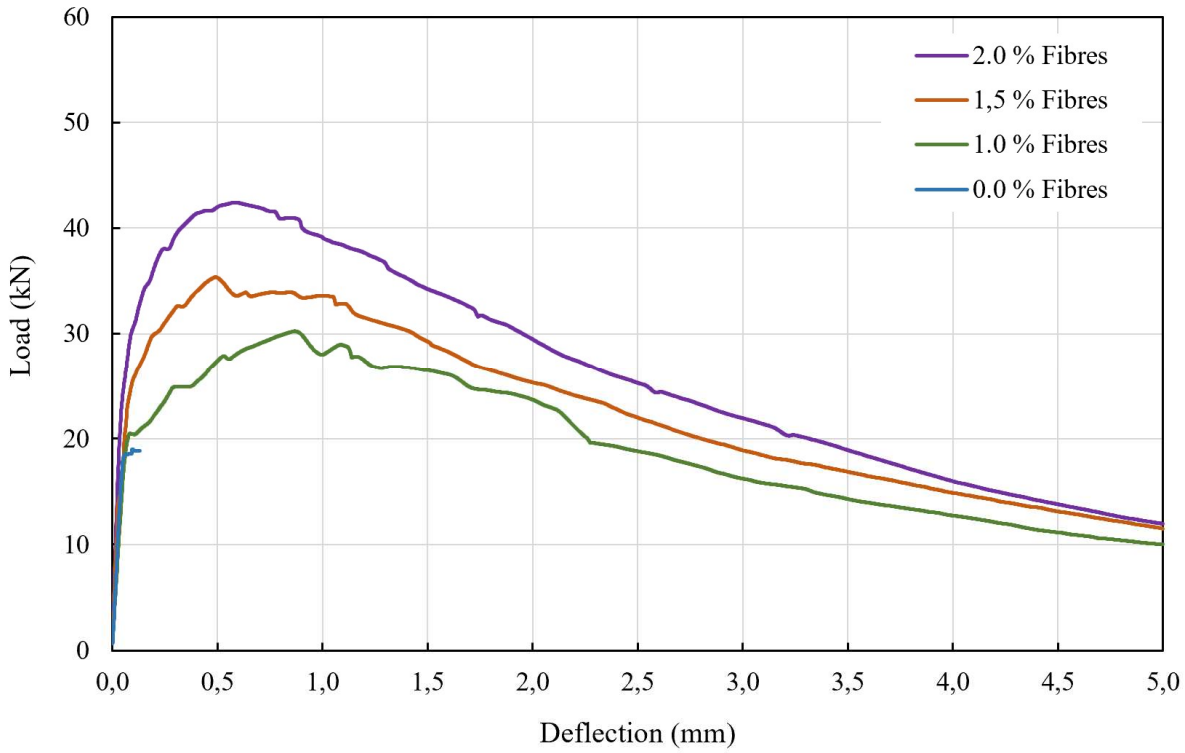

Figure 3-16: Average load-deflection results

3.5.6. MOMENT-CURVATURE RESULTS

As discussed in the literature study, the moment curvature behaviour of a sample indicates its potential moment redistribution capabilities. Understanding the shape of the graphs and how the moment carrying capacity changes as the curvature increases forms a base of reasoning when analysing the moment redistribution capabilities of the respective full-scale indeterminate beams.

The moment curvature for the fibre containing samples in which the crack formed in the constant moment region are illustrated in Figure 3-17. Only the air cured results are shown as only these moment curvature results were required in the inverse analysis to relate to the full-scale beams. The average moment curvature relationships for the three fibre contents, shown in Figure 3-18, were used in the inverse analysis.

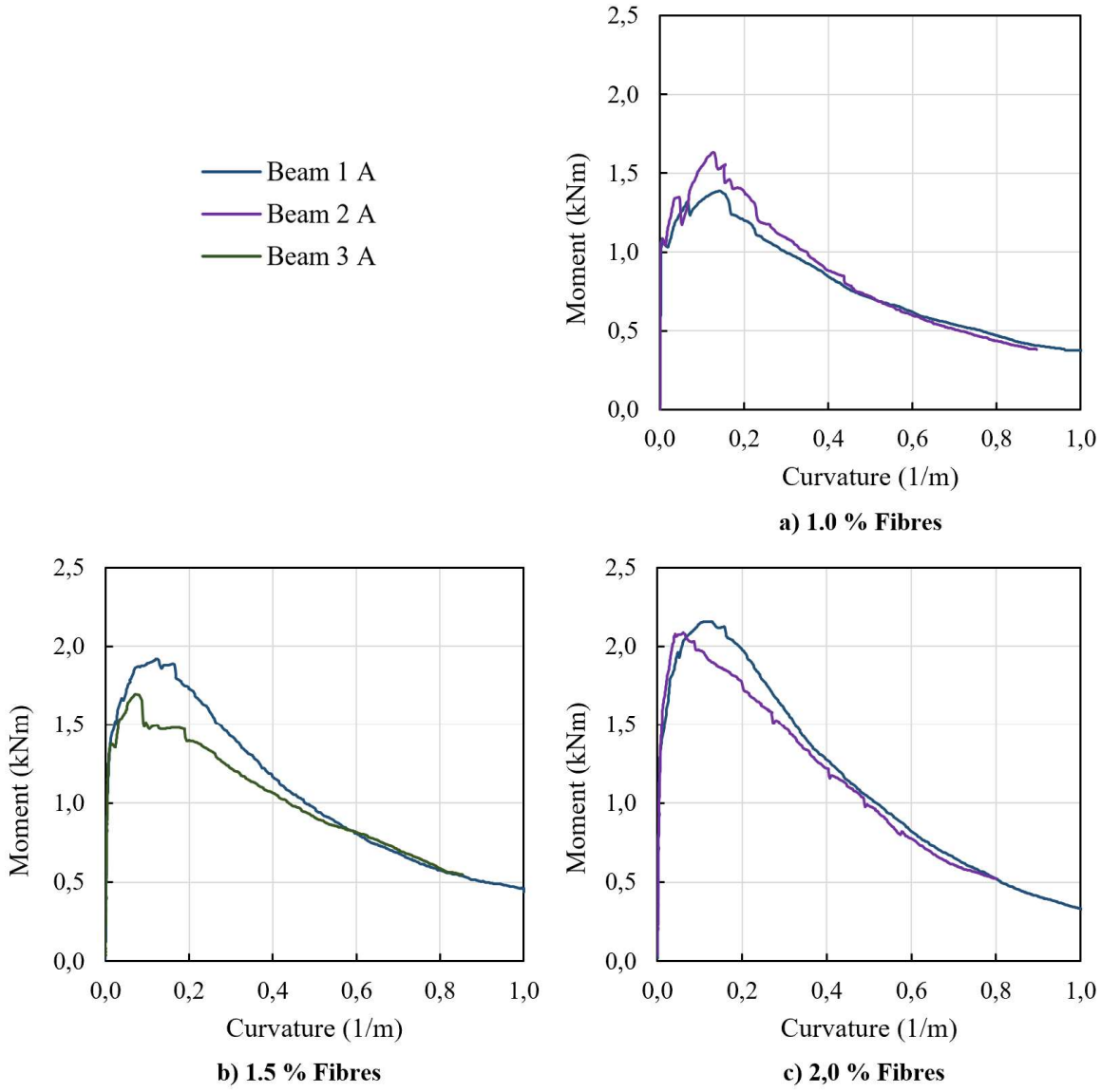

a) 1.0 % Fibres

b) 1.5 % Fibres

c) 2,0 % Fibres

Figure 3-17: Moment curvature responses

Previously, the idea of an optimum fibre content was discussed. Again, this concept is visible in the moment curvature relationships in Figure 3-18. A constant increase in moment at each curvature value is evident when the fibres are increased from 1 % to 1.5 %. This increase is clearly visible as the 1.5 % fibre curve sits mostly parallel above the 1 % curve. This is not true for the 2 % fibre curve, which shows a more rapid decline following the peak moment capacity. Even with a larger number of fibres, performance at higher curvatures for the 2 % fibres samples becomes worse since the full tensile strength of the fibres cannot be reached. With many fibres, the material matrix is unable to bond sufficiently to the fibres resulting in fibre pull-out where the maximum tensile strength of the steel fibres is not reached.

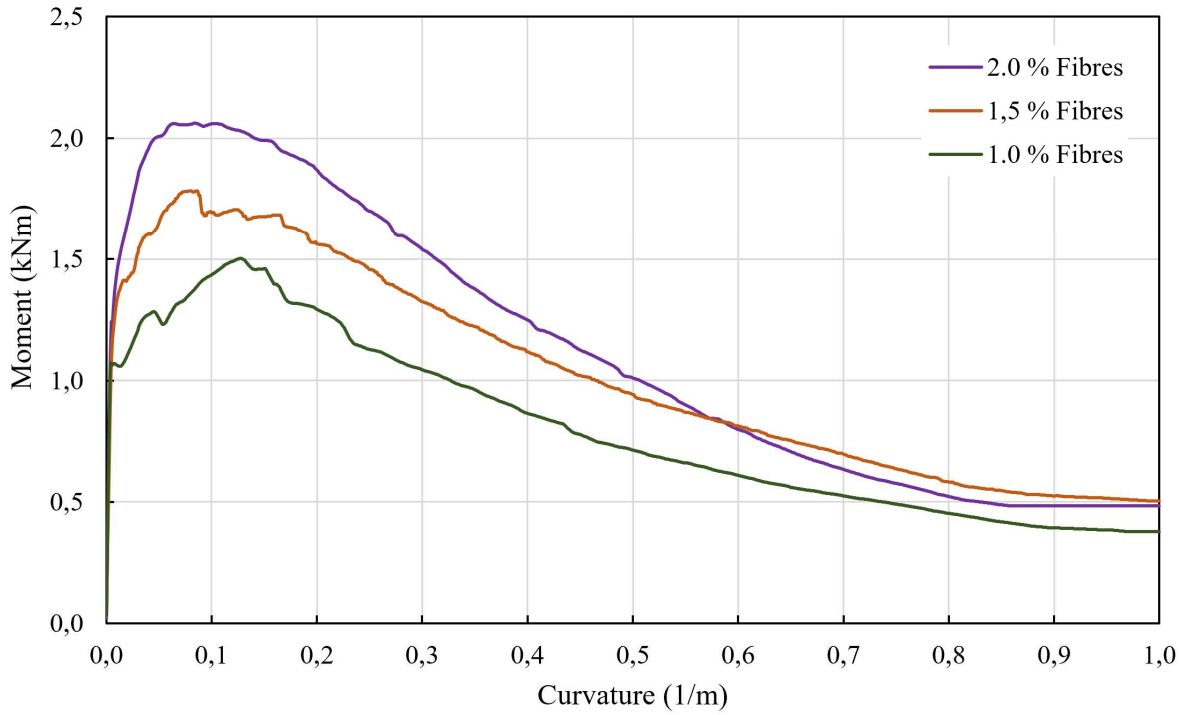

Figure 3-18: Average moment curvature responses

A summary of the average peak moments and the corresponding curvatures is given in Table 3-7. The peak moments for the different fibre contents occur at lower curvatures as the fibre content is increased.

Table 3-7: Peak moments and correlating curvatures

Parameter	1.0 % Fibres	1.5 % Fibres	2.0 % Fibres
Average max moment (kNm)	1.50	1.78	2.06
Average curvature at max moment (1/m)	0.128	0.087	0.084

3.6. CONCLUDING REMARKS

From the experimental test results, it was observed that no significant difference in compressive strength occurred when changing the fibre content. Compressive behaviour after the peak strength showed greater residual compressive capacity with higher steel fibre contents. All mixes presented similar Elastic modulus results since this material property is mostly governed by the concrete. The tensile behaviour was characterised by the split cylinder test results and the load-deflection and moment-curvature responses. An increase in fibre content led to an increase in load and moment capacity, as well as relatively lower deflections and curvature at maximum load. It was observed that the optimum fibre content depended on the property required. An optimum fibre content when considering only deflections would be 1.5% whereas load capacity would still benefit from 2.0% fibres. Moment curvature responses however suggest that 1.0% fibres would provide the best post peak behaviour when

considering moment redistribution. However, this is assuming that the tensile strength of the 1% fibres are sufficient.

Although all material tests have been described, the material properties of the tensile behaviour have not been defined in terms of stresses and strains. The inverse analysis carried out to obtain the simplified tensile stress-strain response is discussed in the next chapter.

CHAPTER 4

STRESS-STRAIN RELATIONSHIP

4.1. INTRODUCTION

Owing to the simplicity of flexural test setups when compared to direct uniaxial tension tests there has been a marked increase in the drive for reliable back-calculation methods to obtain the equivalent uniaxial stress-strain relationship (López et al., 2015, Østergaard et al., 2005, Baby et al., 2012 & 2013, Kanakubo, 2006, Qian & Li, 2008, Rigaud et al., 2012). For this study a generalised analytical method will be used similar to the one proposed by Elsaigh (2007). Inverse analysis is used to determine the stress-strain relationship of concrete based on experimental load-deflection or moment-curvature results. In this study a simplified stress-strain relation was used to match a theoretical moment curvature relationship with the experimentally obtained moment curvature relationship. The theoretical moment curvature relationship is then converted to a theoretical load-deflection response and compared to the experimental results. The back-calculated simplified stress-strain relationship is then altered until there is a close correlation between theoretical and actual moment-curvature and load-deflection relationships.

4.2. ANALYSIS METHOD

The inverse analysis is used to derive M-φ and P-δ relationships by assuming a σ-ε response. An iterative trial and error process is followed by adjusting the σ-ε response until the analytical M-φ or P-δ results match the experimental values. Figure 4-1 shows a schematic diagram of the procedure followed, based on the following major steps:

1. Assume a σ-ε relationship.
2. Calculate the M-φ based on the assumed σ-ε relationship
3. Convert the calculated M-φ relationship into a P-δ response
4. Adjust the σ-ε relationship and repeat steps (2) and (3) until the M-φ and P-δ agree with the experimental results.

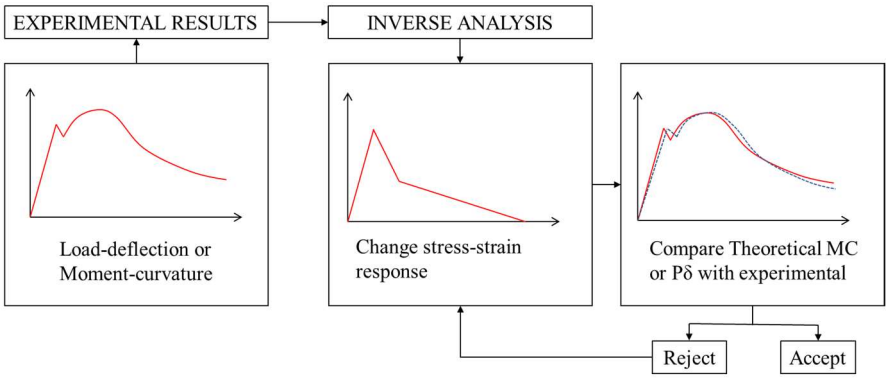

Figure 4-1: Inverse analysis procedure

4.3. PROPOSED STRESS-STRAIN RELATIONSHIP

Owing to the iterative nature of the inverse analysis procedure a simplified σ-ε is proposed. A trilinear tensile response is proposed similar to the that of RILEM TC 162-TDF (2002) along with a standard bilinear compression curve as shown in Figure 4-2.

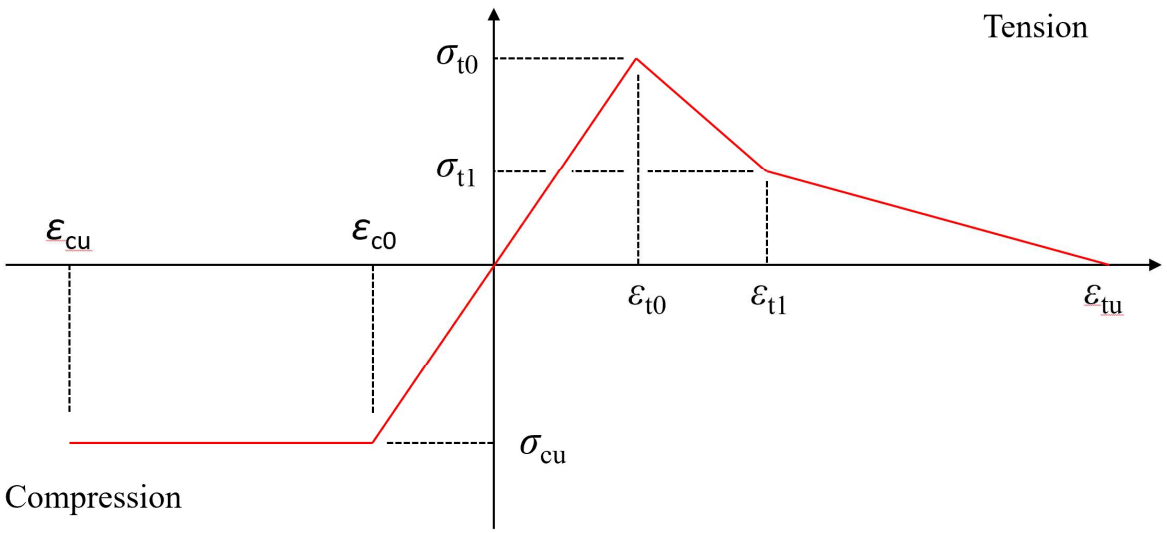

Figure 4-2: Stress-strain Diagram (RILEM TC 162-TDF, 2002)

The parameters shown in Figure 4-2 are described as follows:

- Compression Behaviour:
  - σ_{cu} and ε_{c0} represent the maximum linear elastic stresses and corresponding strains.
  - ε_{cu} represents the ultimate compressive strain
- Tension Behaviour:
  - σ_{t0} and ε_{t0} represent the cracking strength and strain
  - σ_{t1} and ε_{t1} represent the residual stress and strain which indicates a change in slope of the tensile softening curve.
  - ε_{tu} represents the ultimate tensile strain.

The material tests performed in the previous chapter provide the starting points for the assumed stress-strain values thereby reducing the number of variables required to obtain a representative stress-strain relationship. The remaining points are obtained through trial and error until the simplified tensile behaviour provided theoretical M-φ and P-δ responses similar to the those obtained from the experiments.

4.4. MOMENT CURVATURE CALCULATIONS

The iterative procedure performed to obtain a *M-φ* response required the following assumptions to be made (Elsaigh, 2007):

1) Plane sections remain plane during bending.
2) Equilibrium exists between the internal stresses and the externally applied loads.
3) The stress-strain relationship of the material is known.

In this case the stress-strain relationship is described by the simplified stress-strain relationship. The first assumption implies a linear strain distribution across the depth of a cross-section and is valid for slender beams. This assumption allows a relationship between the strains and neutral axis to be described and is illustrated in Figure 4-3 and can be expressed as follows:

$$\varepsilon(y) = \frac{y}{x}\varepsilon_{top} = \left(\frac{y}{h-x}\right)\varepsilon_{bot} \qquad \textit{Equation 4.1}$$

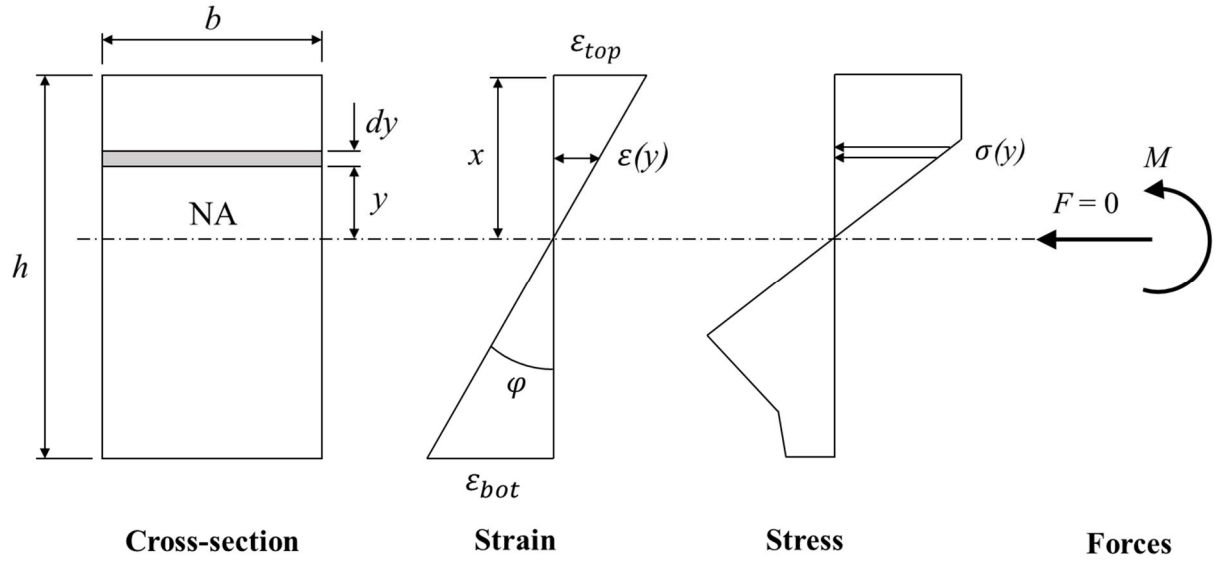

Figure 4-3: Strain Profile

The second assumption generates a second set of equations which relate the internal forces and moments to the internal stresses and strains. The internal forces from the compression and tension stresses equate to zero and the internal moment created by these forces is equal to the applied moment. Force and Moment equilibrium can be expressed as follows:

$$F = \int_{-(h-x)}^{x} \sigma(\varepsilon) b \, dy = 0 \qquad \textit{Equation 4.2}$$

$$M = \int_{-(h-x)}^{x} \sigma(\varepsilon) y b \, dy \qquad \textit{Equation 4.3}$$

The stress function is obtained from the proposed stress-strain relationship in Figure 4-2 and it can be expressed as follows:

$$\sigma(\varepsilon) = \begin{cases} \sigma_{cu} & for\ (\varepsilon_{cu} \leq \varepsilon < \varepsilon_{c0}) \\ E\varepsilon & for\ (\varepsilon_{cu} \leq \varepsilon < \varepsilon_{c0}) \\ \sigma_{t0} + \alpha(\varepsilon - \varepsilon_{t0}) & for\ (\varepsilon_{cu} \leq \varepsilon < \varepsilon_{c0}) \\ \sigma_{tu} + \beta(\varepsilon - \varepsilon_{t1}) & for\ (\varepsilon_{cu} \leq \varepsilon < \varepsilon_{c0}) \end{cases} \qquad \textit{Equation 4.4}$$

Where E, α and β represent the slopes of the lines:

$$E = \frac{\sigma_{cu}}{\varepsilon_{c0}} \qquad \textit{Equation 4.5}$$

$$\alpha = \frac{\sigma_{tu} - \sigma_{t0}}{\varepsilon_{t1} - \varepsilon_{t0}} \qquad \textit{Equation 4.6}$$

$$\beta = \frac{-\sigma_{t0}}{\varepsilon_{tu} - \varepsilon_{t1}} \qquad \textit{Equation 4.7}$$

The Force and Moment equilibrium equations can be simplified so that the integration is in terms of strain. Using the relationship in Equation 4.1, Equation 4.2 and Equation 4.3 can be rewritten as follows:

$$F = \frac{xb}{\varepsilon_{top}} \int_{\varepsilon_{bot}}^{\varepsilon_{top}} \sigma(\varepsilon)\, d\varepsilon = 0 \qquad \textit{Equation 4.8}$$

$$M = \frac{-x^2 b}{\varepsilon_{top}^2} \int_{\varepsilon_{bot}}^{\varepsilon_{top}} \sigma(\varepsilon)\varepsilon\, d\varepsilon \qquad \textit{Equation 4.9}$$

At any applied load, two strains are required to describe the strain distribution of a section, namely the top and bottom strains. Each bottom strain corresponds to a specific top strain since equilibrium is required as described by the force equilibrium Equation 4.8. One can now select a strain value for either the top or bottom strain and calculate the second unknown strain using Equation 4.1 and Equation 4.8. The selected and calculated strains correspond to a certain external applied load. The moment can then be calculated using Equation 4.9 once the strain distribution is known. This moment is equivalent to the moment caused by an external load. This procedure outlines the process in which the strain distribution in the cross-section can be solved for a certain externally applied load. Different strains can be selected to determine the strain distribution for any other external load.

The curvature of the section is described as the gradient of the strain distribution profile and is given by Equation 4.10:

$$\varphi = \frac{\varepsilon_{top}}{x} = \frac{\varepsilon_{bot}}{(h-x)} \qquad \textit{Equation 4.10}$$

The method followed to obtain the analytical *M-φ* relationship is summarised below:

1) Select a value for the bottom strain ε_{bot}
2) Solve for the top strain, ε_{top}, from Equation 4.8. This process is an iterative procedure in which ε_{top} is varied until force equilibrium is achieved.
3) Calculate the moment and curvature from Equation 4.9 and Equation 4.10 respectively. This moment value and curvature value represents one point on the *M-φ* diagram.
4) Select a new value for the bottom strain and repeat steps 2 and 3 until sufficient points have been generated to create a complete *M-φ* diagram.

The method outlined above to generate a complete *M-φ* relationship is based on the initially proposed stress-strain relationship. The stress-strain relationship is then altered and the process to calculate the full *M-φ* relationship is repeated until sufficient similarity with the experimental *M-φ* curve is achieved.

4.5. LOAD DEFLECTION CALCULATIONS

The total deflection in a beam consist of two components; that is deflection caused by flexure and shear. However, since the effects of shear deformations are usually relatively small compared to flexural deformations, it is common practice to neglect them. Specimens used for laboratory testing are, however, much shorter and have a lower span to depth to ratio, therefore the shear stress induced deflections will contribute significantly towards the total deflections.

One can consider a differential element of a beam to illustrate the stresses and deformations caused by a bending moment and a shear force Figure 4-4 (Gere & Timoshenko, 1991). The deformations consist of an extension (ε.dx) caused by the moment M_L and a shear distortion (γ.dx) caused by the shear force V_L. To calculate the total deflection (Δ), which is the sum of the moment deflections (δ_m) and the shear deflections (δ_V), the unit-load method can be used. This method is based upon virtual work and equates the external work, which is 1.Δ, to the internal work, which consists of the internal stresses caused by the bending moment and shear force.

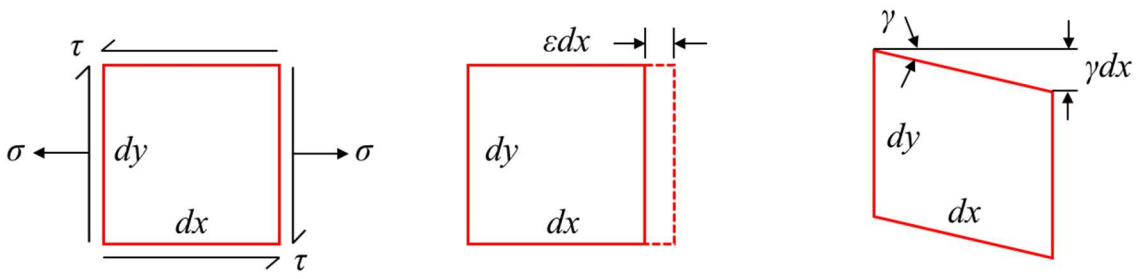

Figure 4-4: Differential element from the beam (Gere & Timoshenko, 1991)

The extensional strain ε and the shear strain γ associated with these deformations are:

$$\varepsilon = \frac{M_L y}{EI} \qquad \textit{Equation 4.11}$$

$$\gamma = \frac{V_L Q}{GIb} \qquad \textit{Equation 4.12}$$

Where M_L and V_L are the moments and shear forces due to an actual load respectively. The total internal work is obtained by integrating throughout the volume of the beam to obtain:

$$W_{int} = \int \frac{M_u M_L y^2}{EI^2} dxdydz + \int \frac{V_u V_L Q^2}{GI^2 b^2} dxdydz \qquad \textit{Equation 4.13}$$

Where M_u and V_u are the moments and shear forces due to a unit load respectively. The expression can be simplified by separating the integrals into components consisting of an integration over the cross-sectional area and an integration along the axis of the beam. This is possible since the following quantities. M_u, M_L, V_u, V_L, E, G and I are constants at a given cross-section. Therefore, the simplified expression is as follows:

$$W_{int} = \int_L \frac{M_u M_L}{EI^2} \left[\int_A y^2 dydz\right] dx + \int_L \frac{V_u V_L}{GI^2} \left[\int_A \frac{Q^2}{b^2} dydz\right] dx \qquad \textit{Equation 4.14}$$

Where L indicates the integration to be carried out over the length of the beam, and A denotes the integration to be carried over the cross-sectional area. The first term in brackets is equivalent to the moment of inertia. The second term in brackets is dependent only on the cross-sectional dimensions of the beam. A new material property can therefore be defined, called the form factor for shear:

$$f_s = \frac{A}{I^2} \int_A \frac{Q^2}{b^2} dA \qquad \textit{Equation 4.15}$$

The form factor is a dimensionless quantity which can be evaluated for different beam shapes and is equal to 6/5 for rectangular beams. Finally, replacing the terms in brackets with the newly defined terms, the total deflection can be written as:

$$\Delta = \delta_m + \delta_\gamma = \int \frac{M_u M_L}{EI} dx + \int \frac{f_s V_u V_L}{GA} dx \qquad \textit{Equation 4.16}$$

4.5.1. MOMENT DEFLECTIONS

For the deflection caused by moments, the following equation can be used:

$$\delta_m = \int \frac{M_u M_L}{EI} dx \qquad \textit{Equation 4.17}$$

Where M_u and M_L are moments due to a unit load and actual load respectively, and EI is the flexural rigidity. The expression, $\frac{M_u}{EI}$, represents the curvature, φ, along the beam. The process required to calculate the deflection based on curvature distribution is illustrated in Figure 4-5. Integration of the

shear force diagram leads to the bending moment diagram, which can be expressed as a curvature distribution. Integration of the curvature then leads to the slope distribution, followed by another integration to reach the deflected shape. The deflection is therefore calculated by double integration of the curvature.

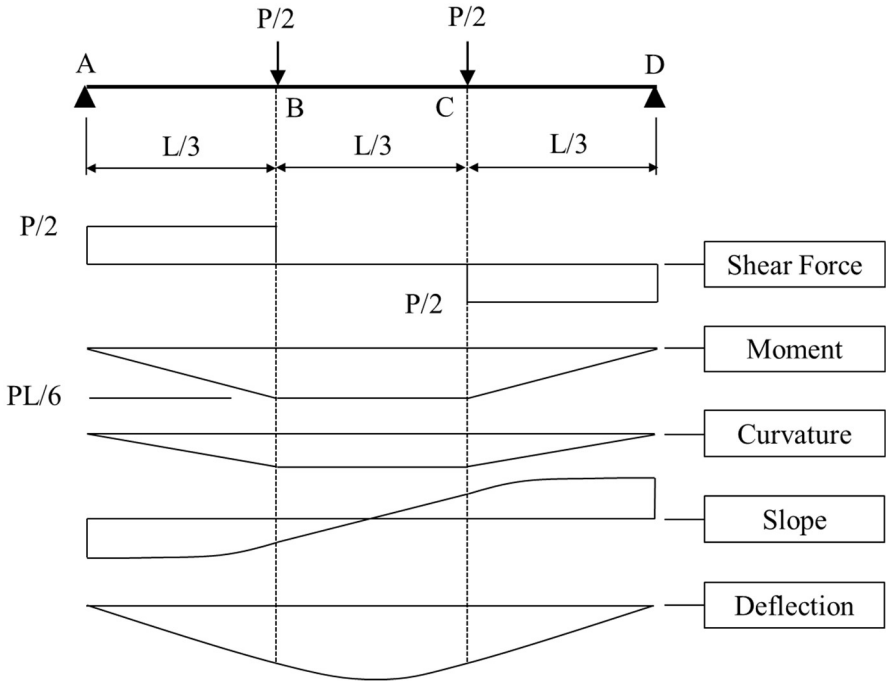

Figure 4-5: Various forces and deformations along the beam

The curvature distribution as shown in Figure 4-5 will depend on the size of the bending moment and the stage of the moment curvature distribution curve. A typical *M-φ* diagram is given in Figure 4-6 representing the change in curvature against the moment at a cross-section. This relationship represents the middle third section of the beam where the moment is constant. An important assumption is made in that the curvature across the constant moment section is assumed to be constant. This means that any cracks are smeared across the constant moment region and represented by an average curvature across this region.

For moments up to the maximum moment M_{max} the curvature along the entire length of the beam is obtained from the *M-φ* curve in Figure 4-6 (a). Figure 4-6 (b) indicates the moment and curvature distributions at two different load stages which correlate the two points on the *M-φ* diagram in Figure 4-6 (a). Beyond the maximum moment, it is assumed that only section BC will follow the softening portion of the *M-φ* diagram. This assumption is based on the fact that once M_{max} has been reached and the primary crack formed in part BC, further increase in curvature will only occur in part BC due to the reduced flexural rigidity. Curvature in parts AB and CD therefore follow the same mostly elastic part

of the M-φ curve up to M_{max} as the moment reduces. The result is that a decrease in moment after M_{max} has been reached (to M_1) leading to a large increase in curvature for section BC and much smaller curvature in sections AB and CD.

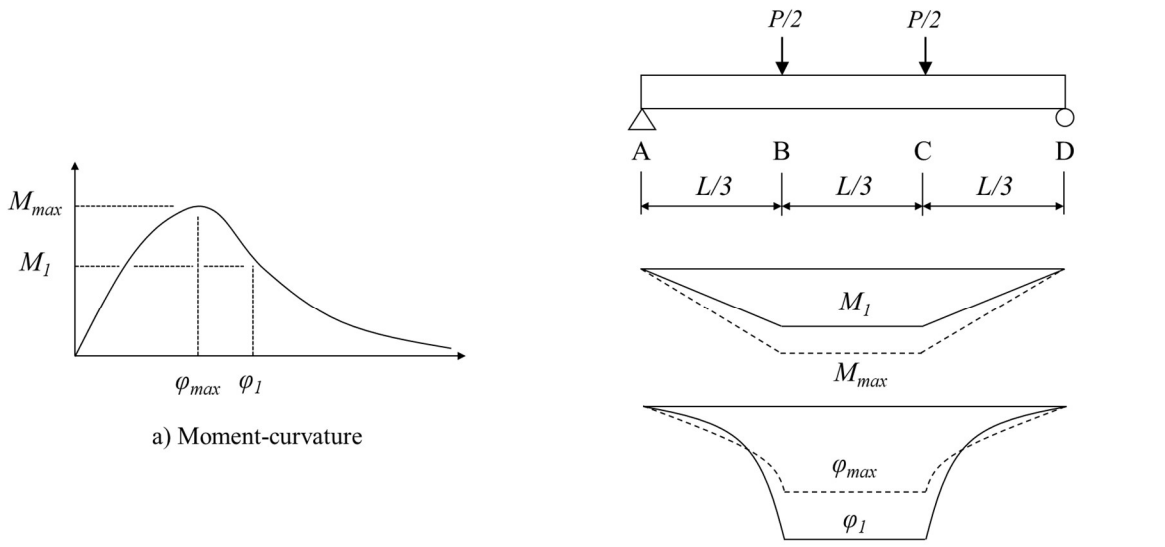

Figure 4-6: Moment-curvature distribution across the beam

4.5.2. SHEAR DEFLECTIONS

Shear deflections result from the strain distribution along the beam and are calculated from the shear forces which are shown in Figure 4-7 (b). The expression for the shear deflections can be written as:

$$\delta_\gamma = \int \frac{f_s V_u V_L}{GA} dx \qquad \textit{Equation 4.18}$$

The distribution of shear strains (γ) is obtained by dividing the shear force (V) by the flexural rigidity, (GA/f_s). The shear strains at any point throughout the loading process correspond to a certain shear force and the relationship between the two is shown in the V-γ graph in Figure 4-7 (a). The V-γ relationship is assumed to be linear elastic up the maximum load, corresponding to V_{max}. Since parts AB and CD unload elastically, the same elastic curve is used to link the decrease in shear forces to the shear strains. This means that unlike curvature which still increases upon further loading after the peak load, the effect of shear forces decreases with an increase in deflections.

Figure 4-7 (a) indicates the shear forces and shear strains at two different loading conditions corresponding to Figure 4-7 (b). It is evident that there are no shear forces in the constant moment region, which justifies the assumption made in the bending moment formula which stated that plane sections remain plane during bending. This assumption would not be true if shear forces were present,

since the induced shear strains are distributed non-linearly through the depth of the beam. The parabolic strain distribution through the depth of the beam would result in originally plane surfaces becoming warped. Therefore, the approach used to calculate deflections caused by moments and shear forces is justified and deemed to be sufficiently accurate so that a successful inverse analysis can be carried out.

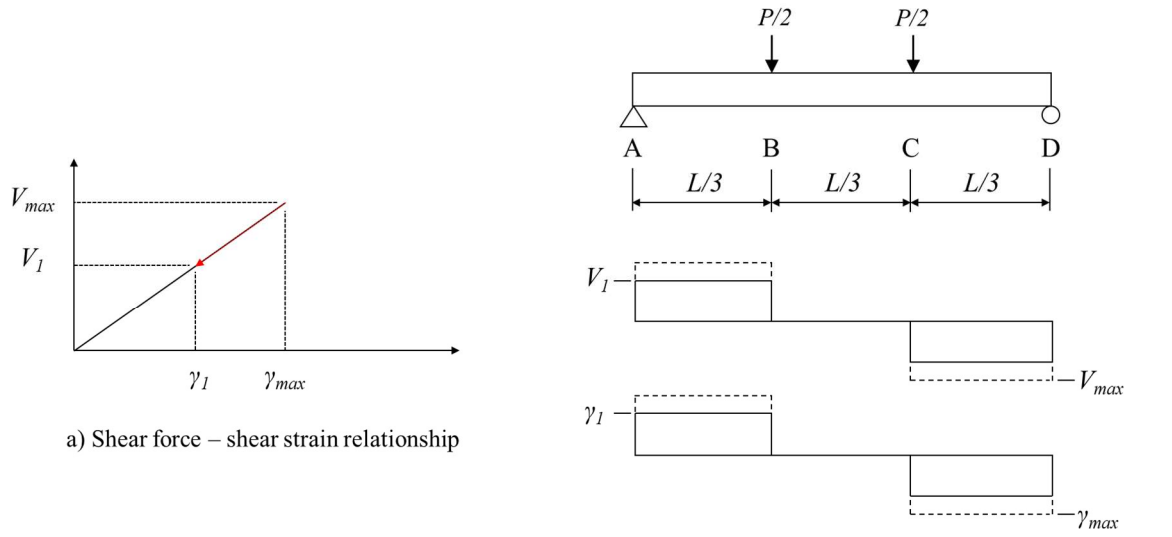

a) Shear force – shear strain relationship

b) Shear force and shear strain distributions for an applied load *P*

Figure 4-7: Shear force and shear-strain distributions along the beam

4.6. PARAMETER STUDY

For the inverse analysis to be efficient and successful, a method had to be developed to ensure systematic refinement of the stress-strain relationship was not purely random. Using the material properties as a rough guideline, certain parameters were changed and the resulting change in the *M-φ* relationship observed. A parameter study was thereby performed which would give a much clearer indication as to how to change the stress-strain parameters in order to achieve the required *M-φ* relationship. The influence of the parameters as shown in Figure 4-8 was investigated:

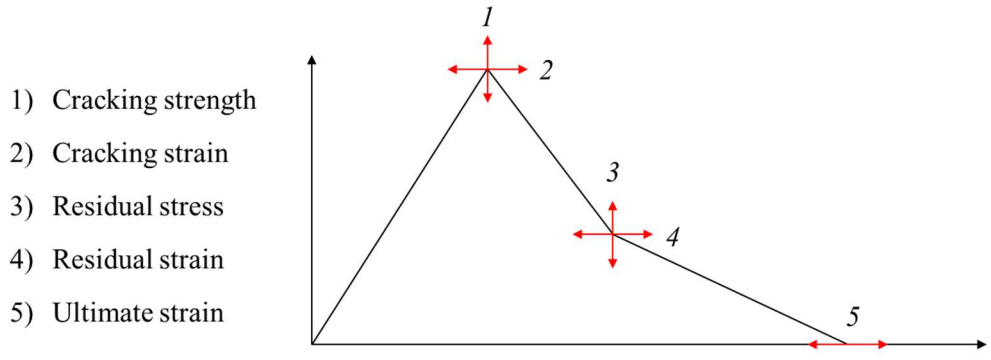

Figure 4-8: Assumed stress-strain relationship

The effect of each parameter on the shape of the *M-φ* and *P-δ* response was established by keeping all other parameters constant. A code was written in Matlab to calculate a total of fifteen different theoretical models, with each of the five parameters having three different values. The hypothetical beams had the same dimensions than the FPBT beams, with the compressive behaviour and elastic moduli varied around the values obtained from the actual tests. It must be noted that the calculated stresses and strains may differ greatly for different material types. The aim of the parameter study was merely to determine the effect of each parameter on the shape of the *M-φ* and *P-δ* diagrams.

4.6.1. EFFECT OF CHANGING THE CRACKING STRENGTH

Figure 4-9 shows the *σ-ε* relationship when changing the cracking strength. Changing the cracking strength will affect the elastic modulus, and hence also affect the compression behaviour. The three different cracking strengths were based on elastic modulus values of 25 GPa, 35 GPa and 45 GPa, as these elastic modulus values are commonly encountered in high strength concrete and cover the range of elastic modulus values obtained in the material tests. The cracking strengths were centred around stress values which resulted in ultimate moment capacities similar to that of the FBTs. The limiting elastic compressive strains was chosen to provide concrete strengths also centred around the values obtained from the material tests.

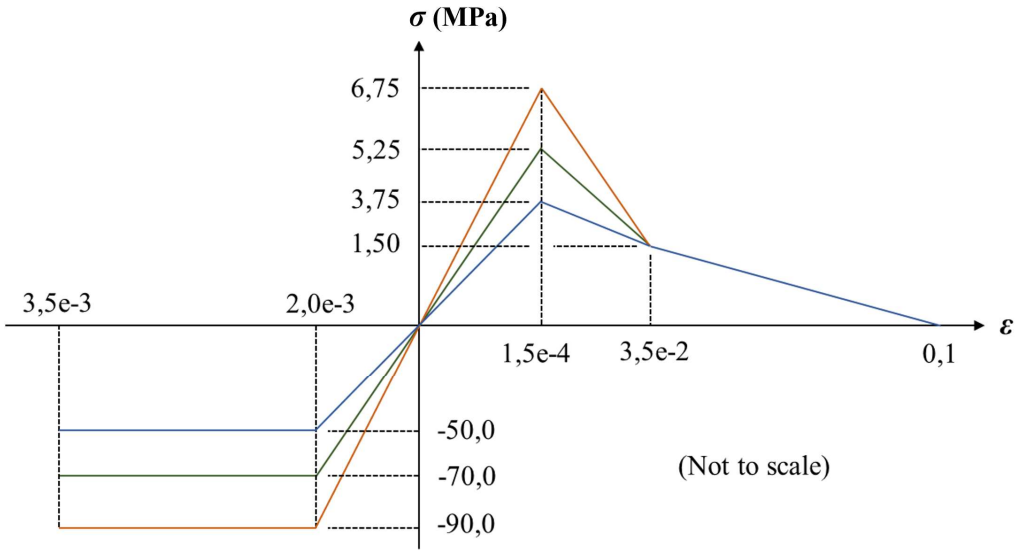

Figure 4-9: Changing cracking stress

Figure 4-10 shows the resulting *M-φ* and *P-δ* relationships. As expected, the peak moments and loads increased with increasing cracking strength. An increase in the cracking strength of 38% and 77% leads to increased peak moments and peak loads of 39% and 80% respectively. The slopes after the peak moments and loads also decrease at a faster rate as the cracking strength increases. This behaviour

follows the shape of the stress-strain graphs. The tensile strains as indicated by crosses in Figure 4-10, indicate at which point the cracking tensile strain (ε_{t0}) and the residual strain (ε_{t1}) are reached. The residual strains indicate a change in slope in the stress-strain graph which is reflected by an inflection point in the *M-φ* relationship.

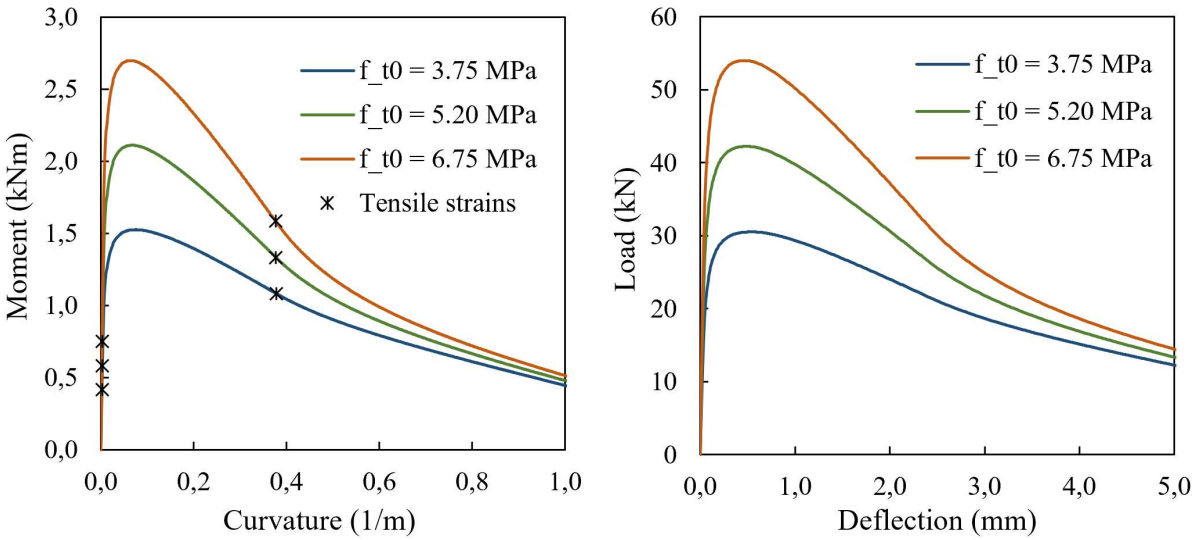

Figure 4-10: *M-φ* and *P-δ* relationships for a changing cracking stress

In every *M-φ* and *P-δ* graph to be discussed with the remaining four parameters, the green curves will be identical models to the curve for f_{t0} = 5.2 MPa as shown in Figure 4-9. This curve will act as a reference to which the influence of all parameters can be compared.

4.6.2. EFFECT OF CHANGING THE CRACKING STRAIN

Figure 4-11 shows the chosen changes in cracking strain and the resulting change in the stress-strain relationship. The cracking strength is taken as 5.2 MPa so that the results of changing the cracking strain are comparable to the change in cracking strength. Again, the same three elastic modulus values of 25, 35 and 45 GPa are used. Shifting the peak stress to the left or right will result in a similar result in the peak moments and loads.

Figure 4-12 shows the *M-φ* and *P-δ* relationships obtained when changing the cracking tensile strain. The results are plotted on the same scale than Figure 4-10 so that the difference in effect is immediately visible. The influence of changing the cracking strain is noticeably less than changing the cracking stress, although this was expected since the relative change in strain was much less than the relative change in stress. Reducing the cracking strain relates to an increased elastic modulus, and vice versa.

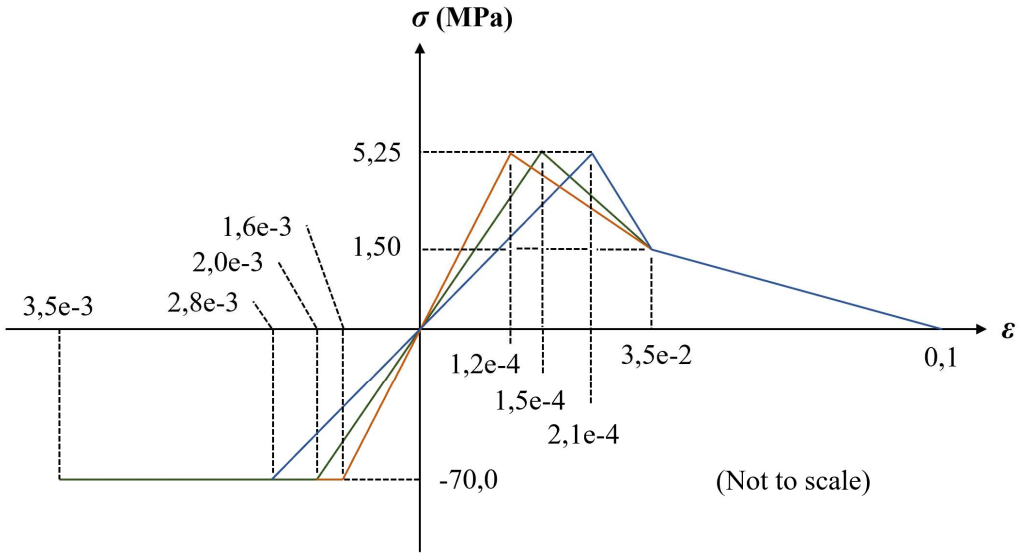

Figure 4-11: Changing cracking strain

The lowest cracking strain of 0.00012 ε therefore correlates to the highest peak moment obtained in Figure 4-12. A 29% increase in the cracking strain (0.00012 ε to 0.00015 ε) leads to a 2.4% increase in peak loads and moments. Increasing the cracking strain by 44% (0.00012 ε to 0.00021 ε) leads a 4.2% increase in peak moment and loads. The horizontal shift in peak stress leads to a 1.0% and 1.6% shift in the curvature at the peak moment. This shift is the same as the 1.7% and 2.7% shift in deflection (in terms of the maximum deflection) at maximum load. It is apparent that a change in the cracking strain has very little effect on the overall *M-φ* and *P-δ* relationships.

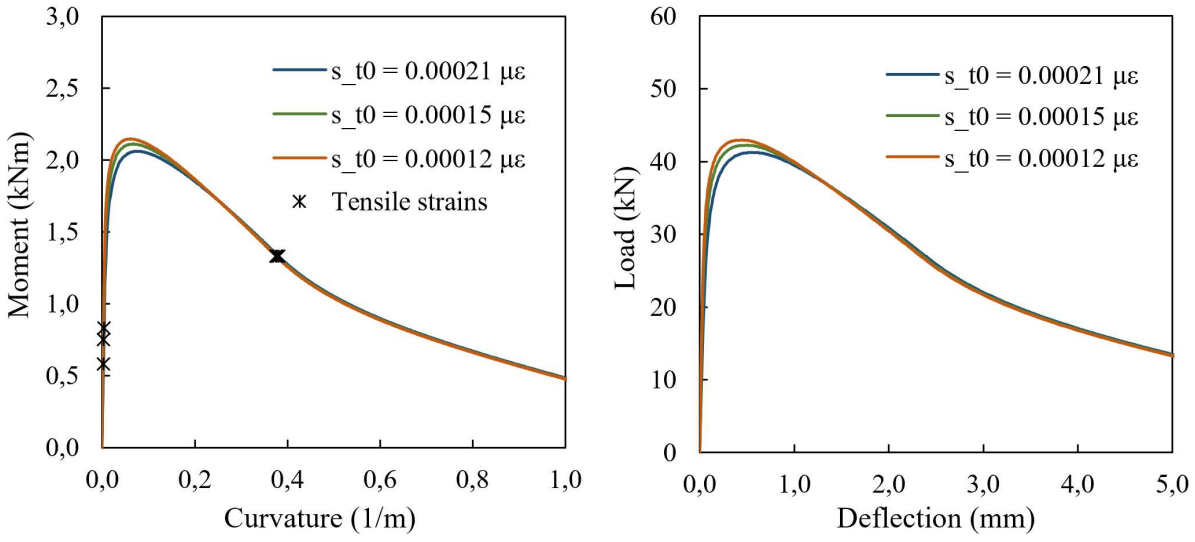

Figure 4-12: *M-φ* and *P-δ* relationships for a changing cracking strain

4.6.3. EFFECT OF CHANGING THE RESIDUAL STRESS

Figure 4-13 indicates the three chosen residual stresses (σ_{t0}) as well as all other stress and strain constants. The residual stresses are centred around the same 1.5 MPa residual stress value used in the cracking stress and strain models. The constant parameters are given the same values as in Figure 4-9.

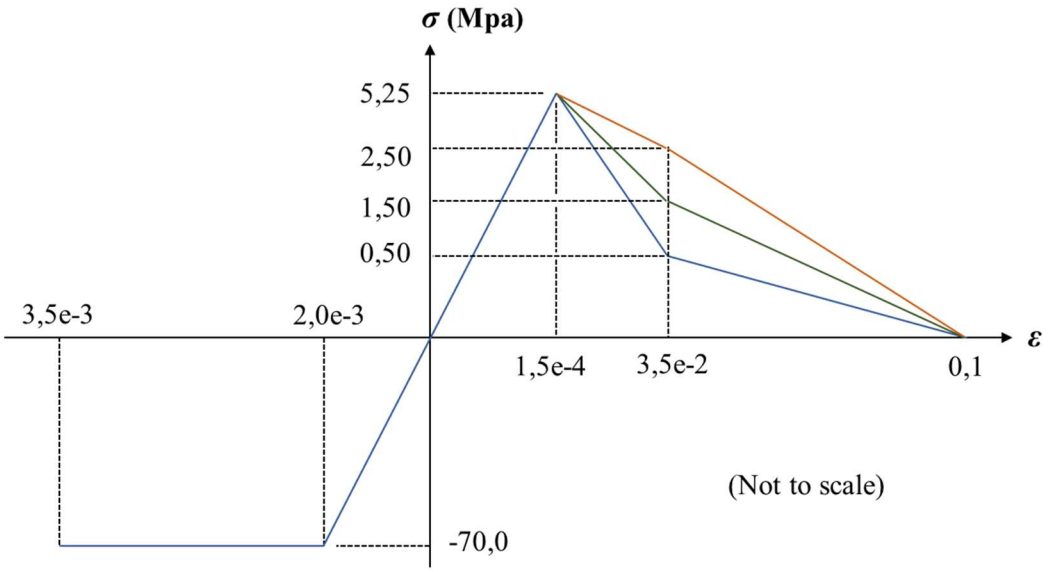

Figure 4-13: Changing residual stress

Figure 4-14 shows the *M-φ* and *P-δ* relationships obtained when changing the residual stresses. The change in residual stress has a greater effect on the latter parts of the curves. The crosses indicate at which point the residual strains correspond to the residual stress, and these points are reached at different moment capacities. These moments increase by 30% and 59% when increasing the residual stress from 0.5 MPa to 1.5 MPa and 2.5 MPa respectively. The difference in moments is even greater shortly after the inflection point is reached. Moment and load values at the maximum considered curvatures and deflections also differ in magnitude similar to the difference at the inflection point. A relatively small change in residual stress therefore leads to noticeable changes in the *M-φ* and *P-δ* relationships after the peak loads.

The peak moments and loads are increased by 1.7% and 3.8% as the residual stresses are increased. The position of the peak moments is also shifted by 0.9% and 2.3% in terms of the curvature and is the same for the percentage change in deflections at the peak loads. Changing the residual stresses will therefore have a slight effect on the peak moments and loads, as well as shifting the position of those peaks.

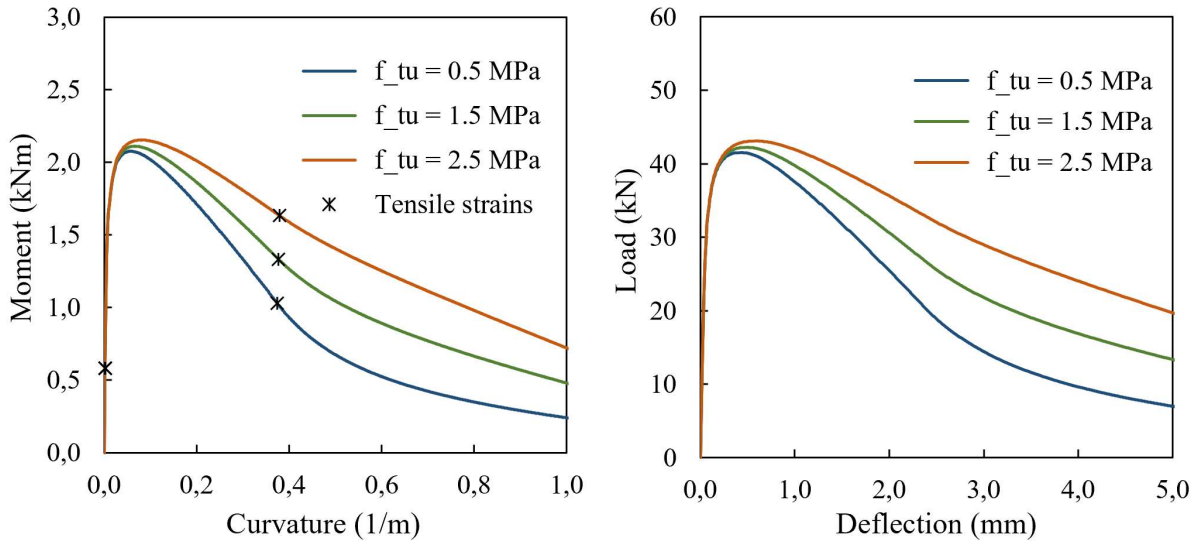

Figure 4-14: *M-φ* and *P-δ* relationships for a changing residual stress

4.6.4. EFFECT OF CHANGING THE RESIDUAL STRAIN

Figure 4-15 indicates the three changes in residual strain as well as all other stress and strain constants. The constant parameters are given the same values as that of the f_{t0} = 5.2 MPa curve in Figure 4-9.

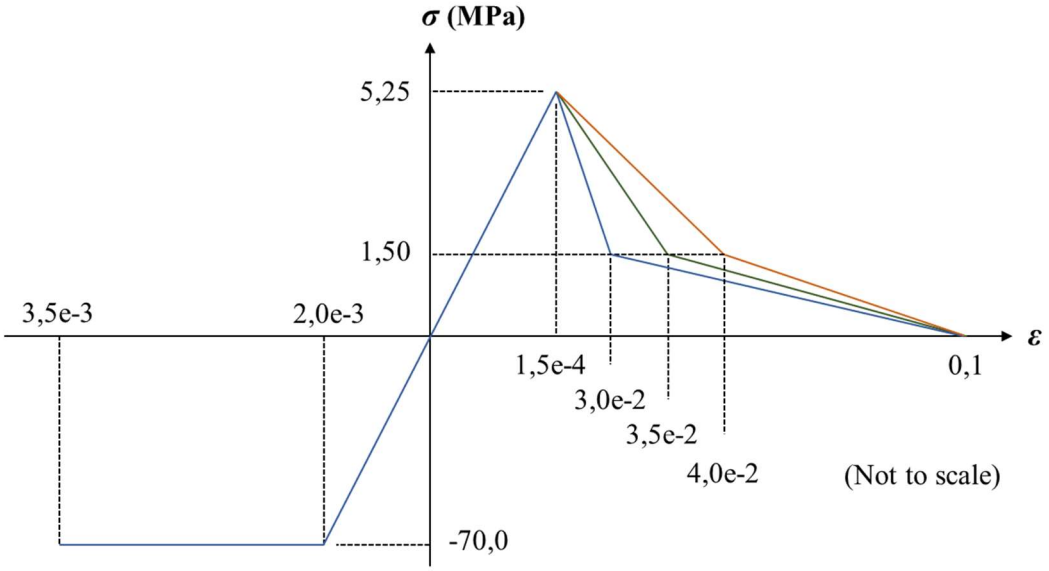

Figure 4-15: Changing residual strain

Figure 4-14 shows the *M-φ* and *P-δ* relationships obtained when changing the residual strains. As expected, the shift in residual stresses results in similar horizontal shifts in the inflection point of the *M-φ* and *P-δ* curves. The residual strain value is therefore useful in deciding at which point in curvature

or deflection a change in behaviour is required. Residual strains of 0.030, 0.035 and 0.040 led to curvature changes of 0.32, 0.38 and 0.43 m^{-1}. This relates to residual strain changes of 0.5% (expressed as a percentage of the ultimate tensile strain of 0.1) resulting in curvature changes of about 5% (expressed as a percentage of the curvature at the ultimate tensile stress). The increase in peak moments and loads is 1.1 and 2.0% respectively. A small shift in the curvature at the peak moments and deflection at the peak loads of 0.6% and 1.1% is caused by the 0.5% increases in residual strains.

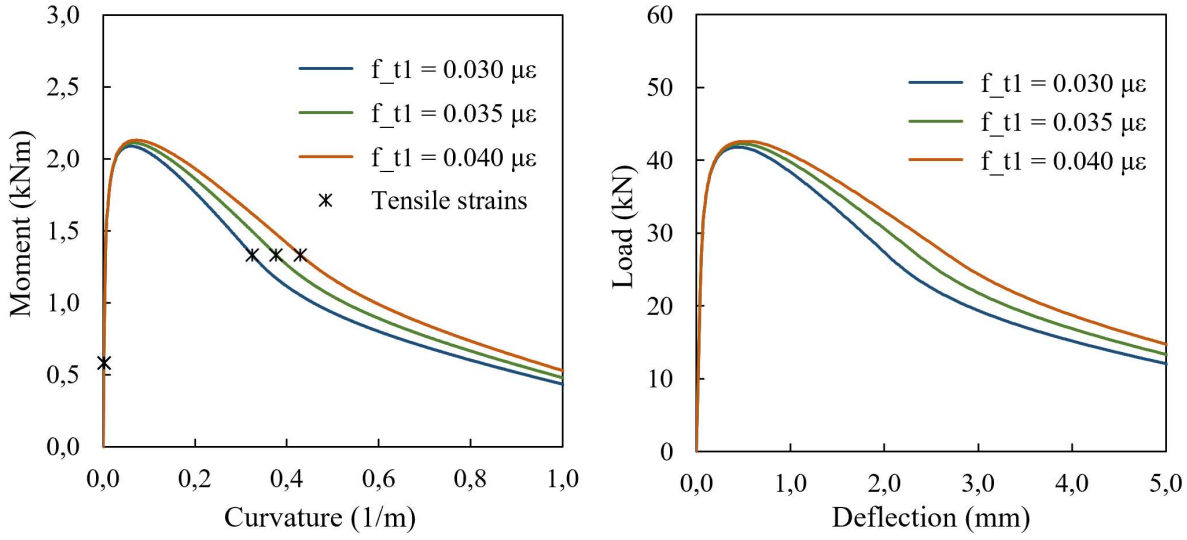

Figure 4-16: *M-φ* and *P-δ* relationships for a changing residual strain

4.6.5. EFFECT OF CHANGING THE ULTIMATE STRAIN

Figure 4-17 indicates the three ultimate strain values used as well as all other stress and strain constants. The constant parameters are given the same values as that of the f_{t0} = 5.2 MPa curve in Figure 4-9. The objective of changing the ultimate strain is to change the behaviour of the tail end of the *M-φ* and *P-δ* relationships.

Figure 4-18 shows the *M-φ* and *P-δ* relationships obtained when changing the ultimate strains. Changing the ultimate strain will change the slope of the curve beyond the inflection point. The ultimate strain can therefore be used to lift or lower the *M-φ* and *P-δ* curves after the residual stress has been reached. The peak moments, loads, and their respective positions are not affected by changing the ultimate strain.

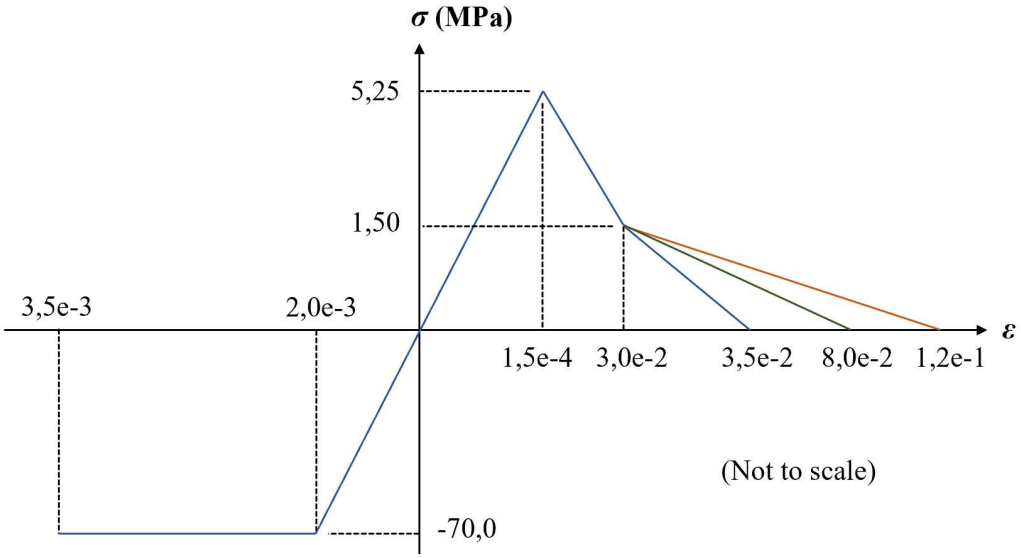

Figure 4-17: Changing ultimate strain

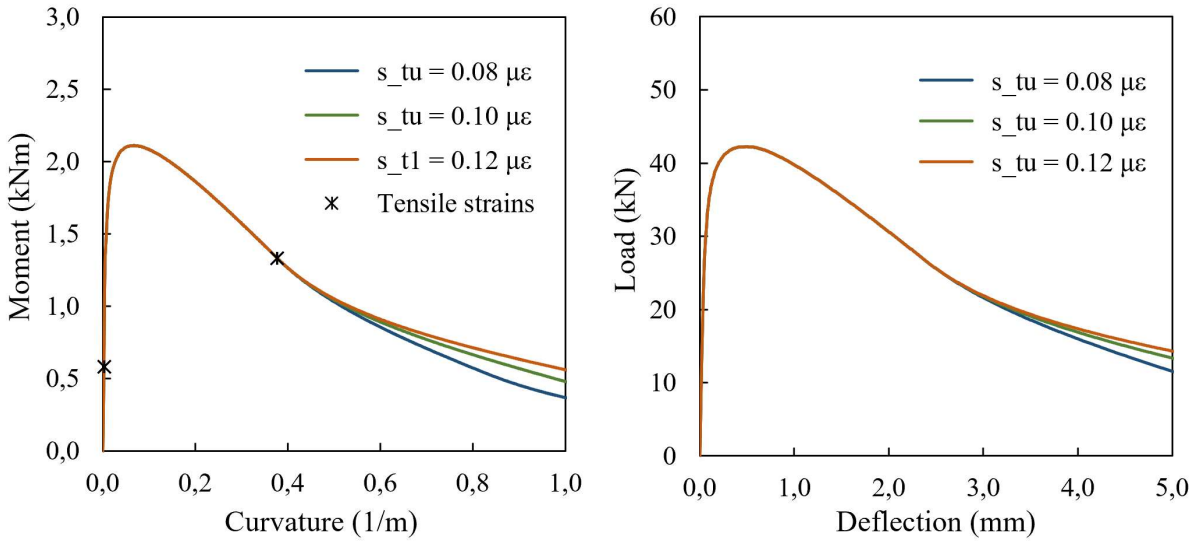

Figure 4-18: *M-φ* and *P-δ* relationships for a changing ultimate strain

4.6.6. REMARKS ON THE PARAMETER STUDY

The accuracy to which the theoretical *M-φ* and *P-δ* relationships can be matched to the experimentally obtained relationships depends on the number of parameters in the stress-strain relationship. Since the proposed stress-strain relationship greatly simplifies the actual stress-strain response, an important stress such as the cracking stress may not be accurately shown on the *M-φ* responses. The inverse analysis was thus compared to both *M-φ* and *P-δ* relationships, to ensure that the calculated stress-strain responses are as reliable as possible. Although the shape of the simplified stress-strain relationship

differs from the actual relationship, the areas under the curves, representing the energy absorbed, are assumed to be similar once the hypothetical *M-φ* and *P-δ* have been matched to the experimental results.

The parameter study highlights the magnitude of changes involved in each of the stress-strain parameters. Some parts of the *M-φ* and *P-δ* curve, such as the peak value are affected by a number of parameters, however, the effect of some parameters is very minor which simplifies the process. Figure 4-19 illustrates a typical *M-φ* relationship, highlighting three important aspects in the shape of the curve. The first being the peak moment (○), followed by the inflection point (□) and finally the required endpoint (◊). Shifting these three points vertically and horizontally will change the slope of the curves between them accordingly. Identifying these three points on the experimental *M-φ* and matching them with the hypothetical results will provide the most accurate match. The shapes of the curves between these points can be adjusted slightly by varying the combination of parameter values whilst still keeping the three main points relatively unchanged. However, the simplified stress-strain diagram will limit the degree to which the curves overlap between these points.

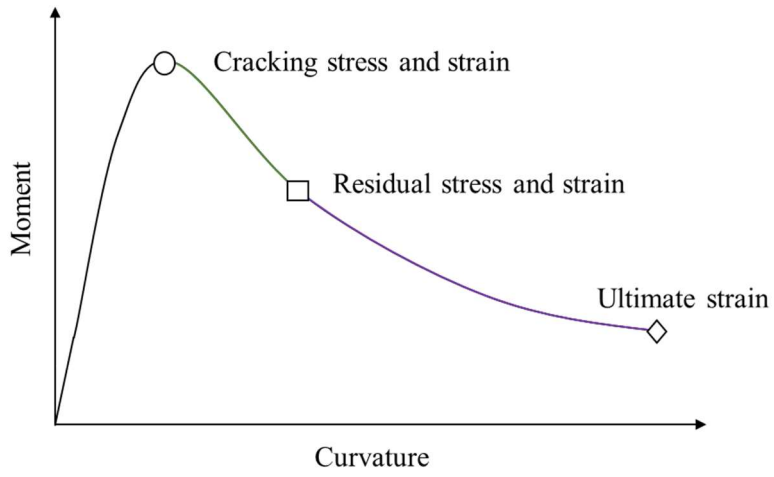

Figure 4-19: Important shape aspects in a typical *M-φ* relationship

4.7. STRESS-STRAIN ESTIMATION GUIDELINE

An initial guess is required when starting the inverse analysis. The guess is then adjusted using the information from the parameter study as a guideline. Based on the experience gained, a method is created highlighting the key aspects of the trial and error procedure. A summary of the steps is given:

1) Establish the compressive *σ-ε* behaviour from the compressive strength test results.
2) Assume the elastic modulus obtained from the cylinder tests is valid for compression and tension and change σ_{t0} to match the peak *M* and peak *P*.
3) Change σ_{t1} and ε_{t1} to match the position of the inflection point (this will affect *M* and *P*).

4) Change ε_{tu} to match the curve following the inflection point.
5) Readjust σ_{t0} to match the peak M and peak P.

If further improvements are required, minor adjustments can then be made to any parameter once an agreeable fit has been reached. In the first step, the compressive behaviour can be simplified into a bilinear relationship defined by the Young's Modulus (E) and the compressive strengths of the cubes (f_{cu}).

4.8. IMPLEMENTING THE INVERSE ANALYSIS

The proposed method of analysis was used to calculate the stress-strain properties of the three concrete mixes containing steel fibres. Both the experimentally obtained moment-curvature results and load-deflection results were used to calibrate the stress-strain response. Stress-strain relationships were based on the average experimental results, resulting in theoretical moment-curvature and load-deflection predictions which closely matched the recorded behaviour, even with the simplified stress-strain relationship.

4.8.1. 1.0 % FIBRE CONTENT

The theoretical results are compared to the experimental results followed by the stress-strain values used to obtain the final theoretical relationships. Comparisons for 1.0% steel fibres are shown in Figure 4-20. The calculated moment-curvature response shows a good correlation to the experimental results. Somewhat greater differences in the P-δ curves were expected since the theoretical P-δ response was derived from the theoretical M-φ curve, and as such, more assumptions were included in the calculations leading to the theoretical P-δ relationship. For this reason, it was also decided to stop the analysis once stress-strain values had been found which correlated well with the M-φ results, while the P-δ results were used to only slightly adjust the stress-strain values so that a reasonable fit for both behaviours could be found.

Values for the 1.0% steel fibre output stress-strain response are given in Figure 4-21. Due to the simplified nature of the stress-strain model it was not possible to model the change in gradient observed at about 1 kNm and 20 kN. Improvements in the model can be made by increasing the complexity of the assumed stress-strain response if more accuracy is required.

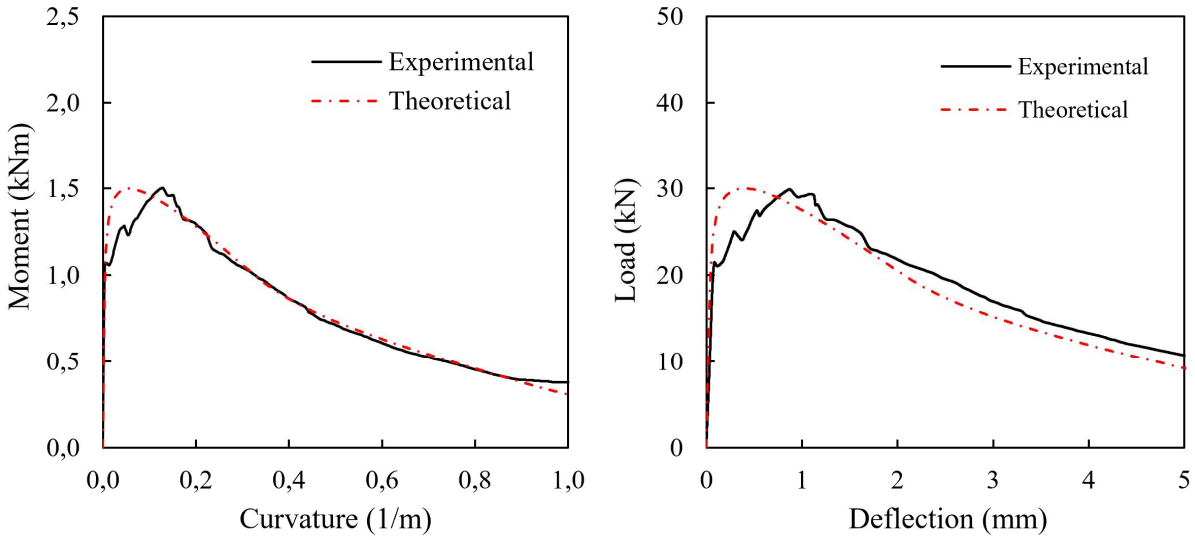

Figure 4-20: Experimental and calculated *M-φ* and *P-δ* responses for 1% steel fibres

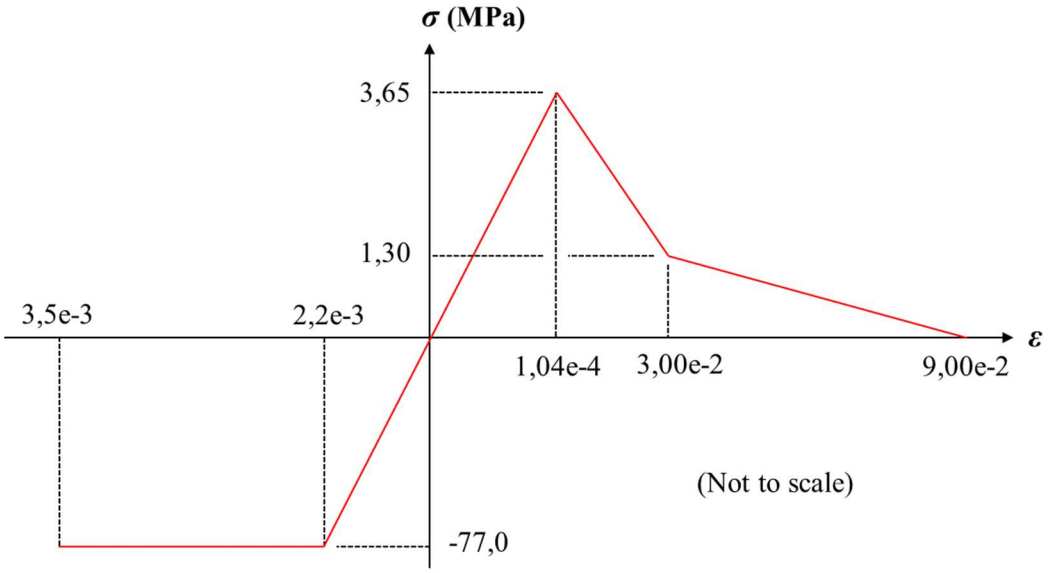

Figure 4-21: Resulting stress-strain response for 1% steel fibres

4.8.2. 1.5 % FIBRE CONTENT

Comparisons between the calculated and experimental results for 1.5% steel fibres are shown in Figure 4-22. A good correlation between both the *M-φ* and *P-δ* was achieved. Deviation between the calculated and experimental values occurs at high curvature values which were a consequence of the simplified stress-strain response. In reality the large decrease in moment capacity at such high curvatures renders the behaviour at this point irrelevant and therefore an improved match was not deemed necessary.

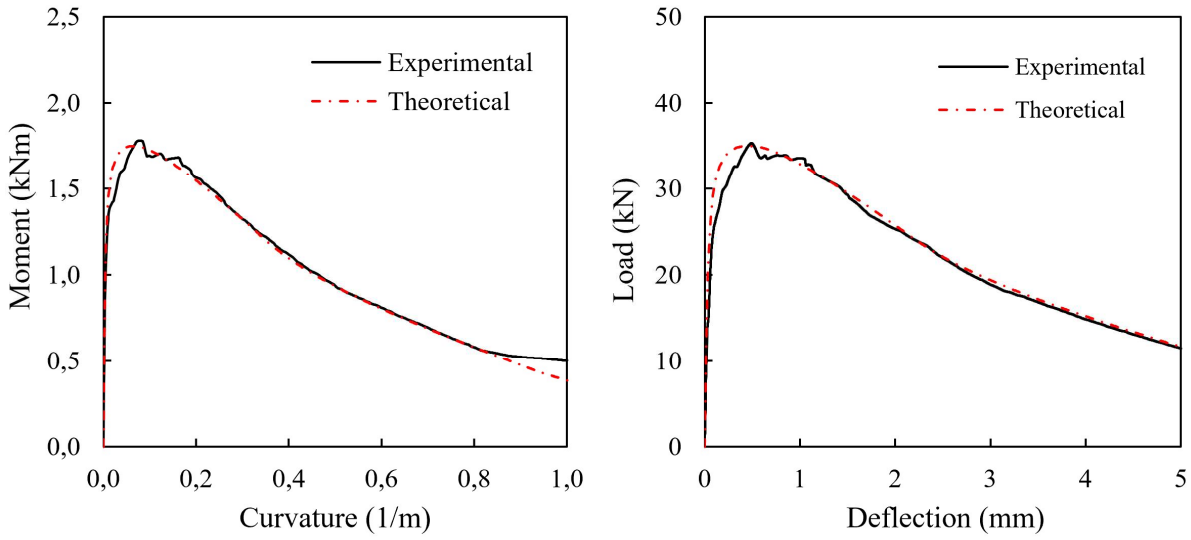

Figure 4-22: Experimental and calculated *M-φ* and *P-δ* responses for 1.5% steel fibres

Values for the output stress-strain response for 1.5% steel fibres are given in Figure 4-23. The residual capacity of the fibres improved the fit between the calculated and experimental values after cracking. The increase in strength from 1.0% fibres to 1.5% fibres is seen in the tensile stress values of 3.65 MPa and 4.28 MPa respectively.

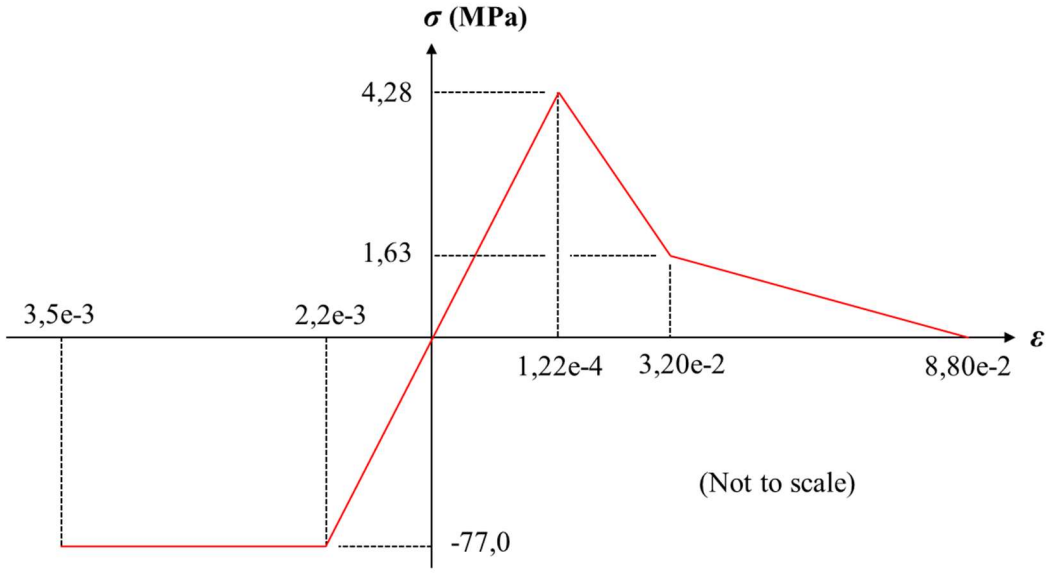

Figure 4-23: Resulting stress-strain response for 1.5% steel fibres

4.8.3. 2.0 % FIBRE CONTENT

Comparisons between the calculated and experimental results for 2.0% steel fibres are shown in Figure 4-24. The ability of the 2.0% steel fibres to further increase the strength of the member following cracking resulted in the actual stress-strain response tending towards the simplified stress-strain

response. As a result, the change in gradient after cracking at about 1.0 kNm and 20 kN is less evident which results in a better correlation between the theoretical and experimental results.

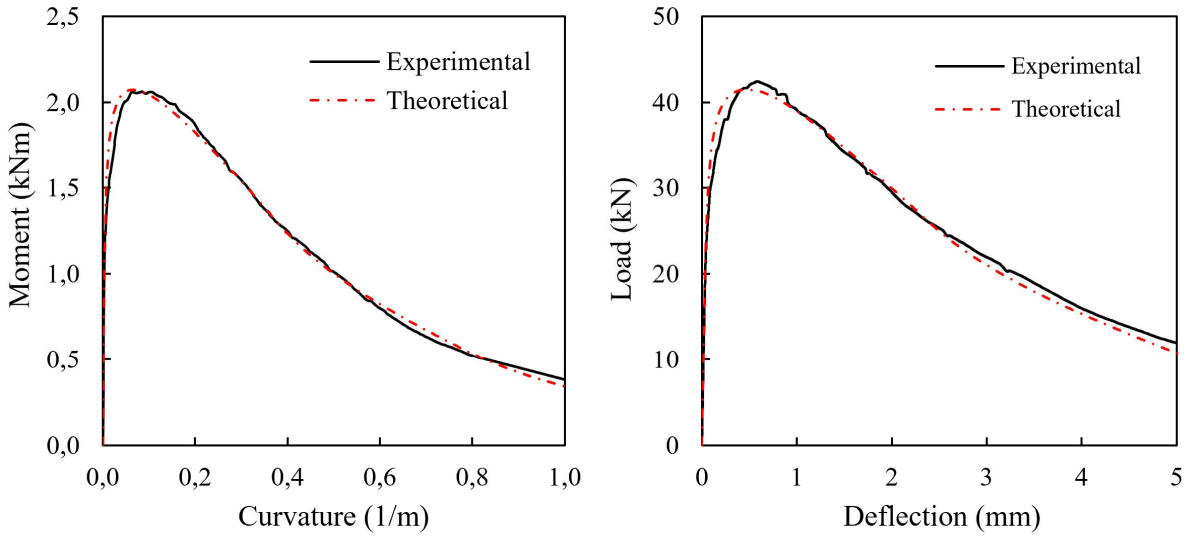

Figure 4-24: Experimental and calculated *M-φ* and *P-δ* responses for 2.0% steel fibres

Values for the output stress-strain response for 2.0% steel fibres are given in Figure 4-25. A further increase in the peak tensile stress to 5.12 MPa can be seen. However, the residual stress decreased from 1.63 MPa to 1.45 MPa from 1.5% fibres to 2.0% fibres. This reduction in stresses following the peak stress corresponds to the steeper downwards slope of the *M-φ* response in the 2.0% fibre samples in comparison to the 1.5% fibre samples.

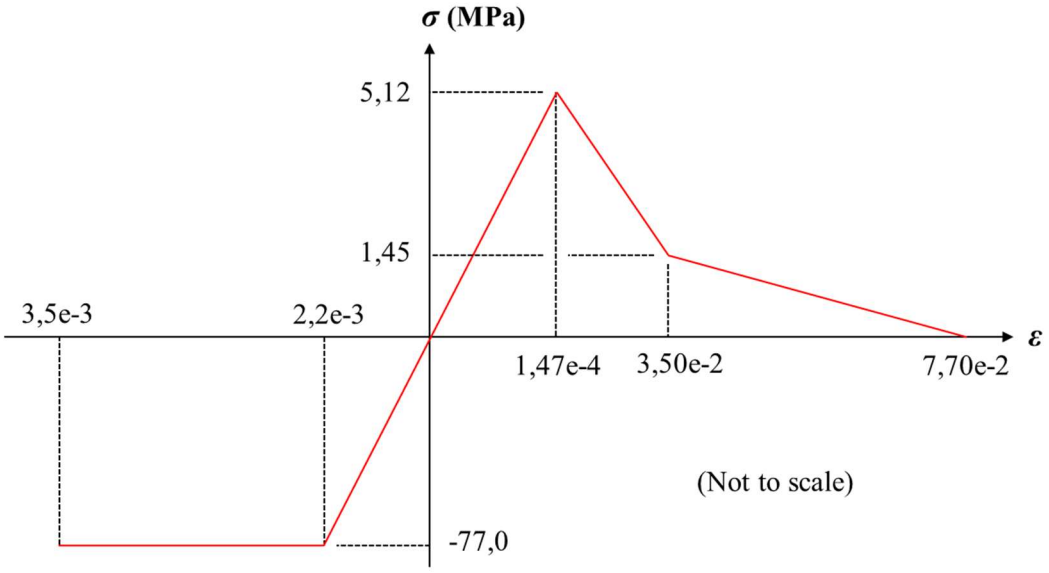

Figure 4-25: Resulting stress-strain response for 2.0% steel fibres

The theoretical stress-strain outputs therefore describe the material properties with sufficient detail to incorporate the key differences in material behaviour between the three fibre content mixes. However, when combining the calculated stress-strain responses with steel reinforcing as will be discussed in the following chapters, greater accuracy may be required, in particular the behaviour before and after cracking. An improvement in the assumed stress-strain response is discussed in the following section so that cracking stress is clearly defined, followed by a more accurate prediction of the residual stress capacity provided by the fibres.

4.9. IMPROVED THEORETICAL ESTIMATIONS

Matching the calculated peak moments and loads with the experimentally obtained results required the peak tensile stress to be adjusted accordingly. The strain at this peak stress was therefore not linked to a true cracking strain which is the result of simplifying the stress-strain response. Two additional points on the stress-strain response were therefore added to more accurately reflect the cracking stress, the sudden drop in stress after cracking, and the residual stress from the fibres once the strains had increased to allow the tensile forces in the fibres to reach their full effect. The improved stress-strain response is compared to the original in Figure 4-26.

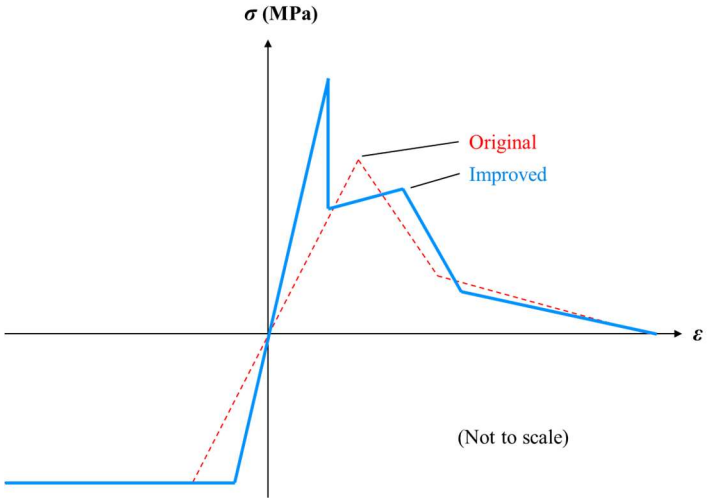

Figure 4-26: Improved assumed stress-strain response

This improved stress-strain response was used to repeat the inverse analysis for each of the three fibre content mixes. Comparisons for all experimental results are shown in Figure 4-27 .In all cases the change in slope following cracking is considered in the improved theoretical predictions. The cracking stress for all three fibre contents was assumed to be the same, since the cracking is dependent on the concrete properties which were similar for all batches. This assumption is deemed reliable since there is a change in moment and load gradient at almost identical moments and loads for beams at around 1 kNm and 20 kN indicating that the cracking strength is constant.

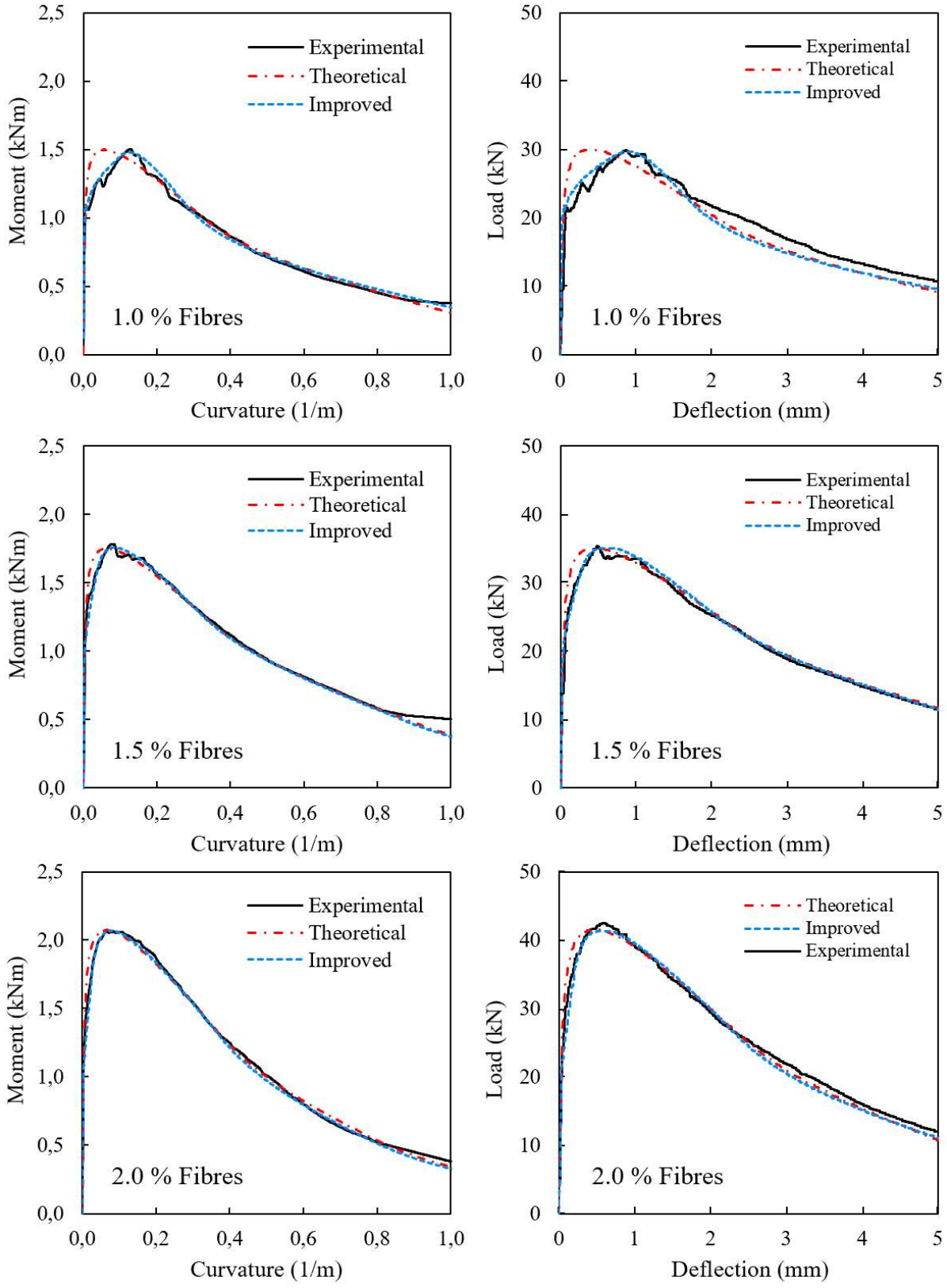

Figure 4-27: Original and improved calculations and experimental *M-φ* and *P-δ* responses

The change in residual stress properties caused by the different fibre contents can be clearly seen in Figure 4-28. There is a visible difference between the material property of the 1.0% fibres and the 1.5% fibres. A smaller difference is seen when increasing the fibre content to 2% which suggests that there exists an optimum fibre content beyond which the benefits of additional fibres begins to fade. The exact calculated stress and strain values are presented in Table 4-1.

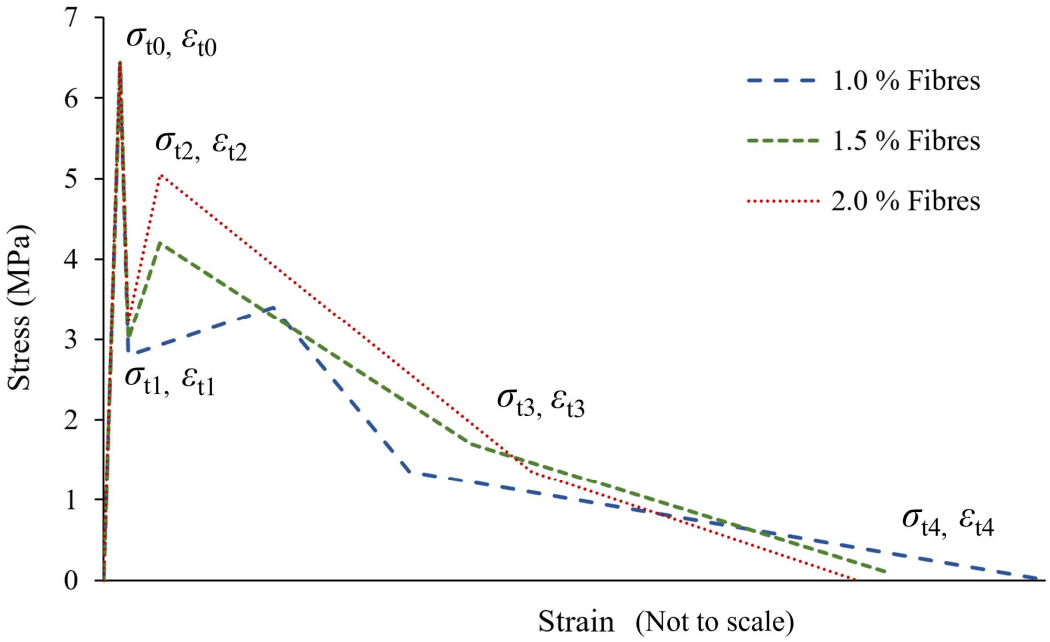

Figure 4-28: Improved stress-strain responses for all three fibre contents

Table 4-1: Stress and strain values for all three fibre contents

Parameter	1.0 % Fibres		1.5 % Fibres		2.0 % Fibres	
σ_{t0} (MPa); ε_{t0}	6.44	1.74e-4	6.44	1.74e-4	6.44	1.74e-4
σ_{t1} (MPa); ε_{t1}	2.80	1.74e-4	3.00	1.74e-4	3.20	1.74e-4
σ_{t2} (MPa); ε_{t2}	3.40	9.00e-3	4.20	3.00e-3	5.05	2.00e-3
σ_{t3} (MPa); ε_{t3}	1.35	2.50e-2	1.70	3.00e-2	1.35	3.50e-2
σ_{t4} (MPa); ε_{t4}	0.00	1.00e-1	0.00	0.83e-1	0.00	0.80e-1

4.10. CONCLUDING REMARKS

The inverse analysis provided simplified stress-strain responses which could be used to successfully match the experimental *M-φ* and *P-δ* responses. The tensile stress-strain properties are therefore considered to be accurate representations of the material properties. Further improvements to the stress-strain response would be possible with additional points used to capture the sudden change in stress after cracking. The improved stress-strain graphs were more complex, however, having already

obtained the original simplified graphs the estimates for the new stresses and strains was made easier with the original values acting as guidelines.

The improved stress-strain responses included the sudden change in behaviour after cracking which better reflects the ability of the fibres to bridge the cracks and provide residual strength. The material properties have now been described sufficiently and thus the indeterminate tests will now be discussed in the following chapters. Not much improvement in the stress strain properties of the fibres are realised by increasing the fibre content from 1.5% to 2%.

CHAPTER 5

EXPERIMENTAL SETUP

5.1. INTRODUCTION

The tests described thus far include the relevant properties of the materials used in the construction of the indeterminate continuous beam setup. In the following section, the indeterminate beam setup from which the effects of steel fibres in combination with reinforcing steel were measured is described. Different measurement techniques were used, and the methods used to obtain various results are discussed.

5.2. BEAM DESIGN

The chosen dimensions for the beam were based on several factors. The length was limited by the maximum permissible distance between supports in the testing equipment resulting in a distance of 4.5 m between the outer supports. The beam width was dependent on the number of reinforcing bars, since the concrete must still be placed to flow between the bars. The aim with the beam height was to keep the samples as flexible as possible thus avoiding shear failure. Since the distance between the outer supports was set at 4.5 m and the beam depth was chosen to be 100 mm, the beam width was set at 200 mm as up to three reinforcing bars were to be placed next to each other. The high strength of the concrete meant that even the most heavily reinforced concrete beam should fail in tension, with the steel yielding. Due to the high compressive strength of the concrete and the small dimensions of the beam, the largest practical bar size was chosen to be 12 mm.

Four steel moulds were constructed, with inner dimensions of 5000 mm x 200 mm x 100 mm (length x width x height) The completed moulds are shown in Figure 5-1. The moulds were constructed from steel, with the side walls bolted into the metal base to allow for demoulding. Each mould represented a beam with a different reinforcing amount. Therefore, one mould required no provisions to be made for reinforcing steel, however the other three moulds which contained either one, two or three reinforcing steel bars had to be modified slightly to allow for the required reinforcing layout.

Figure 5-1: Steel moulds

The shallow depth of the beams was chosen so that shear failure would be avoided and to simplify the construction of the beams since no shear stirrups were required. The reinforcing steel therefore had to be held in position by other means. The simplest solution was to drill small holes into the side of the mould through which a metal wire was pulled and fastened securely for the top reinforcing steel to rest on, an example of this is shown in Figure 5-2. The depth of reinforcing was therefore consistent for all moulds since their position was dependent on the holes in the shutters. The bottom reinforcing lay on evenly spaced concrete spacers which guaranteed the same effective depth throughout the beam. The spacing between the reinforcing, as can be seen in Figure 5-2, was checked for each setup and bars were secured in place with cable-ties or wiring. The layout of the reinforcing can be seen in the cross-section and elevation views shown in Figure 5-3.

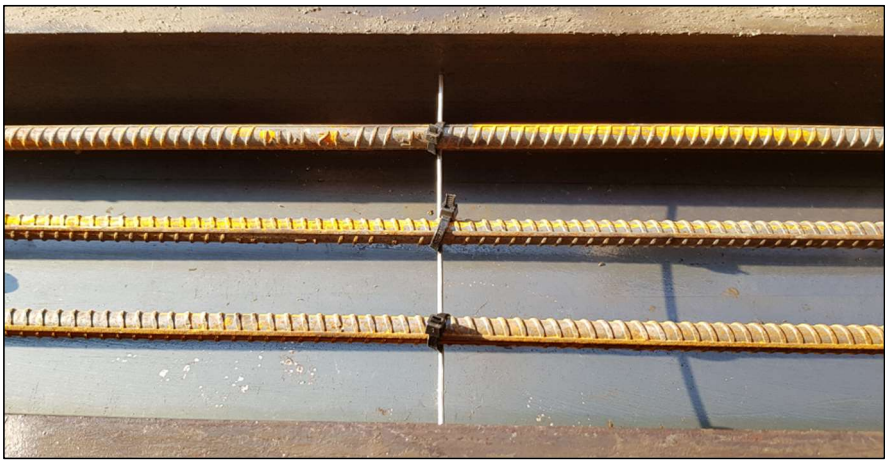

Figure 5-2: Reinforcing spacing

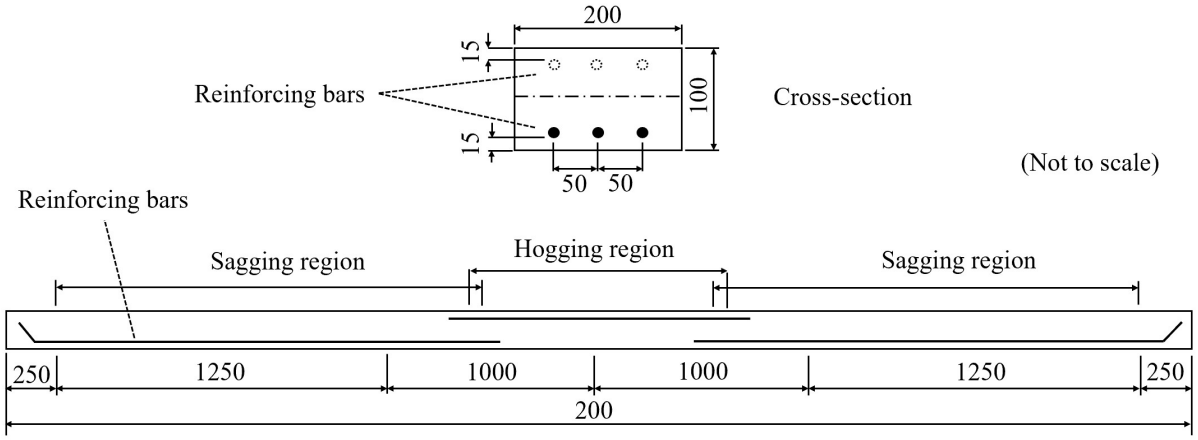

Figure 5-3: Reinforcing layout in the beam

5.3. TEST SETUP

The test setup was designed to create an indeterminate structure, a prerequisite for moment redistribution. A schematic of the five-point bending setup is illustrated in Figure 5-4, indicating not only the locations of loads and supports, but also the dimensions of the setup. The beams were tested in deflection control using a closed-loop Materials System Testing (MTS) with a load capacity of 250 kN. The rate of testing was set at 0.833 mm/min and the test setup can be seen in the photo in Figure 5-5.

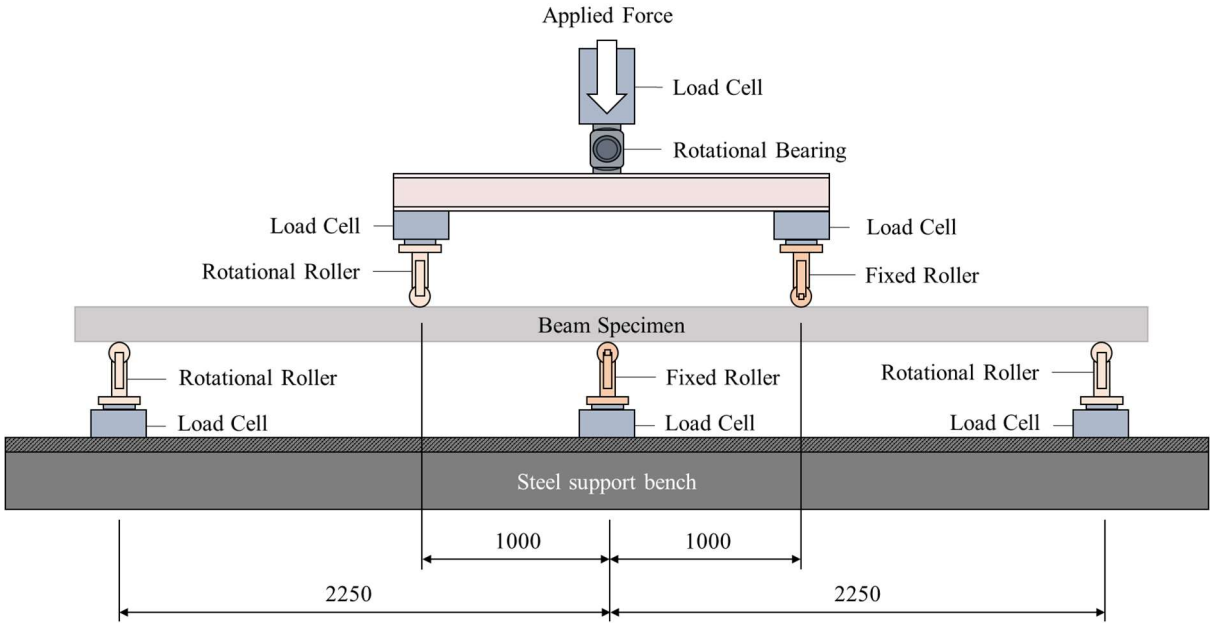

Figure 5-4: Indeterminate beam test setup

Figure 5-5: Photo of the indeterminate beam setup

5.3.1. LOAD MEASUREMENTS

The rotational bearings allowed the ends of the beam to rotate freely, whilst the fixed roller at the centre support was required to keep the structure stable. An H-beam was used to distribute the singular applied point load amongst the two load points. The H-beam was free to rotate in all directions, with the two point-loads underneath applied to the concrete member through roller bearings, one being fixed and the other allowing rotation. This combination of fixed and rotational supports provides both a stable setup and prevents uneven concentrated loads from being applied as the system allows some degree of imperfection.

A total of five load cells were fitted to the three support bearings and two load bearings. The load distribution across the length of the beam could therefore be determined and checked for equilibrium with the externally applied load. Adjustable support heights allowed the beams to be placed with the own weight distributed as close as possible to a perfectly elastic setup. This was done to reduce the divergence between theoretical elastic behaviour and the actual elastic setup.

5.3.2. DEFLECTION MEASUREMENTS

Deflection measurements were taken directly underneath the load points and measured using a similar type of frame as with the FPBTs. Vertical deflection was measured at the top surface of the beam with reference to the mid-height at the end supports. Figure 5-6 shows the positioning of the LVDT and the deflection frame. As shown in Figure 5-7 a reference point at the beam mid-height was not possible due to a possible crack formation through the reference point, therefore the top surface was chosen as this guaranteed consistent deflection measurements regardless of the crack location.

Figure 5-6: Deflection frame

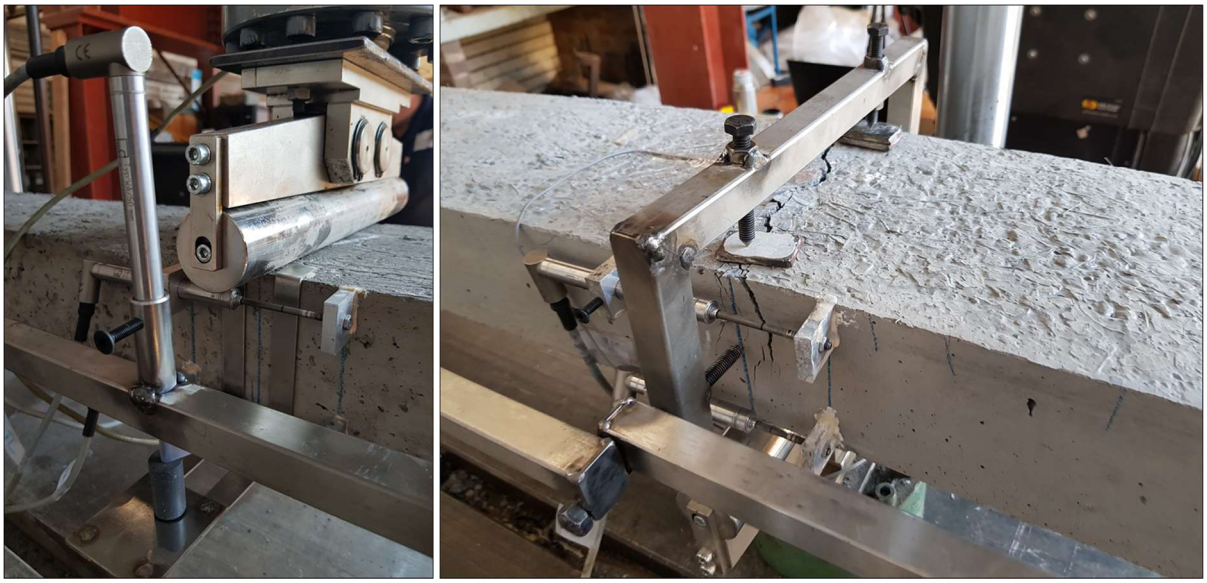

Figure 5-7: Deflection measurements at the load points and central support

5.3.3. CURVATURE MEASUREMENTS

LVDTs were used to measure horizontal deformation required to calculate curvature based on the strains formed where the plastic hinges were expected to form. Unlike the FPBT there was no constant moment region. However, the same gauge length of 100 mm as with the FPBTs was used. This gauge length corresponds to twice the plastic hinge length which is assumed to be half the height of the beam. Theoretical moment curvature calculations relate the moment at a certain cross-section to the curvature at that cross-section. Therefore, the curvature calculated across the 100 mm gauge length is not directly comparable to theoretical predictions, since the moment is not constant over the gauge length. However, it can be assumed that the moment is near constant since the length is so short in relation to the total span length of 2.25 m. In any case, trends will still be visible across all tests as the setup is identical for all tests.

Figure 5-8 shows a typical LVDT setup for horizontal strain measurements with the dimensions shown. These strains readings were taken at the two-point loads and at the centre support. Even if multiple

cracks occurred, it was expected that the main cracks would form within the range of the LVDTs and hence allow a certain degree of comparison between the moment curvature relations to be drawn.

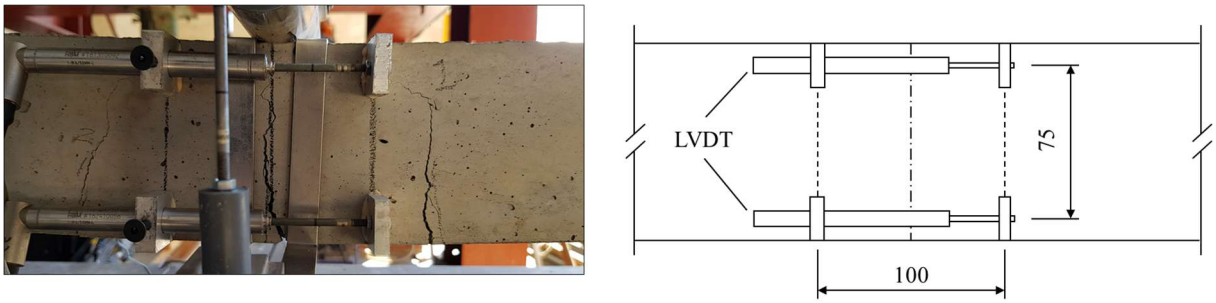

Figure 5-8: LVDT setup for horizontal strain measurements

As with the FPBTs, strain gauges were used to record strains before cracking as they provided a higher and more consistent resolution at small strains. Four strain gauges were used for each beam; two were placed directly under each load point on the bottom tension surface of the beam, and two strain gauges at the centre support, one on top and one below the beam.

5.3.4. SURFACE DEFORMATION MEASUREMENTS

As an additional measure of deformation, two cameras were used to capture the deformation of the entire beam. The same GEO PIV 8 software was used to analyse the images form which various results could be extracted. Recording each beam's entire deformation also acted as a backup for curvature calculations in case data from the LVDTs was lost when for instance a crack could form directly through the glued supports. Any unpredictable behaviours not considered within the measurement setup could also be described with the PIV.

Since these full-scale tests ran for much longer than the FPBTs a photo interval of 5 seconds was deemed sufficient. As previously described, camera settings were set to manual so that the focal length remained constant throughout testing. A sketch of the setup is shown in Figure 5-9. Both cameras were connected to the same PC and synchronised to capture photos as soon as logging of all other data commenced. Any photo could therefore be linked to an exact loading condition. Care had to be taken to ensure that lighting conditions were constant throughout the entire test thus preventing tracking errors.

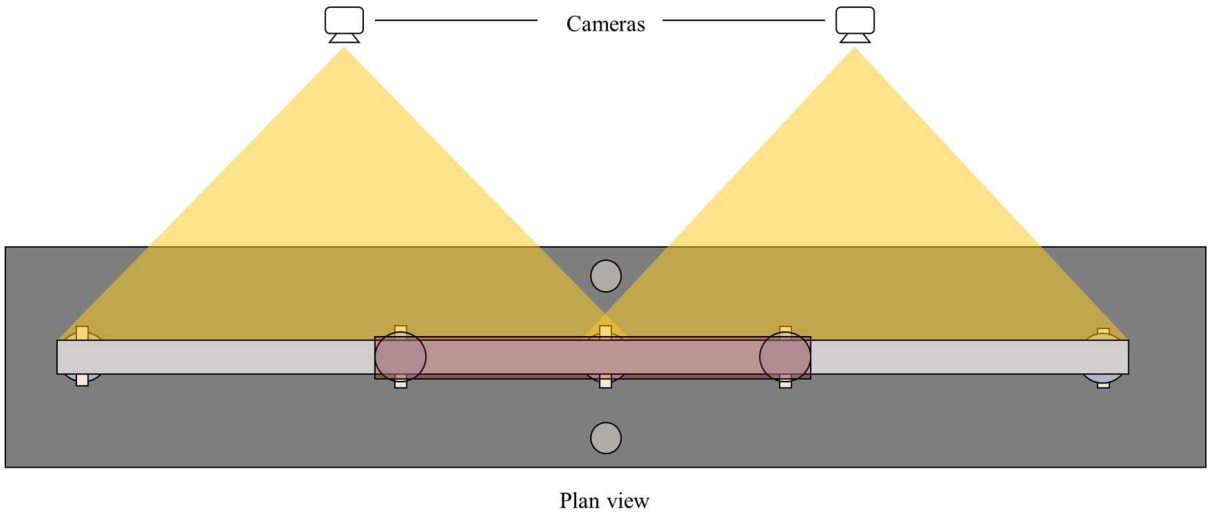

Figure 5-9: Camera positioning for PIV

5.4. CALCULATIONS

5.4.1. ELASTIC MOMENTS

The elastic bending moments across the specimen length are shown in Figure 5-10. The ratios between the moments were calculated using elastic theory and principles of superposition. It is clear that the hogging moment at the centre support is higher than the sagging moments at the point loads. The ratio between the hogging and sagging moments was further increased as a result of the loads acting closer to the centre support instead of at the midspans. This configuration was chosen so that the potential degree of moment redistribution was not limited by the ratio of elastic moments.

To state it differently, in structures, the reinforcing at the hogging moment is reduced so that the moment capacity at the hogging support is decreases resulting in moment redistribution towards the sagging regions. However, to keep the manufacturing procedure as simple as possible, the reinforcing for the hogging and sagging moments in each beam were kept the same and the moment ratios were changed. The end result is the same, where the moment capacity of the hogging support is reached first, followed by the moment capacity at the maximum sagging moment.

The following equations relating the actual moments to the external load were derived:

$$M_S = P_A L_X = P_E L_X \qquad \textit{Equation 5.1}$$

$$M_H = \frac{P_A L_X + (P_A - P_B) L_Y + P_E L_X + (P_E - P_D) L_Y}{2} \qquad \textit{Equation 5.2}$$

The bending moment at the centre support was calculated as the average value obtained from the reaction values at either end supports. Sagging moments were calculated separately for the right or left side. Elastic moments were related to the total external load P with a constant ratio of 0.3155P and

0.4321P for the sagging and hogging elastic moments respectively. These values can be derived when solving for a statically indeterminate structure with the configuration used in Figure 5-10.

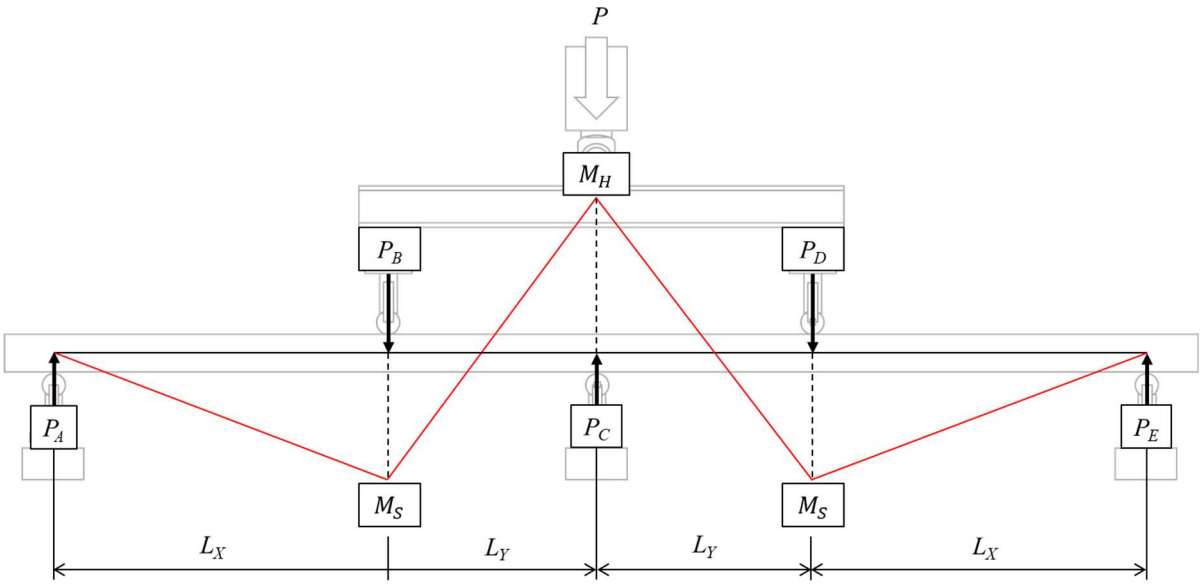

Figure 5-10: Elastic bending moment diagram

5.4.2. CURVATURE

Curvature measurements were calculated from both LVDTs and PIV analysis. Both methods rely on recording strains across a certain distance at two different beam depths. The curvature obtained from these readings therefore represents an average curvature across the distance over which the strains were measured.

The LVDT setup briefly discussed in the FPBT was used for the full-scale beam tests since the curvature was expected to be less severe since span length was longer and the deflections were limited. The LVDTs were glues along one side of the beam, at the three locations where the plastic hinges were expected to form. To obtain some sort of comparable results, the length across which the LVDTs recorded strains was taken as the height of the beam, 100 mm, which is the same length as used in the FPBTs.

Figure 5-11 indicates the dimensions of the setup as well as the variables used in the strain profile from which the curvature was calculated. The strains at the top and bottom LVDT locations are calculated before the curvature can be calculated. Once the strains have been obtained, the curvature is calculated using Equation 5.3:

$$\varphi = \frac{\varepsilon_T - \varepsilon_B}{j} \qquad \textit{Equation 5.3}$$

Where ε_T and ε_B are the top and bottom strains, and j is the distance between the strains. This method of calculating curvature is applied to the PIV analysis. The added benefit of PIV analysis is that strains can be calculated between any points within the mesh generated by the software. For direct comparison, the same width as that of the LVDTs was chosen to measure strains.

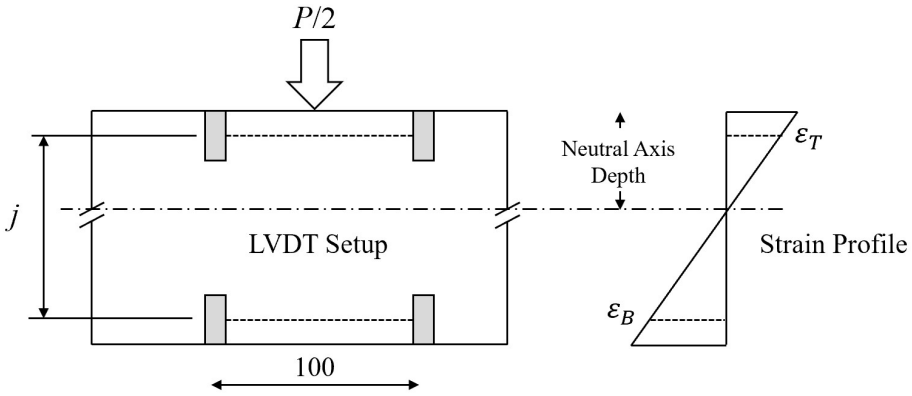

Figure 5-11: LVDT setup and measured strain profile

5.4.3. COMPARISON WITH LVDTs

In this section the moment-curvature results of the LVDTs is compared with that of the PIV. It is expected that the LVDTs are more accurate during low strains, but at higher strains producing larger curvatures, the PIV analysis becomes more accurate. The comparison is taken form the results of a full-scale beam test in which the major crack formed between the LVDTs. An image of the crack is shown in Figure 5-12 which shows the same crack from both sides of the beam. It is immediately apparent that an exact curvature match is not possible since the crack is not uniform across the width of the section. These images were also taken after loading had been increased way beyond the load capacity of the structure. The concrete crushing would therefore not have been present throughout the majority of the test which means that the supports of the LVDTs remained intact throughout realistic deflections.

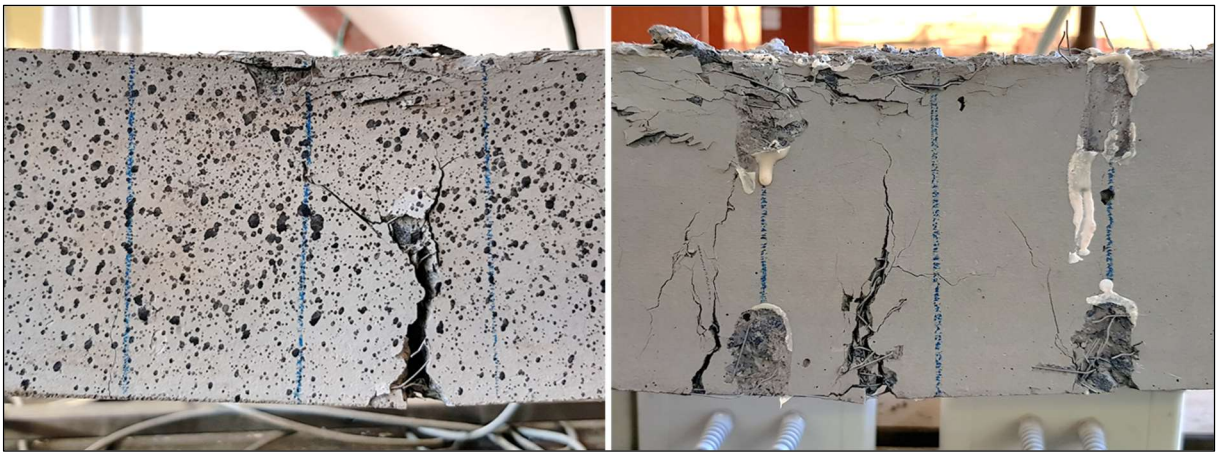

Figure 5-12: Crack formation at the sagging moment

The resulting curvature measurements of both systems are shown in Figure 5-13. The increase in curvature is shown against time to show the divergence of curvatures at later stages in the test. At the start of the test the LVDTs show more precise results when compared to the more variable curve of from the PIV analysis. However, after some time, the curvature increases steadily according to the PIV analysis, whereas the LVDTs indicate a gradually decreasing rate of increase in curvature. This divergence occurs at high curvatures where the LVDT setup becomes less accurate due to the large rotations.

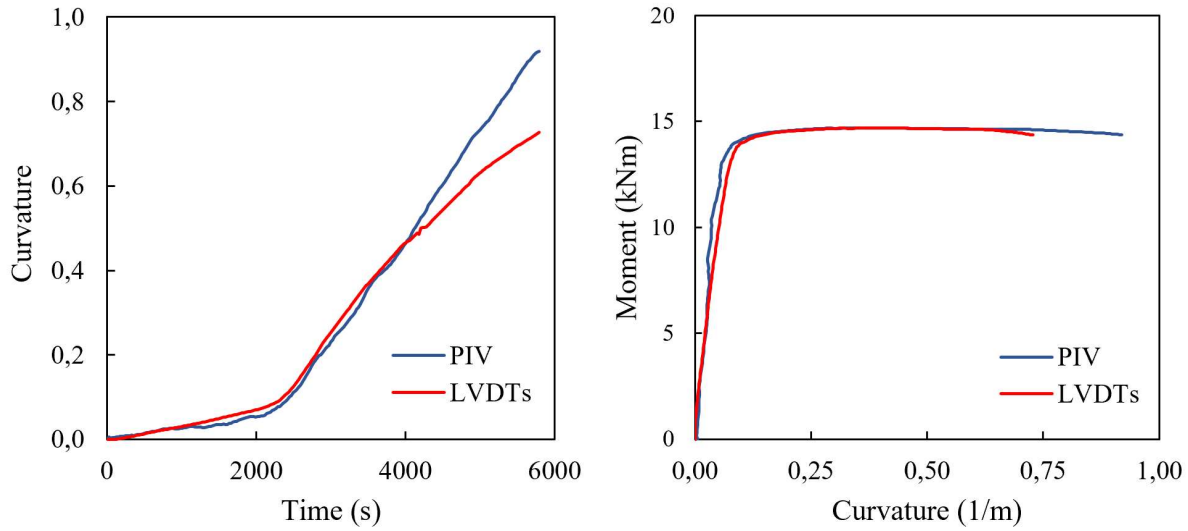

Figure 5-13: Curvature measurements from LVDTs and PIV

In summary, the LVDTs and PIV provided agreeable results, bearing in mind the difference in the cracked surface of either side of the beams. Moment curvature results were therefore taken from the LVDTs due to the greater consistency in readings before cracking as well as just after the peak moment had been reached. The large increase in curvature following the peak moment meant that the results of the PIV analysis were better suited for the latter parts of the test. The similarity between the two methods therefore confirmed that the readings taken by both were comparable.

CHAPTER 6

LOAD DEFLECTION RESULTS

6.1. INTRODUCTION

The objective of the full-scale tests was to investigate the behavioural changes when using different amounts of steel fibres in statically indeterminate structures containing varying amounts of steel reinforcing. A number of structural characteristics such as the load capacity and moment redistribution capabilities were investigated to observe the differences between the fibres and reinforcing when varying the combination of total steel content.

As mentioned before, a total of fifteen beams were tested, with each beam being different, and as a result there were no repetitions. The results obtained therefore represent more of a trend in behavioural changes than statistically meaningful results. Opting for repeated tests would have improved accuracy, with the consequence of removing a variable such as the varying fibre or steel content. Since it is difficult to estimate at which reinforcing ratio the steel fibres would have the most impact, if any, it was decided to opt for the fifteen individual tests to cover a range of scenarios which would provide a higher chance of successful tests.

The fact that each test was unique, meant that the extra care had to be taken with the experimental setup. Key measurements such as the loads were therefore monitored at all supports and load points so that a check for equilibrium of loads could be done throughout the testing. The loads at all three supports were monitored when placing the beam to ensure a correct distribution of load. Image analysis provided backup means of deflection and curvature measurements in an effort to minimise the risk of losing data as well as correcting any irregular results. Due to the large quantity of data a brief overview of the flow of results and discussions will be given.

6.2. OVERVIEW OF RESULTS DISCUSSION

The majority of results obtained directly from measurements are categorised into three major groups, load related results, moment related results and energy. The load related results are presented first as they provide the simplest form of comparison and provide a practical measure of performance. Figure 6-1 indicates the format and sequence in which the results in Section 6 (Load Related Results), Section 7 (Moment Related Results), and Section 8 (Energy) are discussed. The boxes in blue indicate the specific results to be presented. The white boxes indicate in which order the results will be presented. For instance, if the results are presented in terms of constant fibre content, there will be a subsection for each fibre content which will contain the results for varying the steel bar reinforcing. The same idea is applied when the reinforcing bar content is kept constant. For the moment related results, each of the

results in the blue boxes will only be shown with subsections for constant fibre content. The reason for this is to be consistent with the order in which the samples were cast, i.e. each batch had a constant fibre content and was poured into moulds with different reinforcing amounts. Each colour in the table in Figure 6-1 represents a different batch and the intensity of that colour merely indicates the amount of reinforcing steel.

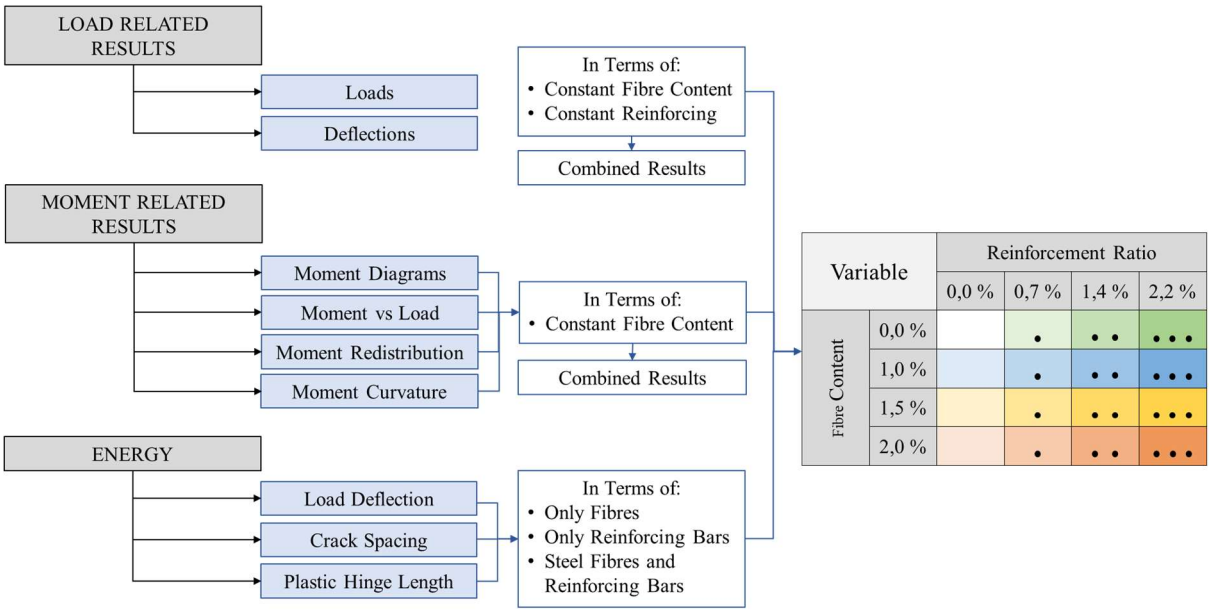

Figure 6-1: Overview of experimental results

The following section provides the load-deflection results of all fifteen beams. The load-deflections results of each beam are discussed briefly to highlight general trends and explain any unexpected behaviour. To show the trends in load-deflection behaviour, the results are presented first in terms of constant steel fibre content with increasing reinforcing content, followed by constant reinforcing content, with increasing fibre content. Thereafter all results are combined to give an overview of the load capacities and deflections. Finally, the load-deflection results are analysed in greater detail by looking at the energy absorbed at different deflections.

The beams will be referred to by codes, for example 0B0.7, where 0 represents the fibre percentage content, B stands for beam, and 0.7 represents the reinforcing ratio percentage. The sample 1.5B2.2 therefore refers to the beam with 1.5 % steel fibres and a reinforcing ratio of 2.2 %. Interesting aspects of each set of results will be noted and then discussed in further detail once a context of all results has been established.

A typical beam failure can be seen in Figure 6-2 where a collapse mechanism formed once three hinges had formed. Images of all beams at various stages of testing can be found in Appendix A.

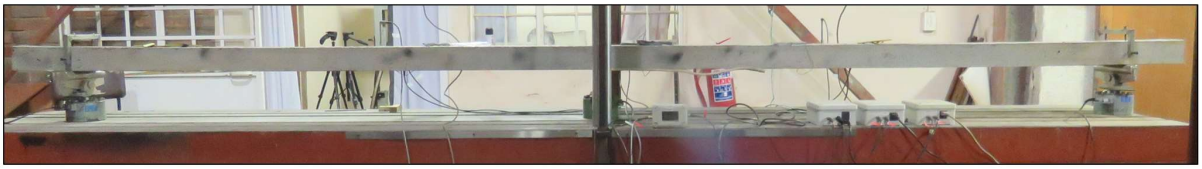

(a) Beam before failure

(a) Beam after failure

Figure 6-2: Typical beam failure before (a) and after (b)

6.3. LOAD DEFLECTION WITH CONSTANT STEEL FIBRES

Load-deflection results are plotted to the same scale for all results to be comparable. Each graph consists of the results of samples with a certain fibre content and varying reinforcing content.

6.3.1. 0 % FIBRE

Figure 6-3 indicates the results for the first batch of samples which contained no steel fibres. The increase in strength is apparent when comparing the beams with a reinforcing ratio of 0.7% and 1.4%. Unfortunately, the concrete in 0B2.2 was not sufficiently compacted. As a result, the concrete failed in a brittle manner with the concrete crushing before the ultimate tensile strength of the beam cross-section could be reached. This result is therefore not included in the remaining analysis but is shown here for completeness. Beam 0B0.7 showed the behaviour of a tension failure, however, as can be seen by the drop-in load after the maximum load, some concrete crushing occurred in the compressive hogging zone. However, since this only occurred near the end of the test, the results are considered adequate. Beam 0B1.4 failed in tension and the test was stopped after the total external load no longer increased.

There was a 22.8 kN increase in strength between the 27.4 kN and 50.2 kN load capacity of 0B0.7 and 0B1.4 respectively. This strength increase is almost double which corresponds to doubling the reinforcing and confirms that the results of 0B0.7 are reasonably accurate. A difference in deflections between the left and right spans occurred since one span failed before the other, and therefore the deflection in the span that cracked first is much higher than the deflection in the other span. The rate of deflection, or the average slope of the load-deflection response up to the peak load, expressed as mm/kN (deflections at the peak load divided by the peak load), reduced when another bar was added from 1.17 mm/kN to 0.77 mm/kN for 0B0.7 to 0B1.4 respectively.

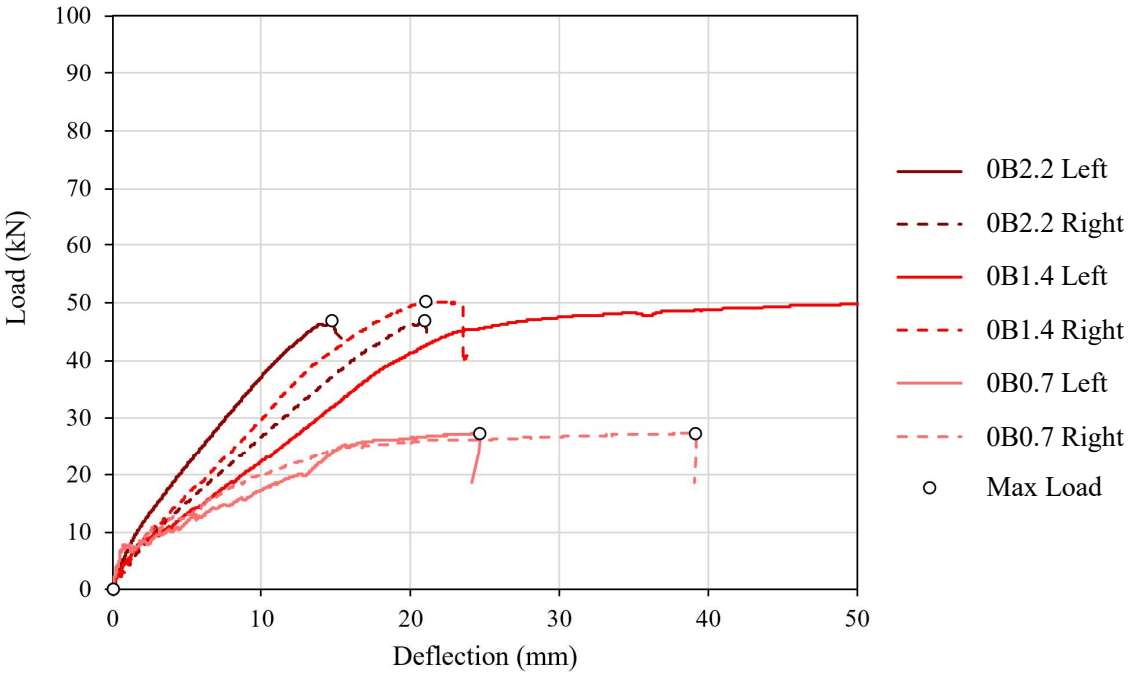

Figure 6-3: Load-Deflection for 0% Fibre

6.3.2. 1 % FIBRE

Figure 6-4 shows the load-deflection results of all four beams with 1 % steel fibres. For this batch the workability was increased by adding more superplasticiser. All four samples were compacted sufficiently and there were no irregularities in the manner in which the beams failed. All four beams failed in tension with the reinforcing steel yielding. The increase in strength from 32.5 kN, to 59.8 kN to 76.0 kN when adding the reinforcing bars is clearly visible. The fibres alone with no reinforcing bars carried a total load of 9.2 kN. This difference is almost the same as the difference in strength between 0B1.4 and 1B1.4 (9.6 kN difference in strength due to the addition of 1% fibres). This difference is not so consistent between 0B0.7 and 1B0.7 (5.1 kN) since 0B0.7 was compacted sufficiently as discussed in the previous section.

Beam 1B0 failed only at the centre support and in the left span. The right span did not fail as the plastic hinges that formed provided insufficient moment carrying capacity for further loading. This behaviour indicates a moment curvature softening shape which means that once a plastic hinge forms, further rotation leads to a decrease in load carrying capacity. The rate of deflections decreased with an increase in the reinforcing ratio, from 0.88 mm/kN in beam 1B0.7 to 0.73 mm/kN and 0.50 mm/kN in beams 1B1.4 and 1B2.2 respectively. Results from beam 1B0 indicated the lowest rate of deflections of 0.11 mm/kN which revealed the improved performance in terms of minimising deflections when compared to steel reinforcing. It must be noted that the 0.11 mm/kN was quite a small value because the maximum load carrying capacity of beam 1B0 was reached at very low deflections. Reduced residual load carrying

capacity occurred after the peak load. The relative deflection value of 0.11 mm/kN is therefore lower than expected since it is calculated as the deflection at the peak load divided by the peak load.

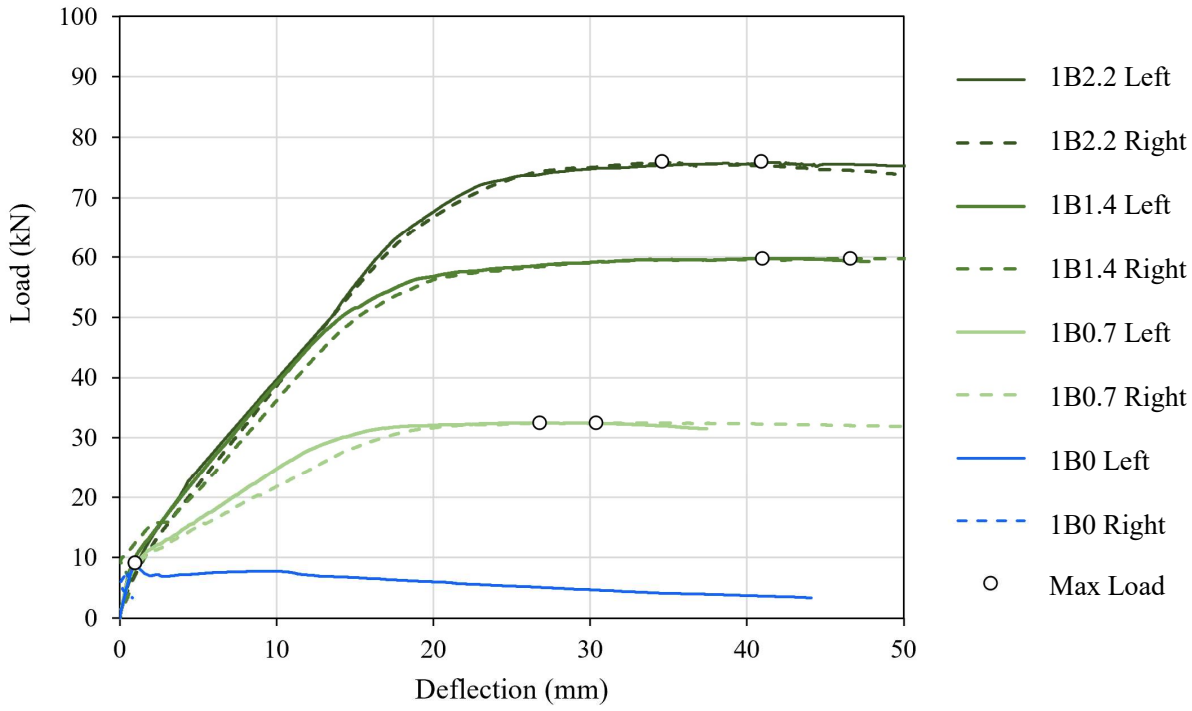

Figure 6-4: Load Deflection for 1% Fibre

6.3.3. 1.5 % FIBRE

Figure 6-5 shows the load-deflection results of all four beams with 1.5% steel fibres. The results are similar to the 1% fibre containing beams, showing only a slight increase in strength. In all three beams containing steel reinforcing, a plastic hinge formed first at the centre support, followed by the left span and then the right span. The increase in strength for the beams containing no steel reinforcing is 5.61 kN (9.15 kN for beam 1B0 to 14.8 kN for beam 1.5B0) when increasing the fibre content from 1% to 1,5%. This strength increase of 61.3% is realistic in terms of the 50% increase in fibres. Beam 1.5B0 containing only fibres failed when two plastic hinges had formed at the centre support and left span.

Increased load capacities from the added steel fibres however become less visible when combined with steel reinforcing. There is a 3.66 kN increase in strength between beams 1B0.7 and 1.5B0.7, and a strength increase of 1.94 kN and 3.86 kN for the beams with a reinforcing ratio of 1.4% and 2.2%. The rate of deflection decreased with an increase in reinforcing ratio, from 0.76 mm/kN in beam 1.5B0.7 to 0.58 mm/kN and 0.45 mm/kN in beams 1.5B1.4 and 1.5B2.2 respectively. Results from beam 1B0 indicate the lowest deflections per unit load of 0.40 mm/kN which highlights advantages of steel fibres in providing a certain load capacity with minimal deflections.

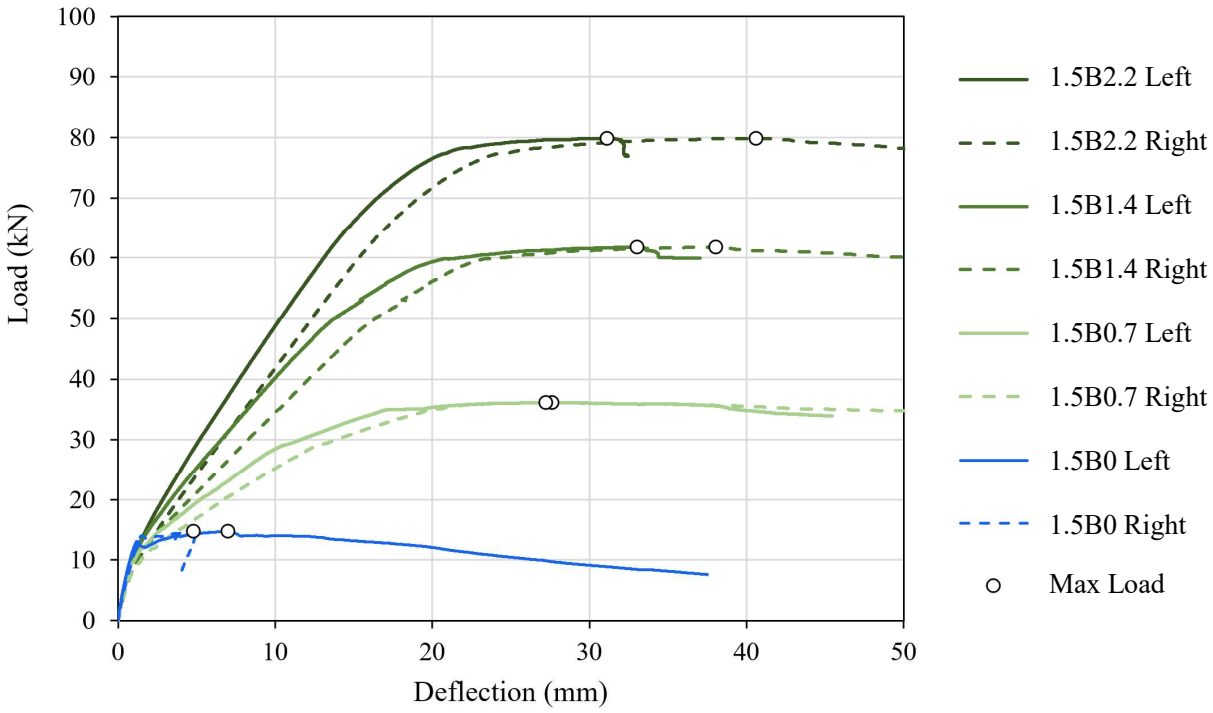

Figure 6-5: Load-Deflection for 1.5% Fibre

6.3.4. 2 % FIBRE

Figure 6-6 shows the load-deflection results of all four beams with 2% steel fibres. Increases in strength for these four tests show the most consistent trend between the load capacity of beams 2B0.7, 2B1.4 and 2B2.2. The load capacity increases from 36.2 kN, to 60.7 kN and then to 83.6 kN for the beams with a reinforcing ratio of 0.7%, 1.4% and 2.2% respectively. Resulting increases between 2B0.7 and 2B1.4, and 2B1.4 and 2B2.2 are 23.0 kN and 24.5 kN respectively which correspond to the strength increases described previously when adding one steel bar.

Beam 2B0, containing only fibres, failed when two plastic hinges had formed at the centre support and right span. This beam carried a peak load of 17.2 kN which translates to a 2.48 kN increase in strength from beam 1.5B0. This increase is lower than the 5.61 kN strength increase between 1B0 and 1.5B0 even though the increase in fibres is the same at 0.5%. Simply increasing the fibre content therefore does not lead to a constant increase in strength, which highlights the importance of finding the optimum fibre content for every mix design.

The deflection per unit load decreased with an increase in steel bars, from 0.91 mm/kN in beam 2B0.7 to 0.67 mm/kN and 0.41 mm/kN in beams 2B1.4 and 2B2.2 respectively. Results from beam 2B0 indicate the lowest deflections per unit load of 0.37 mm/kN which again emphasises the ability of steel fibres to reduce deflections relative to the loads.

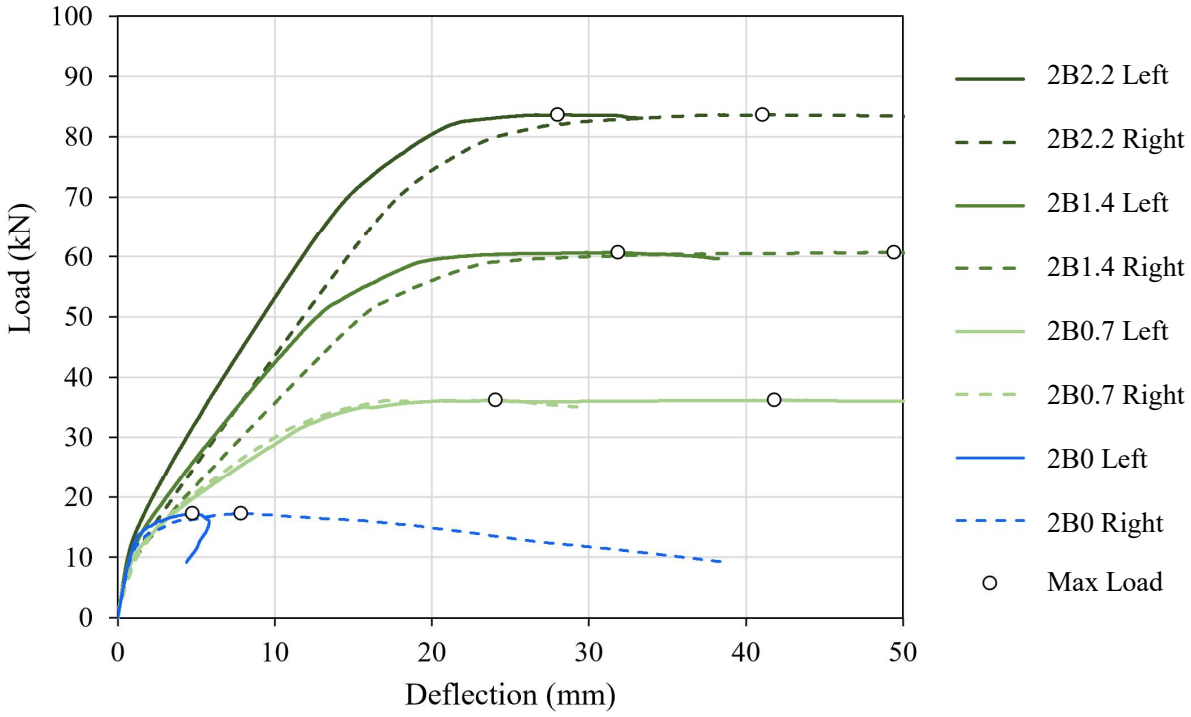

Figure 6-6: Load-Deflection for 2% Fibre

6.4. LOAD DEFLECTION WITH CONSTANT REINFORCING STEEL

Load-deflection results are plotted on the same axes for all results to be comparable. Each graph consists of the results for samples with a certain steel reinforcing content and varying steel fibre content. The results will be discussed briefly since they have already been presented, with additional insight provided by presenting the results in terms of a varying fibre content instead of a varying reinforcing content.

6.4.1. NO REINFORCING BARS

Figure 6-7 shows the load-deflection response for the beams containing no reinforcing bars. A trend of increasing strength is visible where the increase in strength decreases when the fibres are increased from 1.5% to 2% (1.61 times increase, and 1.88 times increase respectively when comparing to beam 1B0). The differences in strength are much smaller when compared to changes caused by individual rebars. These differences are however relative since doubling the fibre content from 1% to 2% leads to a 1.88 times strength increase which is significant when one does not consider any reinforcing. As discussed previously, the increase in strength from 1% to 1,5% fibres is 5.61 kN and only 2.48 kN when increasing the fibre content from 1.5% to 2%.

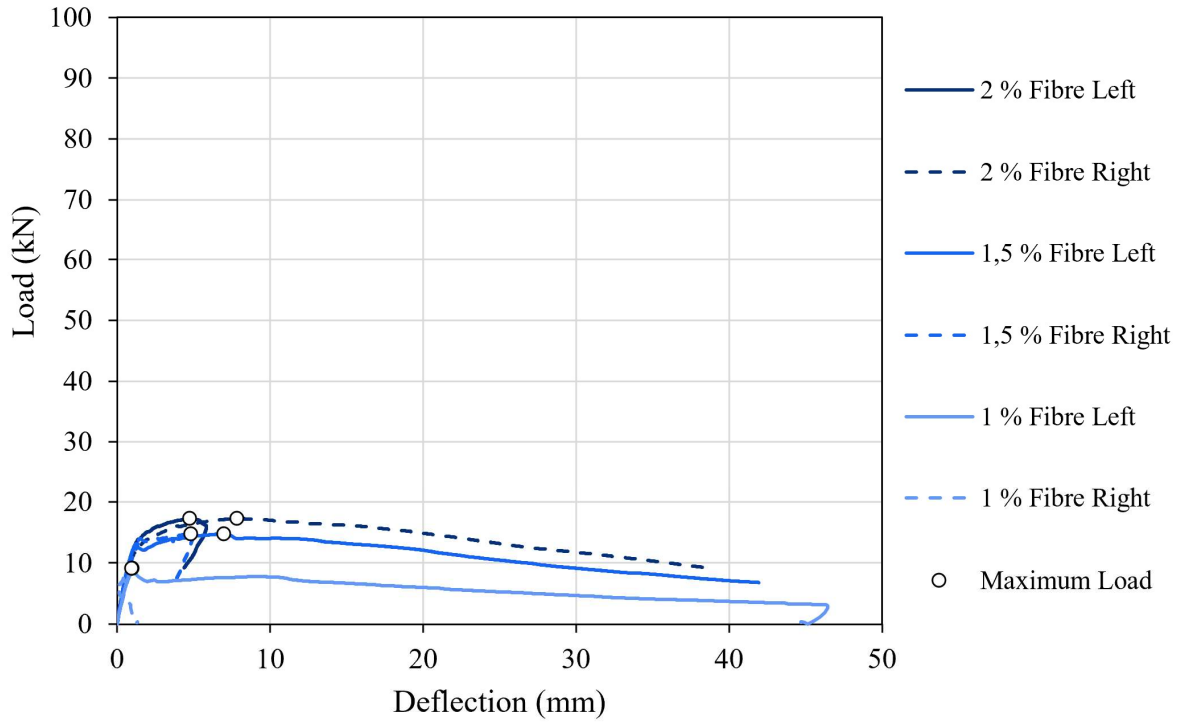

Figure 6-7: Load-Deflection for no reinforcing bars

6.4.2. REINFORCEMENT RATIO OF 0.7%

Figure 6-8 shows the load-deflection response for the beams containing only one reinforcing bar. The deflection hardening properties of the reinforcing steel are evident in the graph where the peak load is maintained even after further deflection. An exception is beam 0B0.7 which had not been compacted sufficiently. The results indicate a similar trend of increasing strength when more fibres are added, except beyond 1.5% fibres where there is no apparent increase in strength. Although the ultimate load capacity of 1.5B1 and 2B1.4 are almost the same at 36.1 kN and 36.2 kN respectively, there is a difference in their behaviour before the peak load is reached. The purple curve representing a 2% fibre content sits above the orange curve of 1.5% which means that the 2% resulted in lower deflections than the 1.5% fibre deflections at the respective loads.

The strength increased with increasing fibre content are as follows; 5.11 kN, 3.66 kN and 0.04 kN. The 5.11 kN increase is the larger since it represents a 1% increase in fibres (from 0% to 1%) instead of 0.5%. These strength increases are lower than those for the beams with no reinforcing bars.

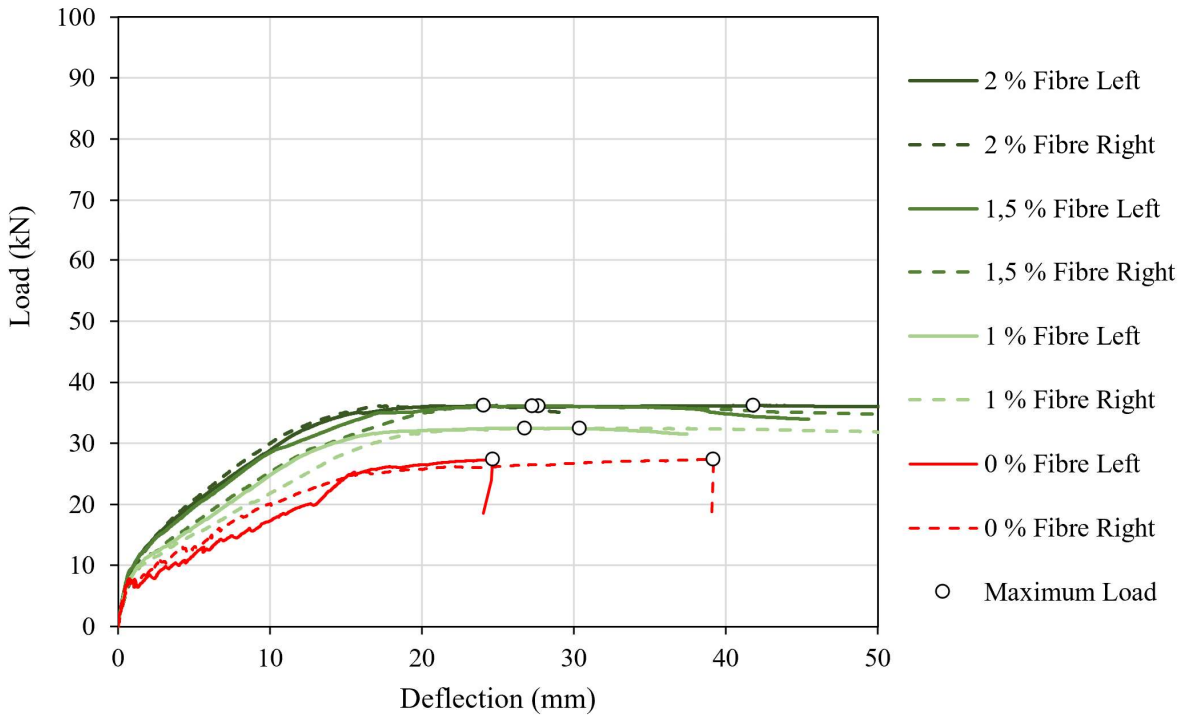

Figure 6-8: Load-Deflection for a reinforcement ratio of 0.7%

6.4.3. REINFORCEMENT RATIO OF 1.4%

Figure 6-9 shows the load-deflection response for the beams containing two reinforcing bars. The benefit of added fibres is less visible in these results. It has been discussed that simply increasing the fibre content does not yield a similar increase in strength. However, the overall trend of increasing strength can still be observed when looking at the gradients of the curves before the peak loads have been reached.

A 9.57 kN strength increase is observed between 0% and 1% fibres of 0B1.4 and 1B1.4 which is significantly higher than the 5.11 kN increase in strength between 0B0.7 and 1B0.7. In comparison the changes in strength for beams 1B2, 1.5B1.4 and 2B1.4 are only 1.94 kN and -1.04 kN. A general increase in strength is observed, where a strength decrease occurs when more than 1.5% are added.

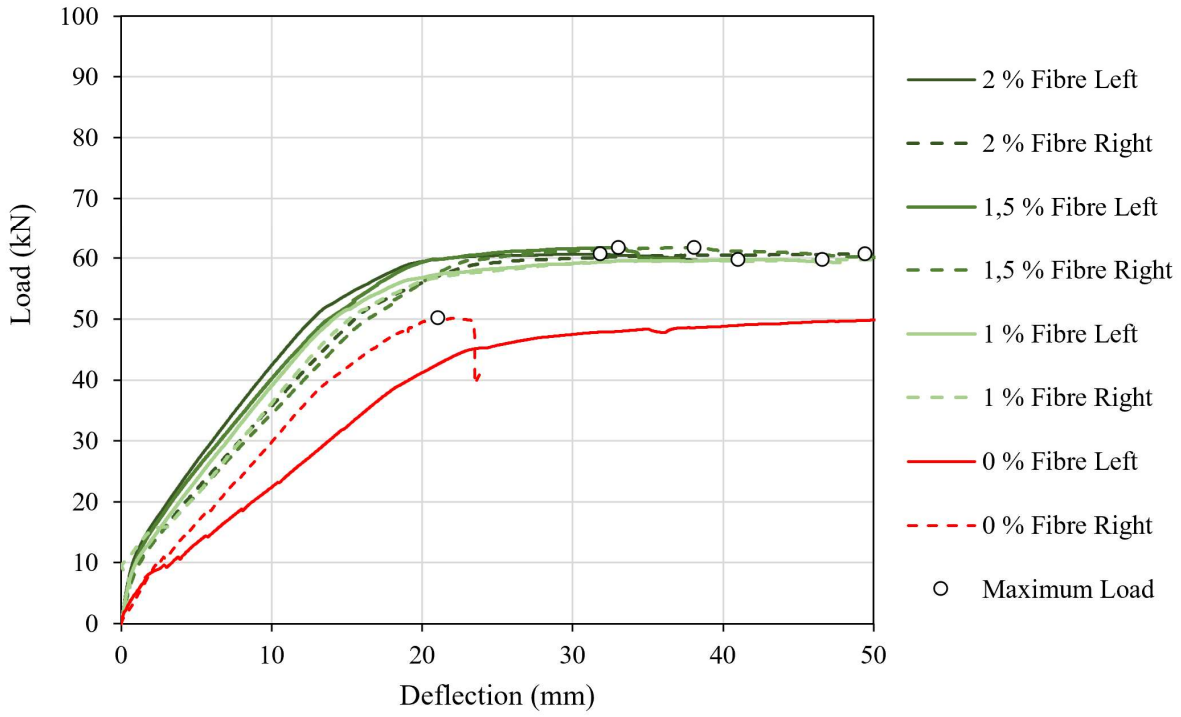

Figure 6-9: Load-Deflection for a reinforcement ratio of 1.4%

6.4.4. REINFORCEMENT RATIO OF 2.2%

Figure 6-10 shows the load-deflection response for the beams containing three reinforcing bars. The results of these tests show a clear separation with an increase in fibre content. A possible explanation to the improved results is that for each batch the beam with three reinforcing bars was always cast first as these beams required the greatest workability, followed by the beams with two, one and no reinforcing bars. As a result, the quality of compaction for the beams with three reinforcing bars may have been more consistent across the different concrete batches.

Beam 0B2.2 is excluded from the discussion due to the compaction issues already mentioned. The strength increase from 1% to 1.5% fibres is 3.86 kN which is slightly more, but very similar to the strength increase of 3.78 kN from 1.5% to 2% fibres. With three reinforcing bars, the influence of the steel fibres in terms of increasing the strength (about 3.8 kN) seems small when compared to the total load capacity between 76.0 kN and 83.6 kN. However, the usefulness of the fibres may again be revealed in terms of the reduction in deflections which can be seen by the increasing gradients of the curves before the peak load.

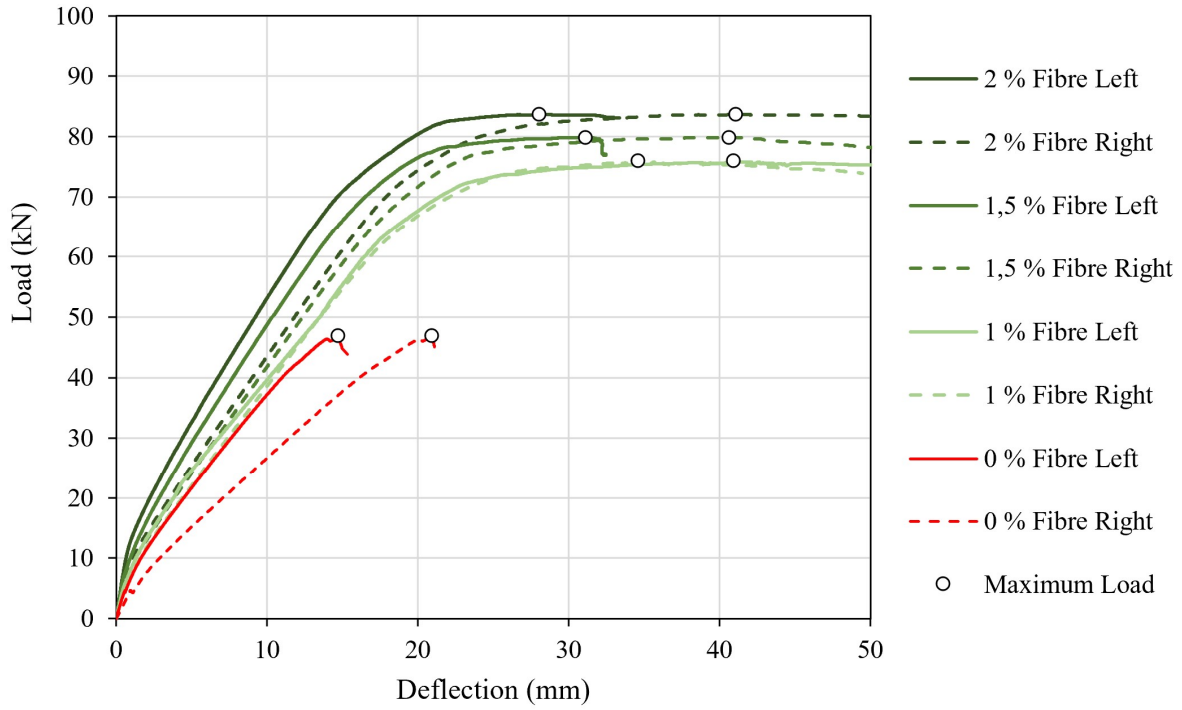

Figure 6-10: Load-Deflection for a reinforcement ratio of 2.2%

6.5. LOAD CARRYING CAPACITIES OF ALL BEAMS

So far, the load-deflection results have been discussed in terms of one variable, being either a changing fibre content, or a changing reinforcing content. To observe the overall trends, it is easiest to plot the parameters of load and relative deflections against both the fibre content and the reinforcing content. The results of all 15 beams are plotted on one graph and organised in a similar pattern to the grid of samples described in Figure 6-1.

Figure 6-11 shows the maximum loads carried by all fifteen beams in terms of a varying reinforcing and fibre content. There is a clear trend of increasing strength as the reinforcing ratio increases, as well as for increasing fibre content albeit of lesser magnitude. The highest strength of 83.6 kN was obtained by beam 2B2.2 which effectively consisted of 4.4 % total steel (2% fibres and 2.4% reinforcing steel) which is 2.58 times greater than the 32.5 kN strength of beam 1B0.7 consisting of 1.8% total steel which is reasonable considering the fact that 2B2.2 contained 2.44 times more steel than 1B0.7.

The strength increase caused by an increase in fibres was most visible with no reinforcing bars. When the fibres were combined with the steel reinforcing, the strength increase was less apparent since the reinforcing was able to elongate significantly more than the 30 mm fibres. As a result, a larger proportion of fibres across the cracked surface will have pulled out or snapped before the steel yielded and reached its maximum tensile stresses. Once the steel reached its maximum stress, a smaller portion

of fibres was then able to provide additional tensile strength. Longer fibres would therefore tend to provide better performance in conjunction with steel reinforcing at the cost of reduced workability.

The increase in strength when adding a reinforcing bar was fairly constant and not much affected by the fibre content. Average increases in strength when adding a reinforcing bar for beams with 1%, 1.5% and 2% fibres were 22.3 kN, 21.7 kN and 22.1 kN respectively. In general, the increase in strength for any fibre content when going from a reinforcing ratio of 0.7% to 1.4% was the highest, at an average of 25.0 kN, which is slightly higher than the strength increase between no bars and a reinforcing ratio of 0.7%, 22.8 kN, and a reinforcing ratio of 1.4% and 2.2%, 19.1 kN. In terms of the load capacity and the amount of steel added, there seems to be an optimum at a reinforcing ratio of 1.4%.

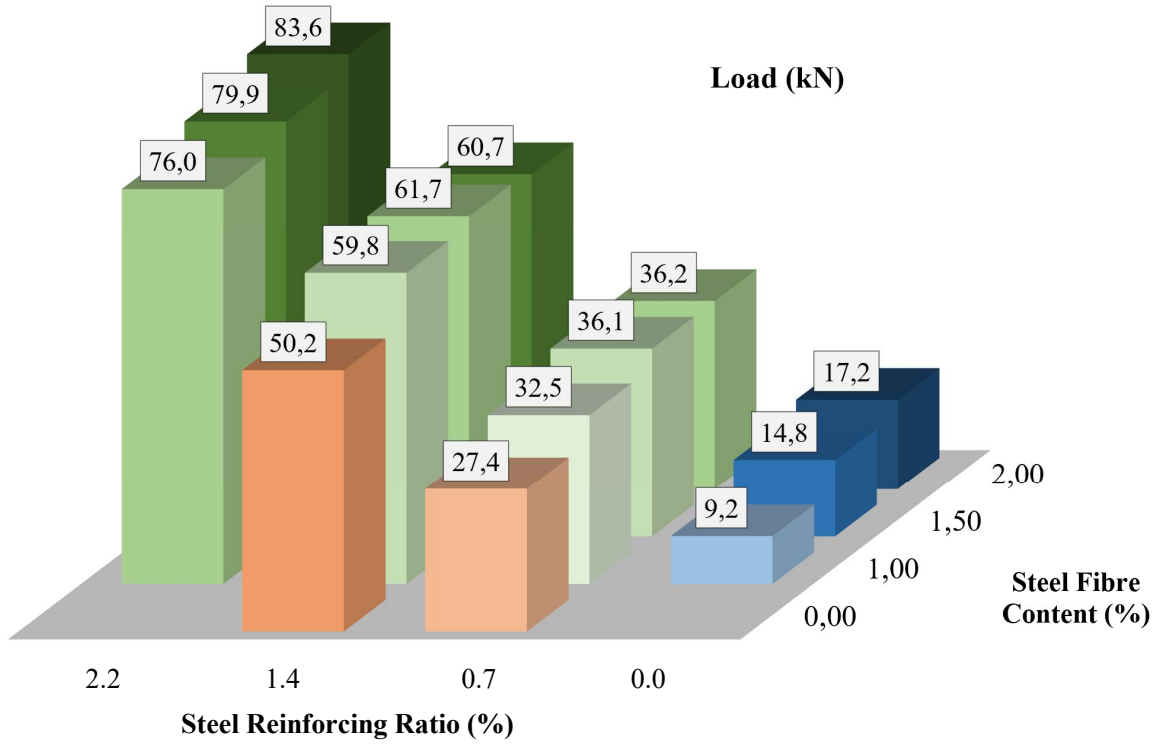

Figure 6-11: Maximum loads for all beams

The efficiency of the beam as expressed by the peak load divided by the steel content is expressed visually in Figure 6-12. The results of beam 0B2.2 were excluded due to the compaction issues. Note that the axis representing the fibre content has been reversed. The higher number of bars indicated a greater return in strength from the respective total steel content.

There is a general trend of improved efficiency with an increased reinforcing ratio up to 1.4%. Increasing the reinforcing ratio to 2.2% provided a higher efficiency only when coupled with 2% fibres, whereas a combination with 1.5% fibres resulted in a similar efficiency to a 1.4% reinforcing ratio, and a combination with 1% fibres led to a reduction in efficiency when compared to a reinforcing ratio of

1.4%. However, in general, an increase in fibre content reduced the efficiency. This behaviour is made clear by beams 0B0.7 and 0B1.4 which contain no fibres and showed the greatest load carrying capacity relative to the total steel content.

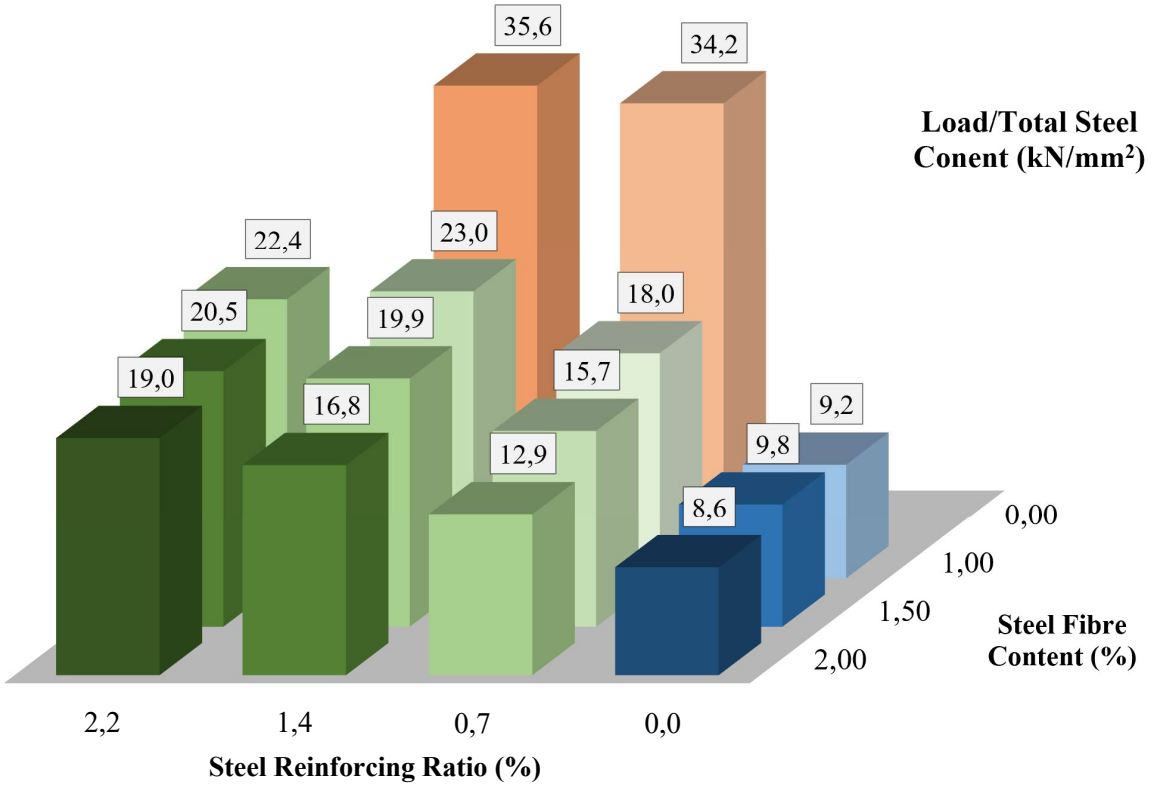

Figure 6-12: Visual representation of load efficiency (load/total steel percentage)

It has been shown that there is not much benefit in adding steel fibres when an increase in ultimate load capacity is required. However, the addition of fibres may change the load deflection behaviour at lower deflections during serviceability loads. The addition of fibres may therefore aid in reducing the deflections when combined with reinforcing bars which results in smaller cracks and hence a potential increase in the service life of the structure.

6.6. LOAD DEFLECTIONS REPSONSES AT LOW DEFLECTIONS FOR ALL BEAMS

The load deflection responses of all beams are summarised in Figure 6-13, with deflections of up to 9 mm, which represents the span/250 limit recommended by EC2 for the appearance and efficiency of a structure. The deflections were averaged between the vertical deflection of the two spans of each beam. Considering first the beams with only fibres in Figure 6-13 (a), a difference was observed between the beam containing 1% fibres and the beams containing 1.5% and 2% fibres. The beam with only 1% fibre showed no further increase in load capacity once the deflections increased after the peak load had been reached. The beams with only 1.5% and 2% fibres showed a slight increase in load

capacity after the change in slope and were able to resist this increased load at higher deflections of up to 9 mm.

For all beams, cracking occurred at a similar deflection value of around 1 mm, which reduced slightly as the number of reinforcing bars is increased. The benefit of the fibres is realised when comparing the load deflection curves of the beams with only reinforcing bars against the beams containing a combination of bars and fibres. In all cases, there was a substantial reduction in deflections at a certain load when comparing a beam with only reinforcing bars to a beam with bars and fibres. For instance, the deflection at 10 kN for 0B0.7 was 3.0 mm, and only 1.1 mm when combined with 2% fibres.

Deflections at a load of 15 kN for the beam with no fibres and a 0.7% reinforcing ratio (Figure 6-13b) were 1.6 times larger than the deflection when 1% fibres were added, and 2.2 and 2.8 times greater than the deflection of the beams at 15 kN with 1.5% and 2% fibres. Similar ratios, although slightly reduced, exist at higher loads.

The reduction in deflections when adding fibres is exaggerated in the beams with a reinforcing ratio of 1.4% (Figure 6-13c) as beam 0B1.4 had pre-existing cracks, and hence deflected more from the start. Nevertheless, at higher deflections of around 9 mm, at which point the beam would have cracked already and the influence of pre-existing cracks is negligible, the benefit of adding fibres is obvious. For a load of 20 kN, the deflections reduced by 1.8, 1.9 and 2.1 times when adding 1%, 1.5% and 2% fibres respectively.

Similar results are obtained for beams with a reinforcing ratio of 2.2% (Figure 6-13d). With a load of 10 kN, deflections reduced from 2.2 mm without fibres, to 1.4 mm, 1.1 mm, and 0.9 mm with 1%. 1.5% and 2% fibres, a reduction in deflection of up to 2.6 times. Nearing the point of 9 mm deflections at a load of 30 kN, the deflections reduced by 1.3, 1.6, and 1.8 times when adding 1%, 1.5%, and 2% fibres.

Although the ultimate increase in load capacity when adding fibres was small in comparison to increasing the number of reinforcing bars, the benefit of the fibres is now evident when considering the deflections at loads representing service loads instead of the ultimate loads. The increase in the slopes of the curves shows the additional strength introduced by the fibres in their ability to bridge small cracks and thereby reduce deflections. Owing to the short length of the fibres, their ability to reduce deflections decreases as the deflections increase, a behaviour which was shown in Figure 6-13 (a), where the strength increase beyond 1 mm deflections was minimal if any.

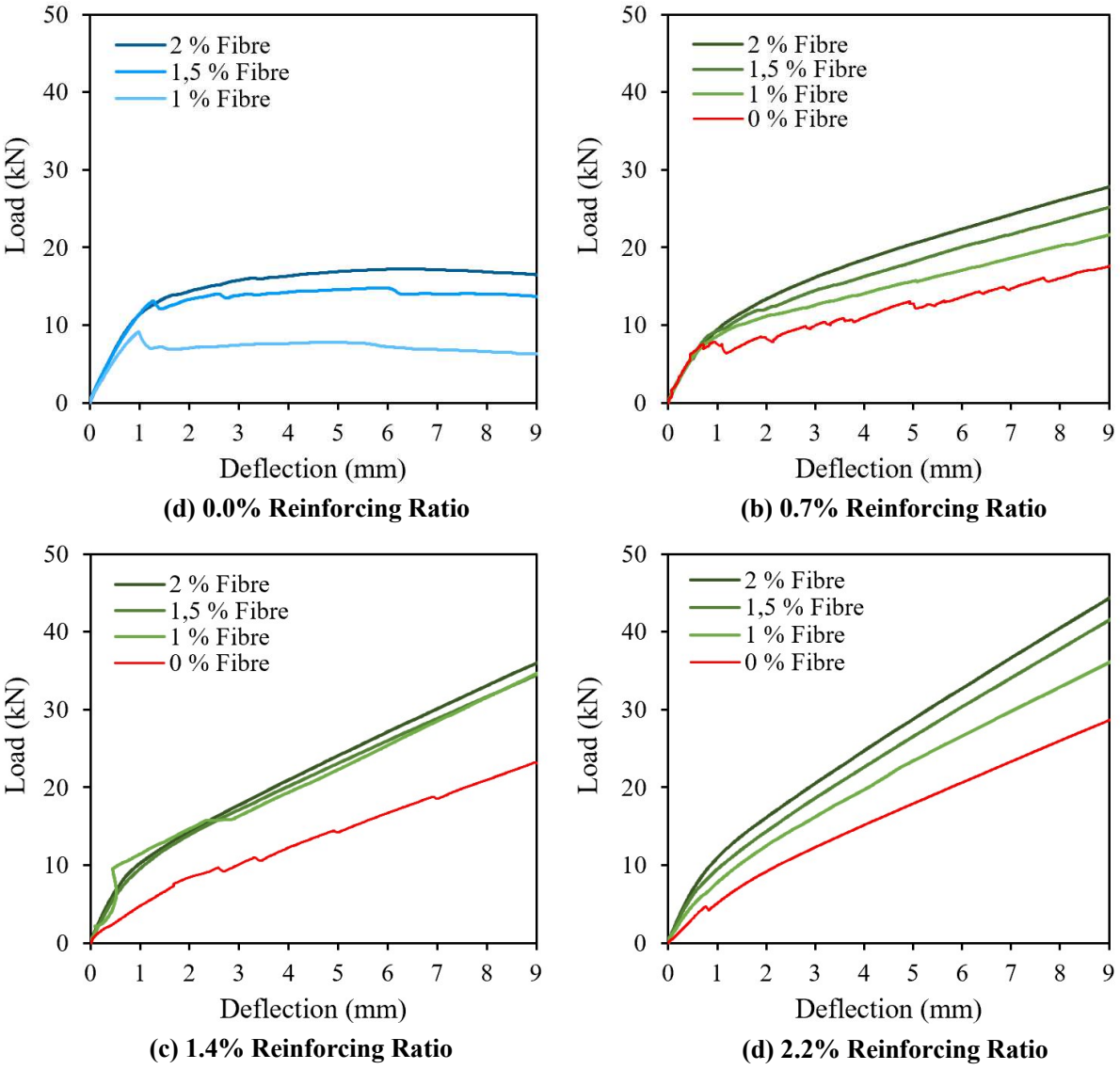

Figure 6-13: All beam deflections up to span/250 mm

6.7. DEFLECTIONS AT ULTIMATE LOADS OF ALL BEAMS

Structures are predominantly limited in their design by deflections. The performance of reinforcing and fibres can therefore also be expressed in terms of the deflections at the ultimate load. Figure 6-14 indicates the deflections at the ultimate loads of all beams. The magnitude of the deflections provides an indication to how far the beam had deformed when it reached its ultimate load.

Beams with no reinforcing bars showed much smaller deflections, as a result of the improved load deflection behaviour shown by the fibres when compared to reinforcing bars, however, the ultimate loads were also much lower than beams with reinforcing bars. In general, the largest deflections were in beams with a reinforcing ratio of 1.4%. The only exception is beam 1.5B2.2 which deflected slightly more than 1.5B1.4. In terms of fibre content, the greatest deflections were observed in beams with 2%

fibres for a reinforcing ratio of 0% or 0.7%, and 1% fibres if combined with a 1.4% or 2.2% reinforcing ratio.

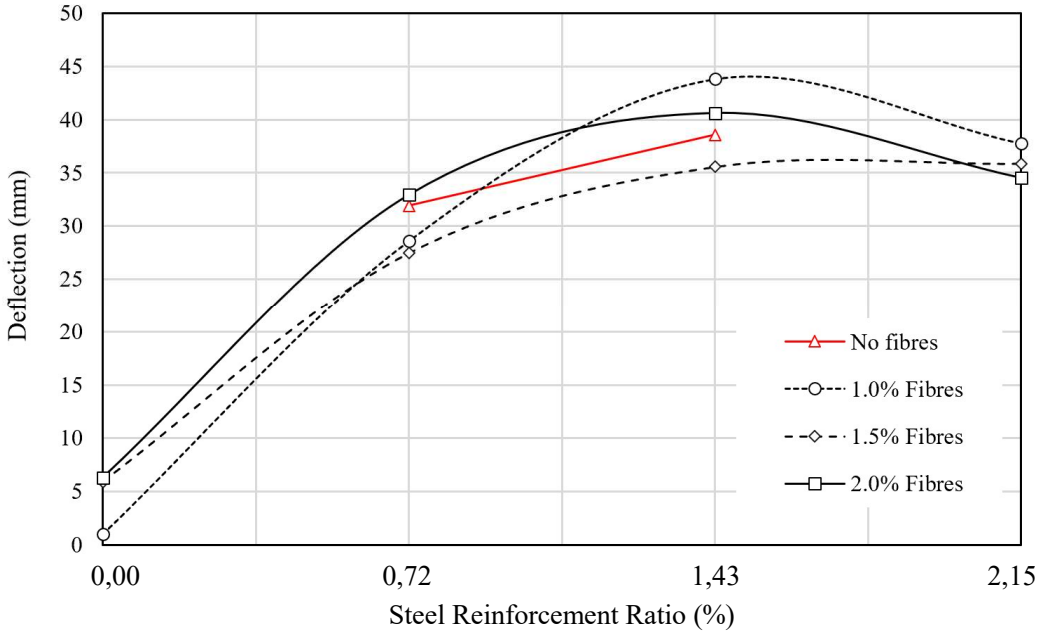

Figure 6-14: Deflections at maximum load

These deflection values are however more meaningful when normalised with respect to the ultimate loads. Figure 6-15 shows the results when the deflection values in Figure 6-14 are divided by the ultimate loads. A lower value indicates improved performance since a combination of lower deflections, higher loads, or a combination of the two is achieved. The worst performing beams when looking at these deflections to ultimate load ratios are beams with a reinforcing ratio of 0.7% with or without fibres. In other words, although their ultimate deflections were less than beams with a reinforcing ratio of 1.4% or 2.2%, their load capacity was much lower.

There is however a big improvement in the performance of beams with a reinforcing ratio of 0.7% when adding fibres. Although this improvement is not seen when adding fibres to the beam with a reinforcing ratio of 1.4%, the improvement in behaviour when adding fibres to reinforcing bars is expected to be similar to the improvement shown by the beams with a reinforcing ratio of 0.7%. This statement is supported by the load deflection curves discussed in Figure 6-13 where a clear increase in load and/or a decrease in deflections is observed.

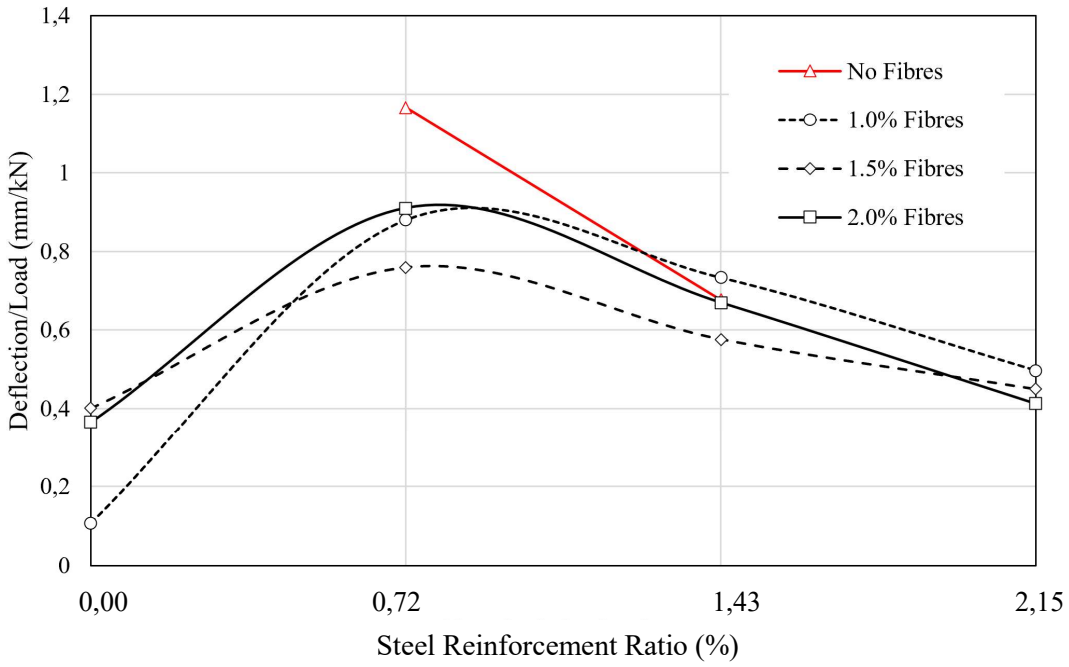

Figure 6-15: Deflections at ultimate load/ultimate load for all beams

Essentially, the results of Figure 6-15 indicate the increase in the stiffness of the structure when the reinforcing ratio and steel fibres increases. While the improved performance is clear when increasing the reinforcing ratio, the influence of the fibres shows a less evident trend. The beams containing only fibres showed the least amount of deflection in terms of their respective peak loads. However, these results must be linked to the shape of the load-deflection responses. A softening response of the load-deflection behaviours was evident in all three beams containing only fibres. Therefore, the peak load occurred early in the deflections, after which the load did not remain constant but decreased. Different fibres may have provided deflection hardening behaviours similar to the behaviour of the steel reinforcing bars. For beams with a reinforcing ratio of 0.7% and 1.4%, adding 1.5% fibres provided the greatest improvement in a combination of reduced deflections and increased loads. For beams with a reinforcing ratio of 2.2%, the optimum fibre content increased to 2%.

The variability of the effectiveness of certain fibre contents changed with each reinforcing bar due to the change in the way the beam deformed. For instance, adding 2% fibres to beams with reinforcing bars changed from the worst performance with a reinforcing ratio of 0.7% to the best performance with a reinforcing ratio of 2.2%. This change in the optimum fibre content for different number of reinforcing bars depends on the number and spacing of cracks formed, which coincides with the length of the plastic hinges formed. More cracks will allow a greater number of fibres to bridge the cracks and therefore increase the total energy absorption of the beam. Beams with a large amount of moment redistribution are able to absorb more energy since the total load applied to the structure can increase beyond the load at which the moment capacity of the first critical section is reached.

Moment redistribution requires a certain degree of hinge rotation at the critical section which translates to increased deformations of the structure. The concept of the ideal performance of a structure having small deflections and a large load capacity does not suit the idea of moment redistribution which requires additional deflections for the additional load capacity to be realised. The ideal moment redistribution behaviour may therefore occur at a completely different combination of reinforcing bars and fibres as the optimum performance shown in Figure 6-15.

6.8. SUMMARY OF LOAD AND DEFLECTION RESULTS

The load deflection responses of all beams were discussed in terms of load capacities, strengths relative to the total steel content, total deflections, and deflections relative to the strengths. Hinges formed at the centre support and left and right spans for beams containing reinforcing bars. Beams with only fibres failed in only one span due to the insufficient load capacity at higher rotations.

The strength increase provided by an increasing fibre content was most visible in beams containing only fibres. When combined with reinforcing bars, the difference in strength increase with different fibre contents was less visible. In terms of load capacity, the reinforcing bars played a much greater role and overshadowed the additional strength provided by the fibres.

In terms of the efficiency of the total steel relative to the resulting load capacity, beams with a reinforcing ratio of 0.7% performed the best. Beams with only fibres all had similar efficiencies. Beams with a combination of fibres and reinforcing bars showed an improvement with more bars and less fibres.

The load deflection results shortly after cracking were discussed to reveal the improved deflection response provided by the addition of fibres. For beams with only fibres, only fibre contents of 1.5% and 2% showed a slight increase in load capacity after cracking. In beams with reinforcing bars and fibres, the deflections at similar loads were reduced when adding more fibres. The addition of fibres allowed the deflections to be halved at loads causing deflections of 9 mm (span/250) when compared to beams without fibres.

The beams with the highest deflections at failure were beams with a reinforcing ratio of 1.4%, regardless of the fibre content. When these ultimate deflections were normalised in terms of the ultimate loads, there was a clear decrease in relative deflections with an increase in reinforcing bar content, where the beams with a reinforcing ratio of 0.7% showed the greatest relative deflections. With a reinforcing ratio of 0.7%, adding 2% fibres resulted in the worst performance, which changed to the best performance when combined with a 2.2% reinforcing ratio. In general, the beams with 1.5% provided better results in terms of the relative deflections.

CHAPTER 7

MOMENT REDISTRIBUTION RESULTS

7.1. MOMENT REDISTRIBUTION COMPARED TO EC2

According to EN 1992-1-1 (2010) "*moment redistribution is the ratio of the redistributed moment to the elastic bending moment*". If the degree of moment redistribution that took place in the experiments is expressed according to this definition, the results are shown in Figure 7-1. Experimental results can be compared to the limits suggested by the Eurocode (EN 1992-1-1, 2010) which is the same as the fib Mode Code (2013) for the concrete used. These limits depend on the neutral axis (x) over effective depth (d) factor at the ultimate load which can easily be calculated by a cross-sectional analysis where the moment is known, and the neutral axis is solved so that equilibrium of the section is achieved.

The experimental results of the beams with a combination of fibres and reinforcing bars is shown in Figure 7-1 where a darker marker indicates an increase in the number of reinforcing bars. An increase in the reinforcing ratio led to an increase in the x/d ratio as well as an increase in the amount of moment redistribution, apart from the beam with a reinforcing ratio of 2.2% and 2% fibres. Over reinforced beams are prone to compression failure where the full tensile strength of the critical section cannot be reached, and hence the degree of moment redistribution is reduced. In terms of fibre content, 1.5% fibres show the highest moment redistribution results with 1% performing the worst, except when combined with a reinforcing ratio of 2.2%. Two beams (1B0.7 and 1B1.4) resulted in less moment redistribution than the limitation set out by the codes.

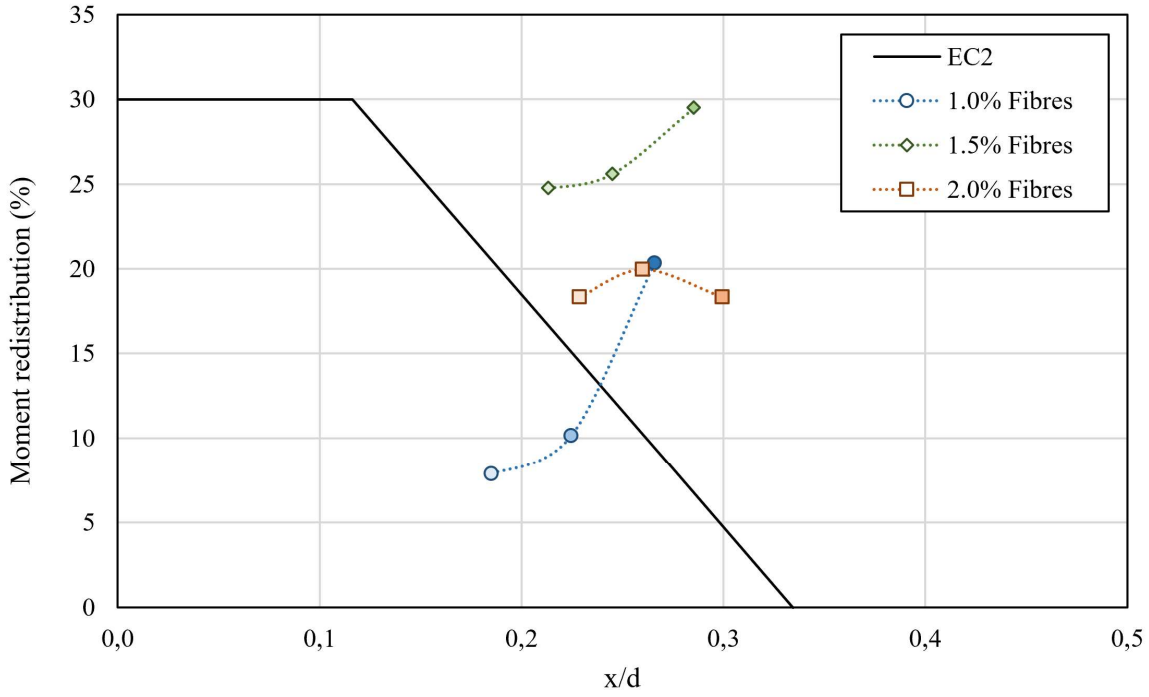

Figure 7-1: Moment redistribution percentages compared against the code

These trends are however based on the definition of moment redistribution, where the final moment is merely compared against the elastic moment. In reality, the behaviour leading to these results is complex and can affect the outcome in many ways. The moment related results of all beams are therefore discussed in detail before visiting the concept of moment redistribution after having gained a better understanding towards the meaning of the results shown in Figure 7-1.

7.2. BENDING MOMENT DIAGRAMS

The bending moment diagram along the length of the beam is shown in the following section. Moments are calculated at the load points and centre support using the loads recorded at the end supports and load points. The moment caused by the measured peak load is shown and can be compared to the expected elastic bending moment for this load. Further moment curves are added at 75%, 50% and 25% of the peak load to show how the bending moment envelope changes with the applied load. Sagging moments are represented by positive bending moments, and negative for the hogging moments.

7.2.1. 0 % FIBRE

Figure 7-2 shows the bending moment diagram for the beams with no fibres, where beam 0B2.2 is excluded. The increasingly darker lines relate to the increase in peak load, and the dotted line represents the elastic moments. A clear increase in moments is observed for both beams as the load increases. The ratio between the moments at the sagging and hogging regions changes especially when comparing the moments at 75% maximum load with the moments at the maximum load. Nearing the maximum load, the moment at the hogging region is expected to increase at a slower rate or stay constant whilst the moments at the sagging region continue to increase as moment redistribution occurs.

For beam 0B0.7 the centre moment remains the same when increasing the load from 75% to the maximum, whilst hogging moment for beam 0B1.4 increases slightly. In both cases, the final moment curve sits above the elastic moment curve which demonstrates that moment redistribution has occurred. The fact that the hogging moment in both cases does not end up at the elastic moment shows that the moment capacity at the centre supports is limited, resulting in an increase in the moment resistance require in the sagging regions.

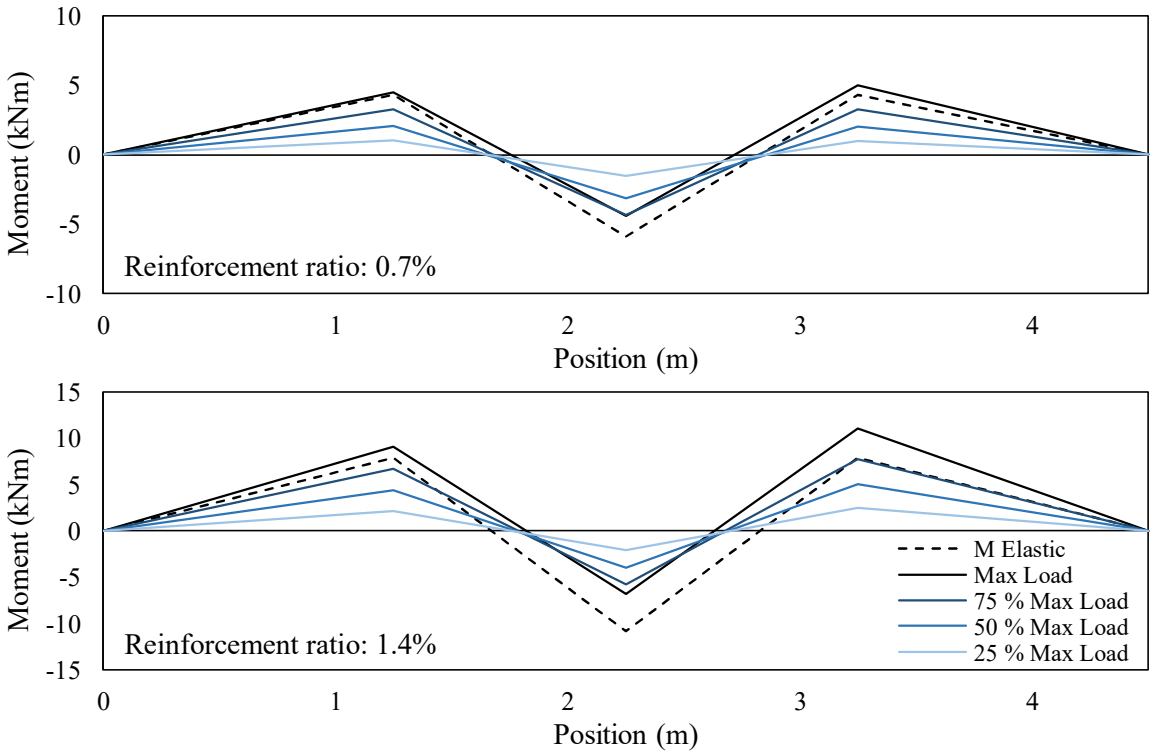

Figure 7-2: Moment diagram for beams with 0% fibres

7.2.2. 1 % FIBRE

Figure 7-3 shows the moment diagrams for beams with 1% fibres. The results are similar to the moment redistribution behaviour shown in the beams with no fibres. In all cases, the rate of increase of the hogging moment decreases nearing the maximum load. This behaviour is the opposite for the sagging moments which increase at an increasing rate as the moment is redistributed away from the centre support.

The behaviour of beam 1B0 with no reinforcing differs slightly from the rest in that the final hogging moment is less than the moment at 75% load. At this point excess rotation has occurred at the centre support so that the moment carrying capacity has been reduced. The test was conducted in deflection control, causing the applied load to reduce once the moment capacity at the centre support reduced, and therefore there was almost no moment redistribution towards the sagging moments since the applied load did not increase. Moment redistribution was evident in the other beams with reinforcing where the final moment curve sits above the elastic moment curve.

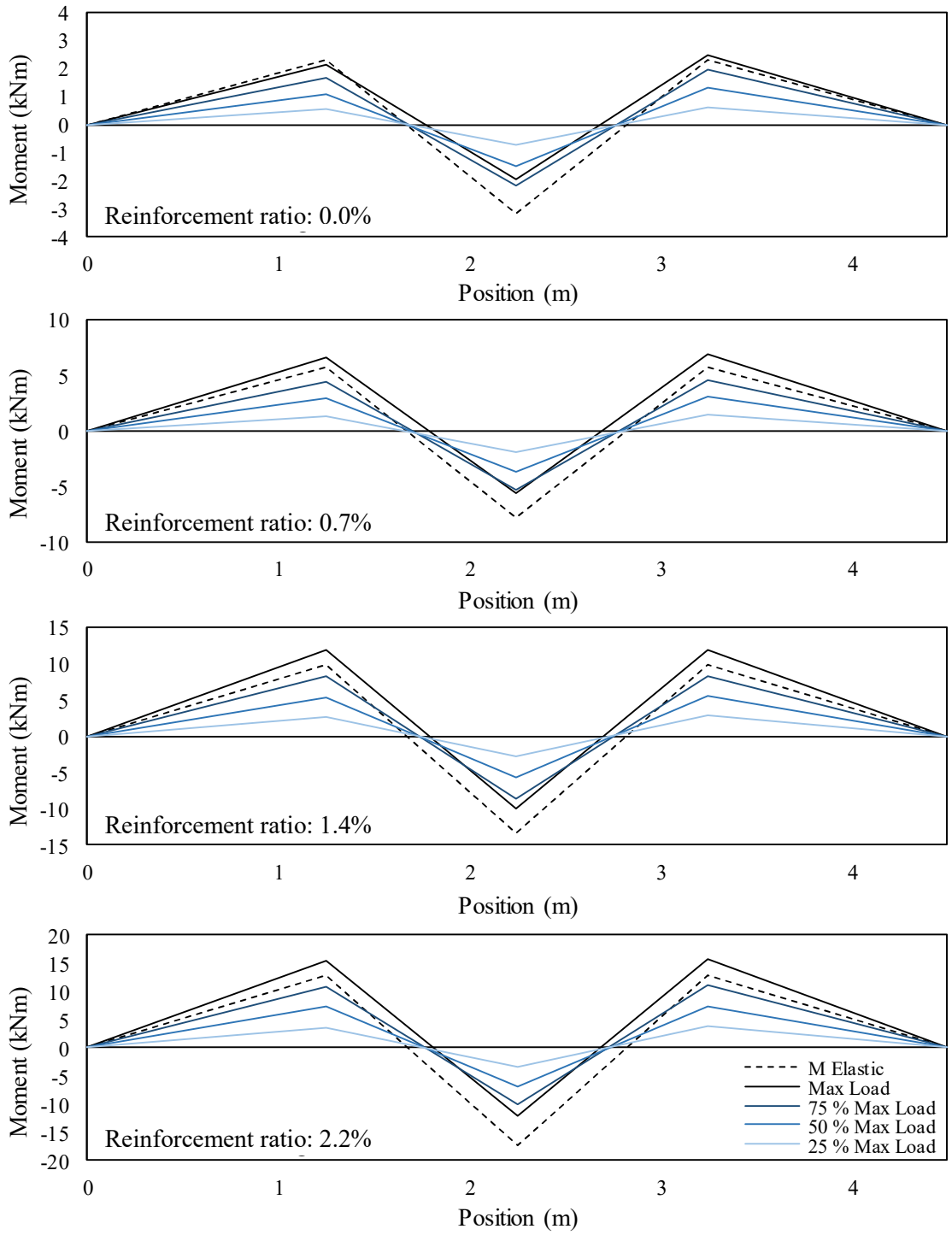

Figure 7-3: Moment diagram for beams with 1% fibres

7.2.3. 1.5 % FIBRE

Figure 7-4 shows the moment diagram for beams containing 1.5% fibres. A similar trend in results is evident in terms of the difference in behaviour between the beam with no reinforcing bars, and the remaining three beams with reinforcing. The bending moments illustrate the ability for moment redistribution to equalise the moments between the hogging and sagging moments.

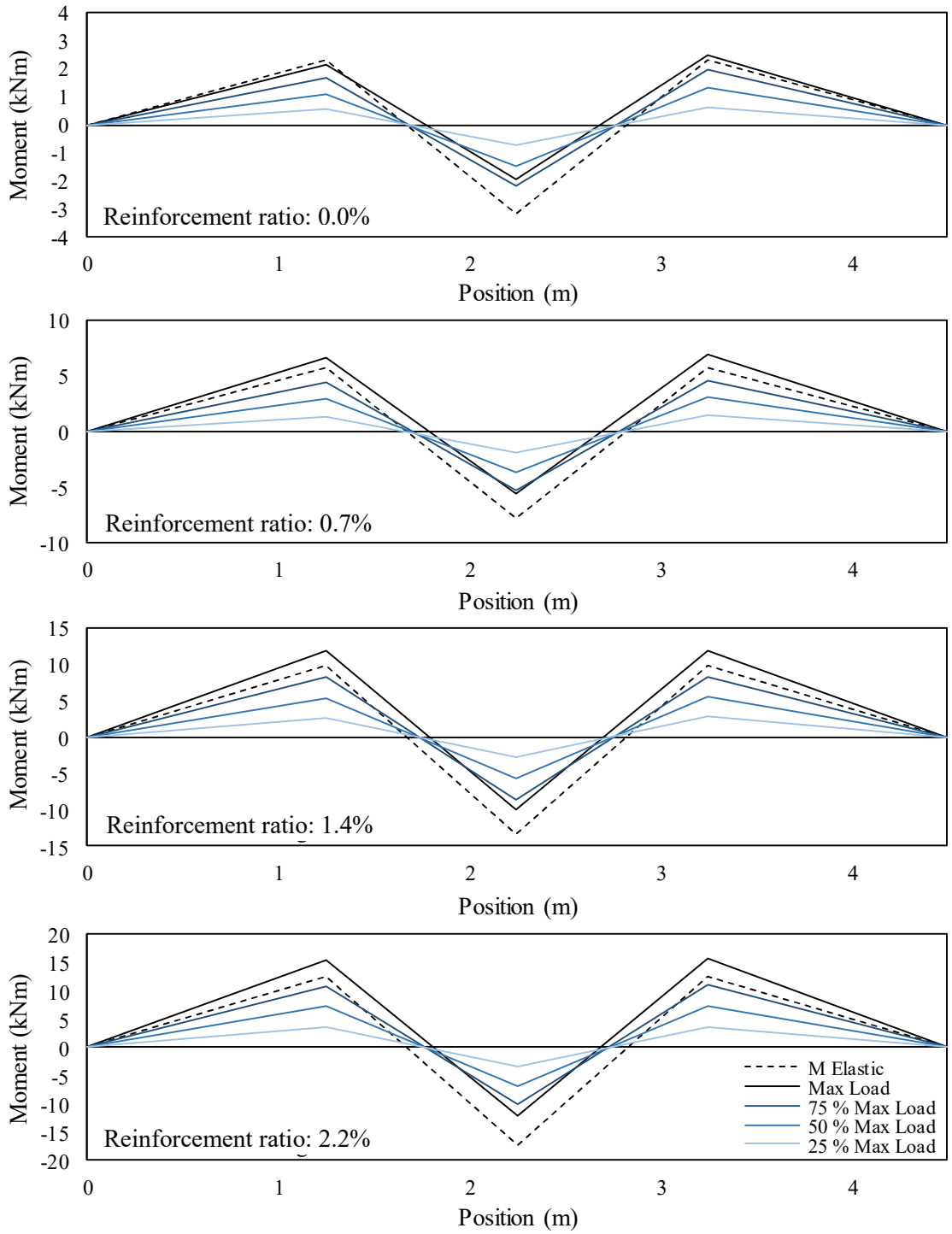

Figure 7-4: Moment diagram for beams with 1.5% fibres

7.2.4. 2 % FIBRE

Figure 7-5 shows the bending moment diagrams for beams with 2% fibres. Observations are similar to the results of beams with 1% and 1.5% fibres. A slight improvement is seen in beam 2B0 where the

final hogging moment is slightly larger than the moment at 75% maximum load, at which point the sagging moments are also higher than the elastic moments. Moment redistribution has therefore also occurred in the beam with only fibres.

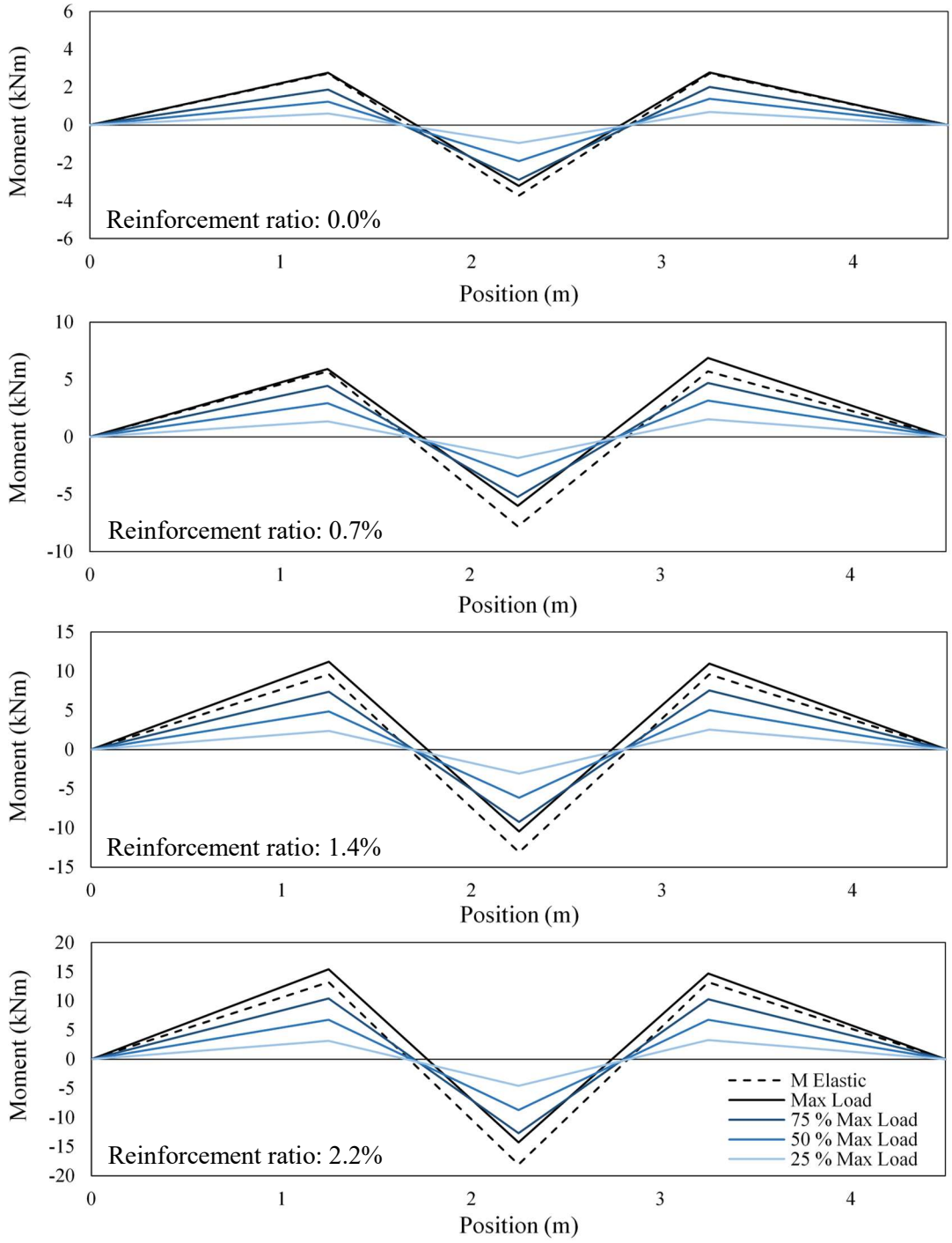

Figure 7-5: Moment diagram for beams with 2% fibres

7.3. MOMENT EVOLUTION WITH APPLIED LOAD

The bending moment diagrams revealed the distribution of moments across the beam at four distinct loading conditions where only the final moment curve was compared to the elastic moment. Plotting the moment evolution against the increase in applied load will provide further insight into the degree to which moment redistribution occurs and when it starts. Moment vs load graphs will be briefly discussed for each beam so that the reasoning for the final moment redistribution value given to each beam can be justified.

7.3.1. 0 % FIBRE

The change in moments with increasing load for beams with no fibres is shown in Figure 7-6. All moments are assigned positive values for ease of comparison. The hogging moments are expected to increase at a faster rate than the sagging moments until moment redistribution starts, whereafter the rate of increase in hogging moments should decrease and the sagging moments should increase at a faster rate. This behaviour is shown in beam 0B0.7 where the moments converge since the moment capacity of the three critical sections are the same. This behaviour is however not shown in the results of beam 0B1.4.

The elastic moments are included in the moment-load results. The hogging and sagging moments for beam 0B1.4 diverge from the elastic moments already at low loads. This behaviour is in line with the observations stated in literature in which redistribution of moments occurs after cracking due to the changes in the flexural stiffness. At higher loads, the rate of moment increase slows down for the hogging moment and increases for the sagging moments. This additional moment redistribution behaviour occurs once the steel has yielded and allows additional moments to be distributed from the hogging to the sagging region during the plastic behaviour. Differences in the ultimate moments may occur if the cover to the reinforcing bars is not the same or if full moment redistribution was not possible, thereby preventing the full moment capacity of all critical sections from being reached.

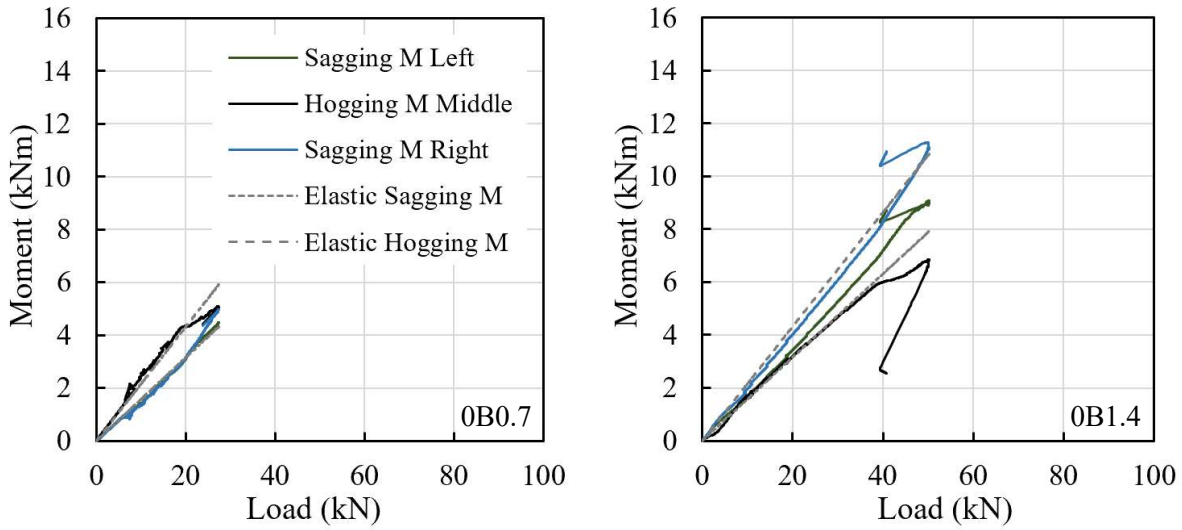

Figure 7-6: Moment vs load diagram for beams with 0% fibre

7.3.2. 1 % FIBRE

Figure 7-7 illustrates the moment-load results of the beams with 1% fibres. As discussed previously, the moment capacities at the critical sections had been designed to be the same. In the ideal case, the final moments (after moment redistribution) would be the same at the critical sections. The ability to achieve the full moment capacity at each critical section requires a certain rotational capacity at the hinge. If the plastic hinge is able to rotate whilst maintaining the moment resistance, further load can be applied to the structure which will be taken up by the external supports, and hence at the sagging moment regions. Structures with insufficient rotational capacity will limit the amount of moment redistribution possible.

The moment load-responses of beam 1B0 shows practically no moment redistribution. The gradients of the hogging and sagging curves do not change up to the maximum load. This behaviour was expected since the results of the FPBTs with 1% fibres showed the peak load to occur just before cracking. Although there was some residual strength, this strength never exceeded the cracking load strength.

The moment-load responses for the three remaining beams shows some degree of moment redistribution in the convergence of the moment values. Beam 1B1.4 follows an almost perfectly elastic response until moment redistribution occurs. Beam 1B0.7 diverges from the elastic moments early on but still shows moment redistribution at higher loads. Beam 1B2.2 reveals linear curves, however at different gradients to the elastic curves with moment redistribution occurring at higher loads. An increase in the reinforcing ratio leads to strain hardening behaviour which results in more cracks. A beam with more cracks will diverge more from the elastic curve due to the changes in the flexural stiffness. Furthermore, the

locations of the reinforcing may vary slightly, and the overlap of top and bottom reinforcing will result in varying flexural stiffness between different beams as well as along the length of each beam.

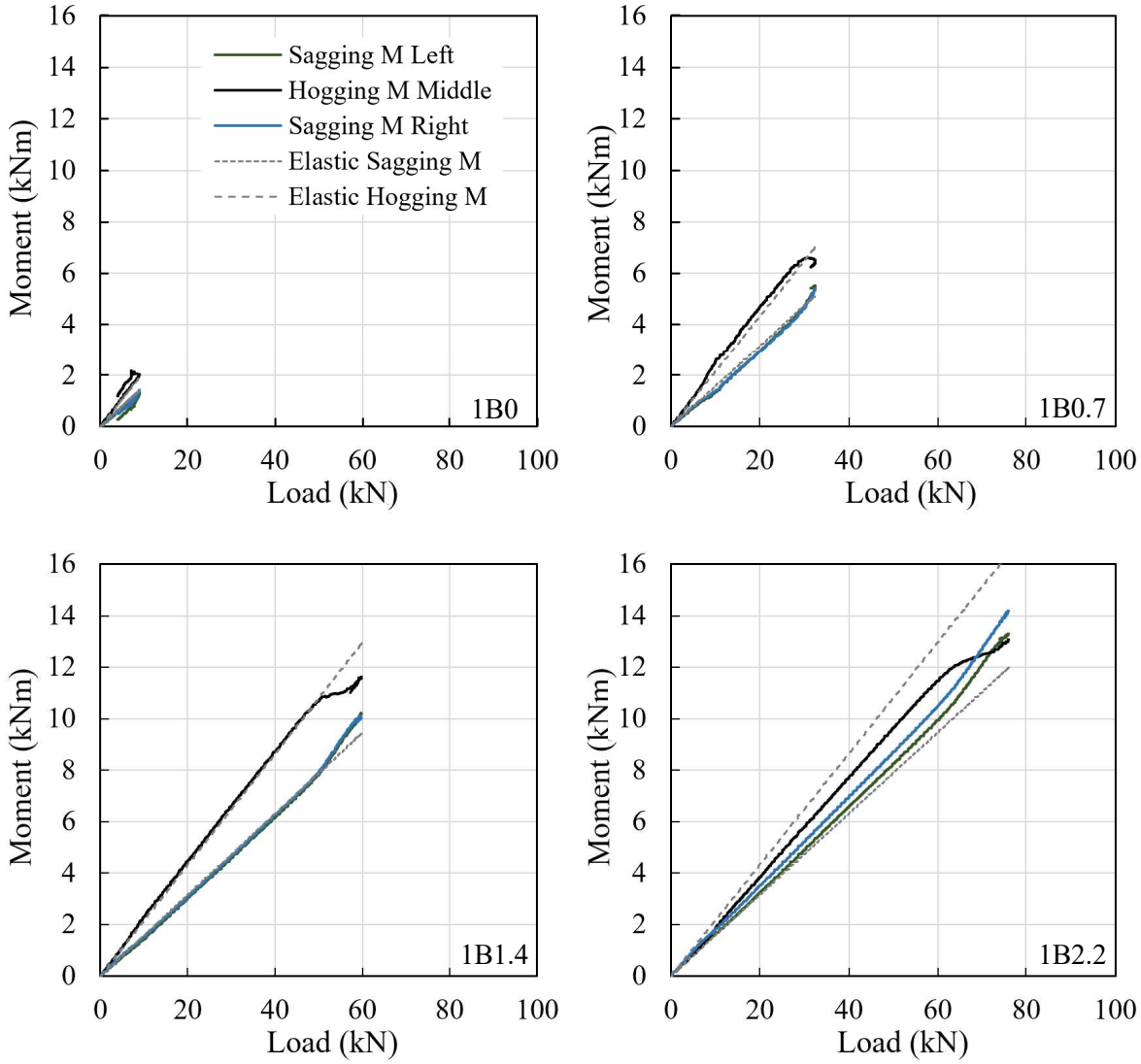

Figure 7-7: Moment vs load diagram for beams with 1% fibres

7.3.3. 1.5 % FIBRE

Figure 7-8 illustrates the moment-load responses of the beams with 1.5% fibres. Beam 1.5B0 shows a different response to the other three beams without reinforcing steel bars. The closest fit to the elastic moments is seen in beam 1.5B0.7. As a result, moment redistribution seems more evident once the steel yields than in beam 1.5B2.2. The change in moments for beam 1.5B2.2 at higher loads is less evident since a significant amount of elastic moment redistribution had already occurred at lower loads due to the formation of cracks.

The ultimate hogging moment is however further from the elastic moment in beam 1.5B2.2 than in beam 1.5B0.7 indicating more moment redistribution when compared against the elastic moments. The same can be said for the sagging moments. For all three beams containing reinforcing, the ultimate hogging and sagging moments diverge from the elastic moments with increasing amounts as the reinforcing ratio is increased. This trend suggests an increasing amount of moment redistribution. In comparison, when looking at just the changes in gradients of the moment curves it is more difficult to reach a conclusion since the shapes differ. For instance, beam 1.5B0.7 displays a greater change in moment gradients at the onset of steel yielding than beam 1.5B2.2. However, when looking at the ultimate moments in context with the elastic moments, beam 1.5B2.2 seems to have redistributed more moments.

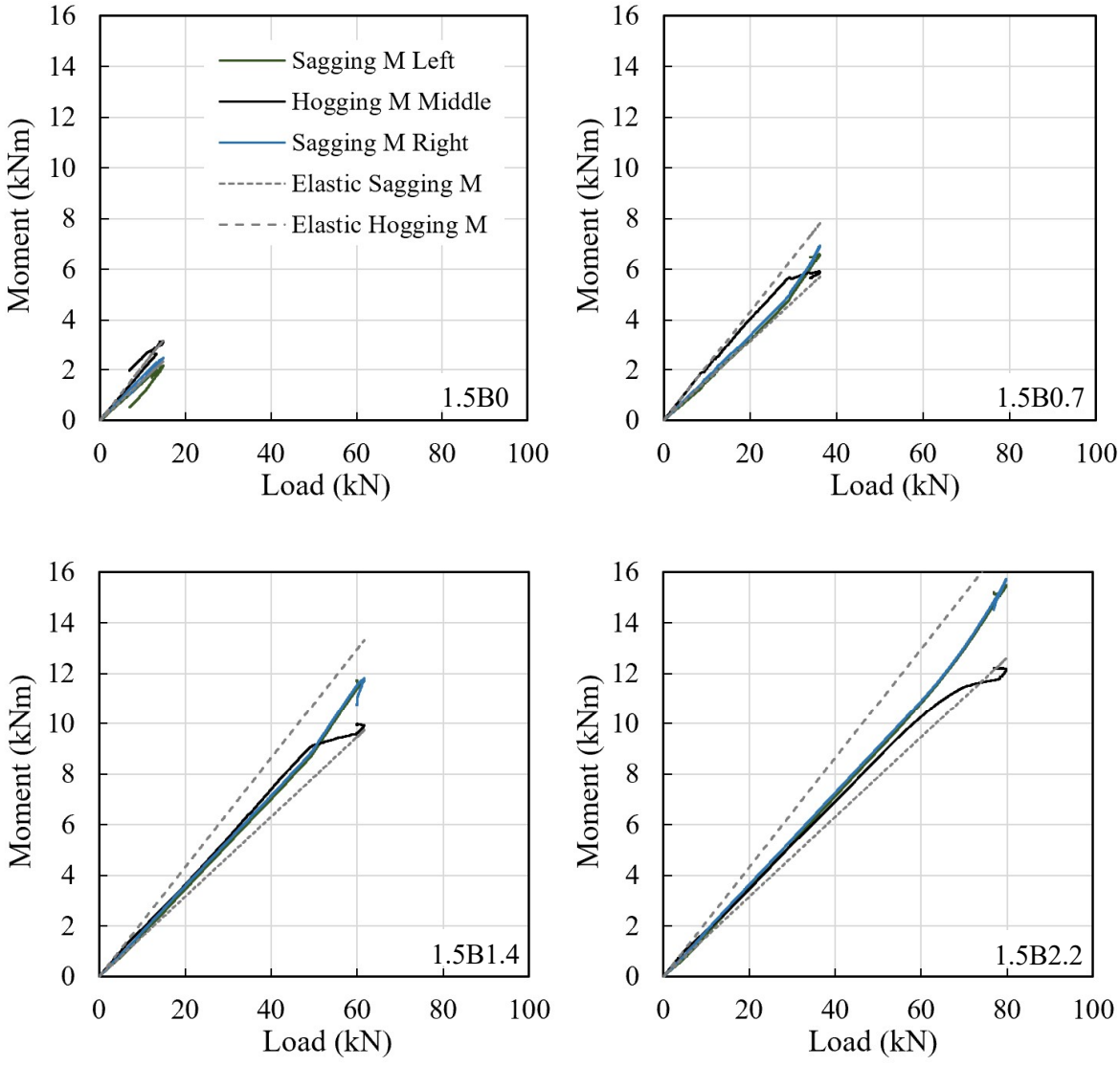

Figure 7-8: Moment vs load diagram for beams with 1.5% fibres

Moment redistribution values assigned to the beams must therefore be referenced in light of the moment-load responses of each beam along with the elastic moment-loads response.

7.3.4. 2 % FIBRE

Figure 7-9 demonstrates the moment-load responses of beams with 2% fibres. In these tests, the result of beam 2B0 with no reinforcing is beginning to show similarities in the shape of the moment-load response. Sufficient fibres are present in the beam to allow some degree of moment redistribution, albeit to a much lesser extent than the beams with steel bar reinforcing. In general, the shapes of the moment-load responses resemble those of the previous tests.

The fact that in some cases the ultimate sagging moments exceeded the ultimate hogging moments may be a result of a difference in the depth of the reinforcing at the centre support and under the load points. As a result, the ultimate moments of resistance would differ slightly between the hogging and sagging moments. The clearest indication of the change in flexural stiffness is seen in beam 2B2.2 where there is a change in slope at about 2 kNm due to cracking, followed by another change at around 14 kNm when the steel yields which corresponds to the three main stages of behavioural changes discussed in the literature.

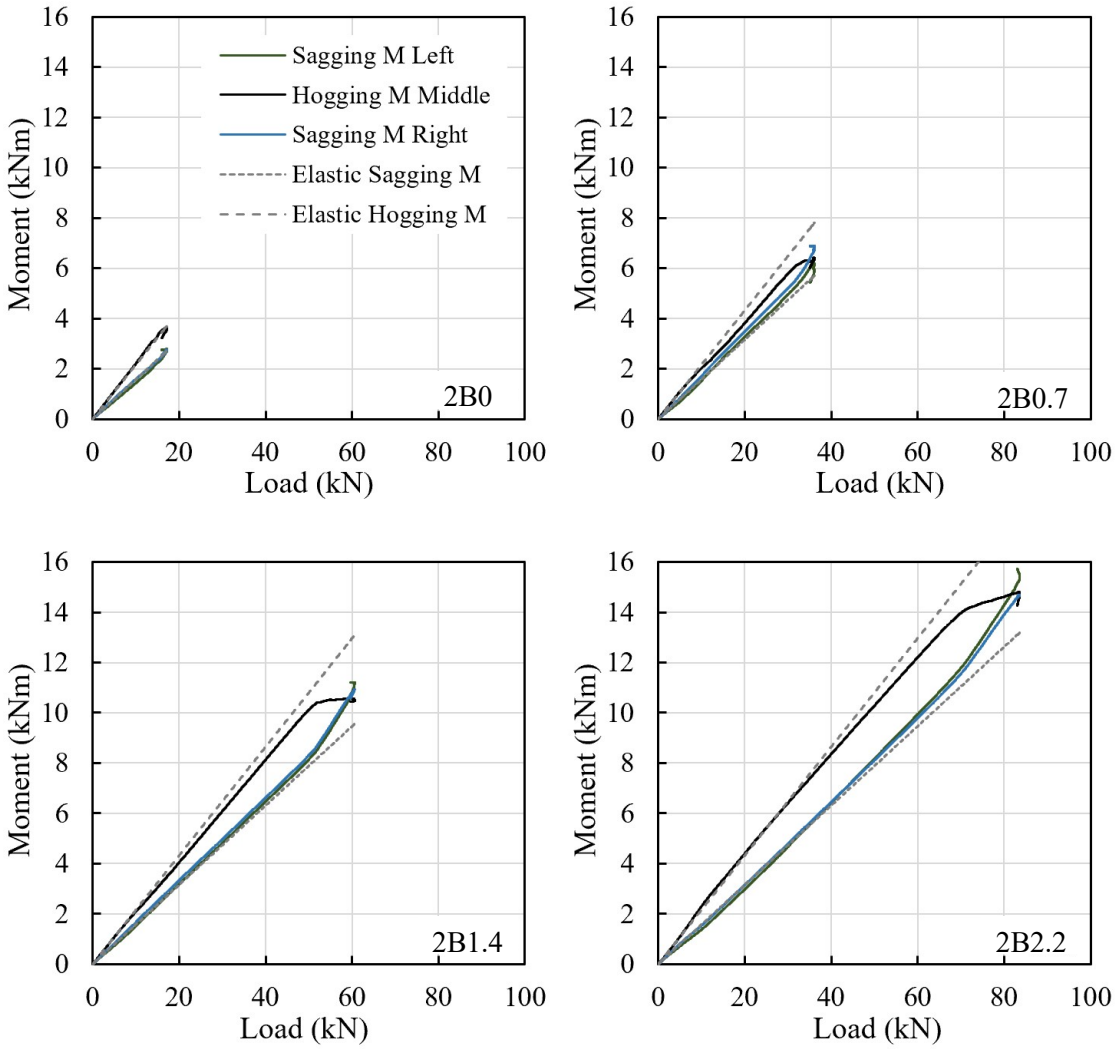

Figure 7-9: Moment vs load diagram for beams with 2% fibres.

7.4. MOMENT REDISTRIBUTION CALCULATIONS

Moment redistribution has been described by the moment-load responses. Ascribing a value to the degree of moment redistribution for each beam requires a comparison of the actual load to the elastic load. The actual moment is compared to the elastic moment, and the greater the difference, the greater the amount of moment redistribution. When using simplified bilinear material behaviour relationships, the actual and elastic moments should be the same until moment redistribution occurs, however as is now evident, there can be significant moment redistribution at relatively low loads.

The moment redistribution of each beam is shown where the moment redistribution percentage was calculated as follows:

$$MR\% = \frac{M_{exp} - M_{el}}{M_{el}} \qquad \textit{Equation 7.1}$$

Where M_{exp} and M_{el} are the moments obtained from the experiments and the calculated elastic moments respectively. In each case it can be observed that moment redistribution occurs at relatively low loads. This behaviour can be attributed to the formation of cracks which change the flexural rigidity of the beam. Furthermore, the elastic moments are calculated from the theoretical test setup discussed in Section 5.4.1 (Elastic Moments). These elastic moments are only valid if all supports are at the same level, and the loads are applied evenly which may be difficult to achieve in reality.

If the test setup differs from the setup used to calculate the elastic moments, Equation 6.1 would suggest that moment redistribution has occurred, which may not be true since the equations used to calculate the elastic moments may no longer be valid. For this reason, the loads at the three supports under the beam were checked before testing to ensure that the load distribution was similar to the assumed elastic moment distribution. If the weight of the beam was not distributed correctly across the supports, adjustments in the height of each support could be made until a close match to the theoretical support load ratios was achieved.

Consider the moment-load response of beam 2B1.4 (Figure 7-9). The moment redistribution, if calculated using Equation 6.1, will result in the response shown in Figure 7-10. Negative values indicate a reduction in moment, and positive values an increase in moment relative to the elastic moments. Moment redistribution described in this manner is evident at the onset of loading and remains constant until plastic moment redistribution occurs. Describing moment redistribution in this manner means that the structure is already redistributing moments during the elastic behaviour, followed by additional redistribution during plastic behaviour. This is true considering the fact that the flexural stiffness along the beam varies as cracks are introduced and the test setup will not be identical to the theoretical setup upon which the elastic moments are based.

Moment redistribution is usually considered to occur during plastic behaviour at the onset of steel yielding. This assumption suggests that no moment redistribution occurs during elastic behaviour and

redistribution only begins once the steel has yielded. However, this was not the case for many beams as discussed previously, where significant deviations from the elastic moments occurred immediately after cracking. As a result, a large proportion of moment redistribution occurred before the steel yielded, which may reduce the ability for further moment redistribution after steel yielding.

Describing moment redistribution and its contributing factors therefore requires more than simply comparing the final ultimate moments to the elastic moments. Figure 7-10 shows the evolution of moment redistribution as the load on the structure is increased. The moments varied before cracking at about 10 kN. Thereafter, the degree of moment redistribution remained consistent until the steel yielded at about 52 kN, at which point the majority of the additional load on the system was taken up by the sagging moment regions. The moment redistribution graphs for all beams can be found in Appendix B.

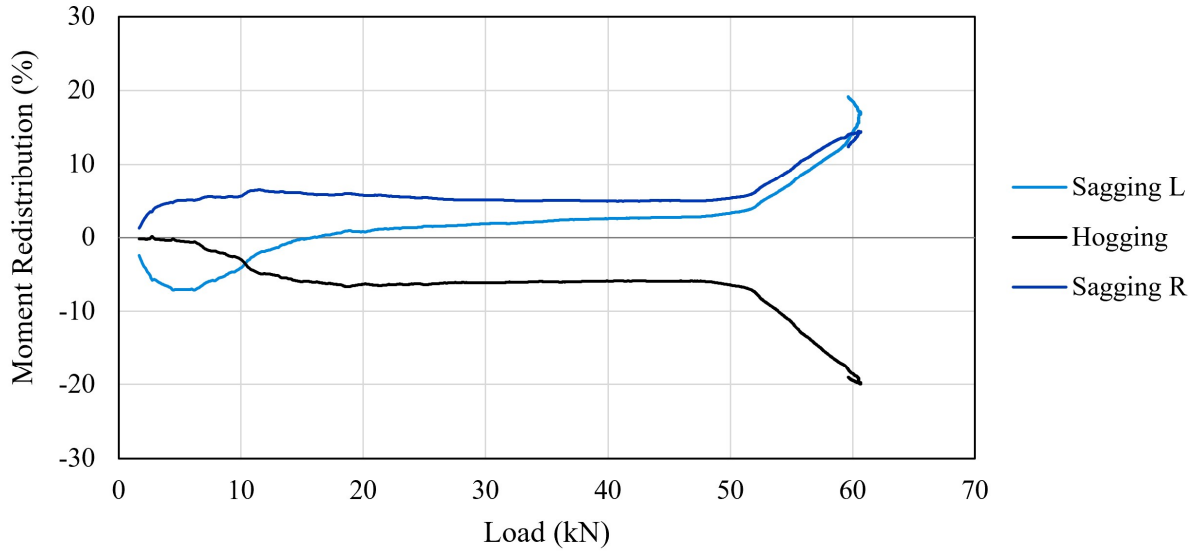

Figure 7-10: Moment redistribution of beam 2B1.4

The moment redistribution due to the yielding of the reinforcing bars can be isolated by adjusting the elastic moment-load relationship to match the experimental results as indicated in Figure 7-11. Plotting the actual moments against the newly defined moment gradients would result in the moment redistribution relationship shown in Figure 7-12. This relationship is more in line with the expected outcome of the simplified bilinear stress-strain relationships assumed in most design methods. The degree of moment redistribution therefore depends upon a combination of elastic and plastic moment redistribution.

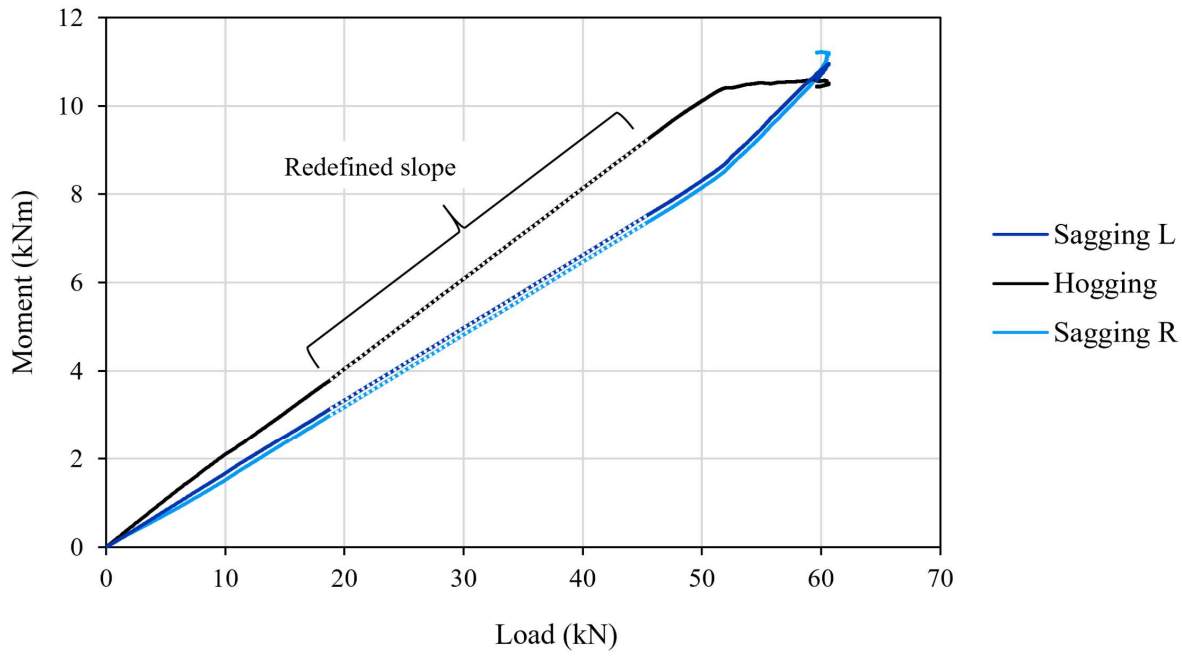

Figure 7-11: Newly defined elastic moment gradients of beam 2B1.4

It is evident that a certain degree of moment redistribution occurred after cracking in almost all beams, followed by further moment redistribution once the reinforcing bars had yielded. The trends observed across all tests may provide insight as to the effects of the different steel fibre and reinforcing bar combinations.

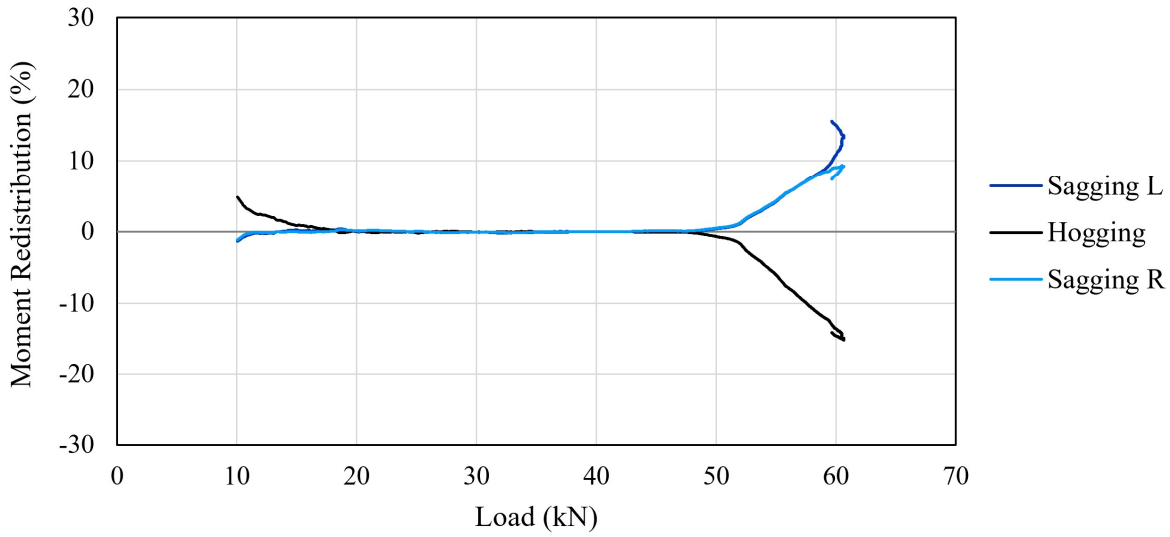

Figure 7-12: Plastic moment redistribution of beam 2B1.4

7.5. MOMENT REDISTRIBUTION RESULTS OF ALL BEAMS

The moment redistribution results from both methods described previously will now be presented. The results for beam 0B1.4 had to be omitted in addition to the results of 0B2.2 as both beams failed in a brittle manner as a result of insufficient concrete compaction. Initial observations for the amount of moment redistribution indicated in Figure 7-13 point towards an optimum steel fibre content of 1.5%. This optimum agrees with previous findings discussed in the load-related results in which optimum fibre contents were seen at 1.5%. Beams containing 2.0% fibres were generally able to redistribute more moments than beams containing 1.0% fibres. Another general trend was observed that when increasing the reinforcing ratio, the amount of moment redistribution increased. The exception to this trend was when combining the reinforcing bars with 2.0% steel fibres.

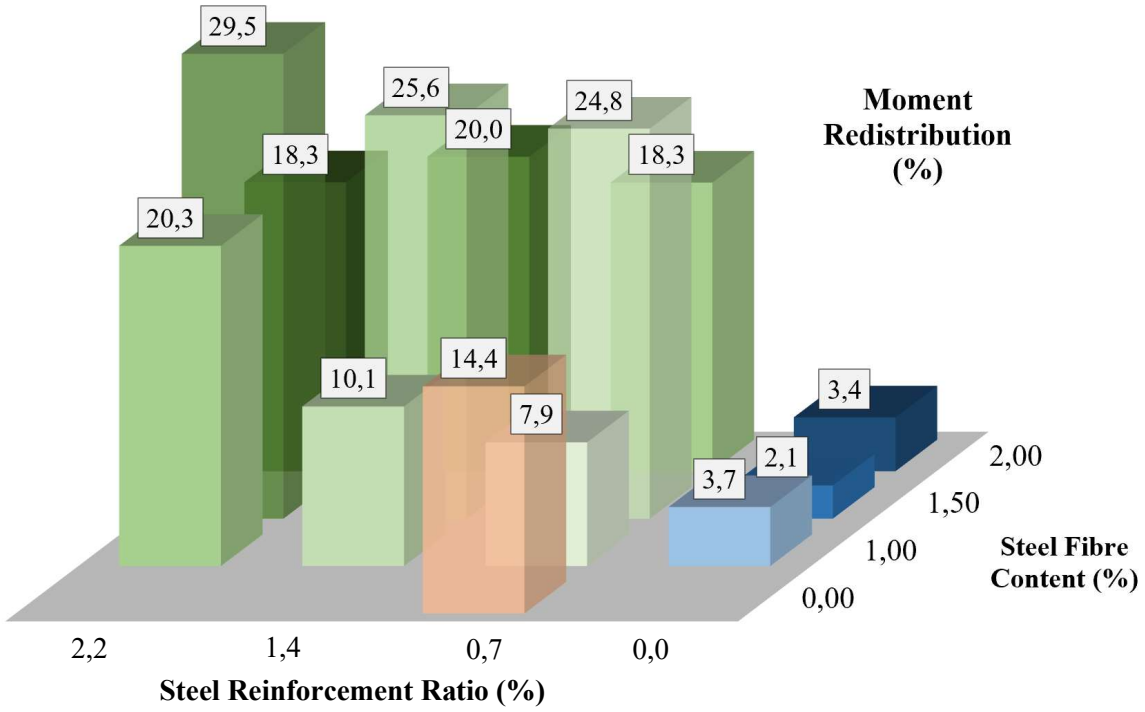

Figure 7-13: Moment redistribution compared to original elastic moments

The difficulty lies in explaining these trends in terms of the structural and material behaviours. A number of material and structural factors are involved in the outcome of these results. In the simplest form, moment redistribution requires a material to form a plastic hinge by maintaining a moment capacity at the hinge whilst being able to rotate. The degree to which this hinge can rotate whilst still maintaining its moment capacity will determine how much additional load the structure can carry before the hinge can no longer rotate without loss in moment capacity, or until enough hinges have formed in adjacent critical spans to form a collapse mechanism.

It is thus evident that material ductility is a major factor since a more ductile material would warrant greater rotations in the hinge. However, the reinforcing bars tested showed strain hardening properties which caused more cracks to form in the beams with more reinforcing bars. This in turn means that the plastic hinge lengths of the beams differ and that the ability of the steel fibres to contribute towards tensile resistance changes since the number of cracks and crack spacing changes.

As an example, it has been shown that the contribution of steel fibres in terms of load capacity are much lower than that of the steel reinforcing bars. The impact of steel fibres is therefore expected to diminish as the reinforcing ratio increases. However, as the reinforcing ratio increased, the number of cracks increased due to strain hardening. The increased number of cracks, combined with longer plastic hinge lengths resulted in smaller strains in each crack, and hence the fibres were still able to bridge the cracks as opposed to a single large crack forming.

The amount of moment redistribution for all beams caused by the yielding of the reinforcing bars is shown in Figure 7-14. The results paint a very different picture in terms of optimum reinforcing bar and steel fibre combinations. For beams with a reinforcing ratio of 0.7%, there is again an optimum fibre content of 1.5%. However, for a reinforcing ratio of 1.4% and 2.2%, there is an improvement in moment redistribution as the fibre content is increased to 2.0%. The change in optimum fibre content for different reinforcing ratios is a result of the change in structural behaviour caused by the strain hardening effects of the reinforcing bars.

For beams with a reinforcing ratio of 2.2%, changes in fibre content did not amount to any significant changes in moment redistribution. This result is expected since the moment redistribution results presented here are at the onset of steel yielding, and therefore the contribution of the steel fibres is minimised particularly at high reinforcing contents. Decreasing the reinforcing ratio resulted in the fibres playing a greater role since the forces on the structure were reduced allowing the fibres to play a relatively greater role.

The beams with only fibres showed a clear increase in moment redistribution as the amount of fibres increased to 2.0% which is more in line with the observations made during the experiments. The behaviour of the fibres therefore changed when combined with reinforcing bars. Due to the low strength of the fibres, beams with only fibres required 2.0% fibres to redistribute some moments. However, when combined with a reinforcing ratio of 0.7%, greater moment redistribution is achieved with only 1.5% fibres.

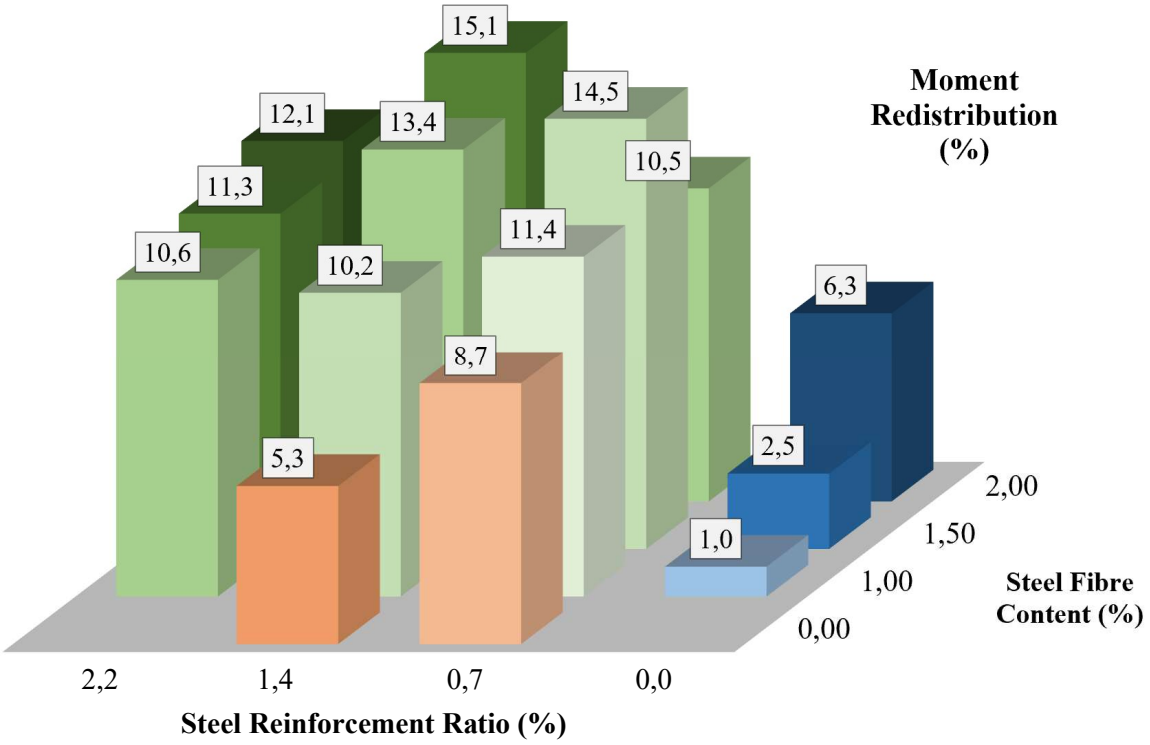

Figure 7-14: Moment redistribution compared to new elastic moments

The optimum combination for moment redistribution at the onset of yielding therefore seems to be with a reinforcing ratio of 1.4% and 2.0% fibres. An increase in the reinforcing ratio resulted in less moment redistribution, which may be due to over reinforcing, leading to less ductile behaviour. Reducing the reinforcing to one bar resulted in less moment redistribution, unless the fibre content was reduced to 1.5% which resulted in only a slight decrease. In general, reducing the fibre content reduced the amount of moment redistribution described in this manner.

It is obvious that finding an optimum fibre and reinforcing bar combination is a complex procedure as the factors affecting moment redistribution are all linked to one another and as such one cannot merely combine the optimum reinforcing ratio with the optimum fibre content and expect the combination of the two to be an improvement. Moment curvature behaviour can provide some insight as to how a structure will deform as the moment is increased. The closer the moment curvature shape is to the ideal bilinear shape, the larger the expected amount of possible moment redistribution.

7.6. FLEXURAL STIFFNESS

The gradient of the hogging moment-load graph illustrated in Figure 7-11 represents a near constant rate of moment increase due to a near constant flexural stiffness. After cracking, the neutral axis depth of the critical sections stabilises and increases only slightly as the moment increases, which translates

to a relatively constant stiffness. This slope of each beam is compared to the corresponding increase in relative load and is shown in Figure 7-15.

The results of only the beams containing a combination of both steel fibres and reinforcing bars are considered. An increase in slope value indicates a greater stiffness, and a lower deviation in from the elastic moments. These results indicate how moment redistribution, if defined as the ratio between ultimate and elastic moments, is affected by the deviations from elastic behaviour after cracking. Flatter slopes (lower values) deviate more from the elastic curve and therefore showed greater moment redistribution as shown in Figure 7-13.

A decrease in moment redistribution is seen as the slope of the hogging moment-load curve increases. In other words, moment redistribution is less effective when the slope of the hogging moment-load curve is steeper. In essence beams with greater stiffness after cracking resulted in less moment redistribution.

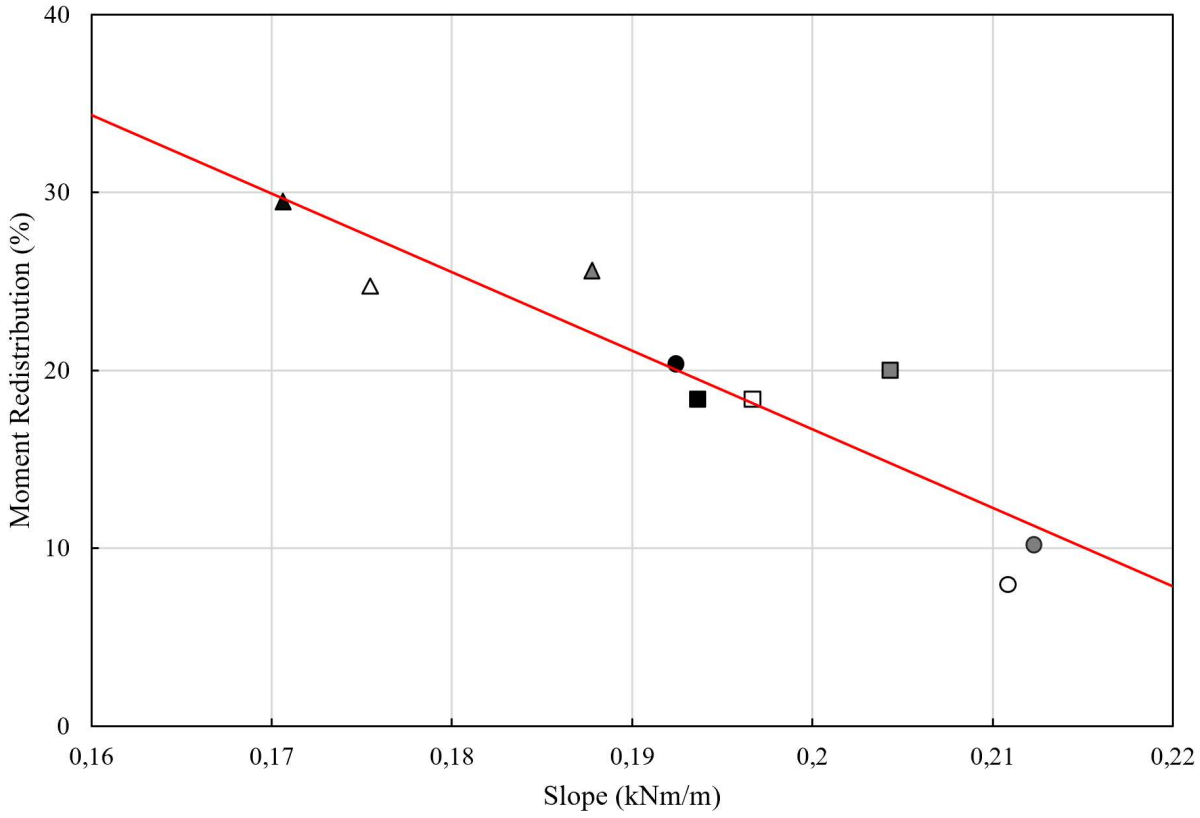

Figure 7-15: Moment redistribution compared against moment-load slope after cracking

7.7. INCREASE IN LOAD CAPACITY DUE TO MOMENT REDISTRIBUTION

Although the following results are load related, they are only discussed here as a comparison to the previously discussed moment redistribution results calculated in terms of moments. The alternative perspective is to observe the increase in load carrying capacity of the structure beyond the yield strength of the critical section. In design, the ultimate load capacity is taken at the point where the yield strength of the steel reinforcing is reached. However, in a statically indeterminate structure once this yield strength has been reached, a hinge can form, and additional load can be applied to the structure. This increase in load capacity of the structure beyond the critical load at which the first section reaches its ultimate moment capacity is possible only in indeterminate structures and is possible if plastic hinges can form with sufficient rotational capacity as well as having suitable moment curvature characteristics.

The effect of the different combinations of reinforcing will now be discussed in terms of the additional loads the structure was able to carry after yielding had occurred in the first critical section. Figure 7-16 represents an example of the changes in load capacity and the strains recorded for the deflection-controlled test. A clear change in behaviour occurred when yielding occurred at the hogging section followed by another change when yielding occurs in the remaining sagging sections. The changes in load curve correspond to the changes in moment observed in all moment-load graphs discussed previously.

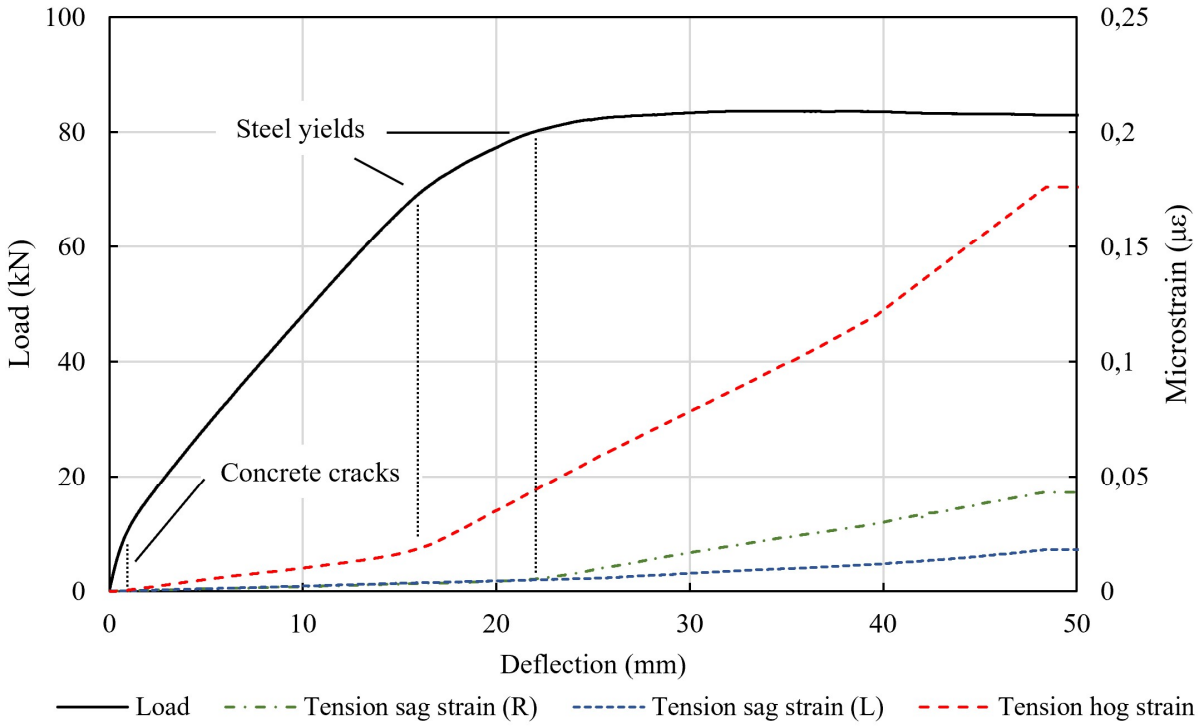

Figure 7-16: Load and strain results of beam 2B2.2

Calculating the relative differences in the maximum load and the load at first yielding for all beams results in the trends shown in Figure 7-17. Similar trends are observed when comparing beams across different fibre contents as for the moment redistribution graphs. Beams with 1.5% fibres show the greatest relative increase in load at any reinforcing ratio. A slight increase in additional load capacity is obtained across any fibre content as the reinforcing ratio is increased. Adding 1.5% fibres to any beam containing reinforcing bars therefore seemingly provides the most improvement in additional load carrying capacity. This behaviour is also evident in the beams containing only steel fibres.

Fibre contents of 1.0% and 2.0% appear to reduce the increase in load capacity when comparing beams with a reinforcing ratio of 0.7%. However, since only one beam without any fibres showed reliable results conclusions between the difference in behaviour are not conclusive. It is also clear that the fibres alone are less effective than when combined with steel reinforcing. For high reinforcing contents of 1.5% fibres or more combined with two or more reinforcing bars little improvements can be observed. An optimum total steel content seems to exist beyond which additional steel can no longer reach its full tensile potential.

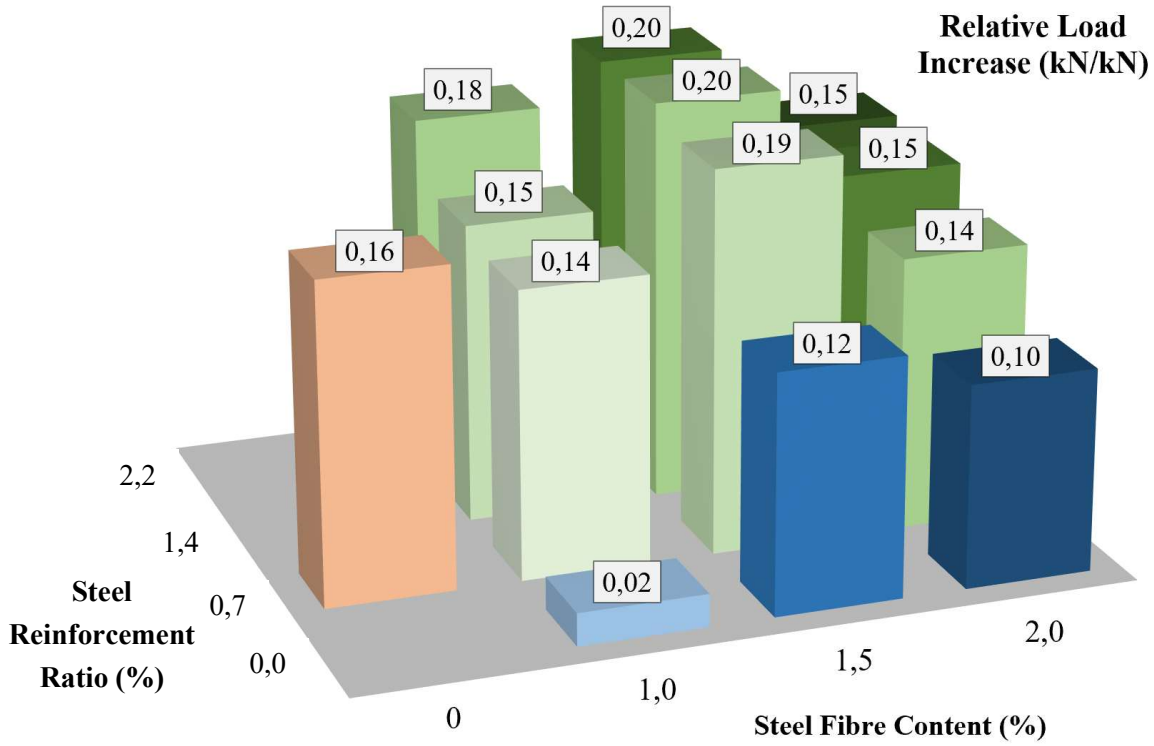

Figure 7-17: Relative increase in load after steel yielding

7.8. THEORETICAL MOMENT CURVATURE

Various aspects of structural performance have been discussed in the results of the indeterminate beam tests. The difference in behaviour between steel fibres and reinforcing bars has been highlighted and compared to the combined effect. For these tests, the reinforcing bars overshadowed the behaviour of the steel fibres particularly at high reinforcing contents owing to the higher tensile strength of the reinforcing bars when compared to the specific fibres used.

The material properties of the two reinforcing types however provide an indication as to the expected structural performance. For the fibres, an optimum moment curvature shape was discussed, where a flatter slope after the peak moment would benefit moment redistribution capabilities. The same concept applies to the ideal bilinear moment curvature slope of reinforcing steel bars. Although it is difficult to accurately define moment curvature when considering the effects of the width across which the curvature was measured, the relationship still provides a good behavioural indicator towards the possible moment redistribution capabilities. Differences between the theoretical and actual moment curvature trends are expected if there is a change in plastic hinge length or number of cracks, or if less than the full strength of steel fibres is utilised.

The method of calculation discussed in Chapter 3 is used to determine the theoretical moment curvature relationships of all fifteen beams. Figure 7-18 indicates the compressive and tensile stress-strain relationships used for the steel fibres, concrete and steel bars. The stresses for the steel fibres and reinforcing bars are plotted on separate axes due to the large difference in stresses.

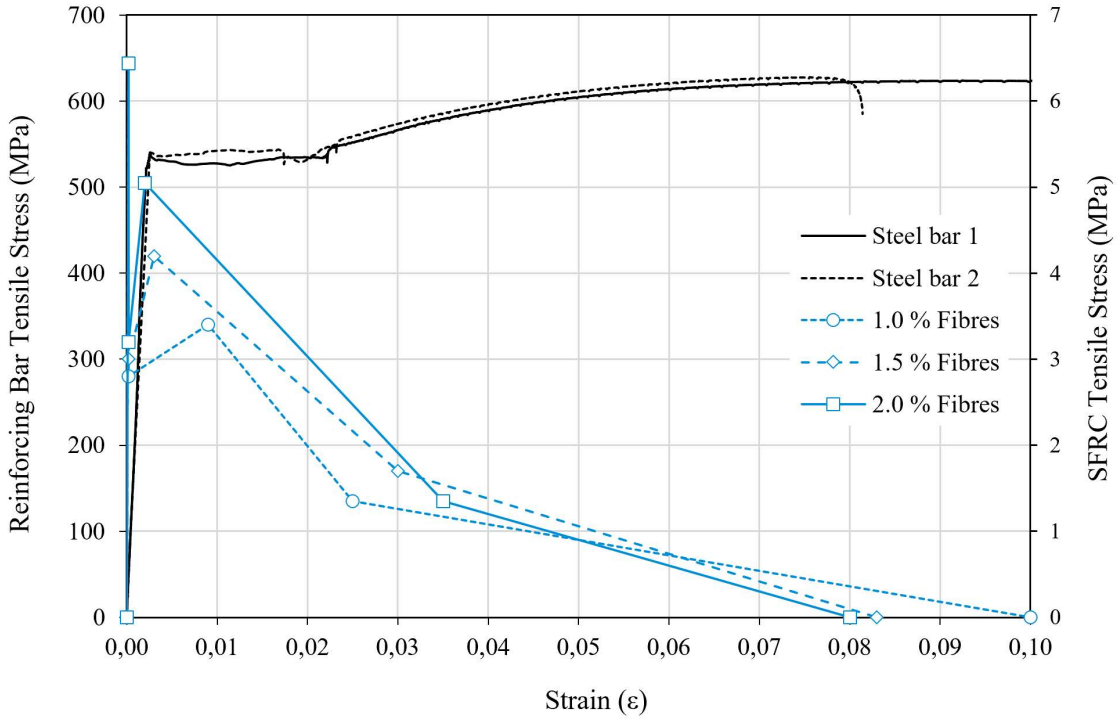

Figure 7-18 Stress-strain relationships

It is evident that there is a rapid decrease in stresses after the peak stress is reached in the steel fibres. This behaviour is in contrast to the strain hardening behaviour shown by the reinforcing bars at strains shortly after the rapid decrease in steel fibre residual strength. By the time the strains have been reached where the bars begin to show a second increase in stress capacity at about 0.02 ε, the steel fibres have already lost almost 50% of their residual strength capacity. The short length of the fibres limits the crack bridging ability of the fibres whereas the bars are able to elongate across much wider cracks.

The benefit of the fibres is more evident at lower strains, which is shown in Figure 7-19. The decrease in strength capacity after the peak residual stress has been reached is most severe for the concrete containing 2.0% fibres. One would expect the fibres to perform better than the reinforcing at low deflections, which was seen when looking at the slope of the load deflection curves at low deflections. In beams with both fibres and bars, the fibres are not expected to provide much additional tensile resistance at large deflections when the strains are high.

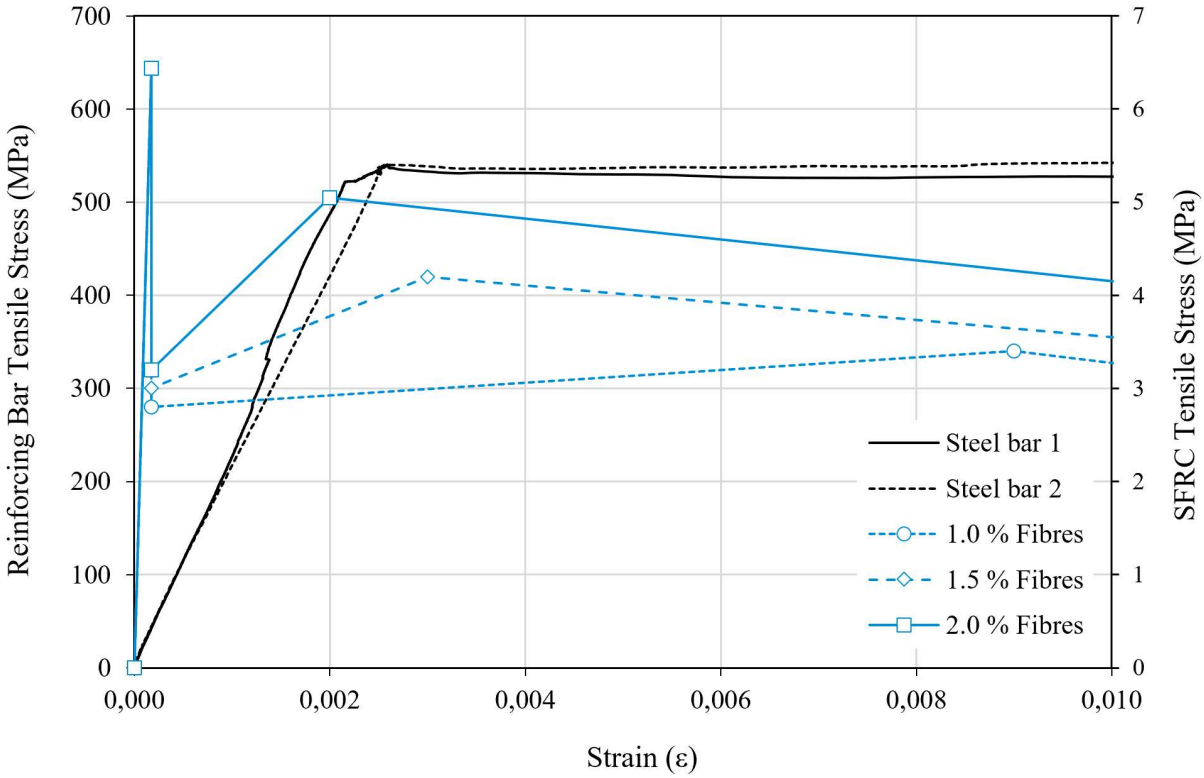

Figure 7-19: Stress-strain relationships at low strains

The moment curvature relationships for each of the fifteen beams are shown in Figure 7-20, with key stress-strain points indicated as shown in Figure 7-21. Moment curvature relationships of beams with both fibres and reinforcing bars are based on the assumption that the full tensile resistance of the fibres and reinforcing bars is utilised. Furthermore, the moment curvature relationships are based purely on the stress-strain properties and therefore only include the cross-sectional behaviour across one crack.

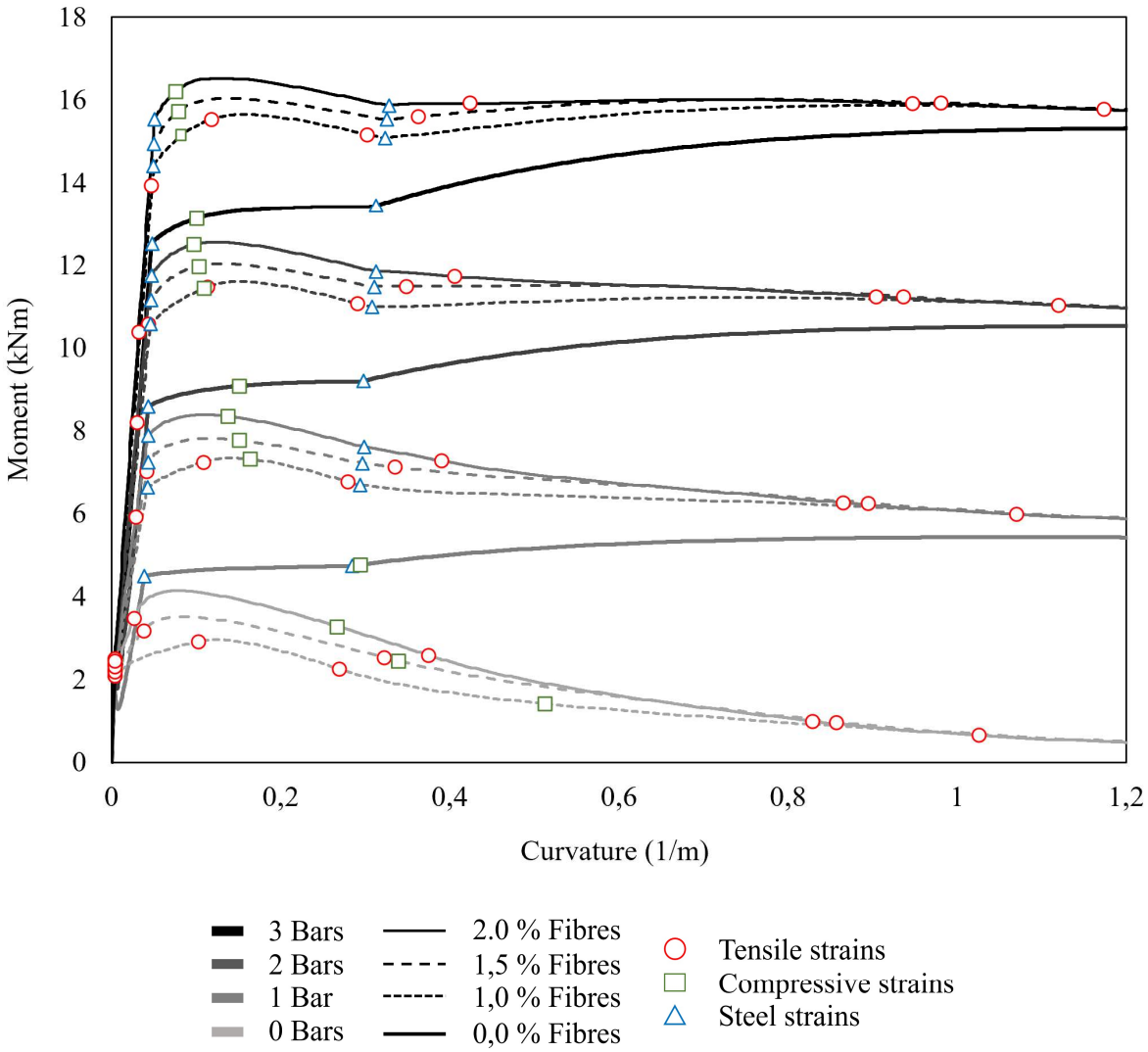

Figure 7-20: Theoretical moment curvature relationships

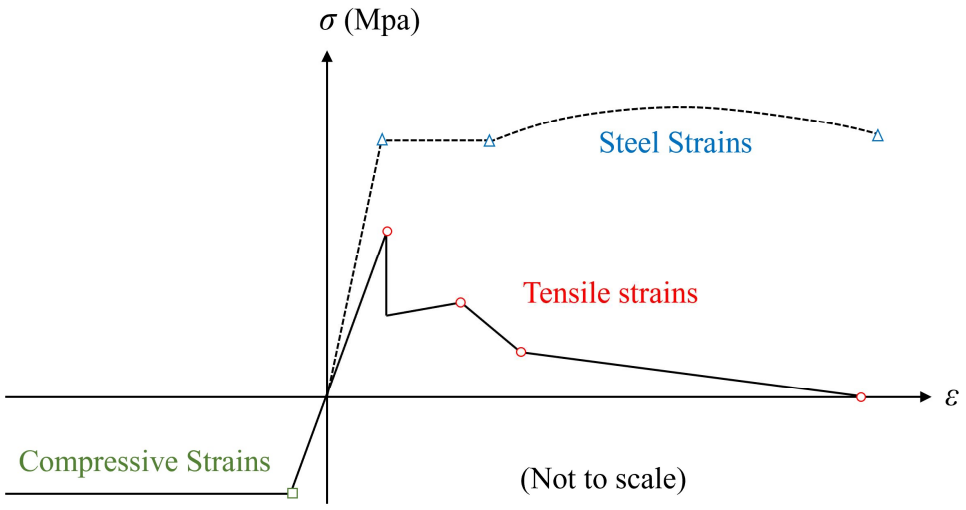

Figure 7-21: Key points in the moment curvature calculations

The actual moment curvature of the beam measured across the plastic hinge will therefore differ since it may include more than one crack. However, the theoretical moment curvature shapes are valuable in explaining the concept of an optimum combination of reinforcing bars and fibres when moment redistribution is required.

The moment curvature relationships of the beams with no fibres show similar shapes in Figure 7-20, with an increase in strain hardening behaviour seen with an increase in the reinforcing ratio. Compressive strains are modelled as bilinear, since the concrete strength was high in comparison to the tensile strength of the reinforcing bars and fibres. Compressive strains were therefore expected to be small and it is shown in Figure 7-20 that the limit of elasticity (0.0022 $\mu\varepsilon$) is only reached before the maximum moment in beams with three reinforcing bars. Although the compressive strains increase after the peak moment has been reached, the increase is minimal as the moments do not increase much beyond this point. A simplified bilinear shape was therefore chosen, since the impact of modelling a softening concrete compressive strain was minimal due to the high strength of the concrete.

The shape of the moment curvature relationships representing beams with only fibres are the same as what was observed in the FPBTs, apart from the magnitude which is doubled due to the width increase from 100 mm to 200 mm. A softening shape is observed instead of the hardening shape as shown by the reinforcing bars. The moment capacity of the beam with 2% fibres is almost as high as the moment capacity as that of the beam with one reinforcing bar even though it was shown that the load capacity of the beam with one reinforcing bar was roughly double that of the beam with only 2% fibres. These differences are evidence of moment redistribution, where almost no additional load capacity was possible in the beam with only fibres.

Beams with fibres alone are unable to redistribute moments since once the peak moment has been reached, further deformation leads to a loss in moment capacity. The structure is therefore unable to carry additional loads once the load capacity of the first section has been reached. Beams with reinforcing are able to deform whilst maintaining the moment, and even increasing the moment of resistance with further deformation. However, if moment redistribution is required, the ideal behaviour would be a bilinear curve where a plateau is reached after the peak moment. In this ideal case, once the peak moment capacity has been reached in the critical section, all further loading is transferred to the remaining critical sections. For the beams with reinforcing bars, not all additional load is transferred away from the first critical section since some additional load can be carried due to the strain hardening behaviour. As a result, the redistribution of moments occurs at a slower rate when increasing the load on the structure than for the ideal bilinear shape.

The curves of the beams in Figure 7-20 with a combination of fibres and reinforcing bars show an increasingly flatter post peak moment gradient with an increase in reinforcing bars. These results however assume that the behaviour of the beam with a combination of fibres and reinforcing bars is equal to the sum of the individual behaviours. This can be seen by the change in the shape of the moment curvature relationship when going from only reinforcing bars to adding steel fibres. The contribution of the steel fibres is essentially added on top of the curve with only reinforcing bars.

Figure 7-22 shows the effect of the higher stress of the fibres than for reinforcing bars at low strains. Immediately after cracking, the beams with no fibres show a dip in the curve where an increase in curvature is required before the same moment of resistance is reached again. Adding as little as 1% steel fibres reduces this dip in the curve which translates to less deflection in the structure after cracking. This behaviour was observed in the beams with an improvement in the load deflection behaviour at lower loads.

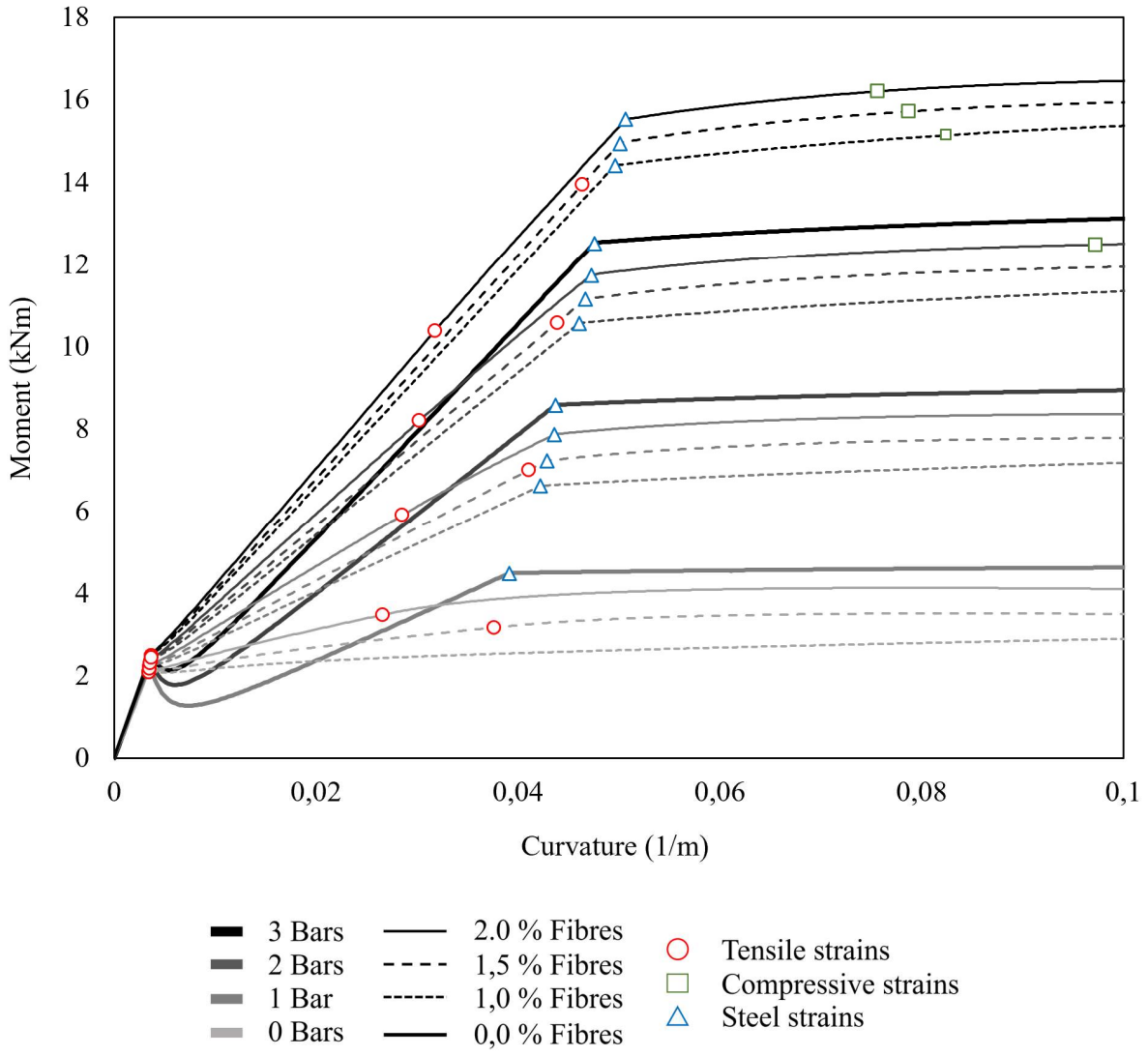

Figure 7-22: Theoretical moment curvature relationships for small curvatures

The neutral axis depths were also calculated and plotted against the ultimate moments in Figure 7-23. Each curve is plotted up to the maximum moment, since the peak moment of the hogging critical section coincided with the ultimate load on the structure. The neutral axis depth reduced rapidly when the cracking moment was reached. In beams with only fibres there was not much strength gain as the neutral axis depth reduced. In contrast, the neutral axis of beams with only reinforcing bars begins to stabilise after the sudden drop. The moment then increases whilst the neutral axis remains almost constant, until the yield point of the steel is reached. Once the steel yields, there is another drop in the neutral axis, which represents the point at which the plastic hinge forms and rotations occur which allow moment redistribution to take place. Owing to the strain hardening stress-strain shape of the reinforcing bars, there is another increase in strength following this drop in the neutral axis. In reality the curve after the steel has yielded will show a smoother change leading to the ultimate moment instead of the two different slopes as seen in Figure 7-23. The reason for this is simply that the stress-strain responses of the materials have been simplified.

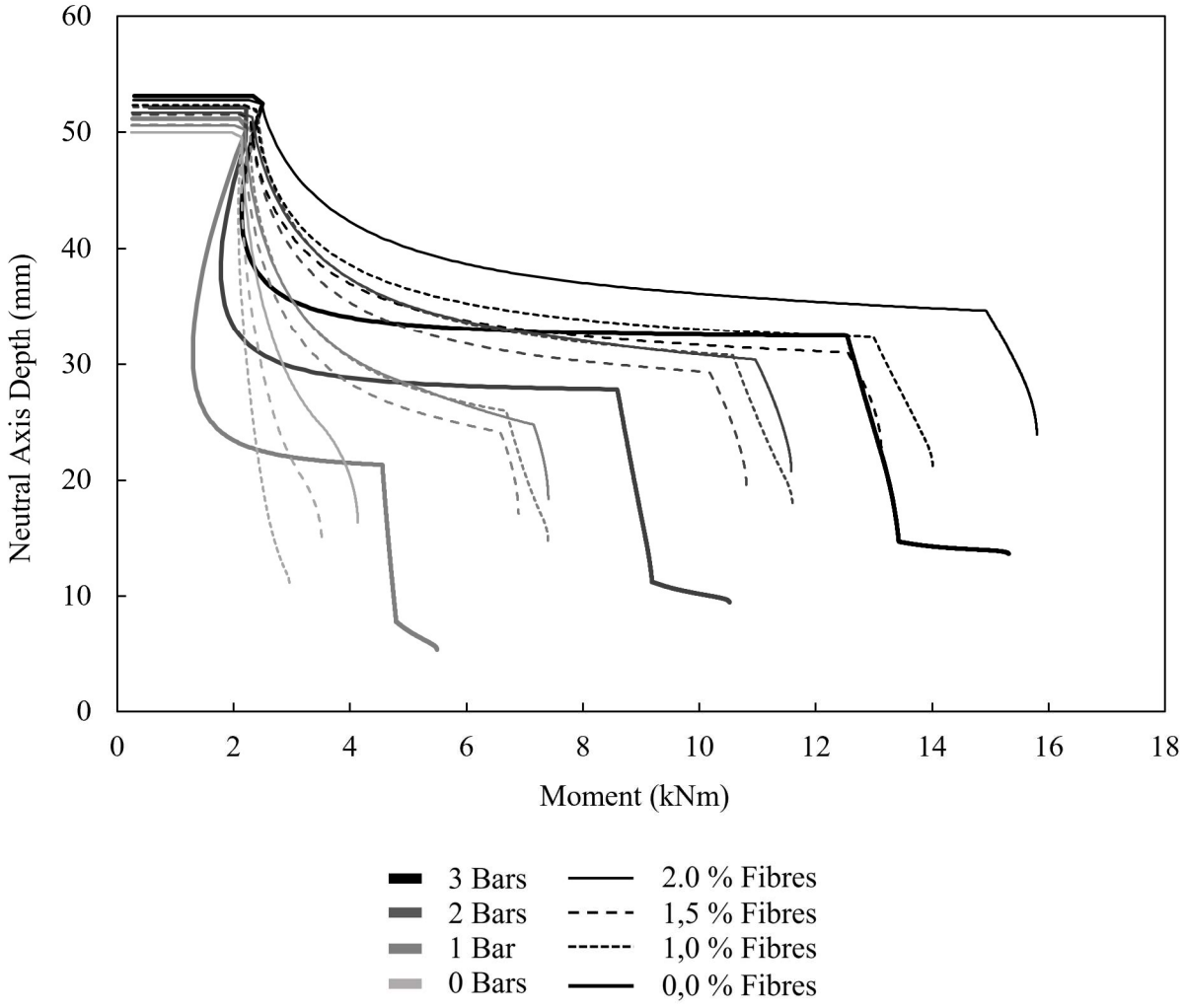

Figure 7-23: Neutral axis depth vs moment relationship of all beams

As a rough indication of the moment redistribution capacity one can look at the drop in the neutral axis depth once the steel has yielded. The calculated neutral axis depths at the ultimate moments were used to plot the moment redistribution on Figure 7-1. A larger reduction in the neutral axis can be attributed to larger rotations, and since the moment capacity is maintained, moments can be redistributed towards the sagging critical sections. In theory, the beams with no fibres should perform the best. Beams with a combination of fibres and reinforcing bars should perform better with more reinforcing bars. The optimum fibre content is again at 1.5% fibres which was observed in the moment redistribution results when comparing the ultimate moments to the elastic moments. However, these trends will differ if the full strength of the fibres or reinforcing bars is not used. Furthermore, changes in the plastic hinge length and crack spacing will affect the ability for the fibres to provide tensile resistance at high deflections.

One can look at the energy absorbed by the beams throughout the loading stage as a method of including all factors such as crack spacing, plastic hinge length, rotations and deflections. The effectiveness of the fibres in the beams with reinforcing bars can then be assessed.

7.9. SUMMARY OF MOMENT RESULTS

In this chapter the moment related results were discussed in terms of moment redistribution as compared to the guidelines provided by the code. Moment gradients along the length of the beam were shown at various loads and compared against the expected elastic moments. The change in the ratio between the hogging and sagging moments was observed as the degree of moment redistribution increased with increasing load.

The hogging and sagging moment evolution was plotted against the total external load and compared against the elastic moments. The redistribution of moments was observed when moments deviated from the elastic moments. The rate of increase in the moments decreased for the hogging moments and increased for the sagging moments at the onset of steel yielding, after which point the majority of moment redistribution occurred.

Moment redistribution was shown to occur after cracking where the elastic moment redistribution could be significant before plastic moment redistribution occurred once the steel had yielded. Moment redistribution when compared against elastic moments, was greatest in beams with 1.5% fibres and any reinforcing ratio. Lower fibre contents of 1% and 1.5% provided more moment redistribution when paired with three reinforcing bars. With 2% fibres, more moment redistribution was seen when combined with a reinforcing ratio of 1.4%.

The portion of moment redistribution occurring after the steel had yielded showed optimum results in beam 2B1.4. With a reinforcing ratio of 0.7%, the optimum fibre content was at 1.5%, whereas with a reinforcing ratio of 1.4% and 2.2%, the increased number of cracks allowed increasing fibre contents of up to 2% to improve the moment redistribution behaviour. There was a general reduction in moment

redistribution with an increase in the reinforcing ratio. The differences observed with different fibre contents is visible with reinforcing ratios of 0.7% and 1.4%, but not with a reinforcing ratio of 2.2%.

The effect of the flexural stiffness after cracking was shown in the value of moment redistribution (compared to elastic moments). A flatter hogging moment slope, representing greater deviations from the elastic moments after cracking, resulted in more moment redistribution since moment redistribution was defined as the ratio of the ultimate to elastic moments.

Three stages in the loading behaviour were observed. A linear stage before cracking, followed by a change in slope as the number of cracks increase, and a final change in slope when the steel yields. There is an increased capacity of the structure beyond the load at which the capacity of the critical section is reached. The greatest increase in load capacity was observed in beams with 1.5% fibres combined with any number of bars. A slight improvement was also observed with an increased number of reinforcing bars.

The moment curvatures and neutral axis depths were calculated to reveal the theoretical behaviours if both the fibres and bars performed at their full potential. The difference in the stress-strain graphs was shown to explain the ability of the fibres to reduce the curvatures and deflections at low moments. Differences in theoretical trends and actual behaviour are to be explained by the energy related results in the next chapter.

The current code approaches shown in Figure 7-1 are suitable for conventionally reinforced concrete upon which such limits are based. The introduction of steel fibres changes the behaviour of the beam, which would suggest that caution should be used when using current code guidelines for beams reinforced with steel fibres. For instance, the degree of moment redistribution was reduced in beam 0B0.7 with the addition of 1% steel fibres. The fibres also affect the depth of the neutral axis at ultimate load which affects the allowable degree of moment redistribution suggested by the code. However, the current code approach is a simplification of a complex procedure, and hence is not expected to accurately reflect actual behaviour, but merely to ensure a certain level of safety. In the case of steel fibre reinforced concrete, the current guidelines may not be suitable, especially in beams reinforced with only fibres, which is to be expected since the properties of steel fibres may differ greatly from that of conventional steel reinforcing bars.

CHAPTER 8

ENERGY

8.1. AREA UNDER THE LOAD DEFLECTION GRAPHS

A structure must possess the ability to provide resistance to forces. This ability can be quantified in terms of the energy absorbed in resisting these forces. To simplify the analysis, the beams containing only fibre or only reinforcing will first be compared at different deflections. Figure 8-1 shows the energy absorption at different deflections, which cover the range of small and large span/deflection ratios suggested by ASTM C1609M (2012) of L/600 (3.75 mm) and L/150 (15 mm). The energy is calculated as the area under the load-deflection graph up to the deflection of interest.

The performance of the different steel bar and fibre contents is much more visible when expressed in terms of the energy as in Figure 8-1 especially since the analysis includes the behaviours at much smaller deflections which is more consistent with deflections expected in actual structures. The beams containing only fibres are represented by dotted lines, where the three different fibre contents are plotted as triangles. The steel reinforcing ratios are represented by the dots, connected by the solid lines. Each colour of line represents the energy absorbed for the different beams at a specific deflection value.

For deflections up to 6 mm, the beams containing only fibres have the ability to absorb more energy than the beams containing reinforcing bars, as long as some fibres are included in the beam. The fibre percentage required to outperform the reinforcing increases as the deflections increase. At 2mm deflection, more than 1.15% fibre content will result in more energy absorbed than the beams containing one, two or three reinforcing bars. This value increases to 1.2% at 4mm and 1.45% at 6 mm. In each case, a fibre content of only 1% absorbs less energy than the beams with reinforcing. At larger deflections (somewhere between 6 mm and 10 mm) the reinforcing absorbs significantly more energy than the fibres.

The benefit of increasing the fibre content can be linked to the gradient of the curves between 1% to 1.5% and 1.5% to 2% fibres. At all deflection values the increase in energy absorption is most evident when increasing the fibre content to 1.5%. The benefit of increasing the fibre content to 2% is not realised at low deflections of 2 and 4 mm but begins to show as the deflections increase.

For the reinforcing steel there is almost no change in energy absorbed when varying the reinforcing content for deflections of up to 6 mm. It is only once the deflections increase beyond 10 mm when the increase in energy absorbed by increasing the reinforcing amount becomes apparent. Once the deflections reach larger values, the reinforcing is able to absorb more energy than the fibres. The fibres are unable to resist the tensile forces across increasingly wider cracks, either due to fibre pull-out, fibres

snapping, or limited efficiency due to their short length. This behaviour of the fibres can of course be improved by using longer fibres of improved quality as well as varying the properties of the concrete matrix to which the fibres bind.

At lower deflections, concrete containing steel fibres is able to absorb more energy than concrete containing steel reinforcing bars. Once the deflections increase beyond a point where the fibres are unable to provide sufficient resistance, the reinforcing takes over. However, the behaviour when the fibres and reinforcing are combined may differ from what is expected.

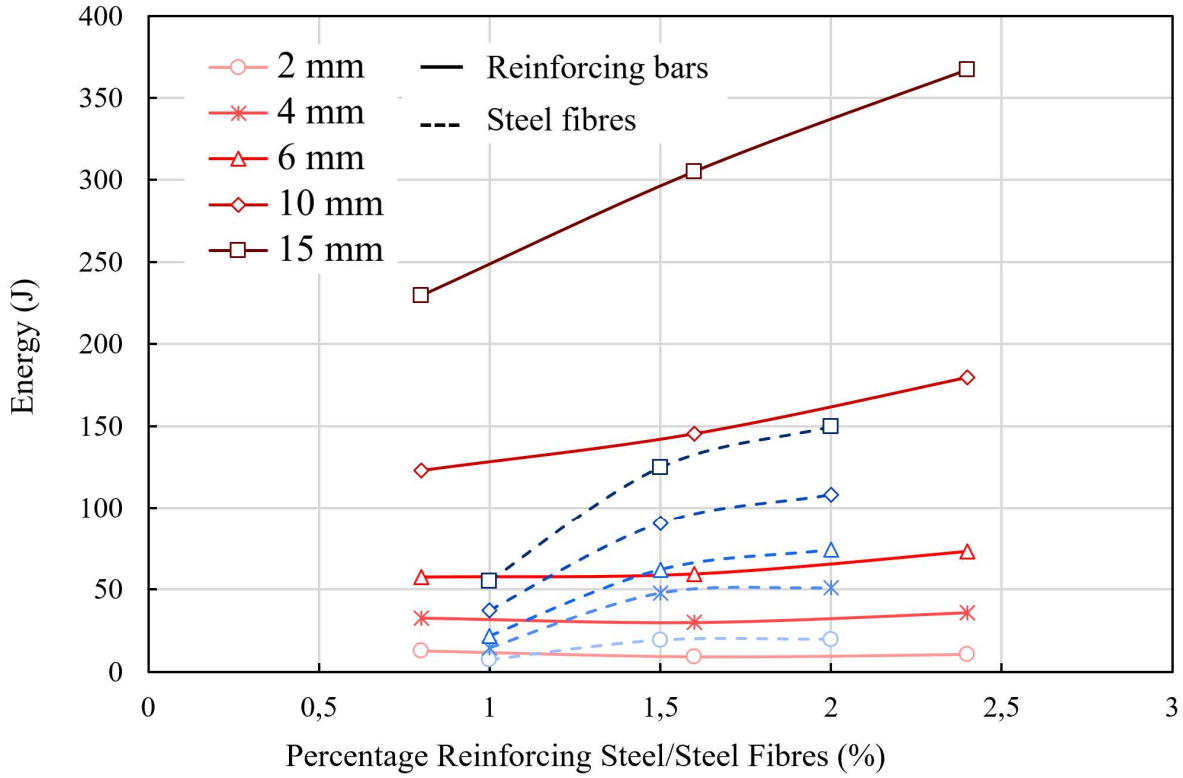

Figure 8-1: Energy absorbed by the beams in terms of the total steel content

So far, the energy absorption capabilities of the fibres and reinforcing have been investigated separately. Next, the results of all beams with the combined fibres and reinforcing are shown in terms of a total steel content in Figure 8-2. Darker shapes indicate an increase in fibre content. At low deflections up to about 6 mm, there is an almost linear increase in energy absorbed with an increase in total steel content, which consist of various combination of fibres and reinforcing. At higher deflections, the increase is still linear, but results are more variable. The increase in scatter is due to the fact that same steel fibre content does not provide the same strength as the same steel reinforcing bar content. Any differences are amplified as the loads and deflections increase.

With Figure 8-1 providing the context, an almost linear curve is expected for deflections up to 6 mm since the energy absorption of the fibres and steel are similar. Beyond 6 mm deflections, the behaviours

differ, leading to the increased scatter shown at 10 mm and 15 mm deflections. In other words, at large deflections, increasing the total steel content with the aid of steel fibres will result in a limited increase in energy absorption. At lower deflections, the total steel content can be increased with either reinforcing bars or fibres, resulting in a comparable increase in the energy absorbed. At larger deflections, an increase in energy is primarily caused by increasing only the reinforcing bar content, where additional fibres provide only minor improvements.

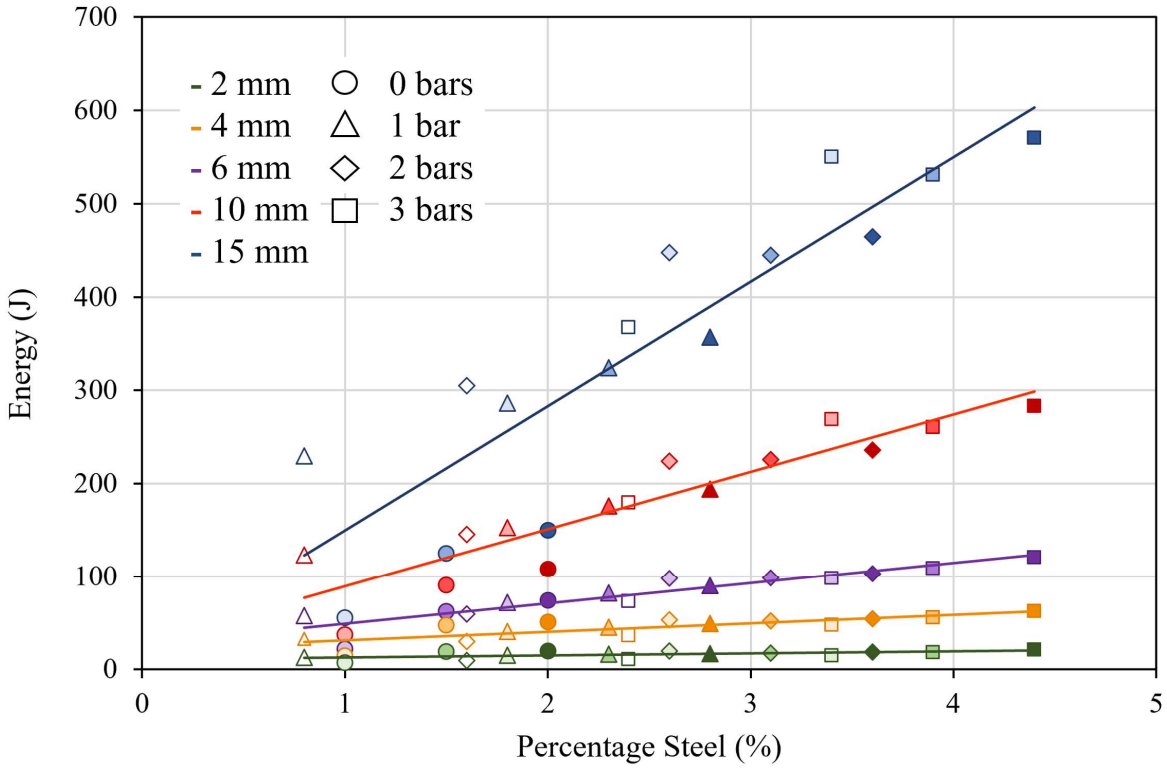

Figure 8-2: Energy absorbed vs total steel content

Before the energy deflection results of all beams are discussed, the idea of the influence of the number of cracks and crack spacing along with the plastic hinge length is investigated.

8.2. CRACK SPACING

To confirm the reasoning behind the improved energy absorption with more reinforcing bars the number of cracks and crack spacing is discussed. Crack spacings were measured and averaged across the beams containing the same number of reinforcing bars, since crack spacing was seen to mainly change with a change in reinforcing bars, with no clear difference seen when changing the fibre content. The average crack spacings are summarised in Table 8-1 which shows a clear decrease in crack spacing as the reinforcing ratio is increased. The beams containing only fibres failed with only one major crack at the critical sections. For the beams with no reinforcing bars and 2% fibres one or two secondary cracks

were observed close to the primary crack. One secondary crack was observed in beam 1.5B0 and no secondary cracks in beam 1B0.

Table 8-1: Average crack spacing

Steel reinforcing ratio (%)	**0**	**0.7**	**1.4**	**2.2**
Average crack spacing (mm)	0	96	67	43

The difference in the crack spacings can be seen for beams 1.5B2.2, 1.5B1.4 and 1.5B0.7 in Figure 8-3. Strain hardening properties of the reinforcing bars are evident in the increased number of cracks and the smaller crack spacing. The strain hardening properties of the reinforcing also led to variations in the plastic hinge length.

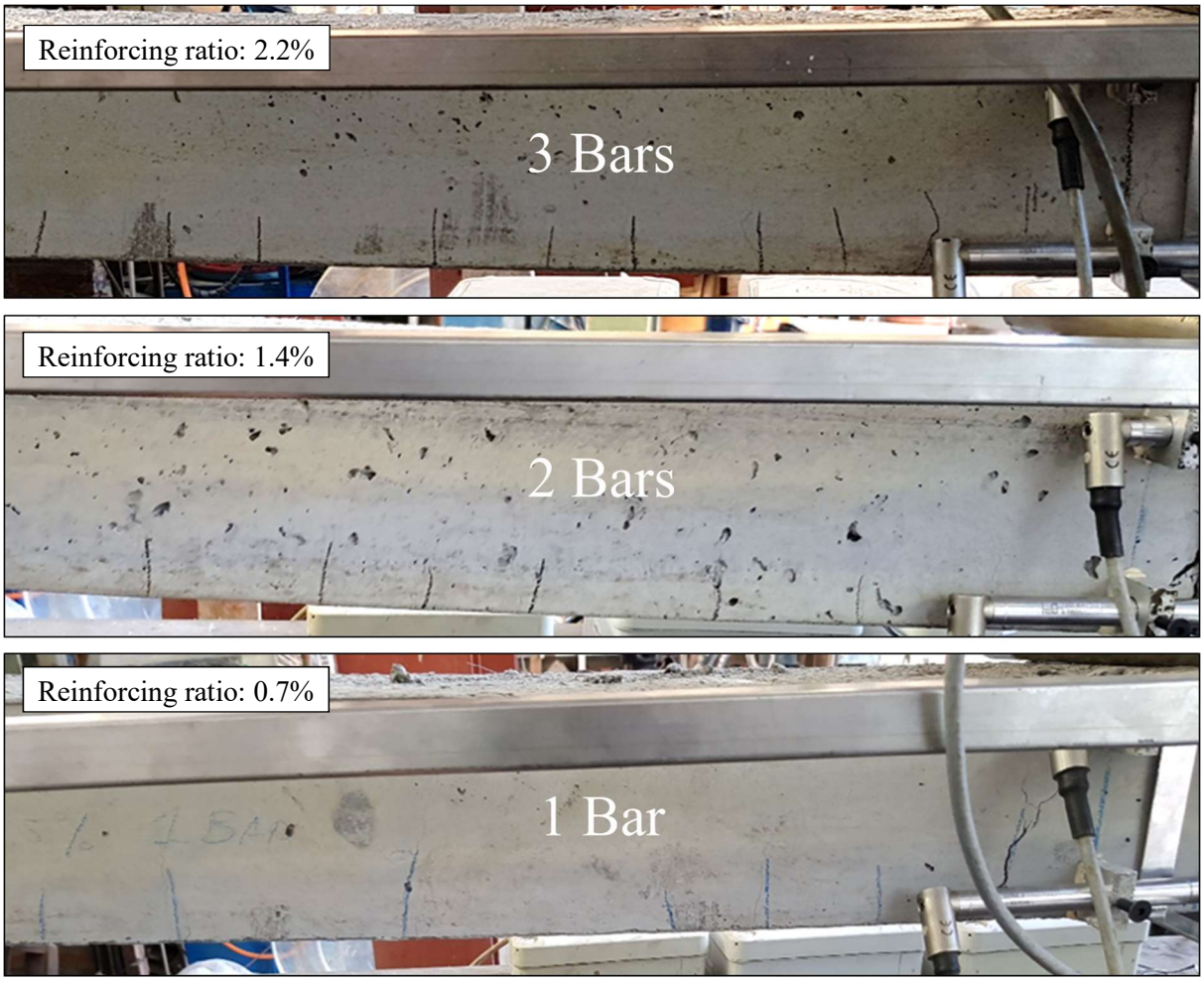

Figure 8-3: Crack spacing for 3 bars, 2 bars and 1 bar

8.3. PLASTIC HINGE LENGTH

A PIV analysis was performed on the failed span of each beam to obtain a deflected shape at the start of the steel yielding and at the ultimate load on the structure. Curvatures were calculated from the

deflected shape of the beam. The deflected shape of the beam as obtained from the image analysis is shown by the dotted lines in Figure 8-4. All blue lines represent the results when the steel in the sagging section had just yielded, and the black lines indicate the maximum load on the structure. Each dot represents an element in the mesh. The gradient along the deflected shape line results in the change in slope line. Finally, plotting the change in gradient of the slope line produces the curvature distribution shown as shown in the figure.

The analysis performed in Figure 8-4 considers only one span of the beam, as each photo covered only half of the beam. The distribution in curvature clearly shows the location of the plastic hinge as well as variations in curvature brought about by the cracks forming further away from the hinge. The inflection point between the hogging and sagging moment is also evident where the curvature changes from positive to negative. The plastic hinge length is calculated as the length across which the curvature is greater than the curvature at yielding. The results for all beams can be found Appendix C.

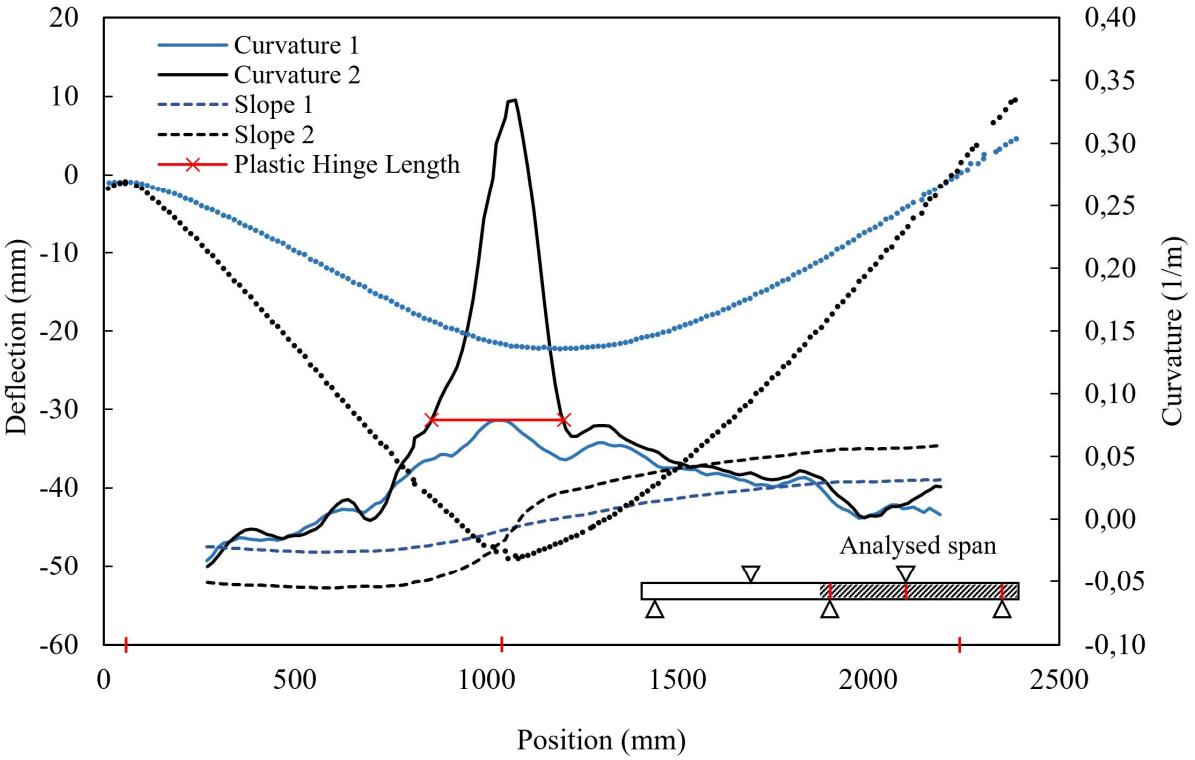

Figure 8-4: Beam deflection, slope and curvature

The curvature distribution indicates the difference in behaviour of a member with different material properties. For instance, rigid beams would show almost no curvature along the length of the beam, with a sharp peak occurring at the plastic hinge if only one crack formed. More slender beams would show a wider peak. Changes in plastic hinge length induced by different reinforcing and fibre amounts are illustrated in Figure 8-5. The values are dependent on the width across which the curvatures were measured, however, the method used to calculate the plastic hinge lengths was consistent for all beams

and therefore the results can be compared with one another. Beams without reinforcing bars were omitted from the calculations since failure occurred in one crack.

There was an increase in the plastic hinge length as the number of reinforcing bars increased. Changes observed with varying fibre contents were less evident, however, a slight trend exists towards an increase in hinge length with an increase in fibre content. The increase in the plastic hinge length can be attributed to the smaller crack spacing as the number of reinforcing bars is increased.

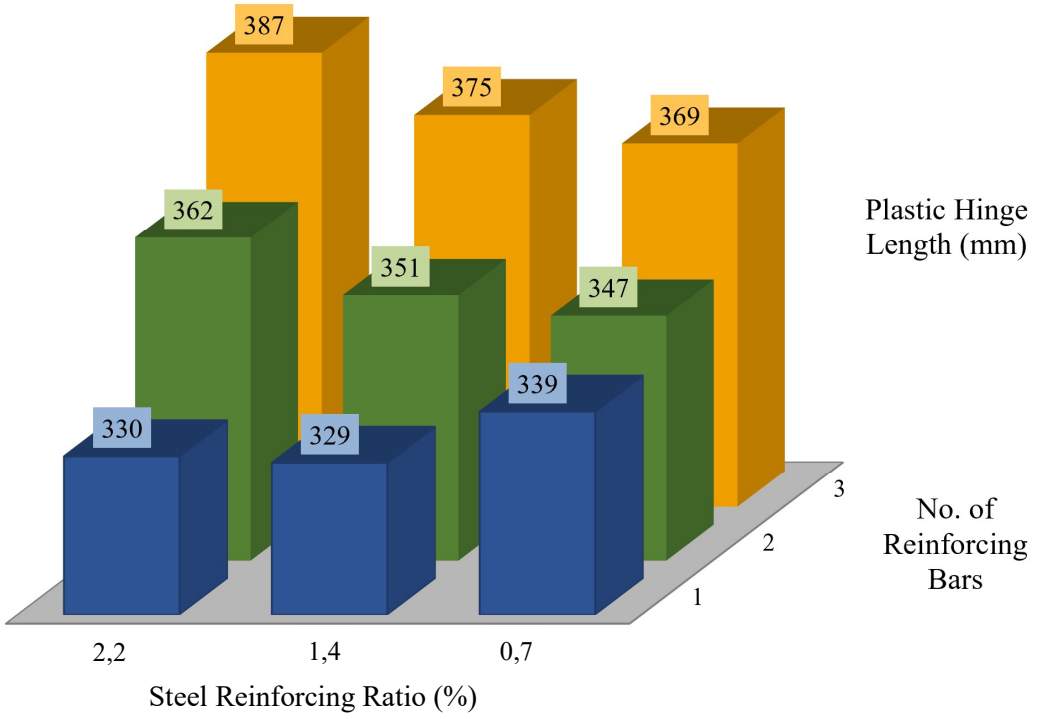

Figure 8-5: Plastic hinge lengths

The increase in plastic hinge length coupled with the increased number of cracks within the plastic hinge length would seem to agree with the idea of an increase in rotation capacity caused by the accumulated curvature across each crack. Considering a cross-section with a certain moment-curvature relationship, forming only one crack would result in a limited rotation capacity before the moment capacity is reduced, or the maximum curvature is obtained. A beam with multiple cracks however is able to rotate more since each crack adds to the total rotation. However, multiple cracks indicate that strain hardening has occurred which changes the rate at which the hogging and sagging moments increase. As a result, the ability for large rotations to improve moment redistribution, may be reduced by additional moment capacity produced by strain hardening. The overall effectiveness of the fibres is now investigated in beams containing both fibres and reinforcing bars to conclude on the overall structural behaviour of beams with steel fibres and reinforcing bars.

8.4. ENERGY FOR BEAMS WITH FIBRES AND REINFORCING BARS

The energy absorbed by beams with only fibres or only reinforcing bars at various deflections is again shown in a different format in Figure 8-6. Fibre contents of 1.5% and 2% are able to absorb more energy than three reinforcing bars up to 6 mm deflections. Thereafter the energy curves for the fibres begins to flatten since the load capacity is reached much earlier, and is also much lower, than for beams reinforced with bars. The energy absorbed by 1.5% fibres is much higher than for 1% fibres, and only a small improvement is seen with 2% fibres. The reinforcing bars are able to absorb energy at an increasing rate as the deflections increase, which is the opposite of the energy absorption behaviour shown by the fibres.

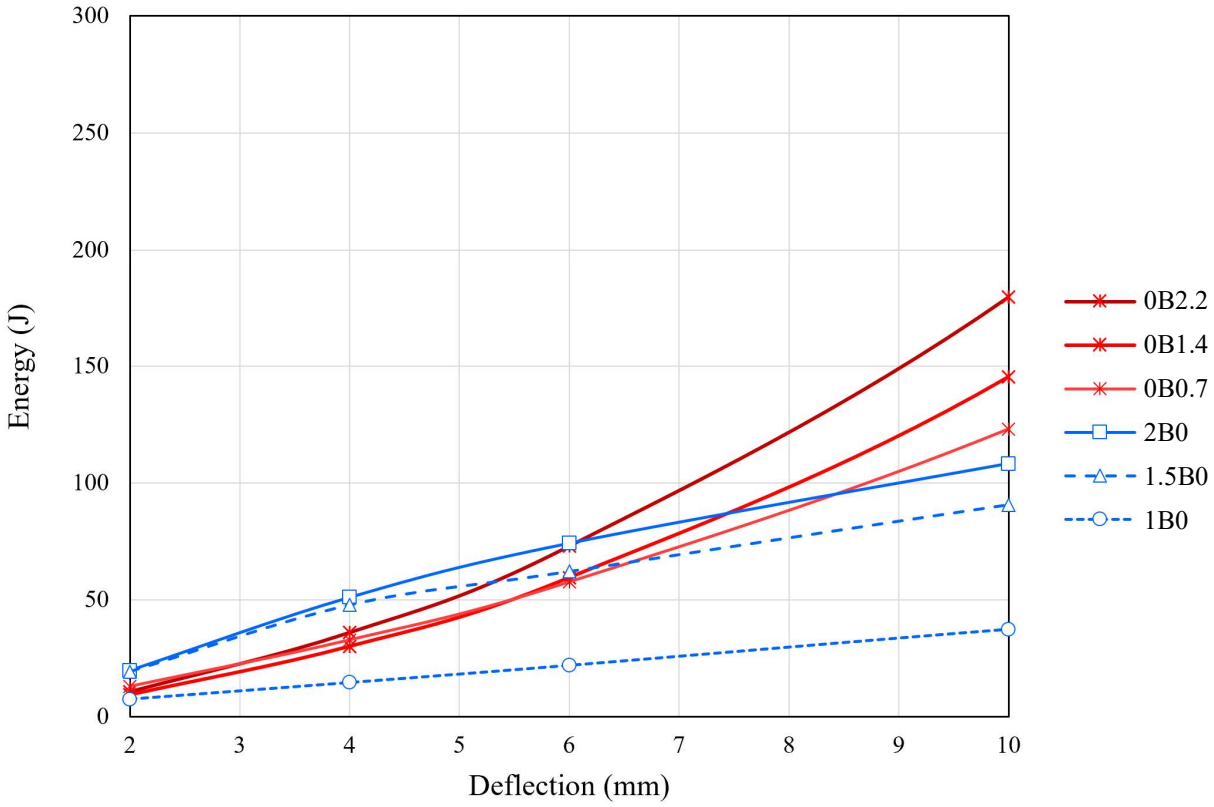

Figure 8-6: Energy absorption vs deflections for beams with only fibres or only reinforcing bars

The energy deflection curves for all remaining beams containing a combination of fibres and reinforcing bars is shown in Figure 8-7. As expected, increasing the reinforcing ratio results in more energy being absorbed. Changes in the energy absorbed caused by varying the fibre content are most visible in the beams with one bar. Since the loads for a reinforcing ratio of 0.7% are much lower, the influence of the fibres is more visible. With a reinforcing ratio of 1.4% and 2.2%, the difference between the three fibre contents is smaller since the strength of the reinforcing bars overshadows that of the fibres.

The energy absorbed by the beams with reinforcing bars and fibres can be compared to the sum of the energy absorbed by the beams with only fibres and only reinforcing bars. Differences in these energy deflection graphs would explain the discrepancy between theory and actual behaviour.

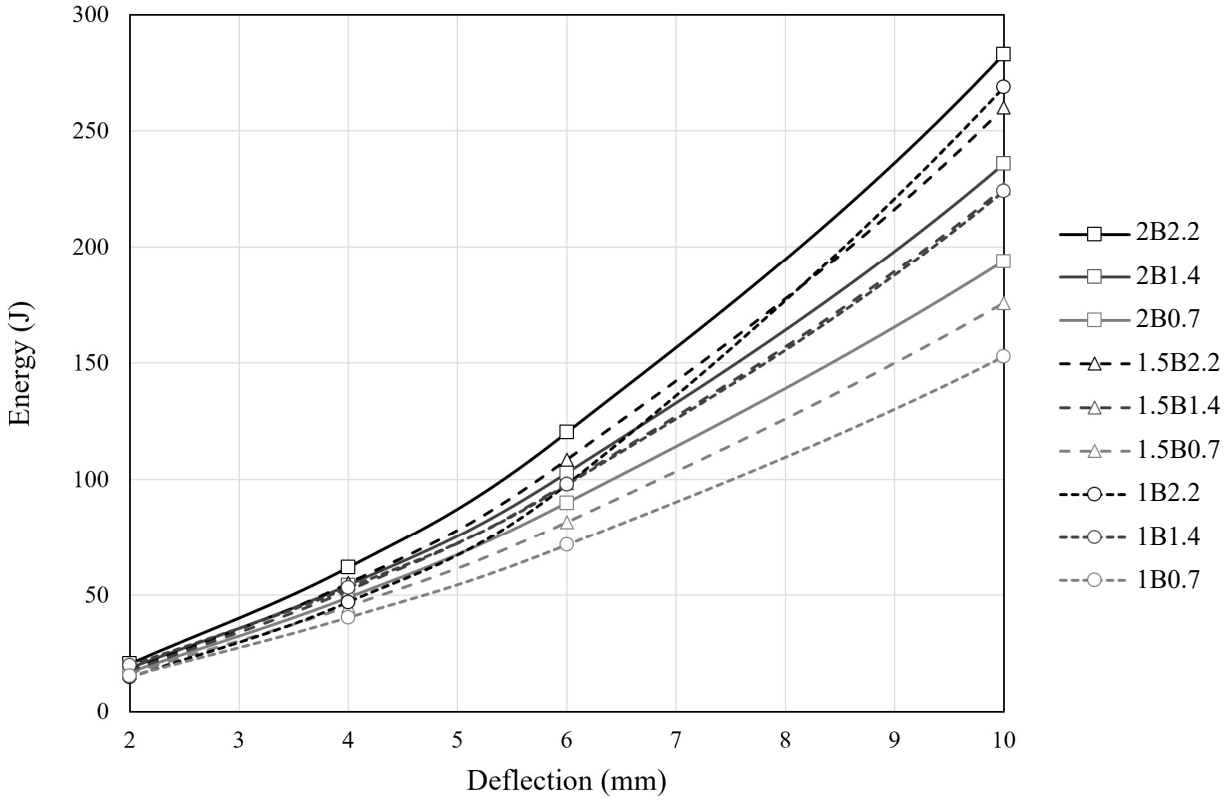

Figure 8-7: Energy absorption vs deflections for beams with fibres and reinforcing bars

8.4.1. ENERGY FOR BEAMS WITH A REINFORCING RATIO OF 0.7%

The energy deflection curves for the beams with a reinforcing ratio of 0.7% and different fibre contents is shown in Figure 8-8. Additionally, curves are plotted which represent the sum of the energy of the relevant fibre content and the reinforcing bar and are denoted with an S after the beam name (e.g. 1B0.7 S). If the strength of the fibres and reinforcing bars was fully utilised, the curves would plot close to the actual results. Clear differences are however observed, particularly at low deflections.

For beam 1B0.7 the sum of 1% fibres and a reinforcing ratio of 0.7% is similar to the actual result. The additional strength of 1.5% and 2% fibres is not realised in beams 1.5B0.7 and 2B0.7 where the actual energy absorbed is much lower than the sum of the fibres and reinforcing bars. This difference decreases slightly as the deflections increase. A reason for this is that as the deflections increase, the number of cracks increase, which allows the fibres to contribute more towards the tensile resistance. The orientation of the fibres around the reinforcing bar may also have resulted in a less effective distribution than in the beams with no reinforcing bars.

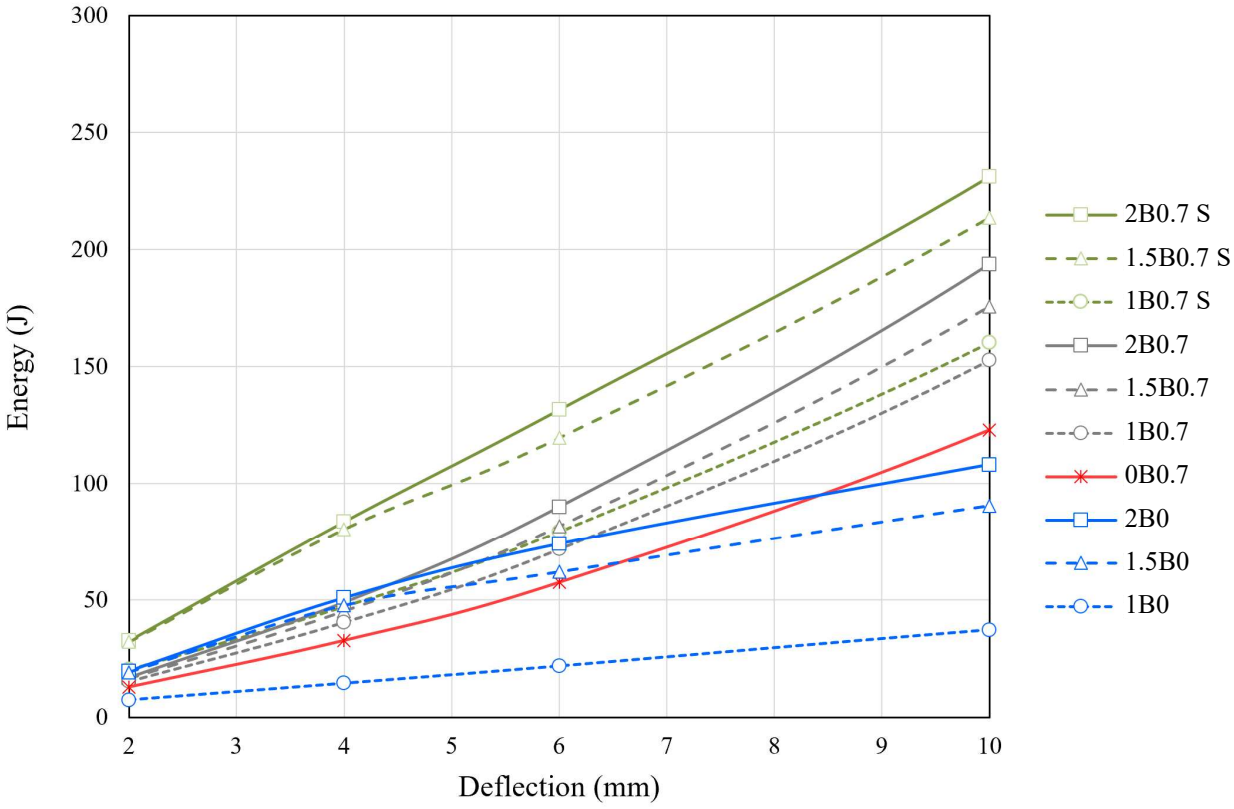

Figure 8-8: Energy absorption vs deflections for beams with fibres and a reinforcing ratio of 0.7%

8.4.2. ENERGY FOR BEAMS WITH A REINFORCING RATIO OF 1.4%

The energy deflection curves for the beams with a reinforcing ratio of 1.4% and different fibre contents is shown in Figure 8-9. Similar observations are made, where the sum of the energies is higher than the actual energy absorbed, apart from the beam with a 1% fibre content. The initial difference between the sum of energies and actual energies is smaller than in the beams with a reinforcing ratio of 0.7%. This can be attributed to the fact that the number of cracks increases with more reinforcing bars which allows the fibres to contribute more effectively towards the tensile strength across the cracks. There is also greater convergence in the sum of energies and the actual energies as the deflections increase, which indicates that the increase in number of cracks allows the full potential of the fibres to be utilised.

Much smaller differences in the behaviour of the different fibre contents are observed which can be attributed to the higher loads being carried with two reinforcing bars relative to the strength of the fibres. An interesting observation is that the actual behaviour of beam 1B1.4 shows more energy absorbed than the sum of the individual components. An explanation to this is that in the beam with only 1% fibres, only one crack formed at the critical sections, with no smaller secondary cracks. The energy absorption was therefore limited since the fibres could only bridge one crack after and the softening behaviour did

allow more cracks to form. However, once the fibres were combined with one reinforcing bar, more than one crack formed at each critical section, which allowed the fibres to bridge across multiple cracks and therefore contribute towards greater energy absorption.

For higher fibre contents of 1.5% and 2% the beams with fibres alone were able to absorb a large amount of energy initially, which is not observed when combined with a reinforcing ratio of 1.4%. The same argument can be made that the distribution of the fibres is made less effective due to the presence of the two reinforcing bars. Furthermore, since initially only one crack exists, the fibres are unable to contribute sufficiently. As the deflections increase and the number of cracks increases, the fibres are then able to contribute more of their tensile resistance to the beam.

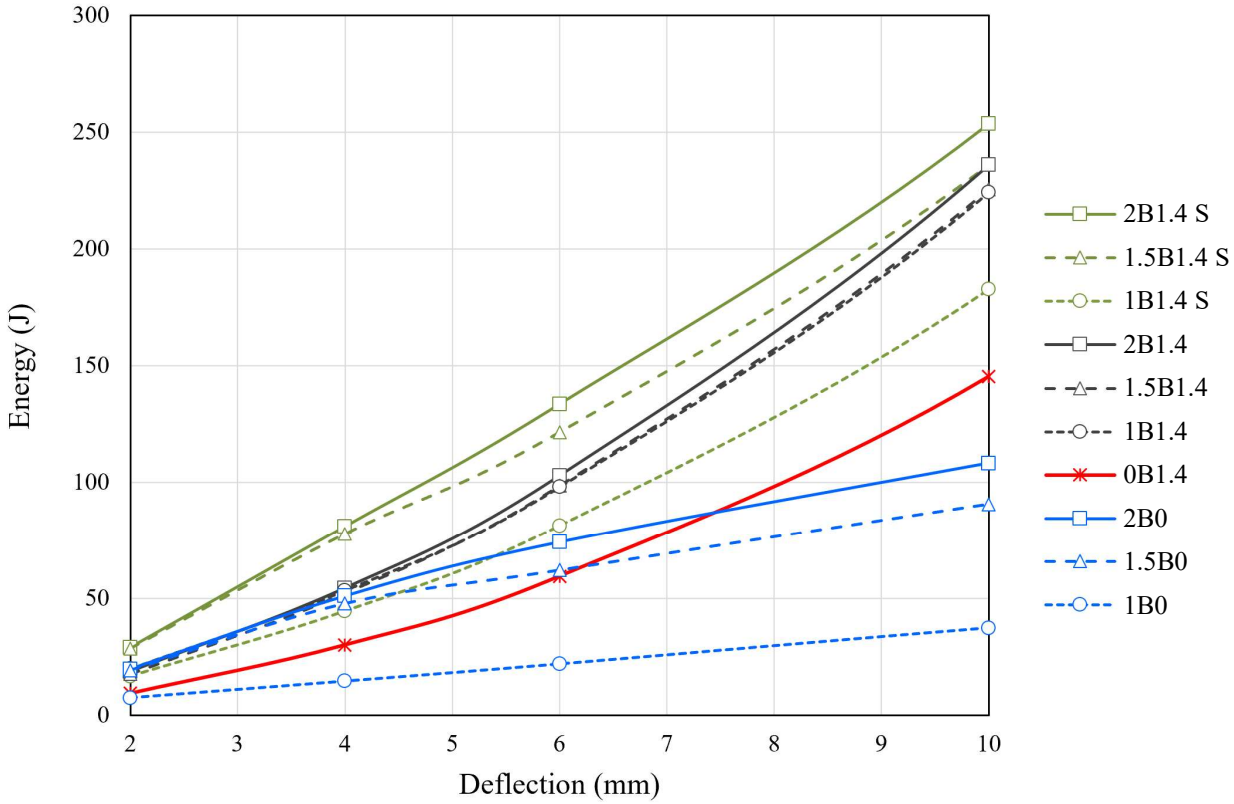

Figure 8-9: Energy absorption vs deflections for beams with fibres and a reinforcing ratio of 1.4%

8.4.3. ENERGY FOR BEAMS WITH A REINFORCING RATIO OF 2.2%

The energy deflection curves for the beams with a reinforcing ratio of 2.2% and different fibre contents is shown in Figure 8-10. In this case, similar differences between the sum and actual energies are observed as for beams with a reinforcing ratio of 1.4%, apart from the fact that there is greater convergence at higher deflections. The initial energy absorbed falls below the sum of energies at low deflections for all fibre contents. However, the actual energy of the beam with 1% fibre exceeds the sum of the energies after 5.5 mm deflection. This behaviour can again be explained by the fact that the

energy absorbed by the beam with only 1% fibres is quite low since only one crack formed at the critical section, whereas multiple cracks form in beams with reinforcing bars.

The convergence towards similar energy values at higher deflections shows how the increased number of cracks brought about by the greater number of reinforcing bars allows the fibres to contribute more significantly towards the structural performance. Although the differences observed between the fibre contents are smaller than when looking at the beams with one reinforcing bar, the contribution is greater. The smaller difference between fibre contents can be explained by the higher loads on the beam compared to the load capacity of the fibres alone. Even though the fibre strength is comparatively much lower than the external loads on the beam, their full strength potential is approached due to the increased number of cracks. Even with a reinforcing ratio of 2.2% potentially disrupting the fibre distribution, there is an improvement in the energy absorbed due to the increased number of cracks.

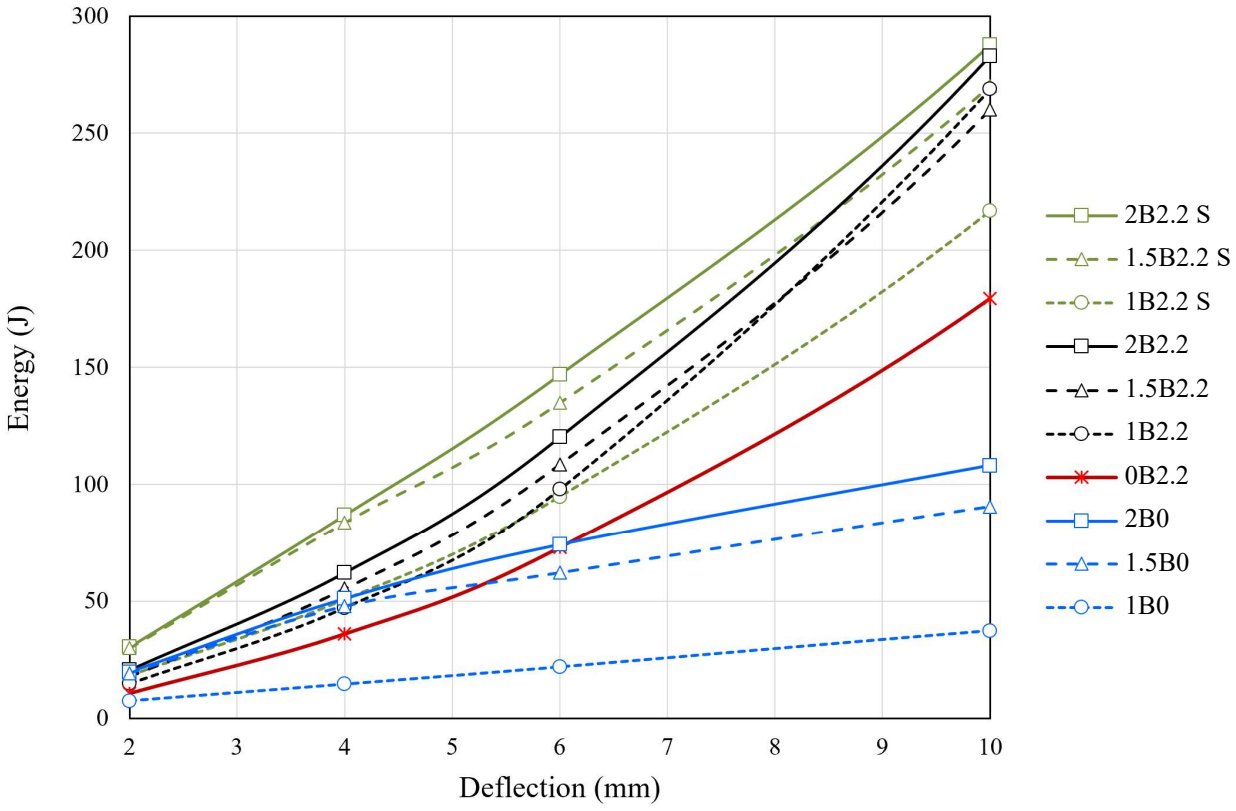

Figure 8-10: Energy absorption vs deflections for beams with fibres and a reinforcing ratio of 2.2%

8.5. SUMMARY OF ENERGY RESULTS

In summary it can be said that the fibres and reinforcing balance each other in that their respective range of greatest influence occurs at different stages. The fibres provide resistance at lower deflections, followed by the reinforcing at higher deflections. Stronger fibres of improved quality have the potential to offer improved performances up to higher loads and deflections. For these tests, a steel fibre content of 1% was able to carry roughly 9 kN of load. In comparison, one steel bar was able to carry on average 27 kN. This translates to roughly 34 kN per 1% of reinforcing steel. A reinforcing bar was therefore able to resist about 3.75 times the amount of load when compared to the fibres. Even with this ratio, the fibres were able to absorb more energy at loads causing no more than 6 mm deflections. A much greater improvement in structural performance is therefore possible by decreasing the strength ratio of 3.75 by using fibres of greater length, strength and quality.

It had been shown that the fibres improve the load deflection behaviour at lower loads and deflections. However, the energy related results revealed how the effectiveness of the fibres at low loads is greatly reduced when combined with reinforcing bars. Only with an increase in deflections do the fibres become more effective since the number of cracks increases.

The number of cracks increased and cracks spacing reduced with a higher reinforcing ratio. Fibres were therefore able to absorb more energy by bridging more cracks. Plastic hinge length increased with a higher reinforcing ratio, with a slight increase observed with a higher fibre content. Beams with a reinforcing ratio of 2.2% allowed the fibres to absorb more energy than the sum of the beams with only fibres and only bars as a result of the strain hardening behaviour of the reinforcing bars being dominant.

Although an increase in fibre content with a reinforcing ratio of 2.2% has a limited effect on the energy absorbed, the overall effectiveness of any fibre content is much higher than for beams with only one reinforcing bar. For a low reinforcing ratio, adding more fibres is beneficial, whereas for a high reinforcing ratio, the optimum fibre content sits at a much lower value.

CHAPTER 9

CONCLUSIONS AND RECOMMENDATIONS

9.1. CONCLUSIONS

The aim of this research was to investigate the effects of different percentages and combinations of steel fibres and reinforcing bars on moment redistribution in high strength concrete. Additional performance parameters were investigated and categorised into loads and deflections, moments, and energy related results in order to determine optimum fibre contents. Standard material test results were used to theoretically calculate moment curvature responses and compared to the trends observed in the experimental results.

The following conclusions can be drawn for the 80 MPa concrete reinforced with combinations of steel fibres and steel reinforcing bars, categorised into the three major performance parameters:

- Loads and deflections:
    - The addition of fibres did not lead to significant increases in the ultimate load capacities
    - The addition of fibres improved the load deflection behaviour by reducing the deflections at lower loads.
    - In terms of ultimate relative deflections, a fibre content of 1.5% generally provided the best results.
    - In terms of ultimate relative deflections, the optimum fibre content increased with an increase in the reinforcement ratio.
- Moment redistribution:
    - Moment redistributions were greater in all beams tested than the limits suggested by EC2 and the fib Model Code apart from the beams with 1% fibres and a reinforcement ratio of 0.7% and 1.4%.
    - Moment redistribution is highly dependent on the definition used
    - Significant changes in the ratio between the hogging and sagging moments occurred after cracking before plastic behaviour occurred.
    - An optimum fibre content of 1.5% was obtained for moment redistribution defined by the ratio of ultimate to elastic moments.
    - Plastic moment redistribution showed an optimum at 2% fibres with a reinforcement ratio of 1.4% and 2.2%, and 1.5% fibres with a reinforcement ratio of 0.7%.
- Energy:
    - Beams with only fibres showed improved energy absorption capabilities in comparison to beams with only reinforcing bars up to deflections of about 6 mm.

- Fibres were less effective in beams containing reinforcing bars at very low deflections and improved as the deflections increased.
- An increase in the reinforcement ratio led to an increase in the effectiveness of the fibres due to the increased number of cracks.

The theoretical moment curvature results provided an explanation into the trends observed in moment redistribution abilities with varying fibre and reinforcing contents. However, exact matches between theory and actual results could not be obtained due to the influence of more complex mechanisms occurring such as the change in crack spacing and number, variation in plastic hinge length, and change in the ability for the fibres to contribute their full tensile strength potential when combined with reinforcing bars.

The following minor conclusions not directly related to the primary objective can be made:

- The load deflection and moment curvature results of the FPBTs allowed predictions to be made in terms of an optimum fibre content of 1.5% which was observed in the various structural performance parameters.
- The inverse analysis method used was successful in providing a simplified and improved simplified stress-strain relationship for the three fibre contents.
- With the inverse analysis, the FPBTs provided information into the load deflection, moment curvature and stress-strain properties of the material as opposed to only stress-strain results in direct tension tests.
- The strain hardening behaviour of the reinforcing bars overshadowed the strain softening behaviour of the fibres.
- A PIV analysis using open source software and ordinary cameras used to successfully monitor surface deformations which allowed deflections, curvatures, and strains to be simultaneously recorded across any location.

Finally, the amount of moment redistribution of beams with only fibres is much less, if any, than beams with ordinary reinforcing bars. The primary benefit of the added fibres was to reduce deflections, particularly at lower loads. Optimum fibre contents can be observed in the moment curvature, load deflection and stress-strain results of the FPBTs.

An optimum fibre content ultimately depends on which property is required since the optimum fibre contents for ultimate load capacities, load deflection behaviours, moment redistribution, and energy absorption is different for each parameter.

9.2. RECOMMENDATIONS FOR FUTURE WORK

In this study various changes in structural behaviour resulting from different combinations of steel fibres and reinforcing contents was investigated. It was shown that it is difficult to predict the trends observed when changing the ratios of fibres and reinforcing bars. Optimum fibre contents vary with different reinforcing bar amounts and depend on which structural improvement is required. Although the range of experiments provided greater insight into the behaviour of indeterminate beams with varying fibre and reinforcing ratios, there is a need to clarify the most important aspects in terms of the mechanisms which most influence the parameters of loads, deflections and moment redistribution.

Predicting an optimum fibre content in combination with reinforcing bars is not possible with only the standard tension and compression tests. In the end, moment redistribution is a complex process, hence requiring more complex input parameters if theoretical predictions are to be made.

The following research aspects should be investigated to provide further insight into the behaviour of steel fibre reinforced indeterminate beams:

- The effect of longer fibres on the structural performance of indeterminate beams so that the relative strength difference between the fibres and reinforcing bars is smaller.
- The effect of different beam geometries on the orientation of fibres which will affect the overall behaviour of the beam.
- The use of steel fibres which show strain-hardening properties which plays a major role in allowing more redistribution.
- Repeat tests should be conducted on beams with the same steel fibre and reinforcing bar to remove uncertainty in the results.
- Emphasis must be placed on a correct support system and initial load distribution of the beams as moment redistribution is greatly affected by the support and loading conditions when compared against assumed elastic moments.
- The difference between moment redistribution occurring during elastic and plastic behaviour should be investigated to establish how this relates to the differences in design and practise.
- The effect of steel fibres at serviceability loads should be investigated in terms of reducing deflections and changes in the elastic moment redistribution.

LIST OF REFERENCES

ACI 318, 2014, ACI 318-14 Building code requirements for structural concrete and commentary, ACI Committee 318.

ACI 440.1R-06, 2006. *Guide for the design and construction of structural concrete reinforced with FRP bars*, ACI committee 440. American Concrete Institute.

Ackermann, F.P. & Schnell, J. 2011. Steel fibre reinforced continuous composite slabs, *Composite Construction in Steel and Concrete VI*. pp. 125–137.

Aiello, M.A. & Ombres, L. 2011. Moment Redistribution in Continuous Fiber-Reinforced Polymer-Strengthened Reinforced Concrete Beams, *ACI Structural Journal*, Title no. 108-S16, pp 158-166.

Ashour, A.F. & Habeeb, M.N., 2008. Continuous concrete beams reinforced with CFRP bars. *Proceedings of the Institution of Civil Engineers - Structures and Buildings.* vol. 161, no. 6, pp. 349-357.

ASTM C1609, 2012. ASTM-C1609.C1609M-12 Standard Test Method for Flexural Performance of Fiber-Reinforced Concrete (Using Beam With Third-Point Loading), ASTM.

ASTM C469-02, 2008. Standard Test Method for Static Modulus of Elasticity and Poisson's Ratio of Concrete in Compression. In Annual book of ASTM standards 2008, section 04.02. ASTM.

Aveston, J. & Kelly, A., 1973. Theory of multiple fracture of fibrous composites. *Journal of Materials Science*. vol. 8, no. 3, pp.352–362.

Baby, F., Graybeal, B., Marchand P., & Toutlemonde F. 2012. A proposed flexural test method and associated inverse analysis for UHPFRC. *ACI Materials Journal*. vol. 109, no. 5, pp. 545–555.

Baby F., Graybeal, B., Marchand, P. & Toutlemonde, F. 2013. UHPFRC tensile behaviour characterization: inverse analysis of four-point bending test results. *Materials and Structures*, vol. 46, pp. 1337–1354.

Baker, A.L.L., 1956. *The Ultimate Load Theory Applied to the Design of Reinforced and Prestressed Concrete Frames*. Concrete Publications Limited. London

Baker, A.L.L. & Amarakone, A.M.N., 1964. Inelastic hyperstatic frame analysis. *ACI Structural Journal*. vol. 12, pp. 85–142.

Balaguru, N. & Shah, SP., 1992. *Fiber reinforced cement composites*. New York: McGraw-Hill 1992, pp. 179-214.

Banthia, N., Trottier, J.F., 1994. Concrete reinforced with deformed steel fibers, part 1: bond-slip mechanisms, *ACI Materials Journal.* vol. 91, no. 5, pp. 435-446.

Banthia, N., Trottier, J.F., 1995. Concrete reinforced with deformed steel fibers, part 2: toughness characterization, *ACI Materials Journal*. vol. 92, no. 2, pp. 146-154.

Barros, J.A.O., Cunha, V.M.C.F., Ribeiro, A.F. & Antunes, J.A.B. 2004. Post-cracking behaviour of steel fibre reinforced concrete. *Materials and Structures*. vol. 38, pp. 47-56.

Bencardino, F., Rizzuti, L., Spadea, G., & Swamy, R.N., 2008. Stress-Strain Behaviour of Steel Fiber-reinforced Concrete in Compression. *Journal of Materials in Civil Engineering*, Vol 20, No. 3, pp. 255-263

Berard, A., 1874. Improvement in artificial stone. Available at: https://www.google.com/patents/US157903

Berry, M.P., Lehman, D.E. & Lowes, L.N. 2008. Lumped-plasticity models for performance simulation of bridge columns. *ACI Structural Journal*. vol. 105, no. 3, pp. 270–279.

Bischoff, P. 2000. Comparison of tension stiffening for plain and steel fibre reinforced concrete, *Proceedings of the Fifth International RILEM Symposium Fibre-Reinforced Concretes (FRC)*, RILEM Publications S.A.R.L. pp. 633-641.

Bischoff, P. 2003. Tension stiffening and cracking of steel fiber-reinforced concrete, *Journal of Materials in Civil Engineering*, vol. 15, no. 2, pp. 174-182.

Brandt, A. M., 2008. Fibre reinforced cement-based (FRC) composites after over 40 years of development in building and civil engineering. *Composite Structures*. vol. 86 no. 1-3, pp. 3-9.

BS 8110, 1995. *Structural use of concrete – Part 1.* British Standards Institution, BSI, London.

CAN-A23.2, 1994. *Code for the design of concrete structures for buildings*, Canadian Standards Association.

CEB-FIP, 1990. *Model code for concrete structures—Europe*, International System of Unified Standard Codes of Practise for Structures.

Chao, S., Naaman, A.E. & Parra-Montesinos, G.J. 2009. Bond Behaviour of Reinforcing Bars in Tensile Strain-Hardening Fiber-reinforced Cement Composites. *ACI Structural Journal*, vol. 106, no. 6, pp. 897-906.

Conforti, A., Zerbino, R., & Plizzari, G.A. 2018. Influence of steel, glass and polymer fibers on the cracking behavior of reinforced concrete beams under flexure, *Structural Concrete*, 1-11.

DAfStb, 2010. *DAfStb-Richtlinie Stahlfaserbeton (Guidelines for Steel Fiber Reinforced concrete) – Part 1.* Deutscher Ausschuss fur Stahlbeton.

Dancygier, A.N, & Berkover, E. 2016. Cracking localization and reduced ductility of fiber-reinforced concrete beams with low reinforcement ratios, *Engineering Structures*, vol. 111, pp 411-424

Dancygier, A.N., Karinski, Y.S. & Navon, Z. 2017. Cracking localization in tensile conventionally reinforced fibrous concrete bars, *Construction and Building Materials*, vol. 149, pp. 53-61.

DBV, 2007. *Guide to Good Practice. Steel Fibre Concrete,* G. S. for Concrete & Concrete Technology, eds., DBV.

Deluce, J.R. & Vecchio, F.J. 2013. Cracking behavior of steel fiber-Reinforced concrete members containing conventional reinforcement. *ACI Structural Journal*, vol. 110, no. 3, pp 481-90.

Denneman, E. 2011. *Fracture in high performance fibre reinforced concrete pavement materials*. PhD Thesis, University of Pretoria.

di Prisco, M., Plizzari, G., Vandewalle, L., 2009. Fibre reinforced concrete: new design perspectives. *Materials and Structures.* vol. 42, no.9, pp. 1261-1281.

DIN1405, 1997. Deutsches Institut fur Normung—German Institute of Standards.

do Carmo, R.N.F. & Lopes, S.M.R. 2005. Ductility and linear analysis with moment redistribution in reinforced high-strength concrete beams. *Canadian Journal of Civil Engineering,* vol. 32, no. 1, pp. 194-203.

El-mogy, M., El-ragaby, A. and El-salakawy, E. 2010. Flexural Behavior of Continuous FRP-Reinforced. *Journal of Composites for Construction*. vol. 14, no. 6 pp. 669–681.

Elsaigh, W.A. 2007. Modelling the behaviour of steel fibre reinforced concrete pavements. PhD Thesis, University of Pretoria.

EN14651, 2007. *DS/EN 14651 Test method for metallic fibre concrete. Measuring the flexural tensile strength (limit of proportionality (LOP), residual)*, Danish Standard.

EN 14889-1, 2007. Fibres for concrete – Part 1: Steel; fibres – Definitions, specifications and conformity.

EN1992-1-1, 2010. *Eurocode 2: Design of concrete structures – Part 1 - 1:Generalrules and rules for buildings*, CEN.

fib Model, 2013. *Fib Model Code for Concrete Structures*. Ernst & Sohn, Berlin, Germany.

Gere, J.M. & Timoshenko, S.P. 1991. *Mechanics of Materials, Third SI Edition*. Chapman and Hall, London, pp. 691-695.

Gere, J.M. & Goodno, B.J., 2011. *Mechanics of Materials, Brief Edition*. Cengage Learning.

Gravina, R.J. & Smith, S.T. 2008. Flexural behaviour of indeterminate concrete beams reinforced with FRP bars. *Engineering Structures.* vol. 30, no. 9, pp. 2370-2380.

Guo, Z. 2014. *Principles of reinforced Concrete.* Elsevier Inc. Oxford, UK.

Guyon, Y. 1960. *Prestressed Concrete: Volume 2*. John Wiley and Sons, Lincoln, United Kingdom.

Hannant, D.J., 1978. *Fibre cements and fibre concretes*, John Wiley and Sons, New York.

Herbert, A. & Sawyer, J.R. 1964. Design of concrete frames for two failure stages, *ACI Structural Journal*, SP-12, pp. 405–437.

Holschemacher, K., Mueller, T. and Ribakov, Y. 2010. Effect of steel fibres on mechanical properties of high-strength concrete. *Materials and Design*. Elsevier Ltd, vol. 31, no. 5, pp. 2604–2615

Illstone, J.M. & Domone, P.L.J., 2002. *Construction Materials, Their nature and behaviour, Third Edition*. Spon Press, London.

JCI-S-002, 2003. *JCI-S-002-2003 Method of test for load-displacement curve of fiber reinforced concrete by use of notched beam*, Japan Concrete Institute Standard.

JCI-S-003, 2007. *JCI-S-003-2007 Method of test for bending moment-curvature curve of fiber-reinforced cementitious composites*, Japan Concrete Institute Standard.

JSCE, 2008. *Recommendations for design and construction of High Performance Fiber Reinforced Cement Composites with fine multiple cracks*, Japan Society of Civil Engineers.

Jungwirth, J. 2006, Zum Tragverhalten von Zugbeanspruchten Bauteilen aus Ultra-Hochleistings-Faserbeton. PhD Thesis, Ecole Polytechnique Federale de Lausanne.

Kanakubo, T. 2006. Tensile characteristics evaluation method for DFRCC. *Journal of Advanced Concrete Technology*, vol. 4, no. 1, pp. 3–17.

Kang, S., Lee, Y., Park, Y. & Kim, J. 2010. Tensile fracture properties of an Ultra High Performance Fiber Reinforced Concrete (UHPFRC) with steel fiber. *Composite Structures*. Elsevier Ltd, vol. 92, no.1, pp. 61–71.

Kara, I.F. & Ashour, A.F., 2013. Moment redistribution in continuous FRP reinforced concrete beams. *Construction and Building Materials.* vol. 49, pp. 939-948.

König, G. & Kützing, L., 1999, Modelling the increase of ductility of HPC under compressive forces, a fracture mechanical approach, *Proceedings of the IIIrd International RILEM Workshop 'High Performance Fibre Reinforced Cementitious Composites (HPFRCC 3),* 1999 Mainz, pp. 251-260.

Kooiman, A.G., 2000. *Modelling Steel Fibre Reinforced Concrete for Structural Design*. PhD Thesis. Technische Universitest Delft.

Lim, T.Y., Paramasivam, P. & Lee, S.L. 1987. Behaviour of Steel-Fiber-Concrete Beams in Flexure. *Journal of Structural Engineering*, vol. 113, no. 12, pp 2439-2458.

Lin, C.H. & Chien, Y.M., 2000. Effect of section ductility on moment redistribution of continuous concrete beams. *Journal of the Chinese Institute of Engineers.* vol. 23, no. 2, pp. 131-141.

Löfgren, I., 2005. Fibre-reinforced Concrete for Industrial Construction. PhD Thesis. Chalmers University of Technology, Department of Civil and Environmental Engineering.

López, J.A., Serna, P., Navarro-Gregori, J. & Camacho, E. 2015. An inverse analysis method based on deflection to curvature transformation to determine the tensile properties of UHPFRC. *Materials and Structures*, vol. 48, pp. 3703-3718.

Lou, T., Lopes, S.M.R. & Lopes, A.V. 2014a. Evaluation of Moment Redistribution in Normal-Strength and High-Strength Reinforced Concrete Beams. *Journal of Structural Engineering,* vol. 140, no. 10.

Lou, T., Lopes, S.M.R. & Lopes, A.V. 2014b. FE modeling of inelastic behavior of reinforced high-strength concrete continuous beams. *Structural Engineering and Mechanics* vol. 49, no. 3, pp. 373-393.

Lou, T., Lopes, S.M.R. & Lopes, A.V., 2015. Neutral axis depth and moment redistribution in FRP and steel reinforced concrete continuous beams. *Composites: Part B.* vol. 70, pp 44-52.

Macchi, G., 1957. Moment Redistribution Beyond Elastic Limit and at Failure in Prestressed Concrete Beams. *Journal of the Prestressed Concrete Institute.* vol. 2, no. 2.

Maidl, B.R., 1995. *Steel Fibre Reinforced Concrete*, Ernst & Sohn, Berlin, p. 292

Mohr, A.W. 2012. Moment redistribution behaviour of SFRC members with varying fibre content. MEng Thesis, University of Stellenbosch.

Morice, P.B. & Lewis, H.E., 1995. The Ultimate Strength of Two-Span Continuous Prestressed Concrete Beams as Affected by Tendon Transformation and Un-tensioned Steel. *F.I.P. Second Congress*. Amsterdam, Session 3a, Paper No. 5.

Mortezai, A. & Ronagh, H.R., 2012. Plastic hinge length of FRP reinforced concrete columns subjected to both far-fault and near-fault found motions. *Scientia Iranica*. vol. 19, no. 6, pp. 1365-1378.

Naaman, A. E., 2003. Engineered Steel Fibers with Optimal Properties for Reinforcement of Cement Composites. *Journal of Advanced Concrete Technology*. vol. 1, no. 3, pp. 241–252.

Naaman, A.E. 2007. Tensile strain-hardening FRC composites: Historical evolution since the 1960's. *Advances in construction materials*, pp.181-202

Naaman, A. & Shah, S., 1979. Fracture and Multiple Cracking of Cementitious Composites. *Fracture Mechanics Applied to Brittle Materials.* vol. 678, pp.183-201.

Nataraja, M.C., Dhang, N. & Gupta, A.P., 1999. Stress-strain curves for steel-fiber reinforced concrete under compression. *Cement & Concrete Composites*. vol 21, pp. 383-390.

Neville, A.M. 1978. *Properties of Concrete*, Pitman International, London, pp. 480-483

Neville, A. M. 1997. Aggregate Bond and Modulus of Elasticity of Concrete. *ACI Materials Journal*, January-February 1997, pp. 71-74.

NT-Build511, 2005. *Wedge splitting test method (WST): fracture testing of fibre-reinforced concrete (mode I)*, Nordtest.

Oehlers, D. J., Haskett, M., Mohamed Ali, M.S. & Griffith, M.C. 2010. Moment redistribution in reinforced concrete beams. *Structures and Buildings,* vol. 163, no. 3, pp. 165-176.

Oehlers, D.J., Ju, G. Liu, I.S.T. & Seracino, R., 2004a. Moment redistribution in continuous plated RC flexural members. Part 1: neutral axis depth approach and tests. *Engineering Structures.* vol. 26, no. 14, pp. 2197-2207.

Oehlers, D.J., Liu, I.S.T., Ju. G. & Seracino, R., 2004b. Moment redistribution in continuous plated RC flexural members. Part 2: Flexural rigidity approach. *Engineering Structures.* vol. 26, no. 14, pp. 2209-2218.

Olivito, R.S. & Zuccarello, F.A., 2010. Composites: Part B: An experimental study on the tensile strength of steel fiber reinforced concrete. *Composites Part B*. vol 41, no.3, pp. 246–255.

Østergaard, L., Walter, R. & Olesen, J.F. 2005. Method for determination of tensile properties of engineered cementitious composites (ECC), *Construction Materials: Proceedings of ConMat'05 and Mindess Symposium*, p. 74.

Paegle, I., 2015. Characterization and modeling of fiber reinforced concrete for structural applications in beams and plates. PhD Thesis. Technical University of Denmark: DTU Civil Engineering.

Paegle, I., Fischer, G., & Jönsson, J., 2015. *Characterization and modelling of fiber reinforced concrete for structural applications in beams and plates*. Technical University of Denmark, Department of Civil Engineering. (BYG Rapport, vol. 327).

Park, R. & Paulay, T. 1975. *Reinforced Concrete Structures*. John Wiley & Sons, Inc. Canada

Park, R., Priestley, M.J.N. & Gill, W.D., 1982. Ductility of square-confined concrete columns. *Journal of Structural Division ASCE*. vol. 108, no. 4, pp. 929–950.

Paulay, T. & Priestley, M.J.N., 1992. *Seismic Design of Reinforced Concrete and Masonry Buildings*, John Wiley and Sons, New York.

Priestley, M.J.N. & Park, R. 1987. Strength and ductility of concrete bridge columns under seismic loading, *ACI Structural Journal*, vol. 84, no. 1, pp. 61–76.

Qian, S. & Li, V.C. 2008. Simplified inverse method for determining the tensile properties of SHCCs. *Journal of Advanced Concrete Technology*, vol. 6, no. 2, pp.353–363.

Reddy, C.S., 2007. *Basic Structural Analysis, Second edition.* Tata McGraw-Hill Publishing Company Limited, New Delhi.

Rigaud, S., Chanvillard, G. & Chen, J.J. 2012. Characterization of bending and tensile behaviours of ultra-high-performance concrete containing glass fibers. *High Performance Fiber Reinforced Cement Composites*, vol 6, pp 373-380.

RILEM TC 162-TDF, 2002. Test and Design Methods for Steel Fibre Reinforced Concrete: Bending test - Final Recommendation. *Journal of Materials and Structures*, V.35. PP 579-582.

Rocco, C., Guinea, G., Planas, J., and Elices, M. 1999. Size effect and boundary conditions in the Brazilian test: theoretical analysis. *Materials and Structures*, vol. 32, pp. 437-444.

Romualdi, J.P. & Mandel, J.A., 1964. Tensile strength of concrete affected by uniformly distributed and closely spaced short lengths of wire reinforcement. *American Concrete Institute – Journal*. vol. 61 no. 6, pp.657–671.

Santos, P., Laranja, G., França & Correia, J.R. 2013. Ductility and moment redistribution capacity of multi-span T-section concrete beams reinforced with GFRP bars. *Construction and Building Materials.* vol. 49, pp. 949-961.

Schumacher, P. 2006. Rotation Capacity of Self-Compacting Steel Fiber Reinforced Concrete. PhD Thesis, Darmstadt University of Technology, Germany.

Scott, R.H. & Whittle, R.T., 2005. Moment redistribution effects in beams. *Magazine of Concrete Research*, vol. 57, no. 1, pp. 9-20.

Shah, B.V. S.P. Rangan, 1971. Fiber reinforced concrete properties. *J Amer Concrete Inst*. vol. 682, pp.126–35.

Shionaga, R. 2006. Structural behavior of high performance fiber reinforced concrete in tension and bending, 6th International PhD symposium in civil engineering, Zürich, August 23-26, 2006, Switzerland.

Sujivorakul, C., Waas, A.M., and Naaman, A.E., 2000. Pull-out response of a smooth fiber with an end anchorage. *Journal of Engineering Mechanics.* September 2000, pp. 986-993.

Swamy, R.N., Mangat, P.S. & Rao, C.V.S.K., 1974. The Mechanics of Fiber Reinforcement of Cement Matrices. *ACI Special Publication*. vol. 44, pp.1–28.

Take, W.A. 2002. The influence seasonal moisture cycles on clay slopes. PhD Thesis, University of Cambridge

Tang, T. 1994. Effects of load-distributed width on split tension of unnotched and notched cylindrical specimens. *Journal of testing and Evaluation*, vol. 22, no.5, pp. 401–409.

Timoshenko, S. & Goodier, J. 1970. *Theory of Elasticity* (3rd edition). McGraw-Hill Book Company.

Visintin, P., Mohamad Ali, M.S. & Sturm, A.B. 2018. Experimental investigation of moment redistribution in ultra-high-performance fibre reinforced concrete beams. *Construction and Building Materials.* vol. 166, pp. 433-444.

Werzbrger, S., Karinski, Y.S. & Dancygier, A.N. 2017. Quantification of cracking localization in fibre-reinforced concrete beams. *IOP Conference Series: Materials Science and Engineering,* vol. 246.

White, D. J. 2002. An investigation into the behaviour of pressed-in piles. PhD Thesis. University of Cambridge.

Wood, R.H., 1968. Some controversial and curious developments in the plastic theory of structures. In Engineering Plasticity (Heyman J and Leckie FA (eds)). *Cambridge University Press*, Cambridge, pp. 665–691.

Yoo, D. & Banthia, N., 2016. Mechanical properties of ultra-high-performance fiber-reinforced concrete: A review. *Cement and Concrete Composites*. vol. 73, pp. 267–280.

Zhao, X., Wu, Y, Leung, A.Y. & Lam, H.F. 2011. Plastic Hinge Length in Reinforced Concrete Flexural Members. *Procedia Engineering*, vol. 14, pp 1266-1274

APPENDIX A
Images of Continuous beam tests

1) BEAM: 0B0.7

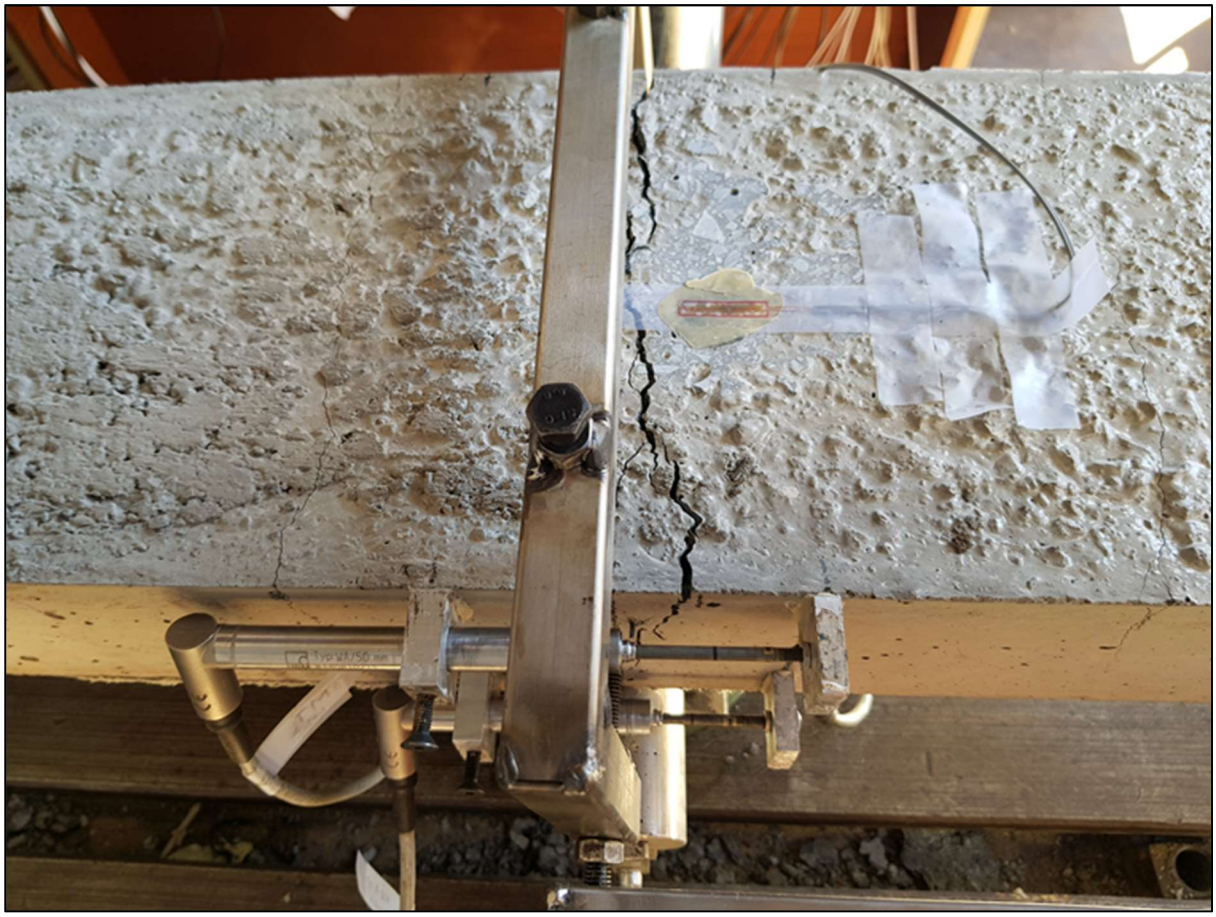

Figure B. 1: Cracked section at centre support

Figure B. 2: Cracked section under left span

2) BEAM: 0B1.4

Figure B. 3: Cracked section at centre support

Figure B. 4: Cracked section at right span after testing

3) BEAM: 1B0

Figure B. 5: Cracking at centre support during testing

4) BEAM: 1B0.7

Figure B. 6: Cracking at centre support during testing

Figure B. 7: Cracked right span after testing

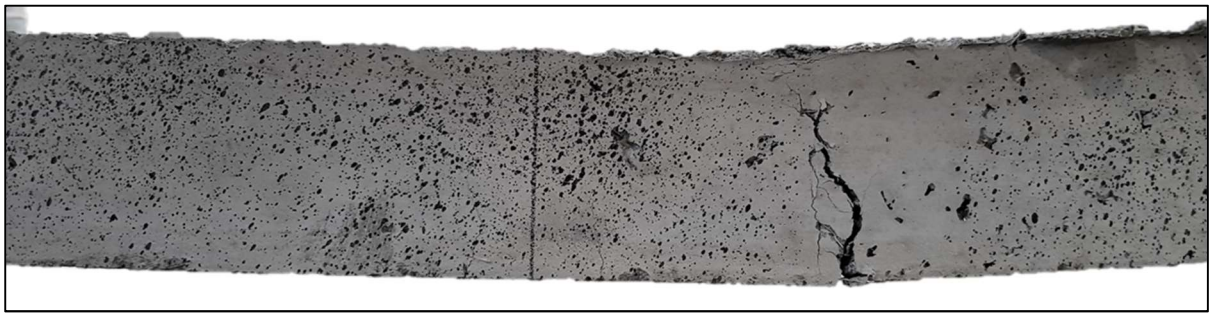

Figure B. 8: Cracked left span after testing

5) BEAM: 1B1.4

Figure B. 9: Crack spacing near centre support during testing

Figure B. 10: Crack spacing along right span during testing

Figure B. 11: Crack spacing along left span during testing

6) BEAM: 1B2.2

Figure B. 12: Cracked section at the centre support after testing

Figure B. 13: Cracks at left span after testing

Figure B. 14: Crack spacing along right span during testing

7) BEAM: 1.5B0

Figure B. 15: Failure at centre support and left span

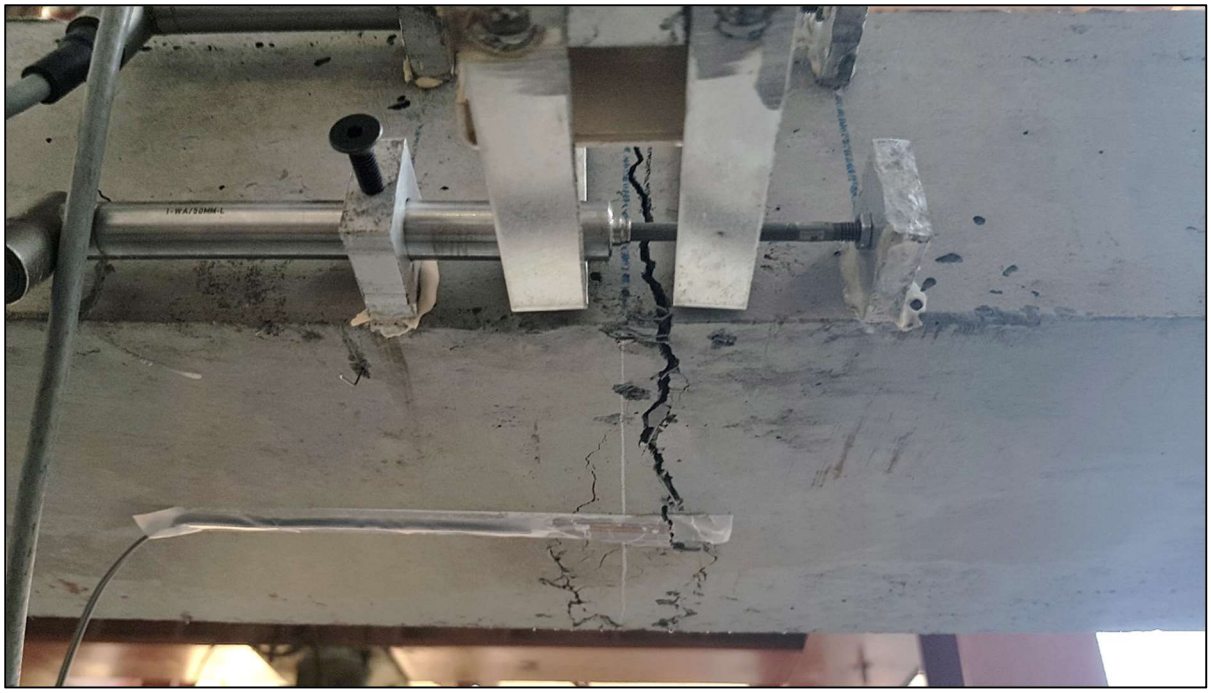

Figure B. 16: Cracking under left span during testing

Figure B. 17: Cracking above centre support during testing

8) BEAM: 1.5B0.7

Figure B. 18: Crack formation near centre support during testing

Figure B. 19: Crack spacing along right span during testing

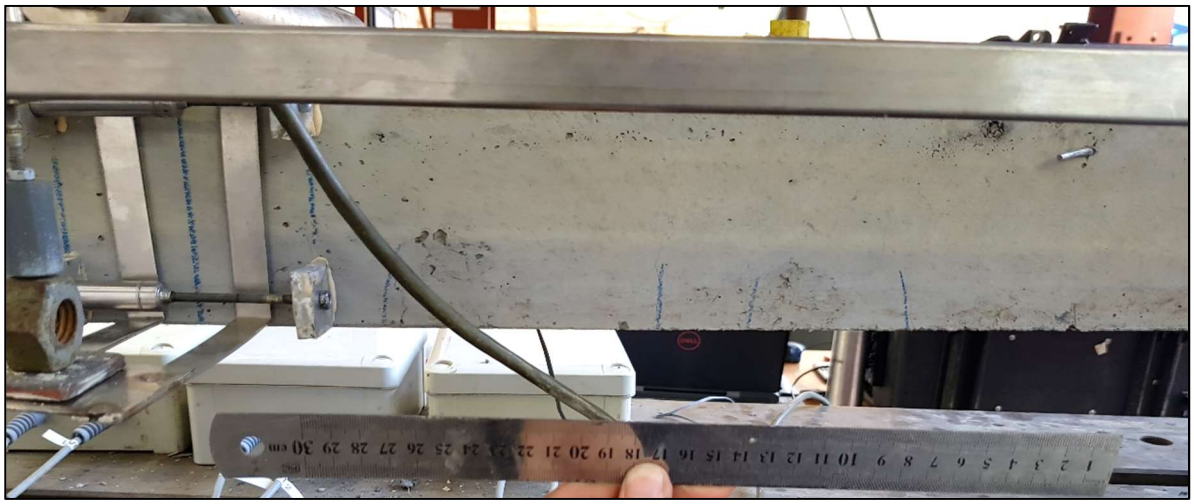

Figure B. 20: Crack spacing along left span during testing

9) BEAM: 1.5B1.4

Figure B. 21: Cracking above centre support after testing

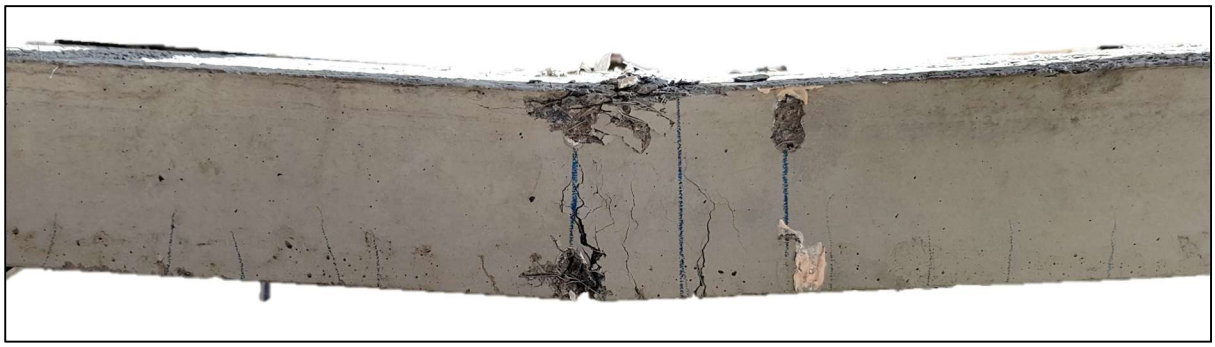

Figure B. 22: Crack formation of left span after testing

Figure B. 23: Crack spacing along right span during testing

10) BEAM: 1.5B2.2

Figure B. 24: Crack formation above centre support during testing

Figure B. 25: Crack formation along right span during testing

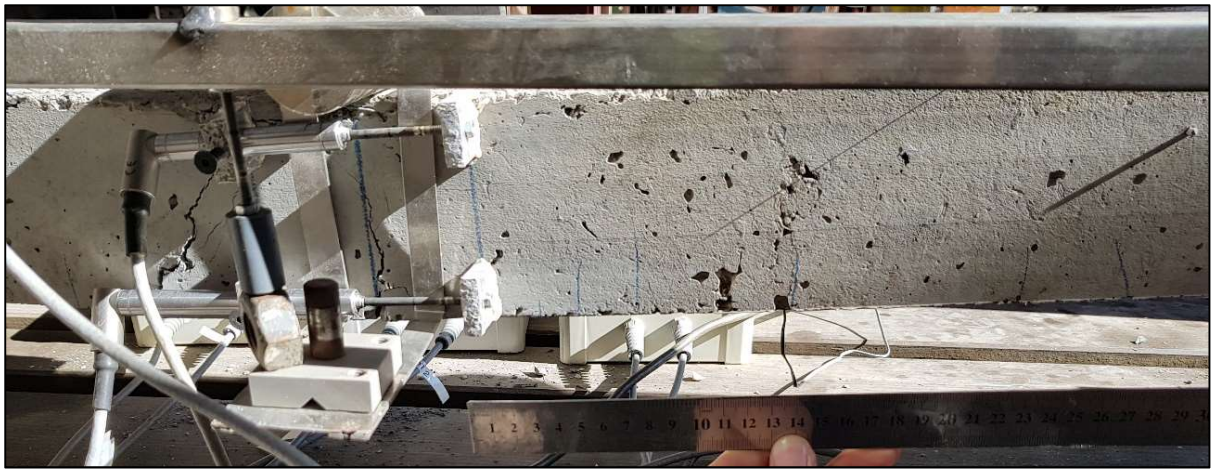

Figure B. 26: Crack spacing along left span during testing

11) BEAM: 2B0

Figure B. 27: Crack formation above centre support during testing

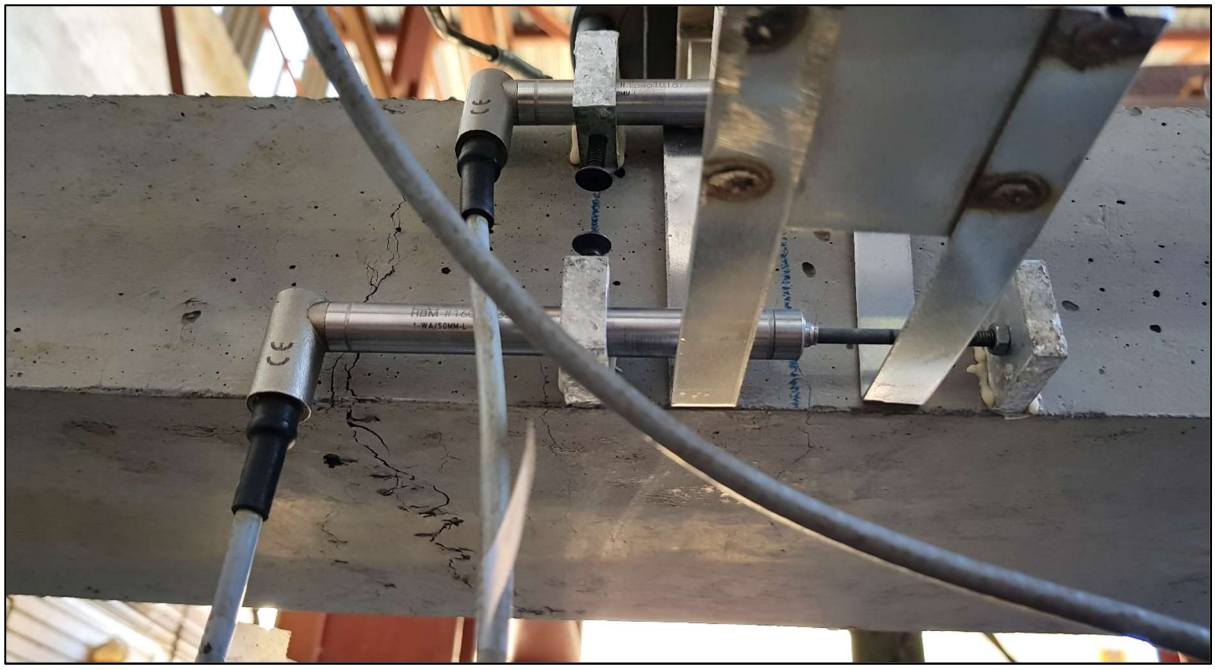

Figure B. 28: Crack formation along right span during testing

12) BEAM: 2B0.7

Figure B. 29: Crack formation above centre support

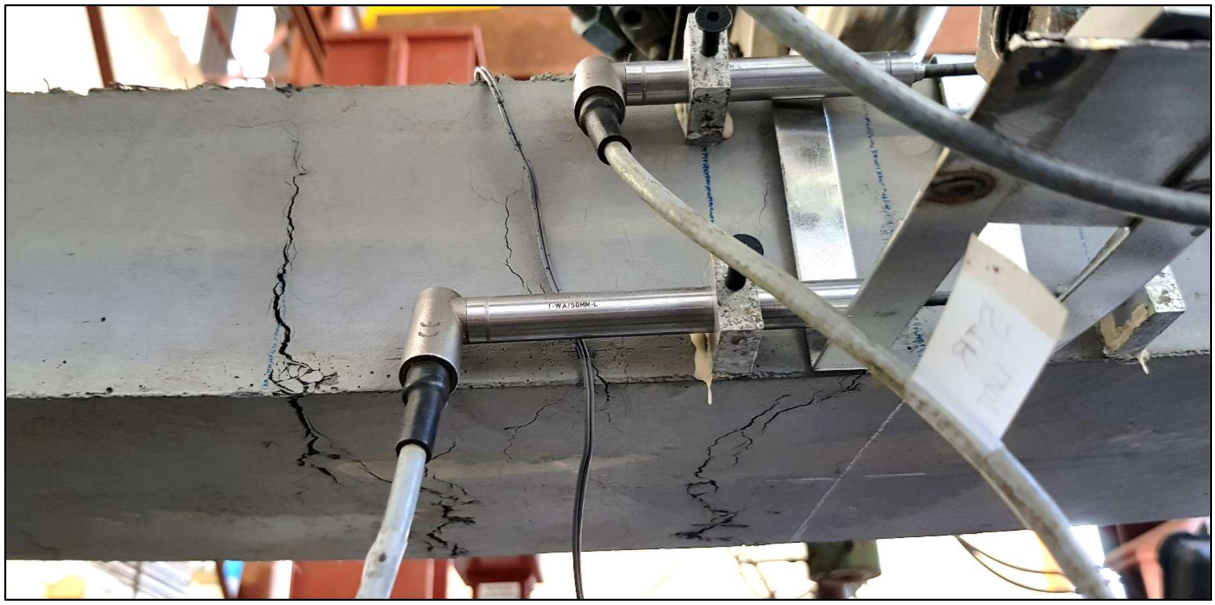

Figure B. 30: Crack formation along right span during testing

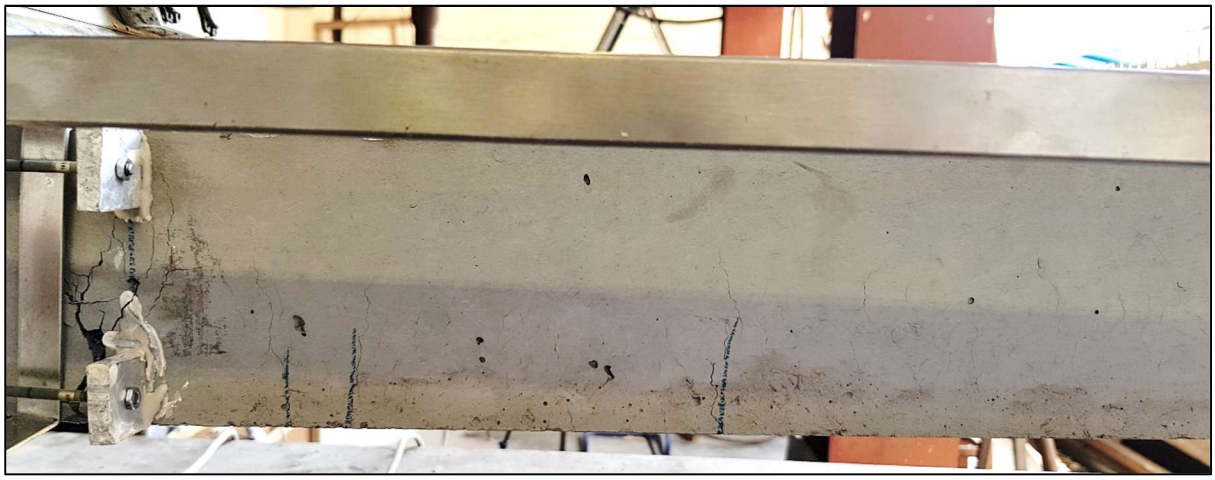

Figure B. 31: Crack spacing along left span during testing

13) BEAM: 2B1.4

Figure B. 32: Crack formation above centre support after testing

Figure B. 33: Crack formation along left span after testing

Figure B. 34: Crack formation along right span after testing

14) BEAM: 2B1.4

Figure B. 35: Crack formation near the centre support during testing

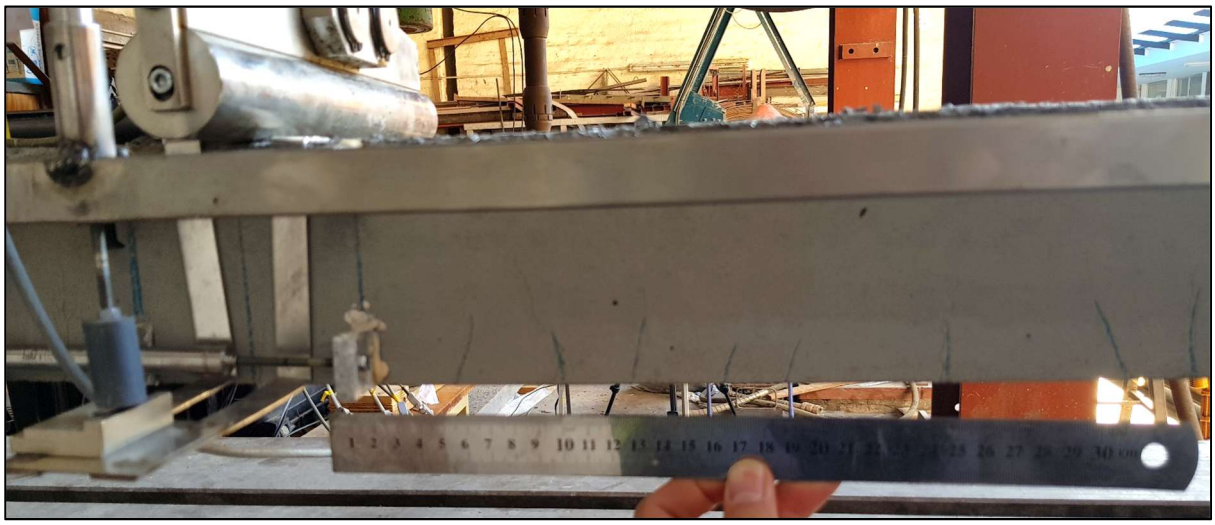

Figure B. 36: Crack formation along the left span during testing

APPENDIX B
Examples of Moment redistribution results

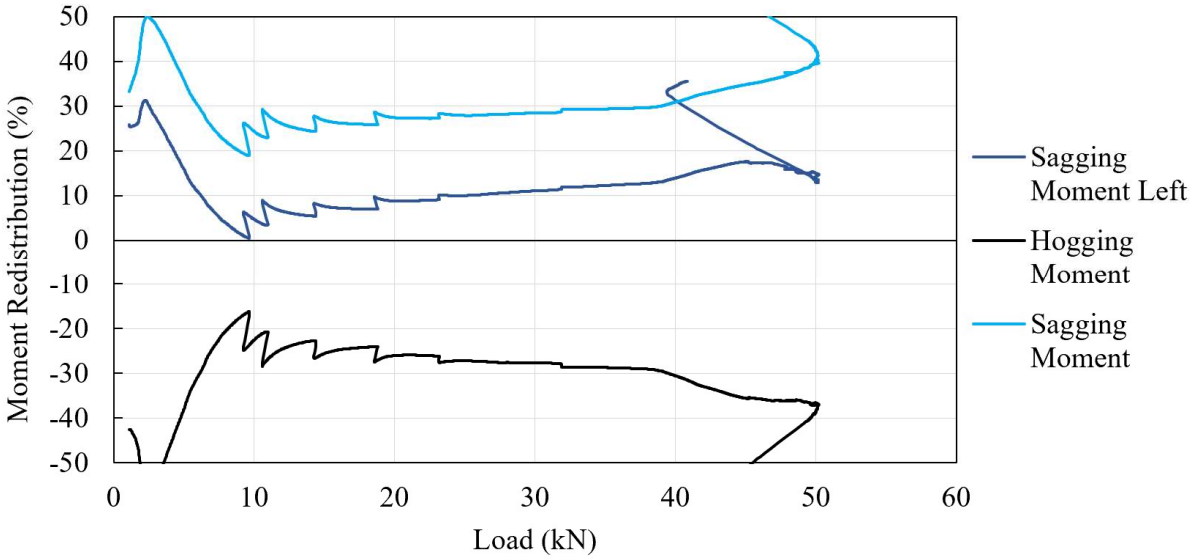

Figure C. 1: Moment redistribution of beam 0B1.4

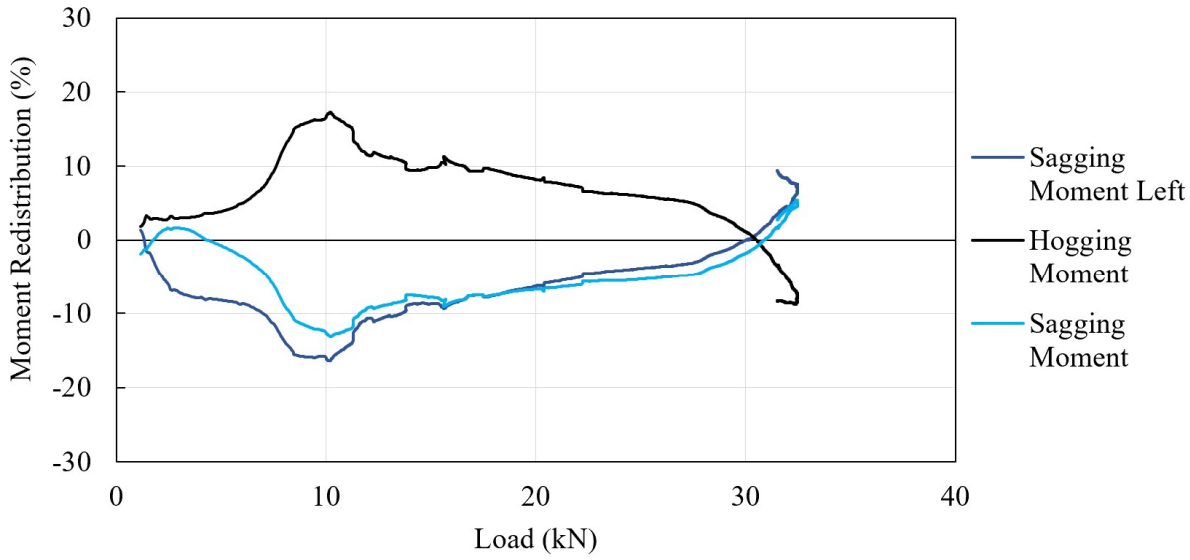

Figure C. 2: Moment redistribution of beam 1B0.7

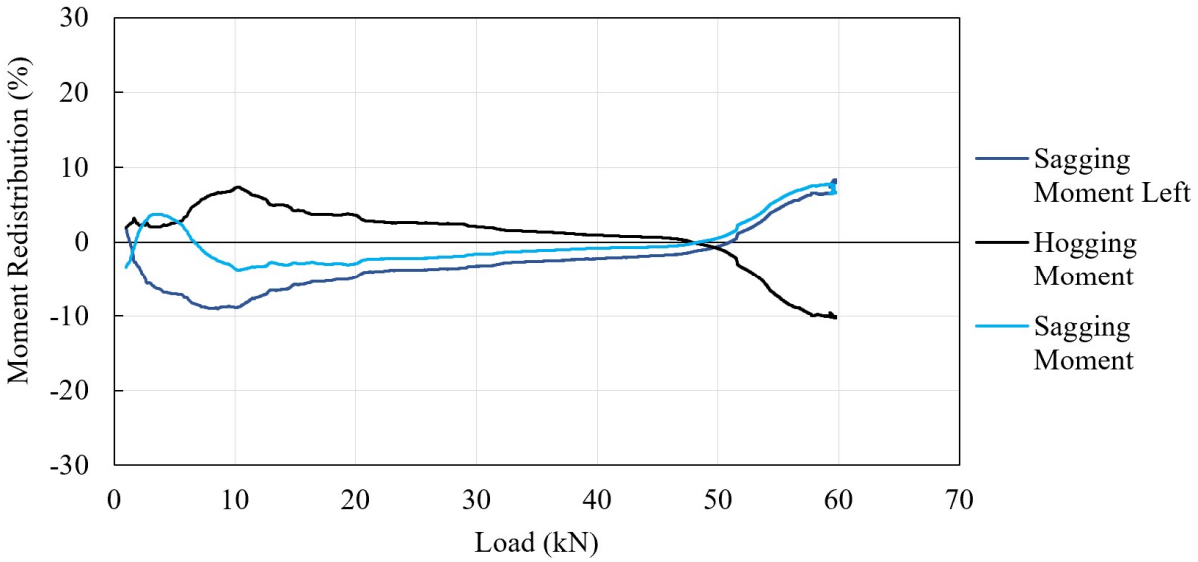

Figure C. 3: Moment redistribution of beam 1B1.4

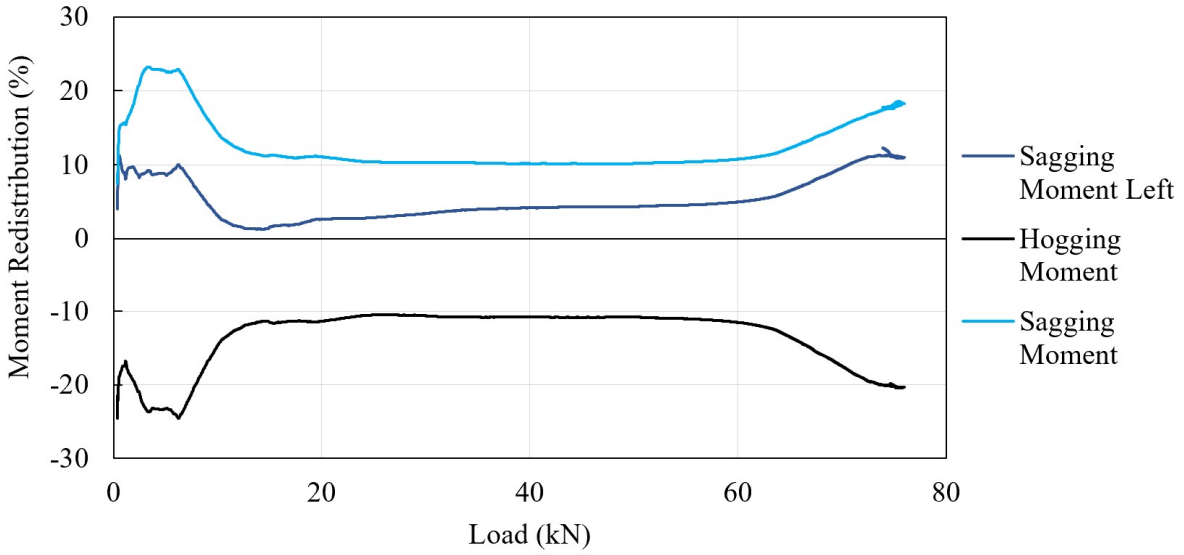

Figure C. 4: Moment redistribution of beam 1B2.2

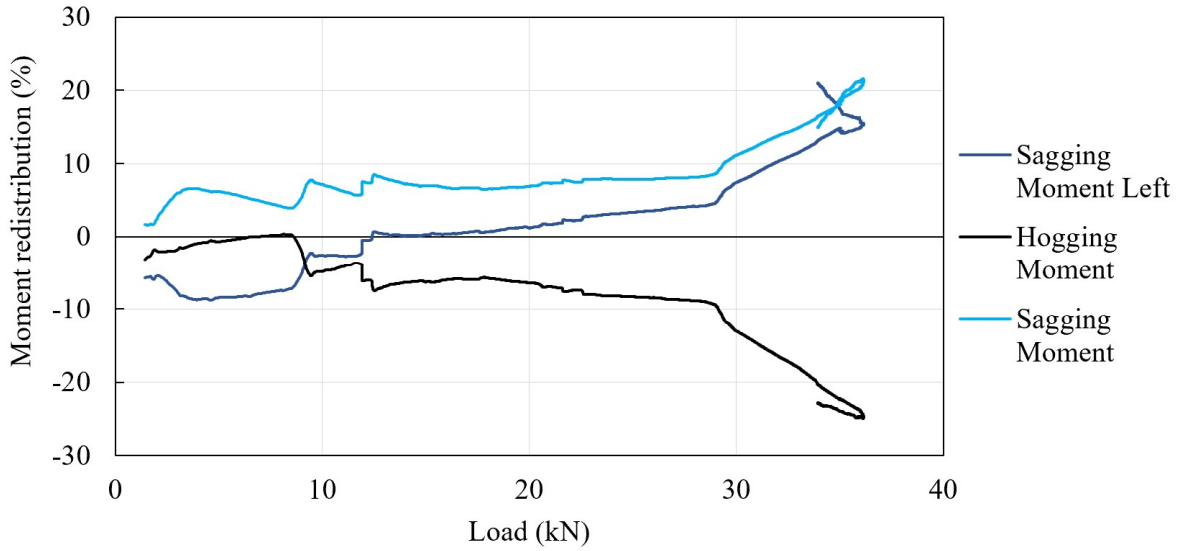

Figure C. 5: Moment redistribution of beam 1.5B0.7

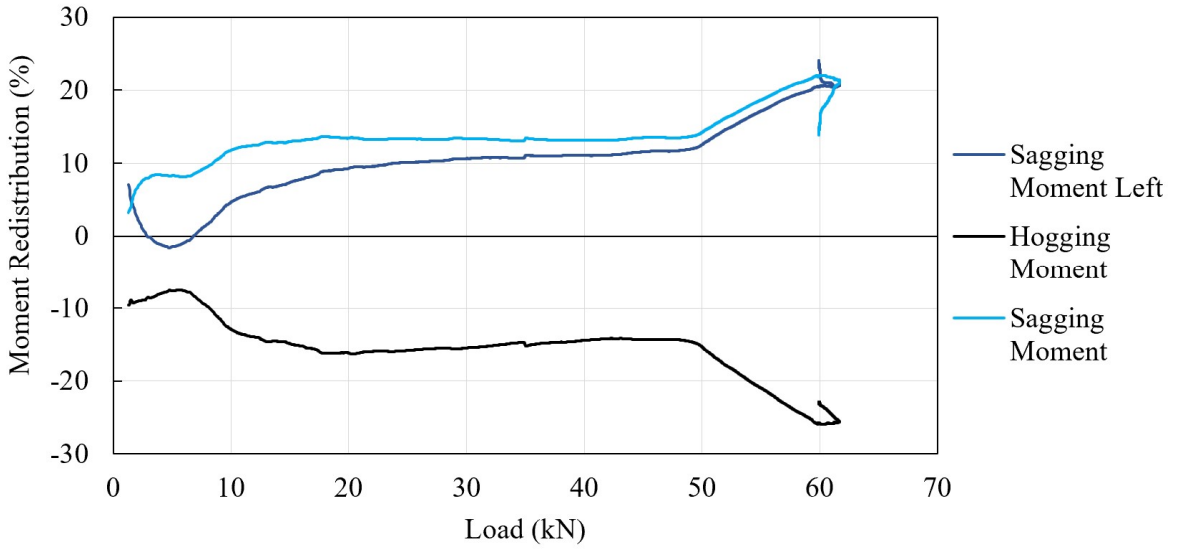

Figure C. 6: Moment redistribution of beam 1.5B1.4

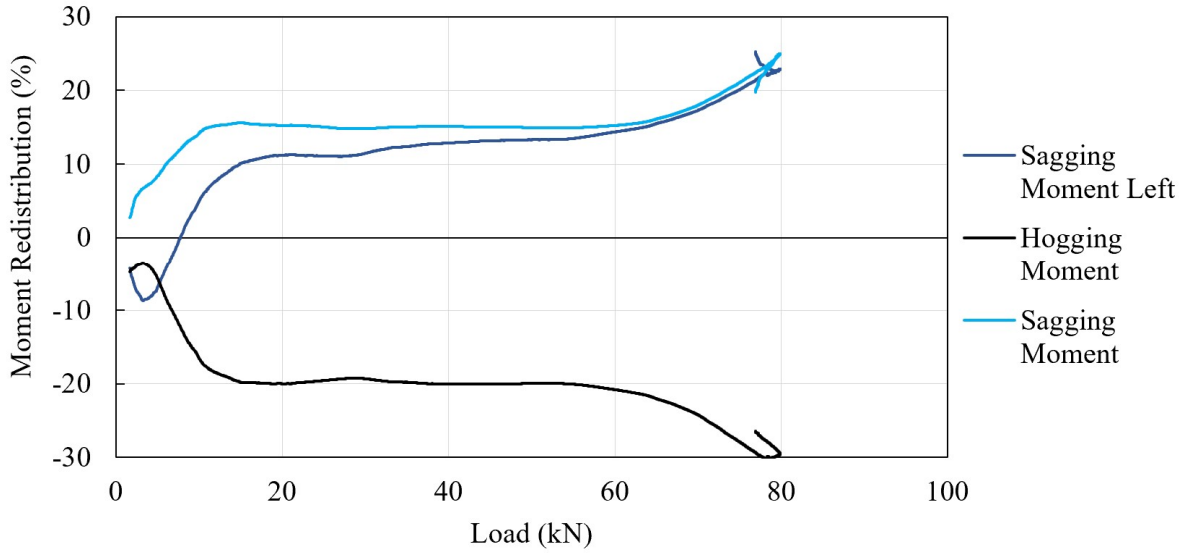

Figure C. 7: Moment redistribution of beam 1.5B2.2

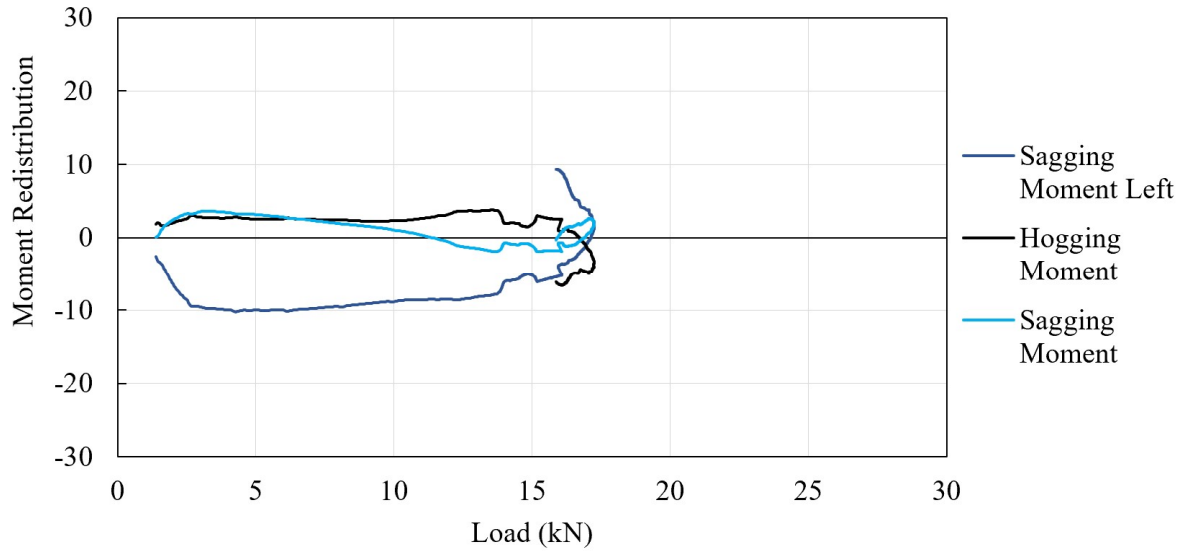

Figure C. 8: Moment redistribution of beam 2B0

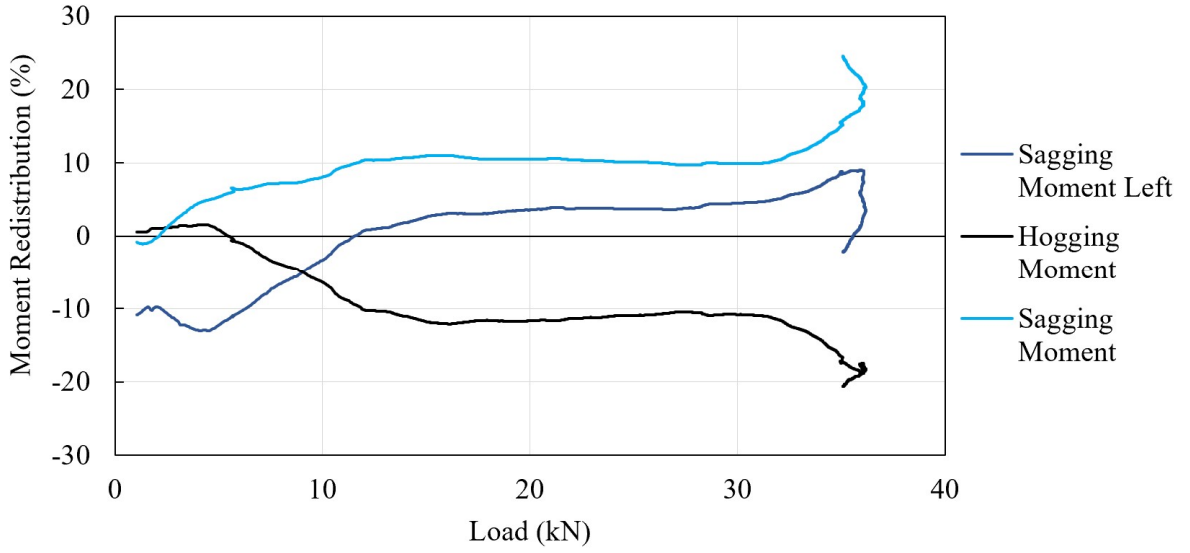

Figure C. 9: Moment redistribution of beam 2B0.7

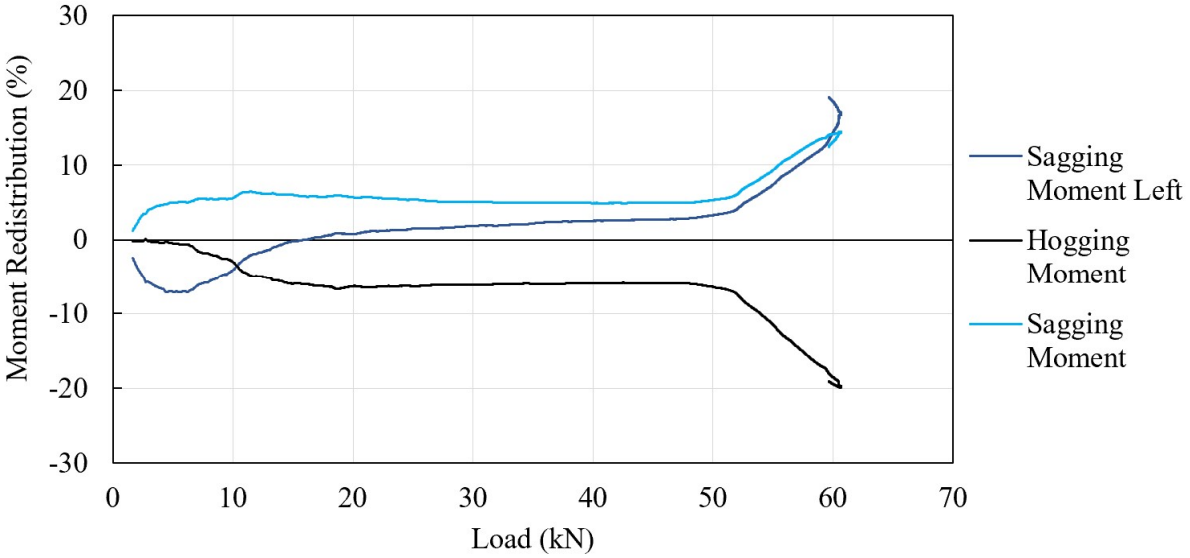

Figure C. 10: Moment redistribution of beam 2B1.4

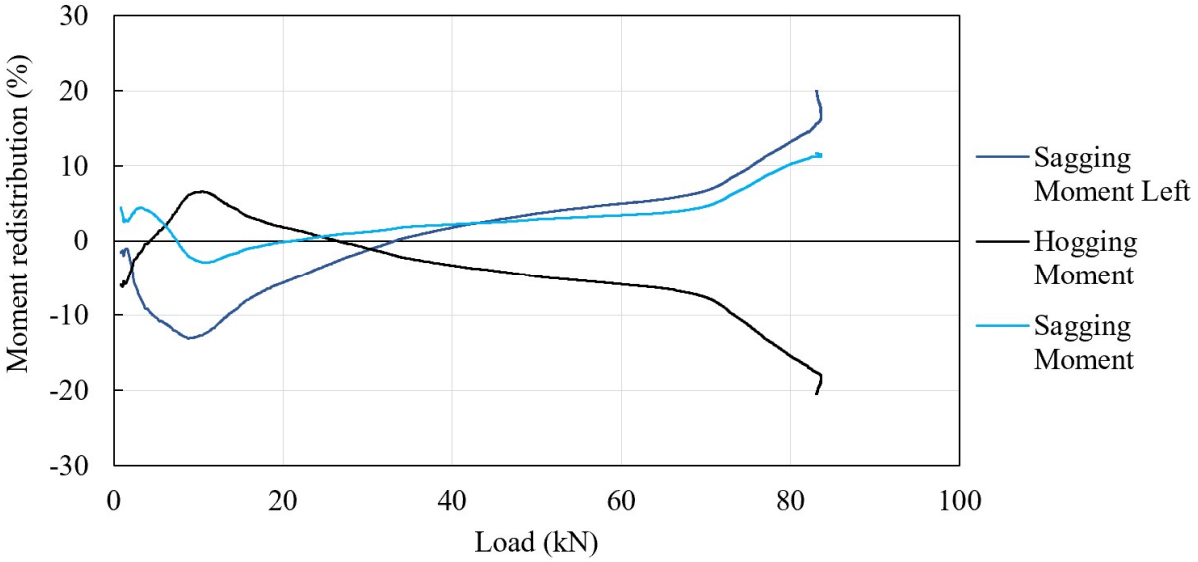

Figure C. 11: Moment redistribution of beam 2B2.2

APPENDIX C
Plastic Hinge Length Graphs

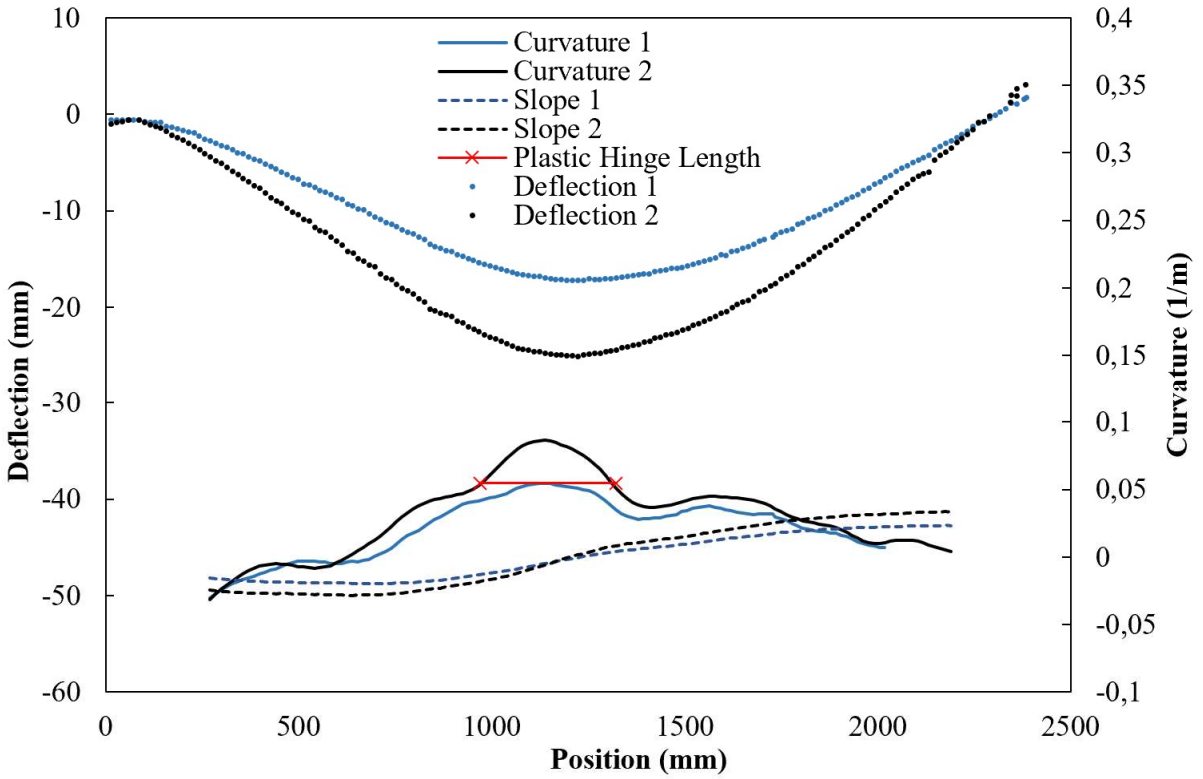

Figure D. 1: Deflection, slope, curvature and plastic hinge length of beam 1B0.7

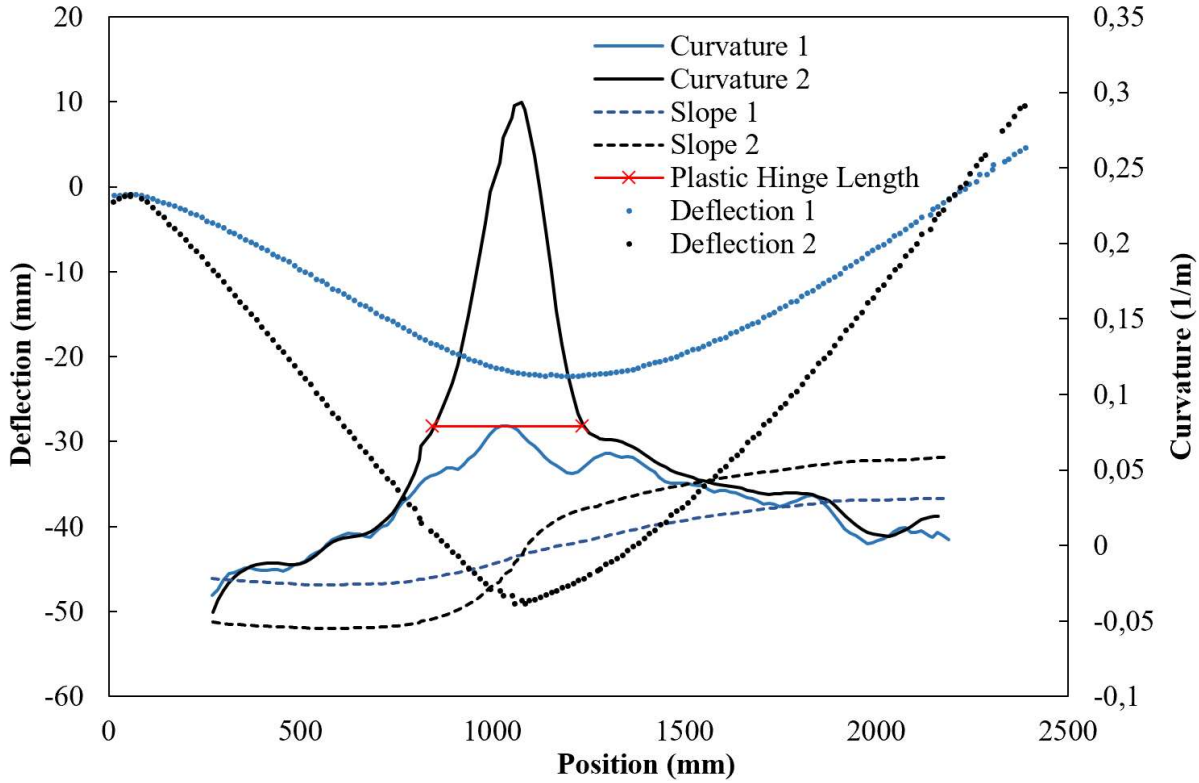

Figure D. 2: Deflection, slope, curvature and plastic hinge length of beam 1B1.4

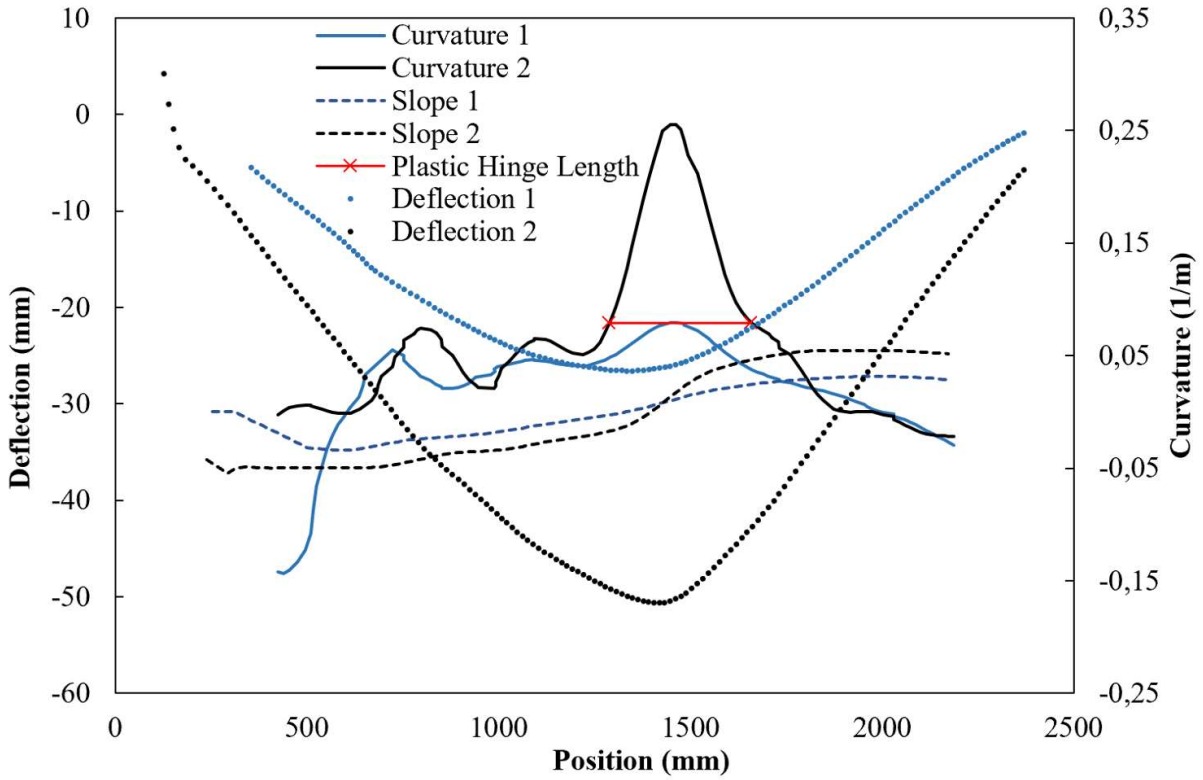

Figure D. 3: Deflection, slope, curvature and plastic hinge length of beam 1B2.2

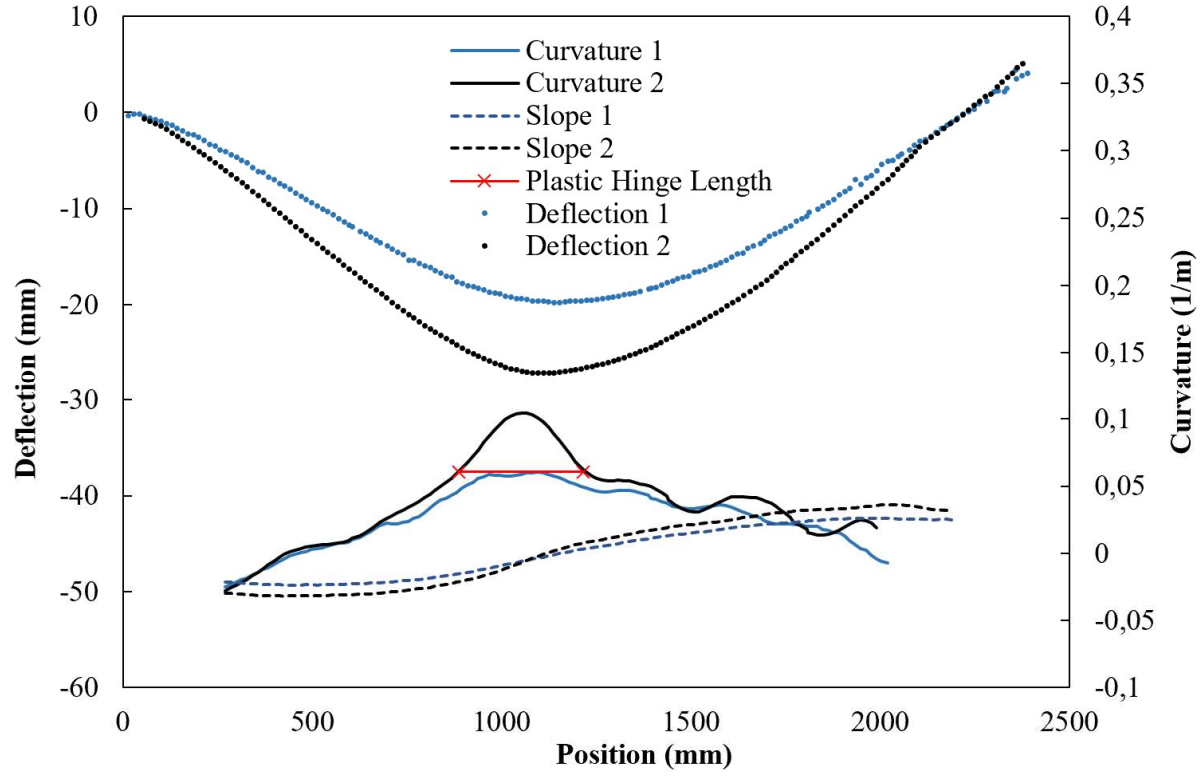

Figure D. 4: Deflection, slope, curvature and plastic hinge length of beam 1.5B0.7

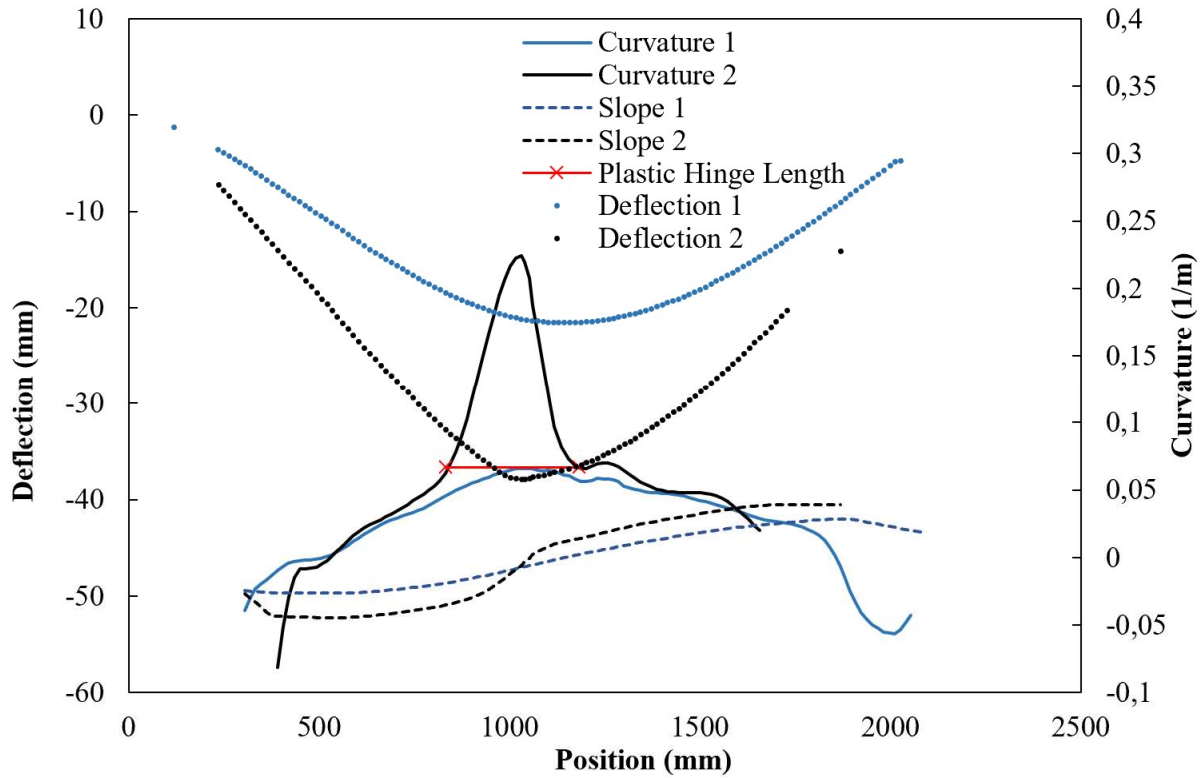

Figure D. 5: Deflection, slope, curvature and plastic hinge length of beam 1.5B1.4

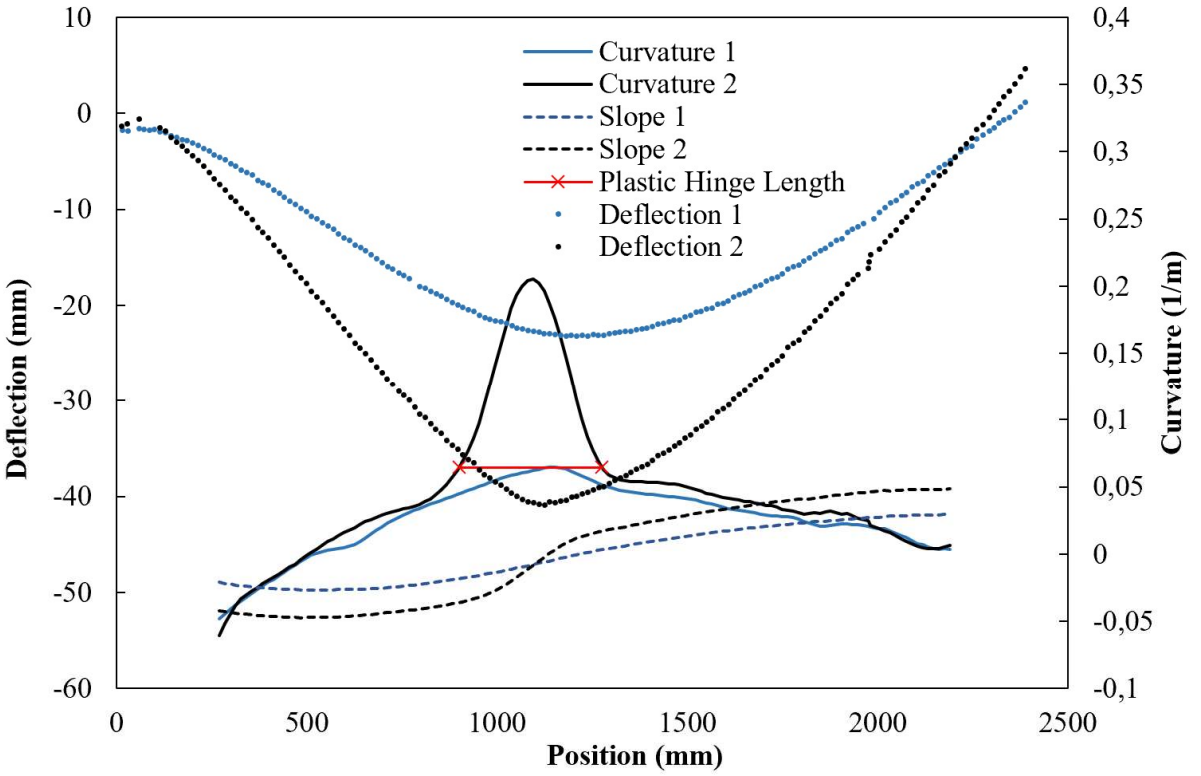

Figure D. 6: Deflection, slope, curvature and plastic hinge length of beam 1.5B2.2

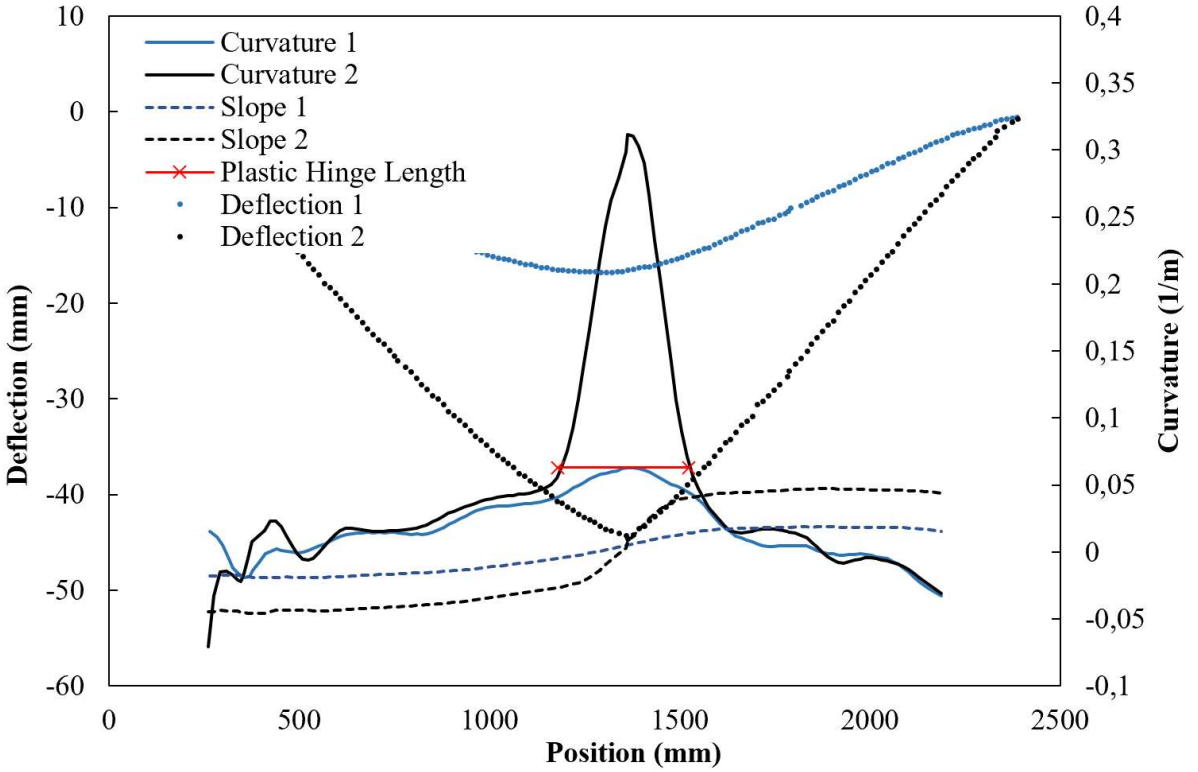

Figure D. 7: Deflection, slope, curvature and plastic hinge length of beam 2B0.7

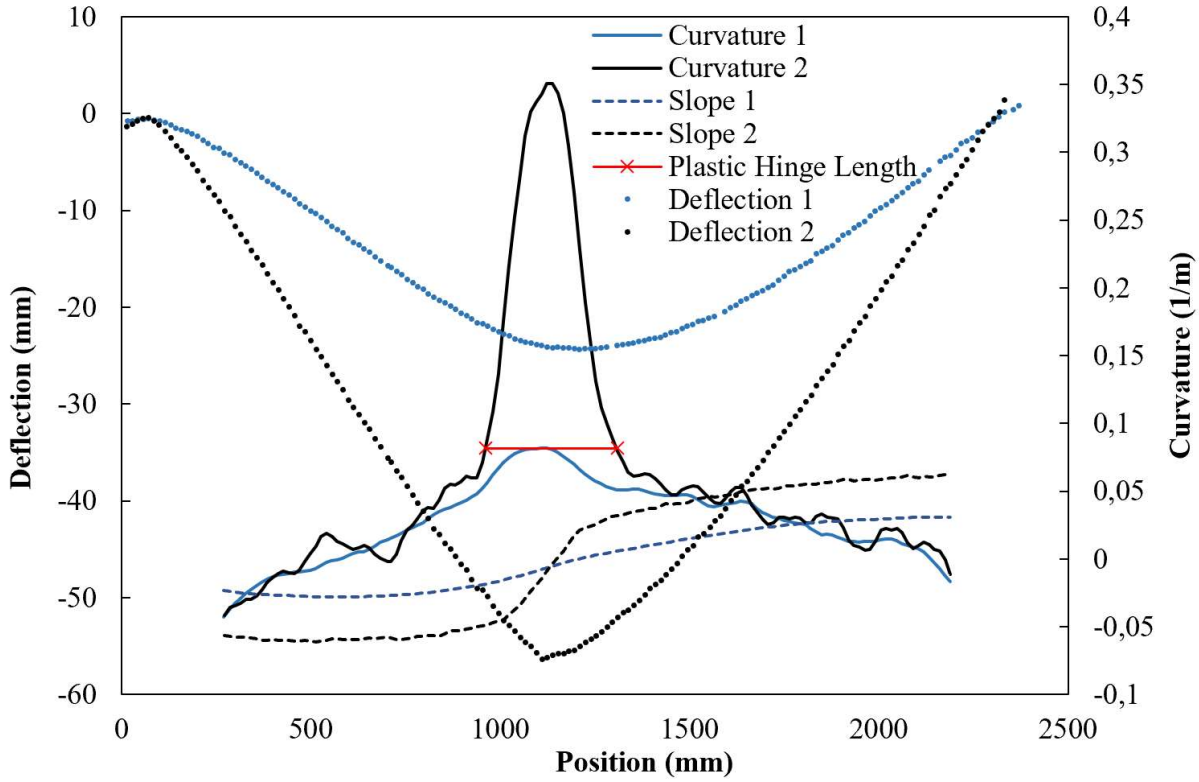

Figure D. 8: Deflection, slope, curvature and plastic hinge length of beam 2B1.4

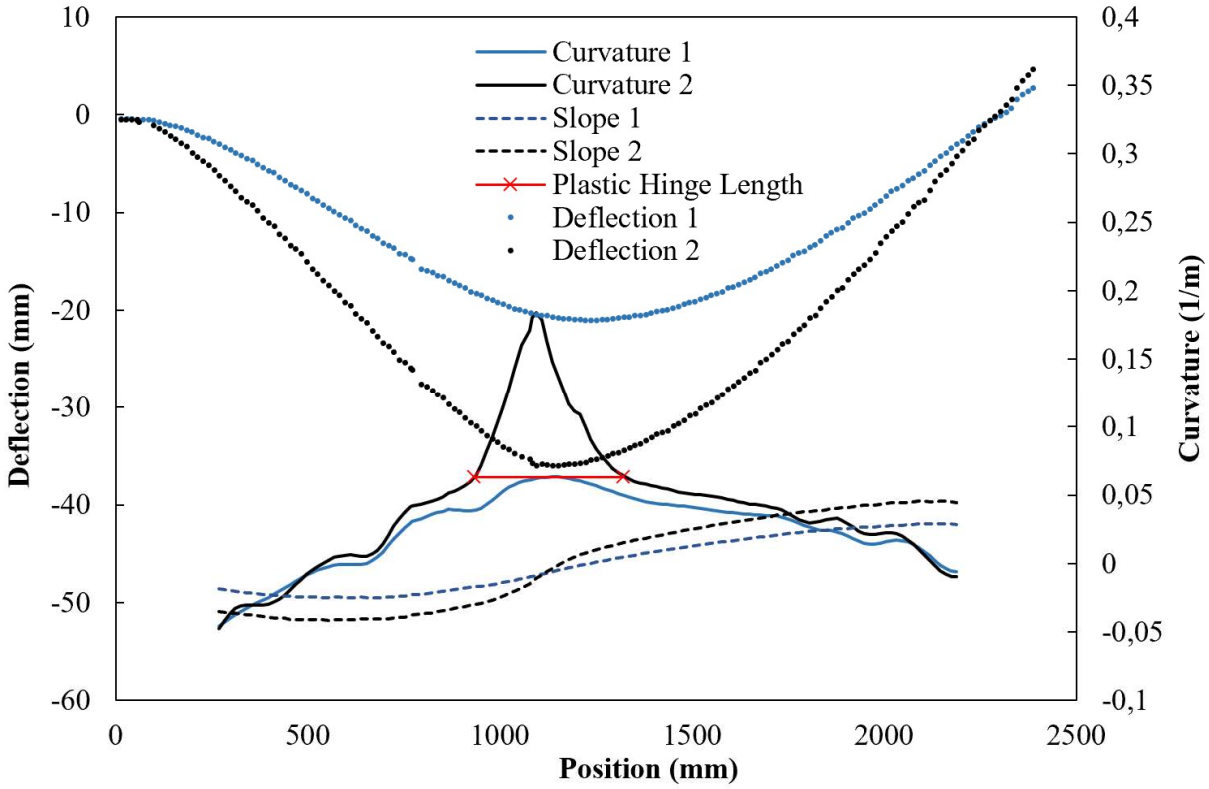

Figure D. 9: Deflection, slope, curvature and plastic hinge length of beam 2B2.2